CRANFIELD UNIVERSITY

HUA WANG

NUMERICAL AND ARTIFICIAL NEURAL NETWORK MODELLING OF FRICTION STIR WELDING

SCHOOL OF APPLIED SCIENCE

PhD THESIS

Academic year: 2007-2011

Supervisor: Dr. Paul Colegrove

November 2011

CRANFIELD UNIVERSITY

SCHOOL OF APPLIED SCIENCE

PhD THESIS

Academic Year 2007-2011

HUA WANG

NUMERICAL AND ARTIFICIAL NEURAL NETWORK MODELLING OF FRICTION STIR WELDING

Supervisor: Dr. Paul Colegrove

November 2011

This thesis is submitted in partial fulfilment of the requirements for the degree of Doctor of Philosophy

Abstract

This thesis is based on the PhD work of investigating the Friction Stir Welding process (FSW) with numerical and Artificial Neural Network (ANN) modelling methods. FSW was developed at TWI in 1991. As a relatively new technology it has great advantages in welding aluminium alloys which are difficult to weld with traditional welding processes. The aim of this thesis was the development of new modelling techniques to predict the thermal and deformation behaviour.

To achieve this aim, a group of Gleeble experiments was conducted on 6082 and 7449 aluminium alloys, to investigate the material constitutive behaviour under high strain-rate, near solidus conditions, which are similar to what the material experiences during the FSW process. By numerically processing the experimental data, new material constitutive constants were found for both alloys and used for the subsequent FSW modelling work. Importantly no significant softening was observed prior to the solidus temperature.

One of the main problems with numerical modelling is determining the values of adjustable parameters in the model. Two common adjustable parameters are the heat input and the coefficients that describe the heat loss to the backing bar. To predict these coefficients more efficiently a hybrid model was created which involved linking a conventional numerical model to an ANN model. The ANN was trained using data from the numerical model. Then thermal profiles were abstracted (summarised) and used as inputs; and the adjustable parameters were used as outputs. The trained ANN could then use abstracted thermal profiles from welding experiments to predict the adjustable parameters in the model.

The first stage involved developing a simplified FE thermal model which represents a typical welding process. It was used to find the coefficients that describe the heat loss to the backing bar, and the amount of power applied in the model. Five different thermal boundary conditions were studied, including both convective and ones that included the backing bar with a contact gap conductance. Three approaches for abstracting the

thermal curves and using as inputs to the ANN were compared. In the study, the characteristics of the ANN model, such as the ANN topology and gradient descent method, were evaluated for each boundary condition for understanding of their influences to the prediction. The outcomes of the study showed that the hybrid model technique was able to determine the adjustable parameters in the model effectively, although the accuracy depended on several factors. One of the most significant effects was the complexity of the boundary condition. While a single factor boundary condition (e.g. constant convective heat loss) could be predicted easily, the boundary condition with two factors proved more difficult. The method for inputting the data into the ANN had a significant effect on the hybrid model performance. A small number of inputs could be used for the single factor boundary condition, while two factors boundary conditions needed more inputs. The influences from the characteristics of the ANN model were smaller, but again thermal model with simpler boundary condition required a less complex ANN model to achieve an accurate prediction, while models with more complex boundary conditions would need a more sophisticated ANN model.

In the next chapter, the hybrid method was applied to a FSW process model developed for the Flexi-stir FSW machine. This machine has been used to analyse the complex phase changes that occur during FSW with synchrotron radiation. This unique machine had a complex backing bar system involving heat transfer from the aluminium alloy workpiece to the copper and steel backing bars. A temperature dependent contact gap conductance which also depends on the material interface type was used. During the investigation, the ANN model topologies (i.e. GFF and MFF) were studied to find the most effective one. Different abstracting methods for the thermal curves were also compared to explore which factors (e.g. the peak temperature in the curve, cooling slope of a curve) were more important to be used as an input. According to close matching between the simulation and experimental thermal profiles, the hybrid model can predict both the power and thermal boundary condition between the workpiece and backing bar. The hybrid model was applied to six different travel speeds, hence six sets of heat input and boundary condition factors were found. A universal set was calculated from the six outcomes and a link was discovered between the accuracy of the temperature predictions and the plunge depth for the welds.

Finally a model with a slip contact condition between the tool and workpiece was used to investigate how the material flow behaviour was affected by the slip boundary condition. This work involved aluminium alloys 6082-T6 and 7449-T7, which have very different mechanical properties. The application of slip boundary condition was found to significantly reduce the strain-rate, compared to a stick condition. The slip condition was applied to the Flexi-stir FSW experiments, and the results indicated that a larger deformation region may form with the slip boundary condition.

The thesis successfully demonstrates a new methodology for determining the adjustable parameters in a process model; improved understanding of the effect of slip boundary conditions on the flow behaviour during FSW and insight in to the behaviour of aluminium alloys at temperatures approaching the solidus and high strain-rates.

Key words: modelling friction stir welding, artificial neural network, constitutive behaviour of aluminium alloys, heat transfer numerical modelling, computational fluid dynamics, CFD

Acknowledgements

This thesis would not be possible without the generous financial sponsorship of Virtual Institute for Improving Performance and Productivity of Integral Structures through Fundamental Understanding of Metallurgical Reactions in Metallic Joints (VI-IPSUS) project. The VI-IPSUS is an initiative of the Helmholtz Association coordinated by the Helmholtz-Zentrum Geesthacht (abbreviation: HZG, former GKSS Forschungszentrum).

I am profoundly grateful to my PhD supervisor, Dr Paul Colegrove, whose illuminating instructions and expert advice, has guided me through every single step of the PhD work. The thesis would never have been accomplished without his accurate and punctual feedback. Moreover he offered me countless inspirations and encouragement not only for my work but also my life.

I would sincerely thanks to Professor Stewart Williams and Dr Jorge dos Santos for the extremely helpful academic guidance. Special thanks to the excellent technical support from Jakob Hilgert, Leon Hütsch and Morelia Renteria at HZG, and Dr Joe Robson and Lee Campbell at University of Manchester. Also thanks to Dr Hans-Michael Mayer from Technische Universität Berlin for the assistance with the Gleeble experiments. The assistance from Professor Norbert Huber and Dr Jörn Mehnen on works with the ANN model was greatly appreciated. Also thanks to Jesko Hussla and Stephanie Koch for arranging the travel to Germany.

My great gratitude also goes to my friends and colleagues in WERC (Welding Engineering Research Centre) in Cranfield. My personal special thanks to my wife Yinghui Zhou for supporting me with her earnest love. Finally, I would like to thank my parents and my brother for their love, support and encouragement.

List of Abbreviations

ALE	Arbitrary Lagrangian Eulerian
ANN	Artificial Neural Networks
BP	Back Propagation
CDRX	Continuous Dynamic Recrystallization
CFD	Computational Fluid Dynamics
CSRR	Contact Shoulder Radius Ratio
DE	Differential Evolution
DRZ	Dynamically Recrystallized Region
FE	Finite Element
FSW	Friction Stir Welding
GFF	Generalized Feedforward
GTAW	Gas Tungsten Arc Welding
HAZ	Heat Affected Zone
HST	Hybrid Simulation Technique
HZG	Helmholtz-Zentrum Geesthacht
LM	Levenberg-Marquardt
MFF	Modular Feedforward
MLP	Multilayer Perceptrons
MRE	Mean Relative Error
NEM	Natural Element Method
SPH	Smoothed Particle Hydrodynamics
TDMA	Tri-Diagonal Matrix Algorithm
TMAZ	Thermomechanically Affected Zone
TWI	The Welding Institute (UK)

List of Contents

List of Figures

List of Tables

CHAPTER 1

Literature Review

Process modelling of FSW presents a multiphysics challenge due to its combination of coupled heat flow, plastic deformation and material microstructure evolution, which all contribute to the material's processability and the consequent quality of the weld[1].

Generally the intention of undertaking process modelling is to simulate some physical phenomena with partial differential equations, which are solved subsequently with a computer. When applied to FSW, the models can predict the temperature field from the heat generation at the tool shoulder and pin. The metal flow needs to be modelled as well since it is fundamental to understanding and developing this industrial process. Therefore two important subjects in modelling of FSW will be discussed in this review: heat transferring which gives the temperature field and fluid flow modelling using both analytical methods and numerical methods. This review will begin by discussing the primary principles behind the different modelling methods and will illustrate these with some simple examples. The next section will focus on FSW specifically.

1.1 Partial differential equations

1.1.1 Overall equation

Since all modelling methods are based on mathematical equations, it is necessary to start with an overall equation, which can summarize mass, momentum or energy conservation. Versteeg[2] explained that each of the conservation equations could be reduced to the following equation for property ϕ:

$$\frac{\partial(\rho \cdot \phi)}{\partial t} + div(\rho \cdot \phi \cdot \mathbf{u}) = div(\Gamma \cdot grad\,\phi) + S_\phi \qquad \text{Eq. 1-1}$$

where ϕ is a general variable which is being conserved, ρ is the density, $\mathbf{u}$ is fluid velocity vector, Γ is the diffusion coefficient and S_ϕ is the source term.

To make it more readable, equation 1-1 can be described in words:

Rate of increase of ϕ of fluid element	+	Net rate of flow of ϕ out of fluid element	=	Rate of increase of ϕ due to diffusion	+	Rate of increase of ϕ due to sources

The following paragraphs will introduce particular conservation situations.

1.1.2 Mass conservation

The mass conservation equation is obtained by replacing the general variable ϕ in equation 1.1 with 1. Therefore $div(\Gamma \cdot grad\phi)$ equals to zero, and the source term is ignored since it is irrelevant to the mass. Thus the mass conservation equation for the unsteady, three-dimensional compressible fluid[2] is

$$\frac{\partial \rho}{\partial t} + div(\rho \cdot \mathbf{u}) = 0 \qquad \text{Eq. 1-2}$$

where ρ is the density, and $\mathbf{u}$ is the velocity. In an incompressible fluid the density ρ is constant and equation 1.2 becomes

$$div(\mathbf{u}) = 0 \qquad \text{Eq. 1-3}$$

Incompressible fluid flow is applicable to FSW modelling, because the material density is constant and independent of the pressure[3].

1.1.3 Momentum conservation

A slightly more complicated derivation is required for the momentum conservation equations[2], which are given by

$$\begin{aligned}
&\frac{\partial(\rho \cdot u_x)}{\partial t} + div(\rho \cdot u_x \cdot \mathbf{u}) + \frac{\partial p}{\partial x} = div[\mu \cdot grad(u_x)] + \frac{\partial[\lambda \cdot div(\mathbf{u})]}{\partial x} + S_x \\
&\frac{\partial(\rho \cdot u_y)}{\partial t} + div(\rho \cdot u_y \cdot \mathbf{u}) + \frac{\partial p}{\partial y} = div[\mu \cdot grad(u_y)] + \frac{\partial[\lambda \cdot div(\mathbf{u})]}{\partial y} + S_y \\
&\frac{\partial(\rho \cdot u_z)}{\partial t} + div(\rho \cdot u_z \cdot \mathbf{u}) + \frac{\partial p}{\partial z} = div[\mu \cdot grad(u_z)] + \frac{\partial[\lambda \cdot div(\mathbf{u})]}{\partial z} + S_z
\end{aligned} \qquad \text{Eq. 1-4}$$

where u_x, u_y and u_z are velocities along x, y and z axis of velocity vector $\mathbf{u}$, ρ is the density, p is the pressure, i, j stand for x, y or z axis, μ is the first dynamic viscosity coefficient to relate stress to linear deformation, λ is the second viscosity coefficient

relating stress to volumetric deformation, and S_x, S_y and S_z are the source terms. Generally equations 1-4 are described as the Navier-Stokes equation for a Newtonian fluid.

It is possible to correct the fourth and fifth terms in equation 1-4 into stress due to the following relationships[2]

$$\tau_{ii} = 2\mu \frac{\partial u_i}{\partial i} + \lambda \cdot div(\mathbf{u})$$
$$\tau_{ij} = 2\mu\left(\frac{\partial u_i}{\partial j} + \frac{\partial u_j}{\partial i}\right) = \tau_{ji} \qquad \text{Eq. 1-5}$$

where the suffices i and j in τ_{ij} indicate that the stress component acts in the j–direction on a surface normal to the i–direction, and $\mathbf{u}$, u_i and u_j are velocity vectors.

Substituting 1.5 into 1.4, the momentum conservation equation gives

$$\frac{\partial(\rho \cdot \mathbf{u})}{\partial t} + div(\rho \cdot \mathbf{u} \cdot \mathbf{u}) + grad(p) = div(\tau) + S_m \qquad \text{Eq. 1-6}$$

where S_m is an integrated source term, and τ is the flow stress[4] which is given by

$$\tau = \mu \cdot \left[grad(\mathbf{u}) + grad(\mathbf{u}^T) - \frac{2}{3} div(\mathbf{u} \cdot \mathbf{I}) \right] \qquad \text{Eq. 1-7}$$

where $\mathbf{I}$ is the unit tensor.

Originally the viscosity is a measure of the resistance of a fluid to being deformed by shear stress, however in the FSW process the material is solid, hence an equivalent value μ is calculated by Colegrove et al.[5] from stress at a given temperature versus strain-rate

$$\mu = \frac{\overline{\sigma}}{3\dot{\overline{\varepsilon}}} \qquad \text{Eq. 1-8}$$

where $\overline{\sigma}$ is the stress and $\dot{\overline{\varepsilon}}$ is the effective strain rate.

When analysing the FSW process, the term $div(\tau)$ dominates over the momentum terms because the material's flow strength $\overline{\sigma}$ is larger than $\frac{\partial(\rho \cdot \mathbf{u})}{\partial t} + div(\rho \cdot \mathbf{u} \cdot \mathbf{u})$. Therefore

the steady state form of the equation 1-6 is a reasonable approximation for the FSW[6], which is given by

$$div(\rho \cdot \mathbf{u} \cdot \mathbf{u}) + grad(\mathbf{p}) = div(\tau) \qquad \text{Eq. 1-9}$$

Note that the conservation of momentum equation is much more complex in turbulent flows due to their high velocity and compressibility[2].

1.1.4 Energy conservation

Versteeg et al.[2] transformed the energy conservation equation from overall equation (equation 1-1) by replacing the general variable ϕ with energy term E

$$\rho \cdot \frac{\partial E}{\partial t} + div(\mathbf{u} \cdot (\rho E + p)) = div[\lambda \cdot grad(T)] + S_E \qquad \text{Eq. 1-10}$$

where E is the internal energy per unit mass

$$E = \int_{Tref}^{T} c_p dT - \frac{p}{\rho} + \frac{\mathbf{u}^2}{2} \qquad \text{Eq. 1-11}$$

where c_p is the specific heat, ρ is the density, T is the temperature, and λ is the thermal conductivity.

The first term in equation 1-10 represents the rate of change of the internal energy, and it can be ignored in a steady state model. The second term calculates the heat flow caused by the convection. The third term describes the heat flow due to the conduction. The fourth term states the heat generation.

The FSW thermal model is an application of the energy conservation above. It solves the partial differential equations for heat flow, to predict the temperature field. In FSW, heat losses from free surfaces by radiation and convection are usually smaller than the conductive heat flow so the temperature distribution can generally be obtained from a fundamental differential equation for heat conduction in solids[7]. It is similar to equation 1-10 but replacing E with T and deleting irrelevant items

$$\frac{\partial T}{\partial t} = a \cdot div(grad(T)) \qquad \text{Eq. 1-12}$$

where t is the time, and a is the thermal diffusivity which is given by

$$a = \frac{\lambda}{\rho \cdot c_p} \qquad \text{Eq. 1-13}$$

1.1.5 Solution types

Solution types are categorised by Versteeg[2] due to two principal physical behaviours, equilibrium and marching.

1.1.5.1 Equilibrium problems

The first category involves the solution of steady state situations, such as the steady state distribution of temperature in a rod of solid material, which are governed by elliptic equations. Laplace's equation which describes incompressible fluid flow as steady state heat conduction is an example of an elliptic equation. Its two dimensional form[2] is

$$\frac{\partial^2 \phi}{\partial x^2} + \frac{\partial^2 \phi}{\partial y^2} = 0 \qquad \text{Eq. 1-14}$$

where ϕ is a general flow variable.

1.1.5.2 Marching problems

The other category is the problems of transient heat transfer, unsteady flow and wave phenomena, called marching problems[2], and are governed by parabolic or hyperbolic equations.

The parabolic equations include the time-dependent term, with an example being the one-dimensional diffusion equation:

$$\frac{\partial \phi}{\partial t} = \alpha \cdot \frac{\partial^2 \phi}{\partial x^2} \qquad \text{Eq. 1-15}$$

where ϕ is a general flow variable, and α is the diffusion coefficient.

The hyperbolic equations on the other hand govern vibration problems. In general they include the time-dependent term as well, even though the amount of dissipation is negligible in this case. An example of a one-dimensional hyperbolic equation is the wave equation

$$\frac{\partial \phi}{\partial t} = c^2 \cdot \frac{\partial^2 \phi}{\partial x^2} \qquad \text{Eq. 1-16}$$

where c is the wave speed.

1.1.5.3 Mach number

To determine whether the system is elliptic, parabolic or hyperbolic, the Mach number needs to be introduced. The Mach number is a dimensionless measurement of flow speed relevant to the speed of sound[8], and is defined as

$$M = \frac{v_o}{v_s} \qquad \text{Eq. 1-17}$$

where v_o is the velocity of the object in a particular medium, and v_s is the velocity of sound in the same medium. Practical calculation of the Mach number is more complex than this equation, and results vary enormously depending on velocity of the fluid.

1.1.5.4 Classification criterion of flow equations

The solution types in Table 1-1 are classified according to their viscidity. Usually the steady state Navier-Stokes equations discussed above, the energy, and the enthalpy equations are elliptic, while the unsteady flows are parabolic.

	Steady flow	Unsteady flow
Viscous flow	Elliptic	Parabolic
Inviscid flow	M<1 : Elliptic	Hyperbolic
	M>1 : Hyperbolic	

Table 1-1: Classification of the main categories of flow equations[9]

The absence of the higher order viscosity terms makes classification of inviscid flow equations different from classification of Navier-Stokes or energy equations[2]. It depends more on fluid compressibility which is the reason why the Mach number M plays such an important role. The elliptic character of inviscid flows at $M < 1$ is caused by the value of fluid pressure since it propagates disturbances at the speed of sound. However when $M > 1$ the fluid velocity domains because pressure is not large enough to cause influences in the upstream direction. This explains why the supersonic inviscid flow equations are hyperbolic.

1.1.6 Boundary conditions

All modelling problems are defined in terms of initial and boundary conditions. It is important that they are accurately specified and their role in different models is understood. Initial conditions give the initial values of all the flow variables in the flow domain. Boundary conditions are usually applied on the boundary domains, which are more complex than initial conditions. They will be illustrated with heat and fluid flow examples respectively in this review. Boundary conditions in analytical methods do not include complex geometries or domains, which are simpler to define.

1.1.6.1 Fluid flow boundary conditions

The following boundary conditions are based on subsonic flow ($M < 1$).

- Inlet

The inlet boundary condition is a wide range concept that permits flow to enter the solution domain. Generally, there are five kinds of inlet boundary conditions: velocity inlet, mass flow inlet, pressure inlet, inlet vent and intake fan[4].

In velocity inlet boundary conditions (which are used in the FSW process model), the flow velocity at domain inlets are specified with fixed values, in term of the flow properties[10]. These relevant scalar properties at the flow inlets are used to compute several flow variables entering the domain across the flow inlet, i.e. mass flow, momentum flux, energy, and species. In this case, it is unnecessary to make a velocity correction under this boundary condition.

- Wall

The wall boundary condition is another frequent boundary condition specified in fluid flow problems. A wall boundary condition is produced at the fluid boundary where it meets a solid wall[4]. Commonly, a no-slip boundary condition is applied at the wall in the viscous flows. If the wall is moving linearly or rotating, the motion of the fluid at the wall matches the motion of the boundary.

In the FSW process, a no-slip wall boundary condition at the rotating tool results in material velocity equalling:

$$v_m = \omega \cdot r \qquad \text{Eq. 1-18}$$

where ω is the tool angular velocity, and r is the tool radius.

An alternative approach assumes that the material slides against the tool surface[3]. In this case the shear stress at the surface is specified and the material velocity normal to the surface is zero i.e.

$$v_m \cdot \mathbf{n} = 0 \qquad \text{Eq. 1-19}$$

1.1.6.2 Heat flow boundary conditions

Normally, there are several types of boundary conditions that can be specified in heat conduction cases[10,11]:

The first is the Dirichlet boundary condition where the temperature is defined on the boundary

$$T = T_0 \qquad \text{Eq. 1-20}$$

The next type is the Neumann boundary condition, in which the heat flux is defined on the boundary

$$-\mathbf{n} \cdot \mathbf{q} = q_0 \qquad \text{Eq. 1-21}$$

where $\mathbf{q}$ is the heat flux, $\mathbf{n}$ is the normal vector at the boundary and q_0 is inward heat flux, normal to the boundary.

There are a couple of variants on the Neumann boundary condition. In one of them, the heat flux is calculated from the heat transfer coefficient and the temperature of the surrounding fluid

$$\mathbf{q} = h \cdot \left(T - T_{\text{inf}}\right) \qquad \text{Eq. 1-22}$$

where h is the heat transfer coefficient, A is the heat flux crossing area, and T_{inf} is the referenced surrounding temperature.

The final boundary considered is the radiation boundary condition, in which the heat transfer is due to electromagnetic radiation which propagates as a result of a temperature difference[12]. Although this phenomenon is exceedingly complex, the calculation as a boundary condition can be defined as

$$\mathbf{q} = \varepsilon \cdot F_G \cdot \sigma \cdot \left(T^4 - T_{\text{inf}}^4\right) \qquad \text{Eq. 1-23}$$

where $\mathbf{q}$ is the heat flux, ε is the emissivity vector, F_G is the geometric function, σ is the Stefan-Boltzmann constant equalling to 5.669×10^{-8} W/m^2 K^4, A is the surface area, and T_{inf} is the reference surrounding temperature.

Analytical and numerical methods are applied to solve the partial differential equations mentioned above. They can both play an important role, although numerical methods dominate because of their flexibility. However analytical methods are often preferred, particularly when analysing heat flow with simple geometries. The next two sections will introduce these two methods[1].

1.2 Analytical solution methods

Analytical methods model physical phenomena with partial differential equations based on simple geometries, enabling an analytical equation to be found for the general variable, ϕ. From a practical point of view, analytical approaches for solving the heat flow problem are preferable, since they are easy to set up and are solved faster than most numerical methods. Although analytical models are still constrained by several simplifying assumptions, these solutions are accurate enough to provide at least a qualitative description of the industrial thermal processes[13]. Section 1.2.1 will introduce an analytical method with examples of arc welding by Rosenthal[14,15], and 1.2.2 gives some brief examples of analytical fluid flow models.

1.2.1 Rosenthal method for moving heat source

The most well-known analytical method for modelling a moving heat source and its temperature distribution was developed by Rosenthal[16], and was later enhanced by Grong[13] and Myhr and Grong[16]. Both of the following situations are analysed as steady state problems, so equation 1-10 is relevant with the first term ignored due to steady state.

- Moving line heat source

For two-dimensional heat flow[15], the boundary conditions are

$$T \to T_0 \text{ for } x \to \pm\infty \text{ and } y \to \pm\infty \qquad \text{Eq. 1-24}$$

$$\frac{\partial T}{\partial z} = 0 \qquad \text{Eq. 1-25}$$

where T_0 is the initial temperature, and Q is the rate of heat of a linear source

$$-\frac{\partial T}{\partial r} \cdot 2 \cdot \pi \cdot r \cdot \lambda \to Q \text{ for } r \to 0 \qquad \text{Eq. 1-26}$$

where considering a circle $2 \cdot \pi \cdot r$ drawn around the heat source, $r = \sqrt{\xi^2 + y^2}$ is the radius, $\xi = x - v \cdot t$ is the distance of the point moved away from the source in time t, and λ is the thermal conductivity of the metal.

The governing equation involves transforming the standard equation for heat transfer 1.10 into the polar co-ordinates. Therefore the solution of temperature field T is given by

$$T - T_0 = K_0\left(\frac{a \cdot v \cdot r}{2}\right) \cdot e^{-\frac{a \cdot v \cdot \xi}{2}} \cdot \frac{Q}{2 \cdot \pi \cdot \lambda} \qquad \text{Eq. 1-27}$$

where v is the velocity of the heat source (the welding speed), a is the thermal diffusivity, and $K_0(\ )$ is the Bessel function.

- Moving point heat source

For three-dimensional heat flow[15], the boundary conditions for a moving point heat source are

$$T \to T_0 \text{ for } x \to \pm\infty,\ y \to \pm\infty \text{ and } z \to \pm\infty \qquad \text{Eq. 1-28}$$

where T_0 is the initial temperature. And Q' is the rate of heat of a point source

$$-\frac{\partial T}{\partial R} \cdot 4 \cdot \pi \cdot R^2 \cdot \lambda \to Q' \text{ for } R \to 0 \qquad \text{Eq. 1-29}$$

where considering a spherical surface $4 \cdot \pi \cdot R^2$ drawn around the heat source, $R = \sqrt{\xi^2 + y^2 + z^2}$ is the radius, and λ is the thermal conductivity.

The governing equation is generated in a similar way as the moving line heat source, and the solution of temperature field T is given by

$$T - T_0 = \frac{Q'}{4 \cdot \pi \cdot \lambda \cdot R} \cdot e^{-\frac{a \cdot v}{2} \cdot (R + \xi)} \qquad \text{Eq. 1-30}$$

where v is the velocity of the heat source, and a is the thermal diffusivity.

These equations and solutions above are sufficient to provide a comprehensive theoretical description of heat flow phenomena for a simple welding geometry[13]. Their solutions can be either applied directly or modified forms can be used for many different kinds of welding or related industrial processes, such as local fusion in arc welding, thermit welding, spot welding and friction welding. In particular, the effects of multiple point heat sources will be introduced in the section on modelling of FSW.

1.2.2 Analytical method for fluid flow

Analytical approaches have also been used for modelling the fluid flow. For instance, Rosenthal et al.[14], Monaghan et al.[17], Kum et al.[18] assumed simplified views of all the flow patterns, trying to predict heat generation. As the metal flow is usually too complicated to approximate with analytical models, it is preferable to switch to numerical meshed methods instead, including smooth particle hydrodynamics, spectral methods, FE analyses, finite difference method and the finite volume method.

1.3 Numerical solution methods

Five distinct streams of numerical solution techniques will be introduced in this section: smooth particle hydrodynamics, spectral method, FE method, finite differences method and finite volume method.

1.3.1 Smooth particle hydrodynamics

The SPH is a numerical modelling method developed to solve computational problem involving fluid flow problems, and it has been used in many fields, such as astrophysics, ballistics simulation and vulcanology investigations.

In SPH, the fluid flow is represented by a series of discrete particles which are affected to the moving fluid, i.e. a Lagrangian approach is used. When using SPH the smoothing length is defined, the physical properties of fluid at a particular point can be calculated from the particles properties with a radius of two smoothing lengths around it[18].

The major drawback of this method is that it requires a large number of particles to represent the flow domain[18]. This results in the method being very slow and it requires large amounts of computer memory. Some improvement can be obtained by using a particle level system.

1.3.2 Spectral methods

The spectral method[19] is a general name for a series of numerical techniques, which solve partial differential equations algebraically. Normally the spectral method and the FE method are based on a similar scheme, which is that they both use a combination of functions in terms of some particular algorithms to approximate the solution. The major difference between them is that when applying the Fourier transformation the spectral method approximation uses continuous functions such as sinusoids and Chebyshev polynomials, while the FE method uses some piecewise functions which need to be nonzero on small subdomains. Due to this distinction, the spectral method is classified as a global approaching method while the FE method is a local one, which is the reason why the spectral method works more precisely in a smooth domain.

1.3.3 FE method

The FE technique has been used for several years to solve complex, practical problems in structural engineering. Mathematicians such as Richard Courant[20] formulated its properties in terms of broad classes of approximations. Since then, the FE method has been modified for a number of problems in heat transfer and fluid dynamics by solving partial differential equations[21,22].

To explain how the FE method works, assume a simplified partial differential equation on a domain $u(x,t)$ where:

$$\frac{\partial u(x,t)}{\partial t} = k \cdot [u(x,t)] + f(x,t) \qquad \text{Eq. 1-31}$$

where $u(x,t)$ is the original function which includes two parameters: x and t. k is either a constant or a function depending on the level of complexity. $f(x,t)$ is another function with the same parameters as $u(x,t)$.

The solution of equation 1-31 is achieved by approximating $u(x,t)$ according to Oran[23]

$$u(x,t) = \sum_{n=1}^{N} [a_n(t) \cdot v_n(x)] \qquad \text{Eq. 1-32}$$

where $u(x,t)$ equals to the superposition of N basis functions $v_n(x)$ multiplying their identical coefficient values $a_n(t)$. Equation 1-33 is set up for each element, and $v_n(x)$ is commonly defined as

$$v_n = \begin{cases} \dfrac{x - x_{n-1}}{x_n - x_{n-1}}, x_{n-1} \le x \le x_n \\ \dfrac{x_{n+1} - x}{x_{n+1} - x_n}, x_n \le x \le x_{n+1} \\ 0, otherwise \end{cases} \qquad \text{Eq. 1-33}$$

where $\{x_n\}$ is a set in range $[x_-, x_+]$, and x_-, x_+ are two random constants. Equations 1-33 show that each v_n consists of two straight lines. Any of them has a positive slope between the nodes x_{n-1} and x_n, while the other line has a negative slope between the nodes x_n and x_{n+1}. The region between every two neighbouring nodes is defined as an element.

Since the FE method requires a large amount of computer storage for the functions mentioned above, the computing system often makes some effort to reduce the modelling complexity, such as ignoring some physical phenomena[23].

1.3.4 Finite difference method

The finite difference method describes an unknown $f(x)$ by means of a grid in the co-ordinate system[23]. The Euler method or truncated Taylor series are often used to generate a finite difference approximation of the derivative $f'(x)$, in terms of the value of $f(x)$ at each grid point and its direct neighbours as Figure 1-1.

For instance, an ordinary differential equation

$$f'(x) = A \cdot f(x) + B \qquad \text{Eq. 1-34}$$

where A, B are constants, and $f'(x)$ is the derivative term. The finite difference method approximates $f'(x)$ in a simpler way

$$f'(x) \approx \frac{f(x+h) - f(x)}{h} \qquad \text{Eq. 1-35}$$

By combining equations 1-34 and 1-35, an approximated result of $f(x+h)$ generates

$$f(x+h) = f(x) + h \cdot (A \cdot f(x) + B) \qquad \text{Eq. 1-36}$$

An equation is created for each grid point which can be solved by matrix methods subject to a set of boundary conditions.

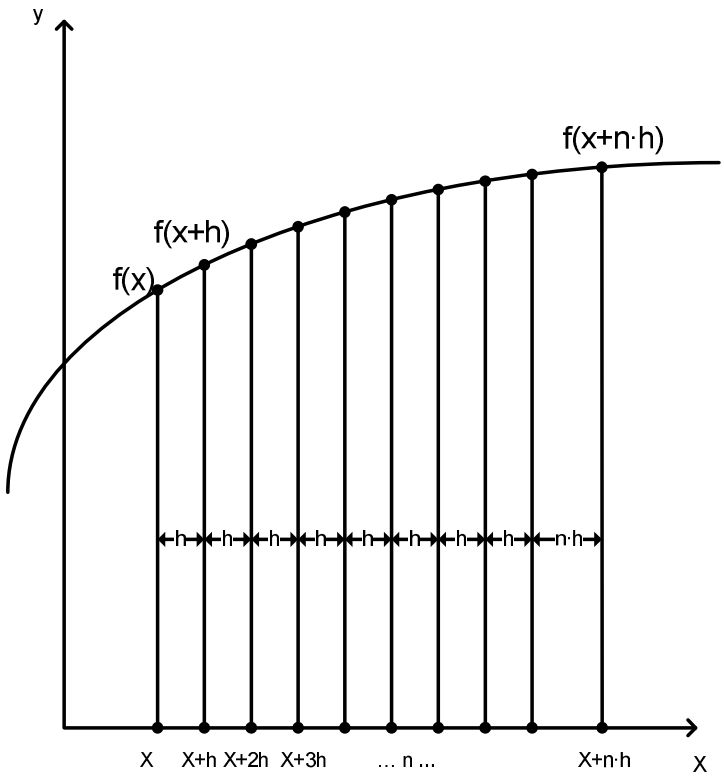

Figure 1-1: Discretizing a simple f(x) on a grid

1.3.5 Finite volume method

The finite volume method evaluates the quantity of flux ϕ that passes through the surface of a volume and enters an adjacent volume by conservation equations, then approximates and solves these partial differential equations by discretizing them into algebraic equations[2].

The basic idea of the finite volume method is similar to the finite difference method, which approximates the partial differential equations with a meshed geometry. However the difference between them is the finite difference method uses a consistent mesh, while the finite volume method uses an irregular mesh. The term volume refers to the small meshes surrounding a node point.

The finite volume method consists of three further steps to obtain the solution. A one-dimensional steady state diffusion example is illustrated from Versteeg[2], and described below.

1. Grid generation

Initially, consider the steady state diffusion of the variable ϕ in a one-dimensional domain which is governed by

$$\frac{d}{dx}\left(\Gamma \cdot \frac{d\phi}{dx}\right) + S = 0 \qquad \text{Eq. 1-37}$$

where Γ is diffusion coefficient, and S is the source term. The boundary value of ϕ is prescribed.

2. Division of the domain/grid

After determining the governing equation, it is necessary to divide the domain into discrete volume. A general nodal point P is identified in a one-dimensional volume. West and east neighbouring nodes of P are defined as W and E respectively. The domain is shown in Figure 1-2.

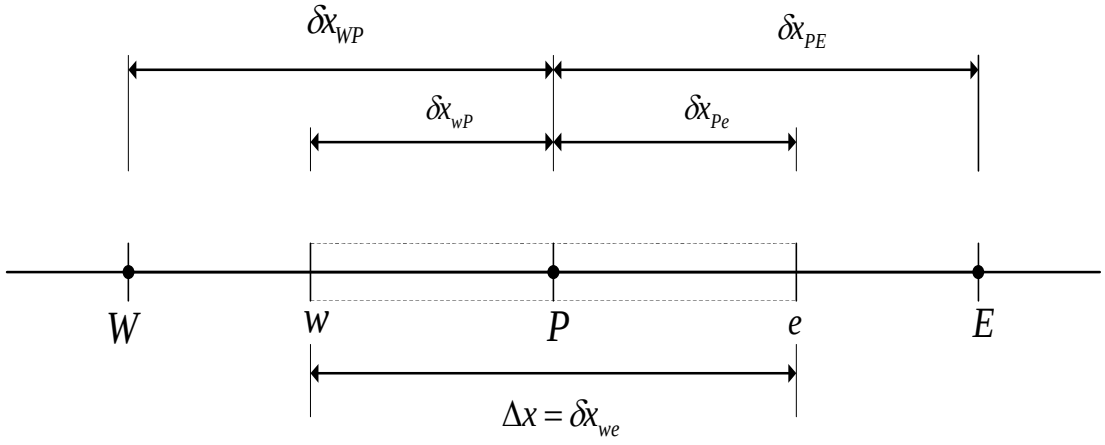

Figure 1-2: The volume of nodal P by Versteeg et al.[2]

3. Discretization of equations

This step is the key in the finite volume method, and it involves the integration of the governing equations over the volume to yield discretised equations at nodal point P. For the volume in Figure 1-2, the discretised equation equals to

$$\int_{\Delta V} \frac{d}{dx}\left(\Gamma \cdot \frac{d\phi}{dx}\right) dV + \int_{\Delta V} S dV = \left(\Gamma \cdot A \cdot \frac{d\phi}{dx}\right)_e - \left(\Gamma \cdot A \cdot \frac{d\phi}{dx}\right)_w + \bar{S} \cdot \Delta V = 0 \qquad \text{Eq. 1-38}$$

where A is the cross-sectional area of volume face, ΔV is the volume and $\bar{S}$ is the averaged source over the volume.

In words, equation 1-38 means that the diffusive flux ϕ leaving the east face minus the one entering the west face is equal to the generation of ϕ, which is the conservation equation of ϕ over the volume.

In order to derive the discretised equations, the diffusion coefficient $\Gamma$and the gradient $\frac{d\phi}{dx}$ are assumed to be linear, i.e.

$$\Gamma_e = \frac{\Gamma_P + \Gamma_E}{2}$$
$$\Gamma_w = \frac{\Gamma_W + \Gamma_P}{2} \qquad \text{Eq. 1-39}$$

$$\left(\frac{d\phi}{dx}\right)_e = \frac{\phi_E - \phi_P}{\delta x_{PE}}$$
$$\left(\frac{d\phi}{dx}\right)_w = \frac{\phi_P - \phi_W}{\delta x_{WP}} \qquad \text{Eq. 1-40}$$

Parameters S_u, S_P and ϕ consist a linear function to evaluate the averaged source $\overline{S}$ over a volume ΔV

$$\overline{S} \cdot \Delta V = S_u + S_P \phi_P \qquad \text{Eq. 1-41}$$

Substitution of equations 1-39, 1-40 and 1-41 into 1-38 gives

$$\Gamma_e A_e \left(\frac{\phi_E - \phi_P}{\delta x_{PE}}\right) - \Gamma_w A_w \left(\frac{\phi_P - \phi_W}{\delta x_{WP}}\right) + \left(S_u + S_P \cdot \phi_P\right) = 0 \qquad \text{Eq. 1-42}$$

Equation 1-42 could be rearranged as

$$\left(\frac{\Gamma_e}{\delta x_{PE}} A_e + \frac{\Gamma_w}{\delta x_{WP}} A_w - S_P\right)\phi_P = \left(\frac{\Gamma_w}{\delta x_{WP}} A_w\right)\phi_W + \left(\frac{\Gamma_e}{\delta x_{PE}} A_e\right)\phi_E + S_u \qquad \text{Eq. 1-43}$$

Which can also be written as

$$a_P \phi_P = a_W \phi_W + a_E \phi_E + S_u \qquad \text{Eq. 1-44}$$

Then by inputting values for a_P, a_W, a_E and ϕ at different positions, a set of algebraic equations can be generated. This is done for each of the nodes in the domain. Note that the above analysis assumes a linear change in the variables. Other schemes such as upwind and hybrid illustrated by Versteeg[2] can give more precise approximated results.

4. Solution of algebraic equations group

The previous step resulted with a system of linear algebraic equations. Although there are several procedures that can be applied to solve them, such as the Gaussian-elimination method[10], the available computer resources set a powerful constraint on the problem. Thomas et al.[24] developed a technique by rapidly solving tri-diagonal system of algebraic equations, which is called the TDMA. In practise, TDMA can directly used to solve the one-dimensional mode, however it can also be used to solve multi-dimensional models by working iteratively in a line-by-line fashion. The algorithm is adopted in many commercial CFD packages such as ANSYS FLUENT[4].

1.4 Other numerical solution methods

1.4.1 The Artificial Neural Network modelling

Another way of numerically representing a process is with an ANN model. The ANN is a mathematical model which is inspired from the biological neural network used by the human brain[25]. An ANN consists of three interconnected layers: input, hidden and output layers, which all include several artificial neurons to compose a complete system. A standard ANN is shown in Figure 1-3. Once it is well trained, it is able to describe and solve a practical problem.

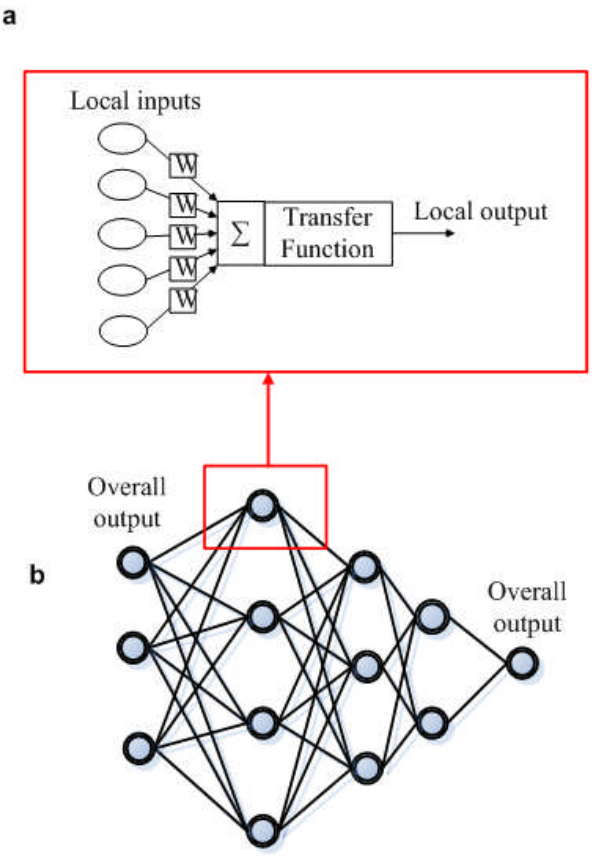

Figure 1-3: Diagrams[26] of a) simple processing neuron; b) architecture of a five-layer neural network. Note that the ANN models is built from different arrangements of simple neurons

The transfer function used at each processing neuron is the Sigmoid equation[27], which is given by:

$$f(x_i, w_i) = \frac{1}{1 + \exp\left(-x_i^{lin}\right)} \qquad \text{Eq. 1-45}$$

where x_i is the local value, w_i is the local weight and *lin* is a scaling factor.

Three common ANN topologies[27] are:

1. The MLP network[28], which is multilayer feed-forward network normally used combined with the static back-propagation algorithm. The MLP method can be used under most circumstances, however the network usually needs a large amount of data for training, as shown in Figure 1-4(a).
2. The GFF network[28], which allows data to flow over one or more layers. The GFF can normally solve problems as effectively as the MLP network but with

less training data, but it requires longer time for training, as shown in Figure 1-4(b).

3. The MFF network[29], which is a geometric combination of several parallel MLP structures. The advantage of the MFF network is it requires less training data, as shown in Figure 1-4(c).

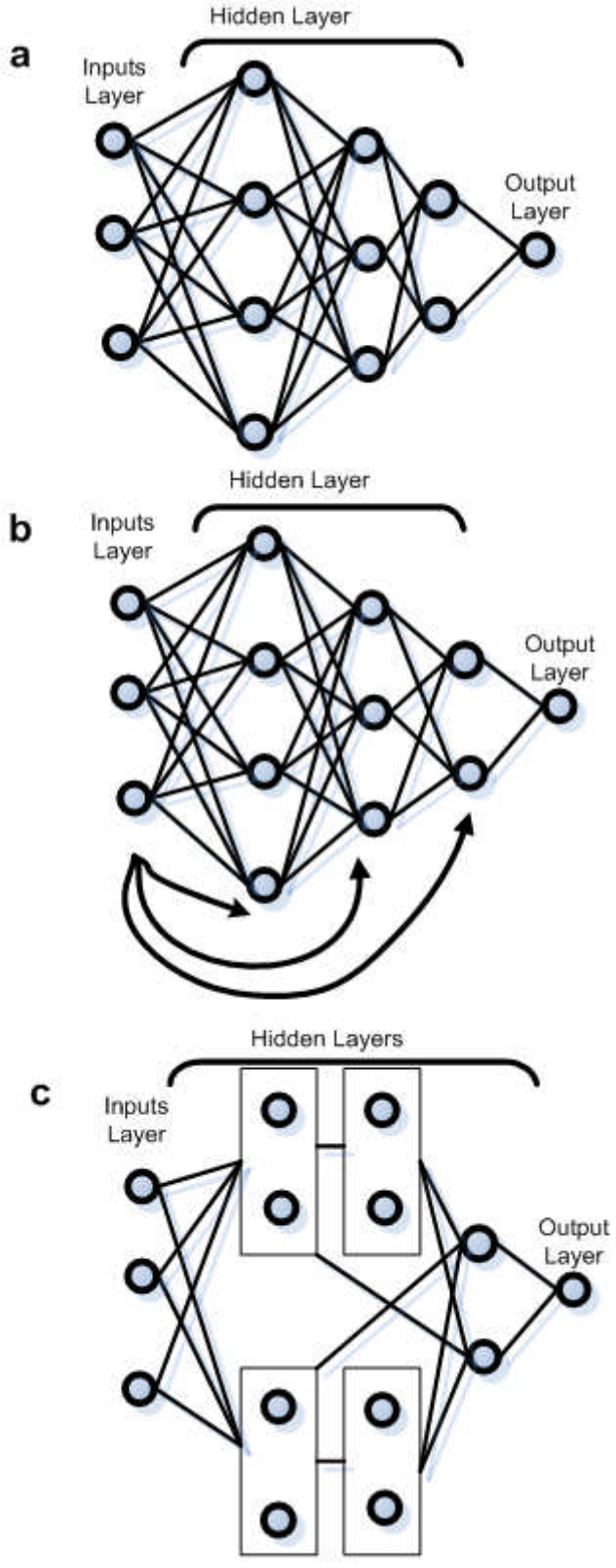

Figure 1-4: Topologies used in the study: a) MLP, b) GFF, c) MFF

There are several training algorithms for constructing an ANN, such as radial basis function, self-organizing and BP network[30]. In the BP network, an error calculation unit is installed between the hidden and output layer, to ensure that the discrepancies between outputs and expected results are always lower than the tolerances, and the unit will back propagate the discrepancies to the adjusted weights. The BP network is a highly efficient algorithm and is applied on most neural network models. The BP network consists of these following steps:

1. First iteration using the training dataset.
2. Compare the outputs to the desired ones, and calculate the gradient at each output neuron.
3. For each neuron input and hidden layer, calculate what the output should have been, and recalculate the local gradient.
4. Adjust the weights to lower the local gradients, using the prescribed gradient descent method.
5. Apply further iterations until an acceptable output is obtained.
6. Test the dataset.

Step 4 describes the use of a gradient descent method for adjusting the weight. Two common gradient descent methods[27] that can be used to adjust the local weights are:

1. The momentum method, which improves the straight gradient descent by memorizing the previous values and applying constant step sizes to improve the weight. The weight improving equation is given by

   $$\Delta w_i(n+1) = \eta_i \nabla w_i + \rho w_i(n) \qquad \text{Eq. 1-46}$$

   where i represents the level in the ANN topology, n is the iteration, η is the local momentum value and ρ is the step size. Note the momentum value and the step size can be manually adjusted.
2. The LM algorithm, is one of the most widely used high-order adaptive algorithms for minimizing the mean squared error of a neural network. As a high-order method, it uses the matrix of second derivatives of the model performance surface instead of the slope of the surface in standard gradient descent algorithm.

1.4.2 Differential evolution

The DE method is mathematical optimization method based on evolutional strategy[31,32], which is also described as a genetic algorithm. For n_p parameter vectors $x_{i,G}, i = 0,1,2,3,...n_p - 1$ defined as a population group G, the algorithm works as follow:

1. Set x_0 is the target vector which is to be optimized, and x_2 is the base vector (randomly picked).
2. Pick up two additional vectors in order to generate a weighted difference vector and add it to the base vector.
3. A trial vector $u_{0,G}$ is calculated from crossover result from step 2.
4. The result from step 2 will be combined with the trial vector $u_{0,G}$, in which way a new $x_{0,G+1}$ is born, and it also means a new population group with the first vector optimized is born.
5. Repeat for $x_{1,g}$, $x_{2,g}$,…$x_{Np-1,g}$.

The flow diagram of a simple DE algorithm is shown in Figure 1-5; however the algorithm can vary depending on the complexity of the target vectors.

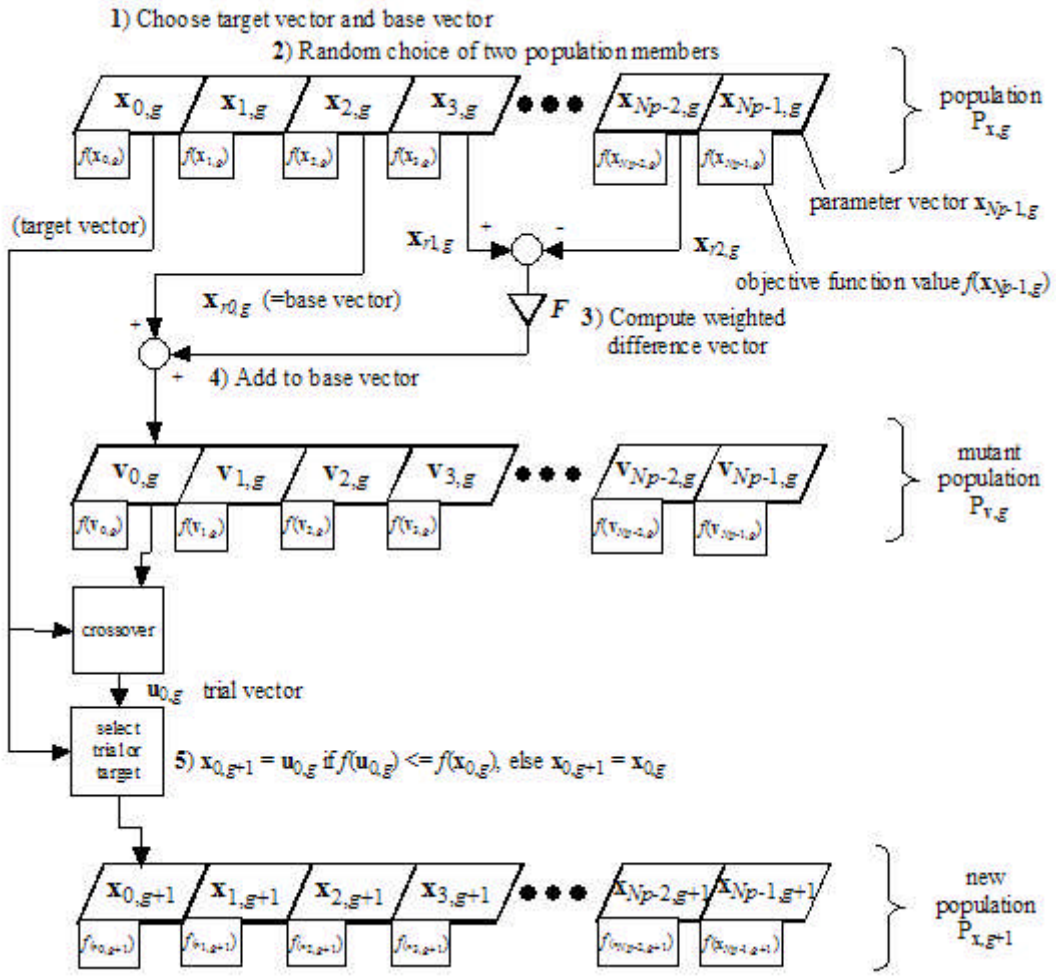

Figure 1-5 Flow diagram for a simple DE algorithm[33]

1.5 Advantages and disadvantages of modelling over experimentation

With the birth of high performance computers and rapid progress of computer graphic capabilities, it is now possible to simulate many industrial processes with either analytical or numerical models.

Modelling methods have the advantage of low equipment cost, shorter time and low human resources. Boris et al.[34] described an analysis of different airfoil shapes carried out in Douglas Corporation, comparing wind tunnel testing and computer simulation. The final results were approximately the same but the wind tunnel experiment took 2 years and cost 600 thousand dollars while the modelling method only took 4 days and cost 10 thousand dollars. Researchers have more freedom and flexibility to adjust their

parameters and modelling provides a better understanding of the principals behind the process. It can also simulate some physical phenomena which are difficult to obtain experimentally such as inside the temperature distribution of a nuclear reactor and the heat flow in a friction welding process. It is easily repeatable which is important for researching turbulence[34].

Often the drawbacks of modelling are ignored. A series of disadvantages are illustrated by Thomas et al.[24] which include: complex models that are time-consuming to build, run and interpret; powerful computer programs that are difficult to operate and complicated to check; and complex calculations generate more possibilities where mistakes can be made. Obtaining material properties for use in the model is often difficult, so estimates are often required. Since the model's accuracy is often highly dependent on these inputs, obtaining an accurate solution is difficult. The most important point to remember is that no matter how sophisticated a model is, it is still an approximation of the real case. Understanding and then quantifying differences between an experiment and the model is always necessary.

Even though there are several limitations to modelling, the rapid progress in mathematical theories and computer capabilities will increase their use in process and system modelling. Modelling methods validated with the experimental measurements are a powerful design tool. Hybrid modelling methods, such as one developed by Andersen et al.[35] are one way of achieving this and are developed in this thesis.

1.6 Friction Stir Welding

1.6.1 Process description and objectives

The FSW process was developed by Thomas et al.[36] at TWI in 1991. As a new technology it has great advantages in welding aluminium alloys which are difficult to weld with traditional welding processes. A schematic diagram in Figure 1-6 illustrates the FSW process. The key part in the whole FSW system is the tool, which consists of the shoulder and pin.

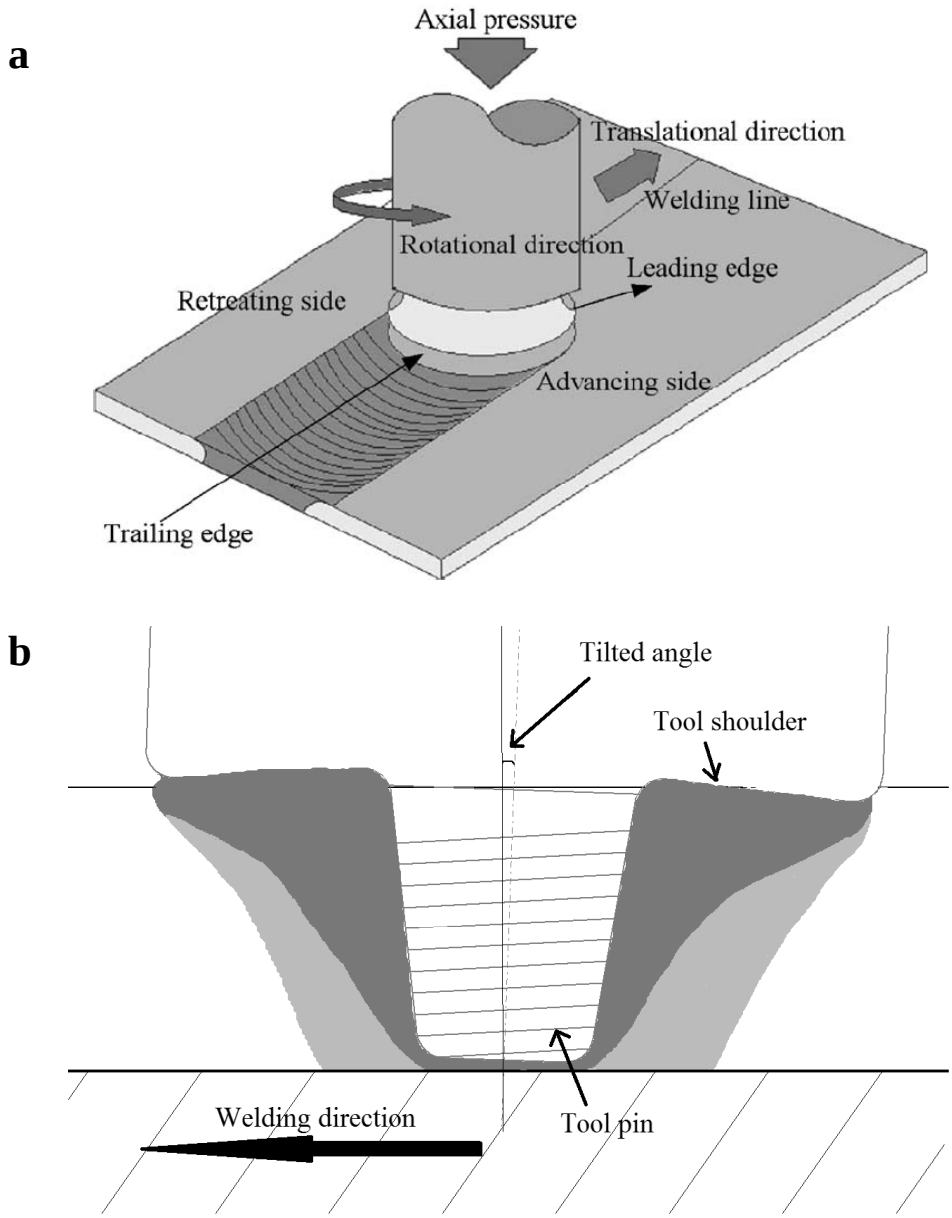

Figure 1-6 Schematic diagram of (a) the FSW[37] and (b) welding tool

Before welding, the two plates to be joined are firmly clamped; the rotating tool is then plunged into the material. The tool normally dwells for a short period which preheats the material, and then travels along the proposed joint line until reaches the end where the tool is withdrawn vertically. The tool is usually tilted at an angle of 1-3° away from the welding direction, although some tools are designed so that they can be used perpendicular to the plate surface[38]. The advancing and retreating sides of the tool are also shown in Figure 1-6. On the advancing side the direction of the tool and the weld are in the same direction, and on the retreating side they are opposite.

The FSW process produces a solid-state weld. This weld is generated behind the welding tool, which is formed from a combination of the elevated welding temperature, high pressure and material plastic deformation.

Process modelling is a way of predicting the thermal and mechanical phenomena in FSW. The following list includes the objectives which are addressed in FSW process models:

- The heat generation evaluation and the subsequently the heat distribution[39-42]
- The metal flow and its visualisation[3,6,43-58]
- Prediction of the mechanical properties of the weld[59]
- Optimization of tool profiles for different workpiece properties, i.e. materials, thicknesses[49,50,60-62]
- Optimization of the welding parameter, i.e. welding speed and rotation speed[39,63]
- Predicting the generation of the defects[64,65]

1.6.2 Tool effects summary

As mentioned above, the tool design influences the quality of the FSW welds. In particular:

- Tool shoulder, which plays the major part in the heat generation during the process, and prevents the expulsion of material. It also guides the material flow rotating around the welding tool near the surface[66].
- Tool pin, which deforms the material along the joint line, and generates some heat as the secondary function.

1.6.3 Advantages and disadvantages

The FSW process was applied industrially in the mid-1990s, and was one of the fastest processes to become industrialised after invention. There are several advantages of FSW compared to traditional welding processes, which are summarised by Threadgill et al.[67]. They are:

- FSW does not lead to solidification cracking problems, because it is a solid phase process.
- Thick plates can be welded by the FSW with a single pass.

- FSW can be an automated easily, which reduces the labour cost.
- The welding cost with FSW are lower since it does not require edge preparation apart from a machined, flat surface, shielding gas or filler metal like traditional welding processes; however the shielding gas is still required for some materials like titanium.
- Low distortion, shrinkage and residual stresses.
- The welds have good mechanical properties due to the low heat input and fine grained microstructure.
- It has a low power input, because it has higher energy efficiency than other processes, i.e. laser welding.
- The process does not cause environmental hazards, i.e. radiation or fumes.
- The process is well suited to welding dissimilar alloys, i.e. Aluminium and Magnesium.

As a result of these advantages, the FSW welding process has a wide range of industrial applications, e.g. the astronautic, aerospace, nuclear, vehicle design, and military industries. Although primarily used for aluminium alloys, it can also be used for nickel alloys[68], titanium[69] and steel[70]. FSW is particularly advantageous for thick section material[71], because of the better welding quality is due to the low heat input.

Despite of these advantages, Threadgill et al.[67] concluded that there are some shortcomings as well:

- The lower welding speed lower than other welding processes, particularly for thin material.
- The necessity of clamping the workpiece against the high forces during the process.
- The requirement of a backing bar behind the workpiece to resist the large vertical force.
- The keyhole, which is left at the end of welding, however some techniques are available to remove or decrease it[38].
- It is difficult to apply the process to fillets welds or other complex geometries.

- The requirement of a large, stiff machine which generates a large amount of normal force for the welding.

1.6.4 Microstructural classification

The earliest microstructural classification is described by Threadgill et al.[72]. Figure 1-7 shows four distinct microstructure regions in a typical FSW weld.

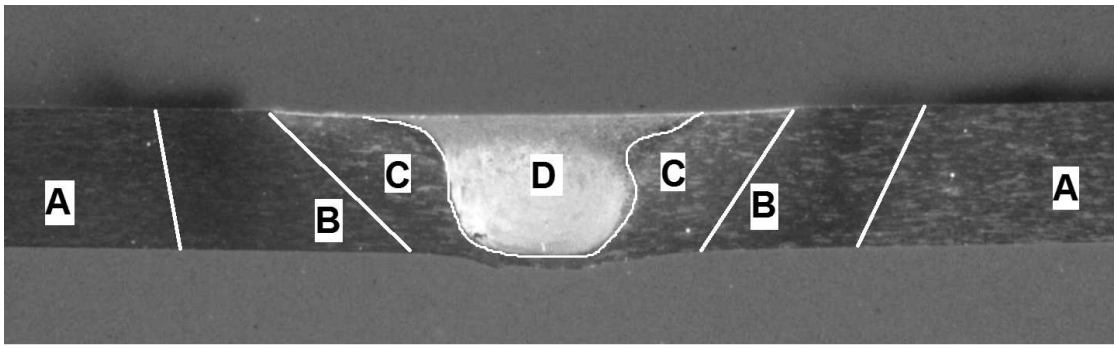

Figure 1-7 Various microstructural regions in the cross section of a friction stir weld. (A) Unaffected workpiece; (B) HAZ; (C) TMZA; (D) Weld nugget or DRZ

- Weld nugget or DRZ: This region of weld is the weld-centre and is fully recrystallized. It is also called the stir zone because it is generated by the stirring pin during the process.
- TMAZ: Material in this region has been plastically deformed by the tool pin, and the thermal cycle cause some change in the material properties. Usually the boundary between DRZ and TMAZ in aluminium alloys is distinct, particularly on the advancing side.
- HAZ: Since material in HAZ is close to the welding centre, there is a thermal influence on its microstructure and mechanical properties. Unlike the TMAZ, plastic deformation does not occur in the HAZ.
- Unaffected workpiece: The material in this region is even further from the tool and like the HAZ is not deformed. There is negligible thermal influence on its microstructure and mechanical properties, due to the low temperatures experienced far from the welding process.

1.6.5 Process modelling types

Process modelling of FSW presents a multiphysics challenge due to its combination of coupled heat flow, plastic deformation at high temperature, and microstructural

evolution. Figure 1-8 illustrates the physical interactions in a process model of FSW from Shercliff and Colegrove[73].

Figure 1-8 shows that the heat generation process plays the core role in the whole FSW modelling system. It results from the friction between the tool and workpiece, and the plastic deformation caused by the tool. The heat is conducted into the surrounding material i.e. the material in the DRZ, TMAZ and HAZ and modifies its microstructure. The heat generation is affected by the welding tool design, the workpiece contact condition with the tool and the welding parameters. Also the metal flow combined with heat generation, determines whether or not a high quality joint is produced.

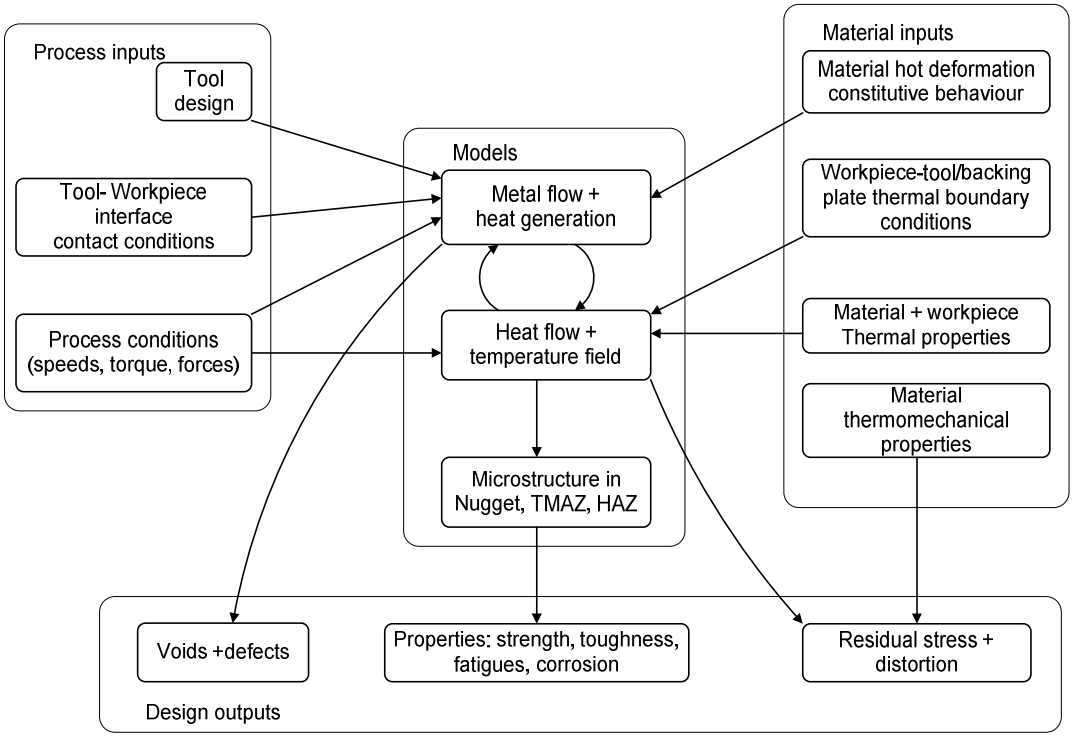

Figure 1-8 Summary of the key physical interactions in FSW, and the models linking process and material input parameters to the outputs needed by designers[73]

1.6.6 Modelling methods

Analytical and numerical methods are both applied to FSW, although the numerical methods dominate due to their ability to solve complex geometries, boundary conditions and material properties. Numerical methods use FE, finite difference or finite volume methods to represent the FSW process. When combined with the predefined boundary conditions, welding geometry and the constitutive behaviour of the material a solution

for the thermal or flow field can be found. A good model is able to analyse a complex problem in a simple way. For example using a 2D model to approximate a 3D behaviour[3,74].

1.7 Thermal models of FSW

1.7.1 Heat generation

As mentioned previously, the tool shoulder generates most of the heat and constrains the deformed material, while the tool pin deforms the material and generates some of the heat. The high rotation speed of the tool results in a shear stress at the interface, which generates heat from sliding frictional heat generation at the interface and viscous dissipation within the deforming material. There are variable boundary conditions at the interface: they may be the stick, in which the material has the same local velocity as the tool, or slip, in which the material velocity is lower than the tool. Both the stick and slip conditions may occur on different parts of the tool at the same time.

The existence of the melting material in the FSW process is still under discussion, although there is some experimental evidence of peak temperature getting close to the solidus temperature[75]. Because the melting of material reduces the shear stress at the interface rapidly, the heat generation will be limited by its occurrence. Although the solidus temperature limits the heat generation, very few FSW microstructures contain evidence of melting. Therefore, the simulation of the heat generation focuses on the interface characterization and the viscous dissipation behaviour of the material. Since the numerical approaches are more relevant to the deformed material and predicted temperature field, they will be introduced in the following sections. Some analytical equations summarizing the heat generation will be introduced as follows.

The simplest heat generation model[76] analyses the heat generation at the whole shoulder by ignoring heat generated at the pin. If the stick boundary condition is assumed the power, q equals:

$$q = \frac{2\pi}{3} k\omega R_s^3 \qquad \text{Eq. 1-47}$$

where ω is the rotational velocity, R_s is the shoulder radius, and k is a constant shear yield stress which is assumed to equal to the half of the tensile yield stress at the temperature close to solidus. An alternative approach[76] is based on a slipping condition and uses a friction coefficient:

$$q = \frac{2\pi}{3}\mu p \omega R_s^3 \qquad \text{Eq. 1-48}$$

where p is the normal pressure, which is calculated by dividing the normal force by the surface area of the tool. The friction coefficient μ is an adjustable constant varying between 0.2 and 0.5. In both cases the whole shoulder surface generates heat. However, this is not the real case, the heat generation part of the shoulder should be the part contacted with the workpiece, and the pin also generates some heat.

Another result used by Schmidt et al.[48], subtracted the contribution from the area inside the pin radius R_p:

$$q = \frac{2}{3}\pi k \omega \cdot \left(R_s{}^3 - R_p^3\right)\left(1 + \tan\alpha\right) \qquad \text{Eq. 1-49}$$

where k is the contact shear stress, and α is the shoulder cone angle.

A constant friction coefficient μ was always assumed in preliminary work, such as Frigaard et al.[77], however Song et al.[78] assumed a linear temperature dependent coefficient, given by:

$$\mu = -0.00027T + 0.5810 \qquad \text{Eq. 1-50}$$

where T is the local temperature at the tool surface. However, the real case for friction coefficient μ is that it depends more on the material surface condition than temperature. Recently, an average value of μ is described by Colligan et al.[40], which equals

$$\mu = \frac{3M_E}{2FR_s} \qquad \text{Eq. 1-51}$$

where M_E is the measured torque, F is the normal force, and R_s is the shoulder radius. Note that this estimate requires the motor torque which defeats the purpose of having a model that can predict the weld power.

There are also some publications that describe the heat generation form the pin. The early works by Chao and Qi[79] estimated an average heat generation considering a slipping boundary condition on the interface of a rotating cylindrical pin with the radius of R_p:

$$q = \frac{F\mu\omega L_p {R_p}^2}{\pi\left({R_s}^2 - R_p^2\right)} \quad \text{Eq. 1-52}$$

where F is the normal force and R_s is the shoulder radius, and $\frac{F}{\pi\left(R_s^2 - R_p^2\right)}$ equals to the pressure on the pin. A sticking boundary condition based method was developed by Shercliff et al.[76] by replacing the normal force and friction coefficient with a constant shear stress k and the length L_p equals:

$$q = 2\pi k\omega L_p R_p^2 \quad \text{Eq. 1-53}$$

Apart from the same results as equation 1-51 on the pin surface heat generation, Schmidt et al.[48] also considered the heat generation from the pin tip:

$$q = 2\pi k\omega R_p^3 \quad \text{Eq. 1-54}$$

On the other hand, a more detailed analysis by Colegrove et al.[44] which included the effect of the thread feature:

$$q = 2\pi \cdot R_p \cdot h \cdot \bar{\sigma} \cdot \frac{V_m}{\sqrt{3}} + \frac{2\mu \cdot \bar{\sigma} \cdot \pi \cdot R_p \cdot h \cdot V_{rp}}{\sqrt{3\left(1+\mu^2\right)}} + \frac{4F \cdot \mu \cdot V_m \cos\theta}{\pi} \quad \text{Eq. 1-55}$$

where:

$\bar{\sigma}$ is the averaged flow stress;

h is the thickness of the material;

F is the welding traversing force;

λ is the helix angle of the thread;

$\theta = 90 - \lambda - \tan^{-1}(\mu)$;

$V_m = \frac{\sin\lambda}{\sin(180 - \theta - \lambda)} V_p$;

$$V_m = \frac{\sin\theta}{\sin(180-\theta-\lambda)} V_p;$$

$$V_p = \omega \cdot R_p$$

As discussed earlier, the heat generation depends on the boundary condition between the tool and material. Schmidt et al.[80] integrated both in one model using a dimensionless slip rate δ:

$$\begin{aligned} q_{total} &= \delta q_{sticking} + (1-\delta) q_{slipping} \\ &= \frac{2}{3}\pi\omega\left[\delta k + (1-\delta)\mu p\right]\cdot\left[\left(R_s^3 - R_p^3\right)(1+\tan\alpha) + R_p^3 + 3R_p^2 H_p\right] \end{aligned} \qquad \text{Eq. 1-56}$$

which was later applied on his steady-state thermal pseudo-mechanical model[80] by assuming $k = \tau_{friction} = \tau_{yield} = \frac{\sigma_{yield}}{\sqrt{3}}$, and the heat flux applied on the tool surface is given by:

$$dq = \omega r k(T) \qquad \text{Eq. 1-57}$$

where ω is the rotation speed, r is the radius, and $\tau(T)$ is a temperature dependent shear yield stress. This model calculates the surface heat flux as a temperature dependent value, but ignores the influence from the strain-rate.

Hamilton et al.[81] used a slip coefficient as well, which was based on energy per unit length of the weld, and was calibrated from an experimental study of the linear relationship between the maximum welding temperature, the solidus temperature and the heat input.

$$\tau_{total} = 2\mu F\left(\frac{R_s}{3} + \frac{{R_p}^2}{R_s^2} H_p\right) \qquad \text{Eq. 1-58}$$

$$E_l = \tau_{total}\frac{\omega}{v} \qquad \text{Eq. 1-59}$$

$$(E_l)_{eff} = \frac{H_p}{H_{thickness}} E_l \qquad \text{Eq. 1-60}$$

$$\frac{T_{\max}}{T_{solidus}} = 0.000156(E_l)_{eff} + 0.54 \qquad \text{Eq. 1-61}$$

where τ_{total} is the total torque, F is the normal force, E_l is the energy per unit length of weld, v is the welding velocity (mm/s), and ω is the tool angular velocity (s^{-1}), and $(E_l)_{eff}$ is the effective energy per unit length of the weld. If the maximum welding temperature $T_{\max}$ reaches solidus temperature $T_{solidus}$, $(E_l)_{\max}$ can be calculated, the slip coefficient equals:

$$\delta = \exp\left(-\frac{(E_l)_{eff}}{(E_l)_{\max}}\right) \qquad \text{Eq. 1-62}$$

Considering a complete slipping boundary condition, the heat flux is given by:

$$dq = \delta \mu P \omega r \qquad \text{Eq. 1-63}$$

where P is the normal pressure on tool surface. Their model successfully predicted the maximum welding temperature over different heat input, but it tends to underestimate the temperature of DRZ for low heat input. This is reasonable because the friction coefficient was calibrated depending on the heat input, and thermal properties, i.e. thermal conductivity and specific heat, are defined as temperature dependent which is questionable. Another project named iSTIR[82] (as shown in Figure 1-9) is a process that empirically discovers the relationship among the thermal profile, welding parameters and analytical equations, which outputs the power. A statistical model developed by Pew et al.[83] found the weld power is relative to the travel speed, depth, rotation speed and combination of the three factors, and can be derived from on empirical data.

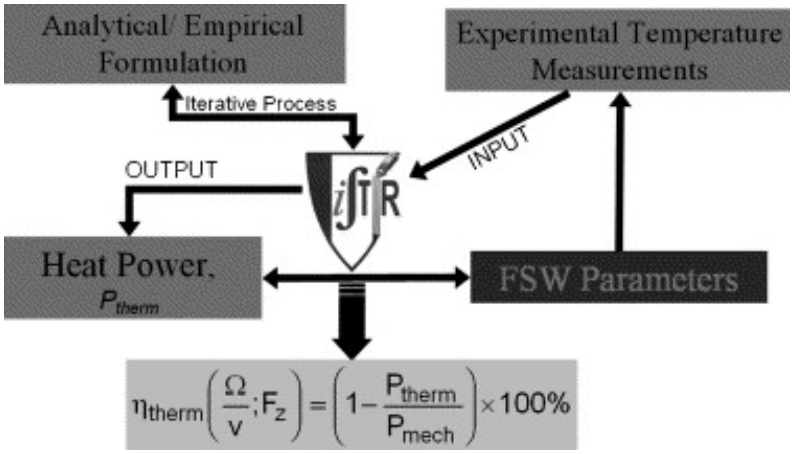

Figure 1-9 Diagram of project iSTIR[82]

1.7.2 Heat transfer

As shown Figure 1-8, the temperature field predicted from a thermal model is the central to the modelling of FSW. The results are used to optimize the welding parameters, and as an input to models which predict the weld microstructure, properties, distortion, and residual stress. In some cases they are also coupled with a flow model[39].

A thermal model of FSW involves solving the partial differential equations for the heat flow, with some specified boundary conditions, and outputting the temperature fields as a function of time and position. The thermal modelling of FSW considers the following issues:

- Distribution and intensity of the heat input
- Heat loss
- Influence from the initially dwelling
- Transients along the weld induced by finite plate effects.

Two types of thermal models are normally developed, steady-state and transient model. A steady-state model predicts the thermal profile when the weld achieves steady-state condition, and effects such as the initial plunge can be ignored. The steady-state model solves in considerably shorter time than the transient model. An equation for determining whether a steady-state condition has been reached was suggested by Grong et al.[13]. The transient model usually simulates the whole process of FSW[37,84], i.e. the initial plunge, dwell, weld and final withdraw. The transient model is more realistic but more time and resource consuming. Hilgert et al.[85] compared three types of FSW thermal models using a bobbin tool, including full steady state, moving heat source model excluding tool and full transient model. All models gave very close prediction of the thermal history, although comparing to the experimental data, the model failed to capture the cooling slope accurately which was claimed to be due to the limited length of geometry.

1.7.2.1 Analytical method

The earliest works were based on the analytical methods developed by Rosenthal et al.[14,15], which is detailed in the previous section on modelling methods. The basic equation for point heat source is given by

$$T - T_0 = \frac{Q/d}{\rho \cdot c \cdot (4 \cdot \pi \cdot a \cdot t)} \cdot \exp(\frac{-r^2}{4 \cdot a \cdot t}) \qquad \text{Eq. 1-64}$$

where T is the predicted temperature at a point in the material, T_0 is the workpiece initial temperature, t is the processing time, Q is the net heat input released initially, d is the thickness of the plate in model, r is the radial distance from the heat source, ρ is the density of workpiece, c is the specific heat and a is the thermal diffusivity which is given by

$$a = \frac{\lambda}{\rho \cdot c} \qquad \text{Eq. 1-65}$$

where λ is the thermal conductivity of the material. This method was extended by Myhr and Grong[16] and Grong[13] later. These analytical methods assume that the length of the workpiece is infinite in 2D or 3D dimensions, and they all work with constant material thermal properties.

The distribution of the heat source is included in the later models, such as assuming a uniform power density over a prescribed area or using only a power density that increases with the tool shoulder radius[42,86]. However in these more detailed models, the influence of other issues on the heat source become significant, i.e. the thermal boundary condition. Although the effect of thermal boundary conditions can be included with the multiple heat sources[87], these methods are rarely used.

1.7.2.2 Numerical method

The numerical method provides many advantages comparing to the analytical methods. There are three numerical methods commonly applied: the FE method, finite difference method, and finite volume method. The FE method is more widely used than the finite difference method and the finite volume method, which are usually used when coupled to a flow model. It is important to find out the important model parameters, in order to identify which parameters have the most influence on the model[39,63,88,89]. Ignoring or

simplifying the less important parameters makes the problem easier. However modern software tends to increase the complexity of the models, which is bad practice and should be resisted.

Another major issue is the different meshing methods used to discretize the model domains. The Lagrangian formulation is more generally used for the transient modelling, with the mesh being fixed to the material, and the temperature changes along the mesh with the movement of the heat source. The mesh in the Eulerian formulation is fixed, the material is allowed to flow through. This is more suitable to the steady-state problem. The mesh shape and size also have high influence on the solution of the material[90]. In most cases, a finer mesh is used near the heat source, where the temperature gradients are higher. Since the effects of the mesh size and type are important, the mesh sensitivity calibration always plays an important role in the numerical modelling.

- Material thermal properties

The simulation of heat flow in FSW process involves two key material thermal properties: specific heat and thermal conductivity, which are both temperature dependent, and can be included in FE simulation. In analytical methods, the material thermal properties are normally constant[14,15]. Obtaining temperature dependent values of the thermal conductivity and specific heat is difficult, especially for heat treatable aluminium alloys where the microstructure changes during the weld. A typical plot of thermal properties against temperature is shown in Figure 1-10. Commonly, modellers use published temperature dependent values in which the microstructure evolution is neglected such as Hamilton and Hamilton et al.[81]. Others use a constant room temperature value[39], since the short thermal cycle in FSW is unable to dissolve the precipitates which affect the material thermal properties.

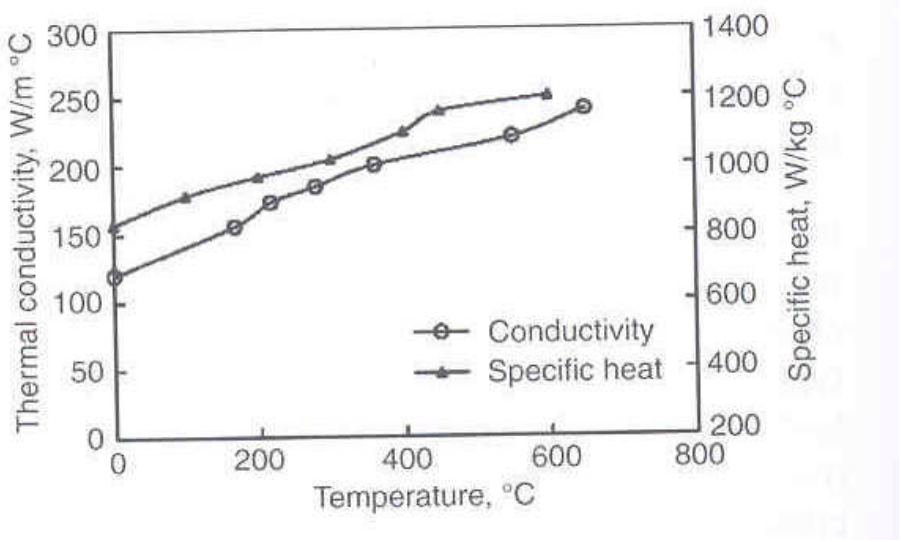

Figure 1-10 Thermal properties for Aluminium alloy 2024[91,92]

- Thermal boundary conditions

During and after the process of FSW, the heat is lost to the surrounding environment, backing bar and welding tool.

The heat loss to the surrounding environment is considered as convective, which is generally low due to the low convective heat transfer coefficient to air (10 W/m^2K) from Shi et al.[93]. The heat loss to the backing bar is more significant. Two methods can be used to represent this effect: including the backing bar with a contact resistance between the backing bar and welded material, or ignoring the backing bar and using a convective heat transfer coefficient[94]. To test these two approaches, Simar et al.[95] compared three types of boundary conditions: no backing bar (case1), perfect contact between workpiece and backing bar (case2), and perfect contact under the tool region and welded part (case3). The comparison indicated that a large amount of heat loss through the backing bar (Figure 1-11). Colegrove et al.[39] used a modified version of the contact resistance between the work piece and backing bar in his modelling work. The contact resistance with the backing bar are divided into two parts: the first part is the area which has experienced pressure from the tool shoulder and has a very low contact resistance. The second is the area outside of this which a much poorer contact resistance due to the lack of pressure between the two surfaces. Khandkar et al.[94] replaced the backing bar with a convective heat transfer coefficient to achieve more rapid solutions.

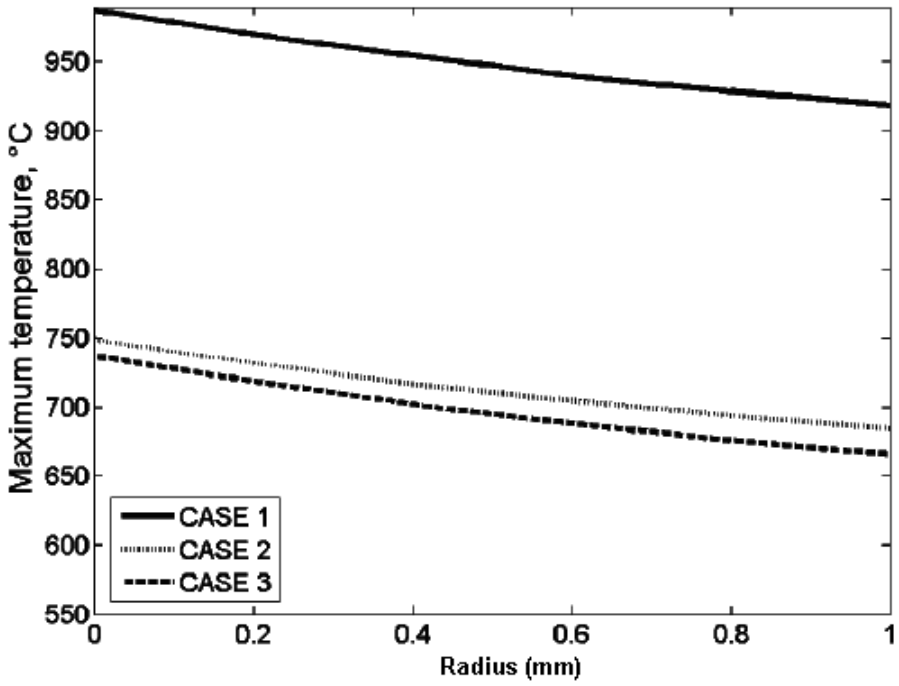

Figure 1-11 Three types of boundary conditions comparison[95]

One final method used by Shi and Dickerson[96] used a temperature dependent convective heat transfer coefficients.

1.7.3 Experimental validation

As with other industrial process, the modelling of FSW requires experimental validation. Most published works measure the temperature field with thermocouples. There are several difficulties using standard thermocouples to evaluate the temperature field during the FSW[97], such as:

- Insufficient time for thermocouples to react to temperature rise during the FSW
- Accurately locating the thermocouples
- Obtaining good contact between the workpiece and thermocouples. Unlike steel, it is not possible to weld thermocouples to aluminium easily.

1.8 Flow models of FSW

Modelling material flow of the FSW is challenging, but it is essential to understand and improve this process. As shown in Figure 1-8, the fluid flow models try to find out how the material flows around the tool. The major functionality is:

- Visual explanation of the movement of the metal flow and how the joint is formed[98]
- Improving the thermal models by understanding how the heat is generated with the material flow[39]
- An efficient optimisation technique for welding tool design[99]
- An efficient optimisation technique for process conditions, such as the maximum welding and rotation speed[61]
- Predicting the generation of defects[65].

1.8.1 Material interface boundary condition studies

The FSW models vary from 2D isothermal models with simple stick boundary condition to 3D fully coupled models with thermally dependent stick/slip boundary condition. Determining the interface boundary condition is important to the FSW process. Because it is practically impossible to observe the material behaviour at the interface boundaries, it is necessary to assume a boundary condition for numerical modelling. Four types of boundaries are normally applied, based on material velocity or interface shear stress prescription:

- Stick condition[3], in which the material local velocity equals to the tool interface velocity everywhere, or the same case for shear stress
- Slip condition[100,101,102], in which the material rotating speed equals to a constant fraction (commonly named slip coefficient) of the interface tool rotating speed. The total amount and ratio of heat generation due to slip and stick is found to be relative to the travel and rotation speed of the process[101].
- Stick/slip condition[3], in which the shear stress is limited to a constant value. On some parts of the tool a stick condition will exist while on others a slip condition will exist.
- Coulomb condition[65], in which the shear stress is limited to a value dependent to the material local normal pressure. Because of this character, this boundary condition is always applied within FE method which includes the material's elastic properties; however a calibrated friction coefficient is required. Zhang and Chen[103] modified the Coulomb law which is limited to a critical limit of

shear stress. Assidi et al.[104] applied the Coulomb condition and claimed that it is able to predict the temperature at the tool more accurately.

1.8.2 Material constitutive behaviour

As discussed in the heat generation section, the viscous dissipation heat generation is calculated from material viscosity, which is defined by $\mu = \bar{\sigma}/\bar{\dot{\varepsilon}}$, from flow stress $\bar{\sigma}$ and averaged strain-rate $\bar{\dot{\varepsilon}}$. The Sellars-Tegart law[105] is the most usual formulation to determine the steady-state flow stress in the FSW, and calculates the flow stress σ from the Zener-Hollomon parameter Z:

$$Z = \dot{\varepsilon} \exp\left(\frac{Q}{RT}\right) = A(\sinh \alpha\sigma)^n \qquad \text{Eq. 1-66}$$

where T is the temperature, $\dot{\varepsilon}$ is the strain rate, Q is an activation energy, R is the gas constant, and α, A and n are material dependent parameters. An alternative to using this equation, particularly if it is difficult to fit the experimental data to this equation is to interpolate the experimental data.

The practical problem is that the experimental test temperatures seldom reach the solidus temperature, so it is unclear what happens at temperatures approaching the solidus. The assumption of empirical softening regimes was used[6,39,62,74,106]. In Figure 1-12, a linear empirical softening regime is applied, where there is critical loss of flow strength from an arbitrarily defined melting temperature T_m to the solidus temperature T_s.

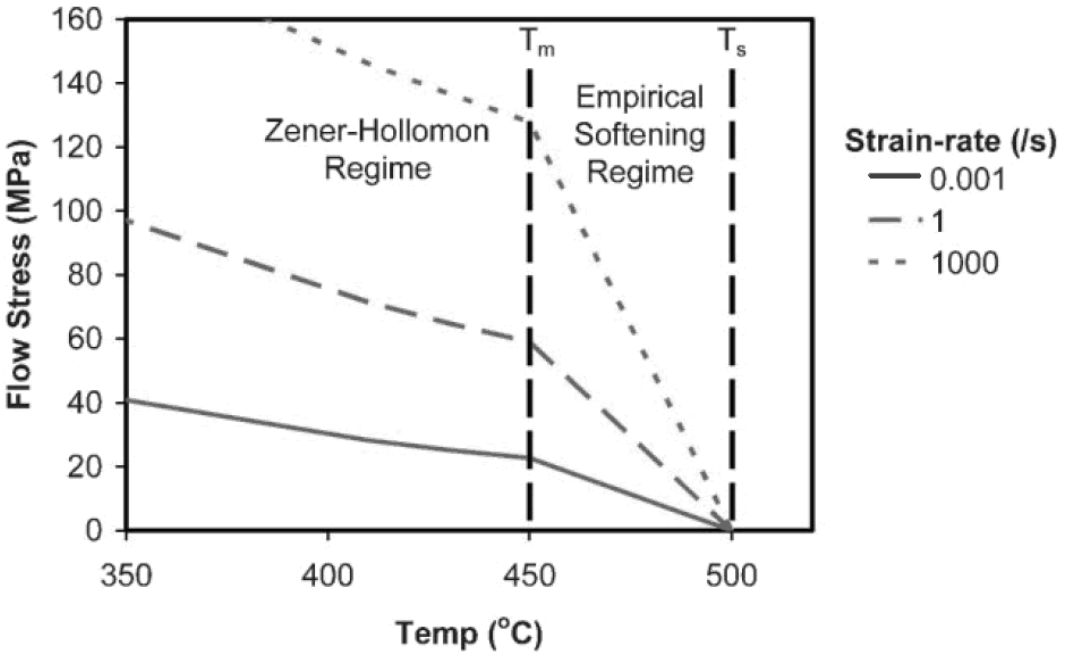

Figure 1-12 Constitutive behaviour data for aluminium 7449[39]

Another constitutive law used for FSW flow modelling is the Johnson-Cook model[107] which has been used by Askari et al.[108] and Schmidt et al.[65,109]:

$$\sigma = \left(A + B\varepsilon^{n}\right)\cdot\left(1 + C\ln\left(\dot{\varepsilon}/\dot{\varepsilon}_{0}\right)\right)\cdot\left(1 - \frac{T - T_{0}}{T_{m} - T_{0}}\right) \qquad \text{Eq. 1-67}$$

where A, B, n, C and m are material constant, $\dot{\varepsilon}$ is the strain rate, $\dot{\varepsilon}_{0} = 1$, T_m is the melting temperature, and T_0 is the environmental temperature. In this equation the flow strength reduces to zero at the melting temperature, so no additional softening region is required.

The Norton-Hoff model is applied in Liechty and Webb[110,111] for simulating the material flow in FSW:

$$\sigma = k_{0}\exp\left(-\beta T\right)\varepsilon^{n}\dot{\varepsilon}^{m} \qquad \text{Eq. 1-68}$$

where k_0, β, n and m are material constants. Assidi et al.[104] also used Norton-Hoff model for temperature over the solidus, and the Hansel-Spittle model is applied at lower temperature. The Hansel-Spittle model is given by

$$\sigma = A_{1}\exp\left(m_{1}T\right)\varepsilon^{m_{2}}\dot{\varepsilon}^{m_{3}}\exp\left(\frac{m_{4}}{\varepsilon}\right) \qquad \text{Eq. 1-69}$$

where A_1, m_1, m_2, m_3 and m_4 are the material constants.

Some other modellers[103,112] used von Mises law extended by Ponthot[113], which included the elastic behaviour of material:

$$\sigma = \sigma_0(T) + \eta\left(\varepsilon^p\right)^n\left(\dot{\varepsilon}^p\right)^m \qquad \text{Eq. 1-70}$$

where $\sigma_0(T)$ is the temperature dependent yield stress, m is the viscosity exponent, p is material constant, and n is the strain hardening exponent, and η is the viscosity coefficient.

For 304 stainless steel, Nandan et al.[54] applied simplified Hart's law, which included both the plastic and elastic contributions. Due to the complex nature of these equations they are not reproduced in this documents. The complexity is due to the microstructural changes that occur in the steel.

1.8.3 Analytical models

There are a number of analytical approaches to fluid flow in the FSW process, and they use simplifying assumptions such as the flow parameters and the interface boundary conditions.

An early analytical model by Stewart et al.[114] compared a mixed-zone model with a single slip surface model, which was analysed to be close to the experimental results. The analytical model built by Shercliff and Colegrove et al.[76] calculates the deformation size around the tool, based on a kinematically constrained flow. This model was further developed by Schmidt et al.[52] to simulate the shear layer assuming the velocity decreases linearly away from the tool, which was further validated with a CT-image analysis[115]. However this model was two-dimensional, and did not include the vortex flow and the shoulder's effect on the material under the shoulder[116]. In other analytical models developed by Heurtier et al.[117] the velocity field was modelled using a combination of rotating, transition and vortex flows, which enabled the prediction of strain, strain-rate and temperature. Arbegaest[118] analytically divided the material flow near the tool into five zones based on their individual velocity and force characteristics. The defects produced by FSW were analysed from the calculated movement of material flow in each zone. Subsequently a mass deficiency factor is introduced to represent the volumetric defect.

As the fluid flow behaviour is complicated and difficult to implement with analytical models, numerical methods are more commonly used.

1.8.4 Numerical models

Three numerical modelling methods have been applied to FSW: the FE method[37,52,80,84,95,119,120], the finite volume method[1,3,5,6,49-51,53,62,109,121] and a CTH code[108]. The FE method and volume methods have been previously discussed in the review of modelling methods. The CTH code was invented by Sandia National Laboratory in USA[122] and was original intended to be used for high speed impact and penetration physics in ballistics. The following sections will describe how these methods have been applied to the flow modelling of FSW.

1.8.4.1 Two-dimensional models

Some 2D models have been developed with the FE and finite volume methods to study the rotation flow pattern around the pin, from steady state models with a simple cylindrical pin[69,74,123-125] to fully coupled transient models with profiled pin (Figure 1-20)[49,50,73,126]. 2D models are reasonable simplification because:

1. As discussed, the main functionality of the tool shoulder is heat generation, while the tool pin deforms the material producing the weld (the influence from the shoulder will be discussed in the next section).
2. Normally the deformation is assumed to occur in a thin shear layer surrounding the tool surface. The influence from the shoulder is often small, so a two-dimensional model of the pin gives a reasonable prediction.
3. They solve more rapidly than their 3-dimensional counterparts and are therefore useful, particularly when looking at parametric studies.

- Flow visualisation

Flow visualisation is used to aid understanding of how the material flows around the pin. Two methods can be used: examining the flow of particles around the tool and streamlines. These will both be considered in the following sections.

- Particle plot study

Xu et al.[45] developed a 2D steady-state model using the FE method, which described the material tending to flow around the retreating side of the pin and was compared with an experimental study (Figure 1-13). These models also discussed the influences from process parameters on the material flow.

Colegrove et al.[126] also applied a number of particle plot investigations. For example Figure 1-14 shows a group of material particles being swept behind the pin.

Zhang et al.[127] also developed a 2D FE model using a modified coulomb boundary condition (Figure 1-15). This model proclaimed that material from advancing side would rotate with the pin for several revolutions before being deposited behind the tool (Figure 1-16). The material on the retreating side would never be captured in the flow near the pin (Figure 1-17). The highest deformed zone was suggested from the plastic strain plot.

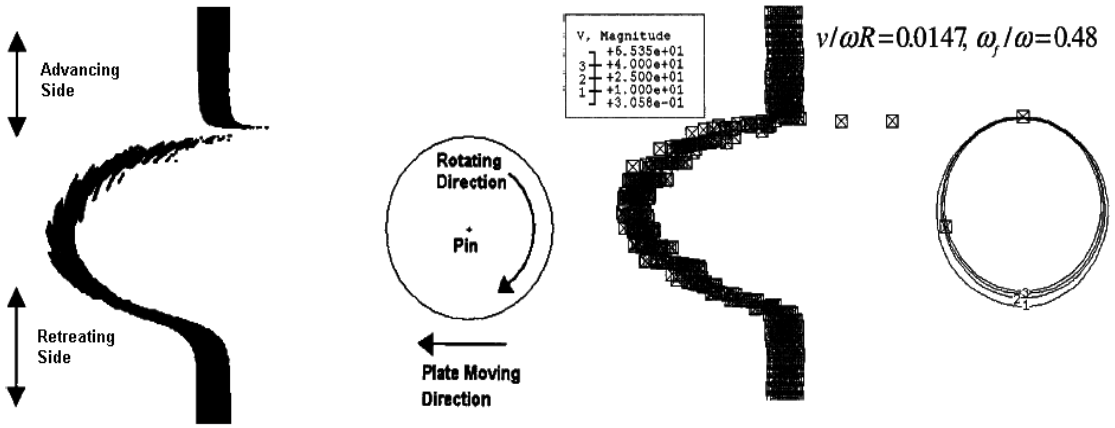

Figure 1-13 Comparison with experimental study from Xu et al. [45]

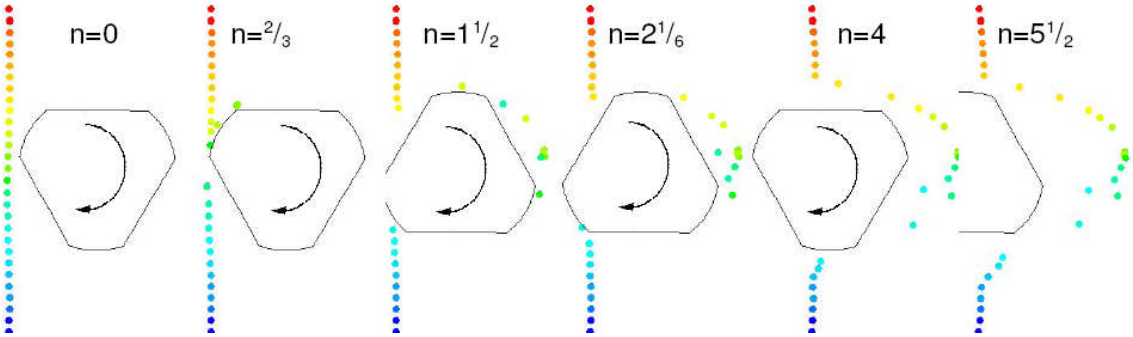

Figure 1-14 Sequence of particle plots for the 2024 models[126]

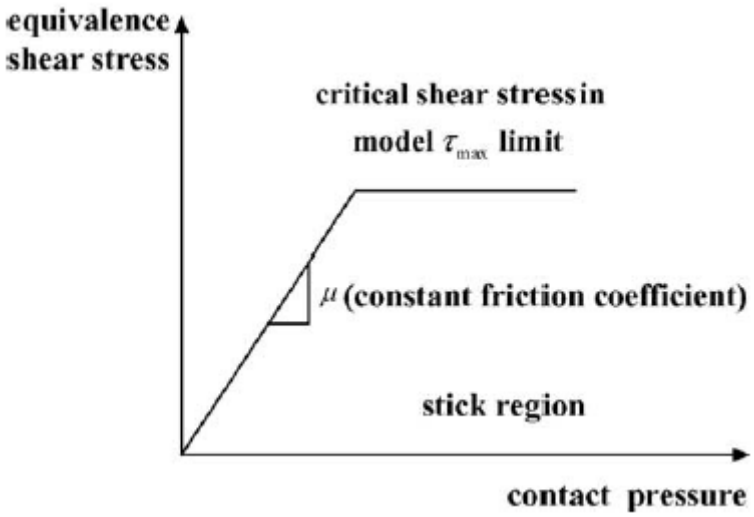

Figure 1-15 Modified coulomb boundary condition[127]

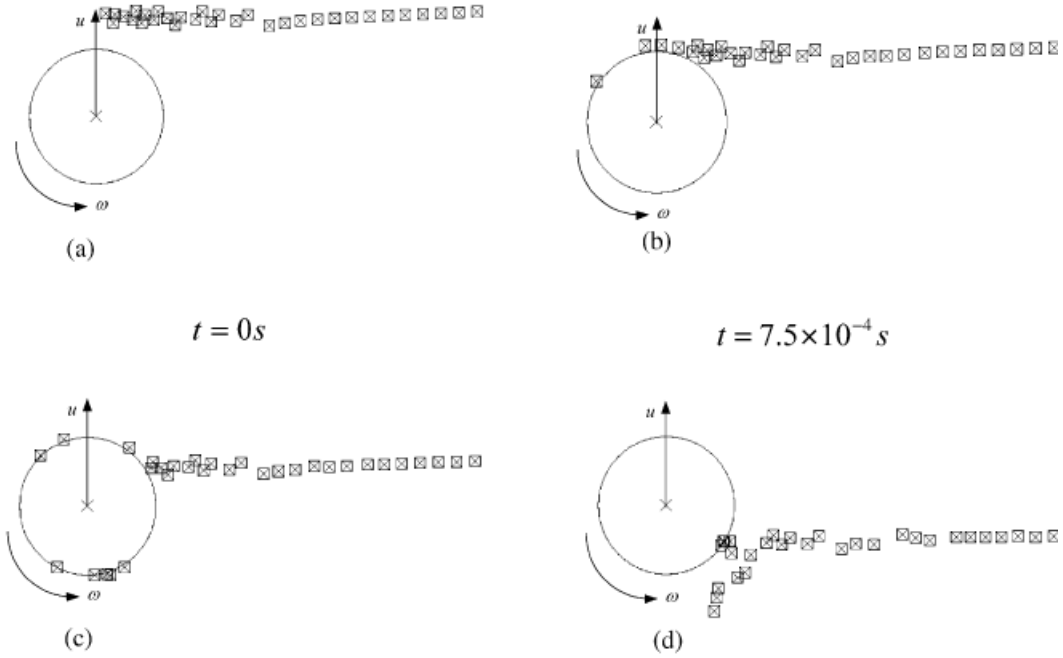

Figure 1-16 Material from the advancing side[127]

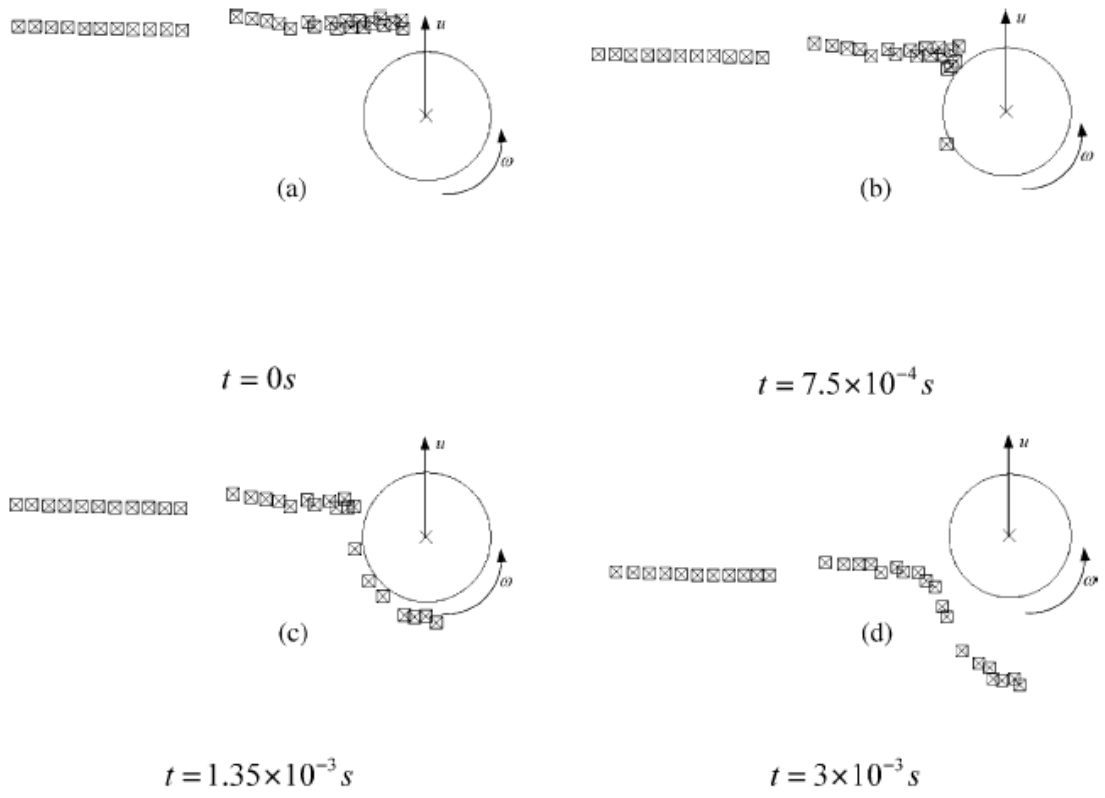

Figure 1-17 Material from retreating side[127]

- Streamline plot study

A streamline plot by Seidel et al.[74] (Figure 1-18) shows the velocity field around a FSW pin, in which a compression region is formed in the advancing side while two tensile regions at the retreating side. The plot showed the material from the leading side was swept around the retreating side and left behind the pin.

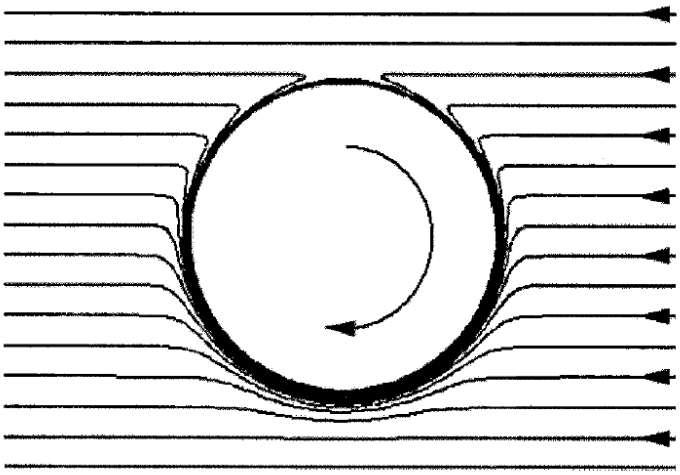

Figure 1-18 Streamline plot of velocity field around the pin[74]

Schmidt et al.[52] applied a streamline plot to investigate the shape of velocity field around the pin under different welding speeds. He proclaimed a shear layer around the tool pin, which would be introduced in section 3.2.3.1. The combined plot including both streamline and particle was approached to determine the size of the shear layer (dashed circle around the pin). The plots showed that under high welding speed the size of the shear layer could be larger.

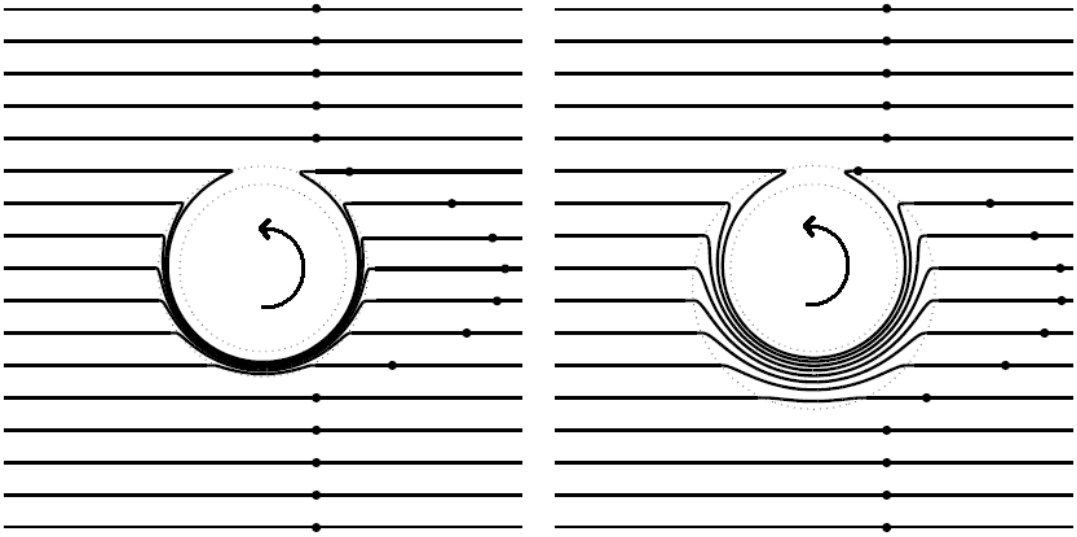

(a) For $u_{weld} = 2$ mm s^{-1} (b) For $u_{weld} = 10$ mm s^{-1}

Figure 1-19 Streamline and particle plots to investigate the shear layer (dashed circles) size around the pin under different welding speed[52]

- Effects of tool profiles and boundary condition variation

Apart from particle plot researches, Colegrove et al.[3] also applied several streamline plots, and one purpose of them is to study influence from the different pin profiles. He simplified 2D profiles pin as Figure 1-20, which are able to capture the features like flats or flutes, with two different boundary conditions: slip and stick (Figure 1-21). The slip model showed significant difference from the stick model. By examining the traversing force and welding torque parameters, a more efficient tool shape was suggested. He also used velocity vectors plots to investigate the deformation size and flow pattern around the pin (Figure 1-22). The strain-rate equalling to 2 s^{-1} boundary is used to show the deformation region. By comparing (a) and (b), it is shown the deformation region on advancing side is much smaller in slip model, and by comparing (b) from (c), it demonstrates that the flats have a significant effect on the material flow. The influence of the pin angle (angle of the sides of the pin relative to the rotation axis) to the process was studied by Buffa et al.[128], and it was suggested that increasing the pin angle would increase the size of HAZ and TMAZ, and the overall temperature will increase. A better deformation in the nugget can be achieved with increasing the pin angle.

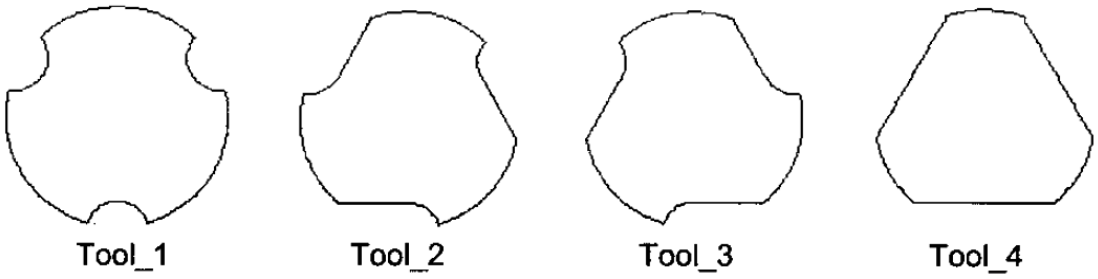

Figure 1-20 2D idealized tool features[3]

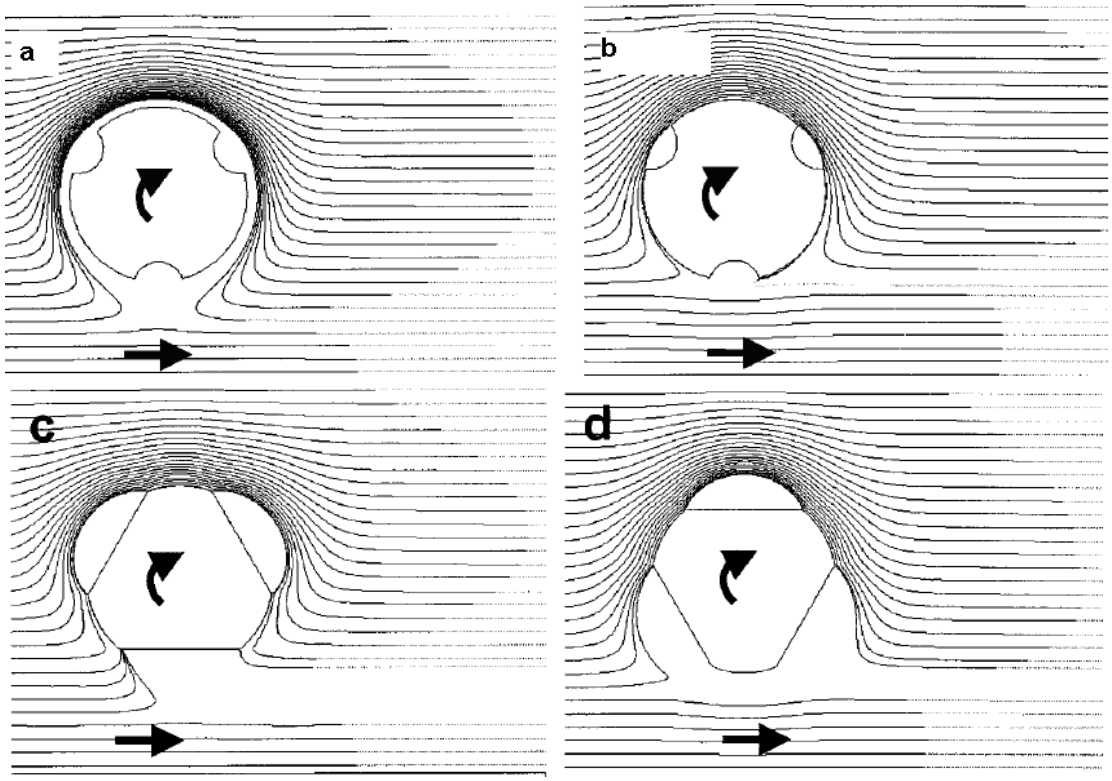

Figure 1-21 Effects from different tool profiles and the interface boundary conditions[3]: stick (a); slip (b, c, d)

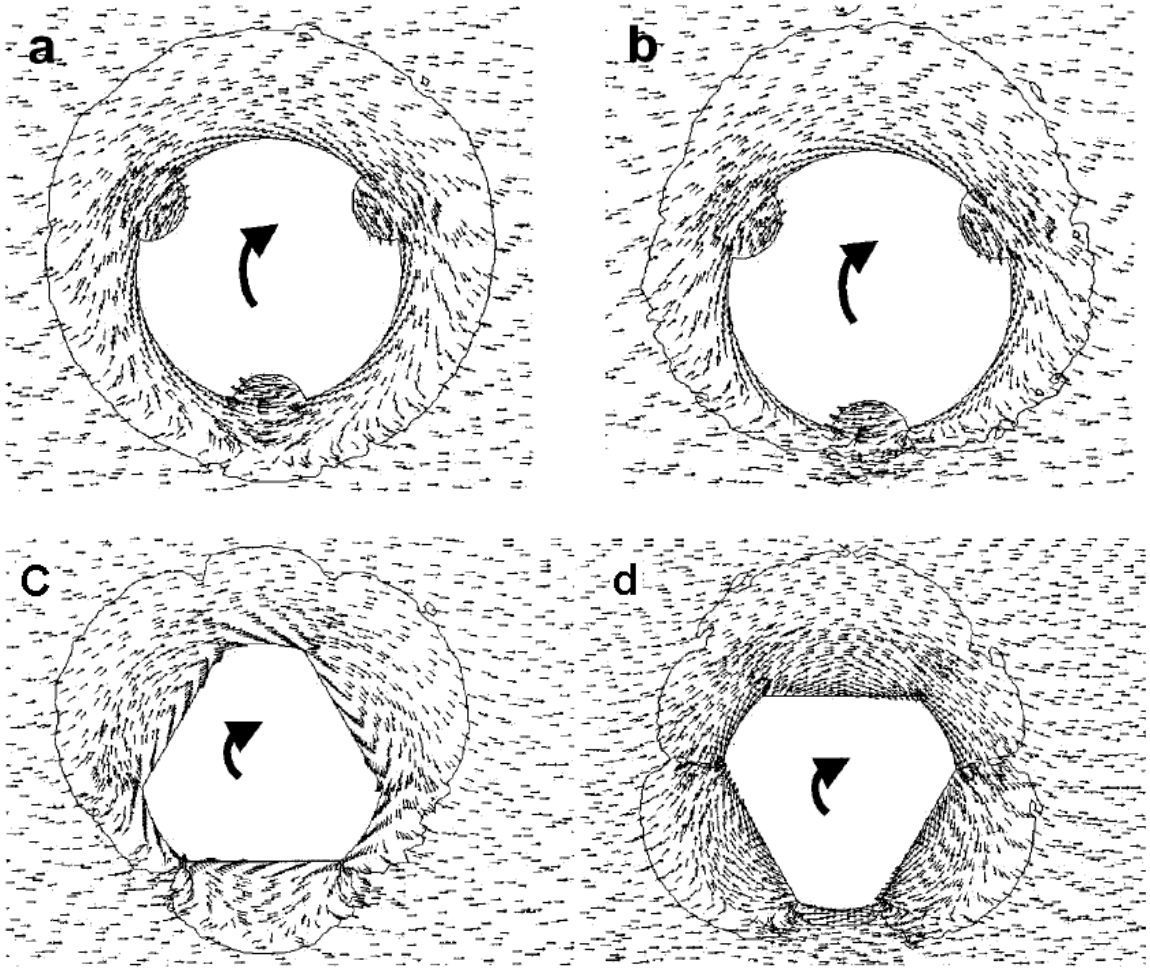

Figure 1-22 Velocity vectors plots and strain-rate $2s^{-1}$ contours: a, stick; b, slip with limiting shear stress 40MPa; c and d, slip with limiting shear stress 40MPa

1.8.4.2 Three-dimensional models

Material flow in the FSW process was categorized by Heurtier et al.[117] into three types: rotating, vortex flow near tool, and transition flow throughout the workpiece, which was experimentally validated by Guerra et al.[116] using copper foil. The 2D models above may be sophisticated enough to simulate the rotation flow and transition flow, but vortex flow needs 3D modelling. Some three-dimensional models with complex geometry have been developed to study the full material flow in the FSW process.

- Flow visualisation

An early model by Chao et al.[79] used a 3D thermal-mechanical model and the FE method. The model predicted the reduction of yield stress near the pin, but it did not

describe the complex flow behaviour. The CTH model by Askari et al.[108] predicted the material flow including an upward material movement in the mid-plate, which was supported by experimental observation. Xu et al.[129] also extended their 2D models to 3D ones to capture the vortex flow around pin during FSW. A model developed by Manufacturing oriented FE tool (MORFEO) FE code[130] simulated rotation, translation and vertical flow around a profiled tool pin.

Influence on the flow pattern from shoulder was included in 3D models. A comparison of velocity vectors fields across different heights of cylindrical pin by Colegrove and Shercliff[5] (Figure 1-23) showed the influence from the tool shoulder (c) and pin (a, b) on the material flow. Nandan et al.[58] applied streamline plots across different heights of the tool pin, to study the material flow. However, he assumed there is a thin layer of plasticity rotating near the tool (Figure 1-24). Zhang et al.[37] (Figure 1-25) showed that the shoulder rotation could accelerate the material flow near top surface. This result was also obtained by Wang et al.[57].

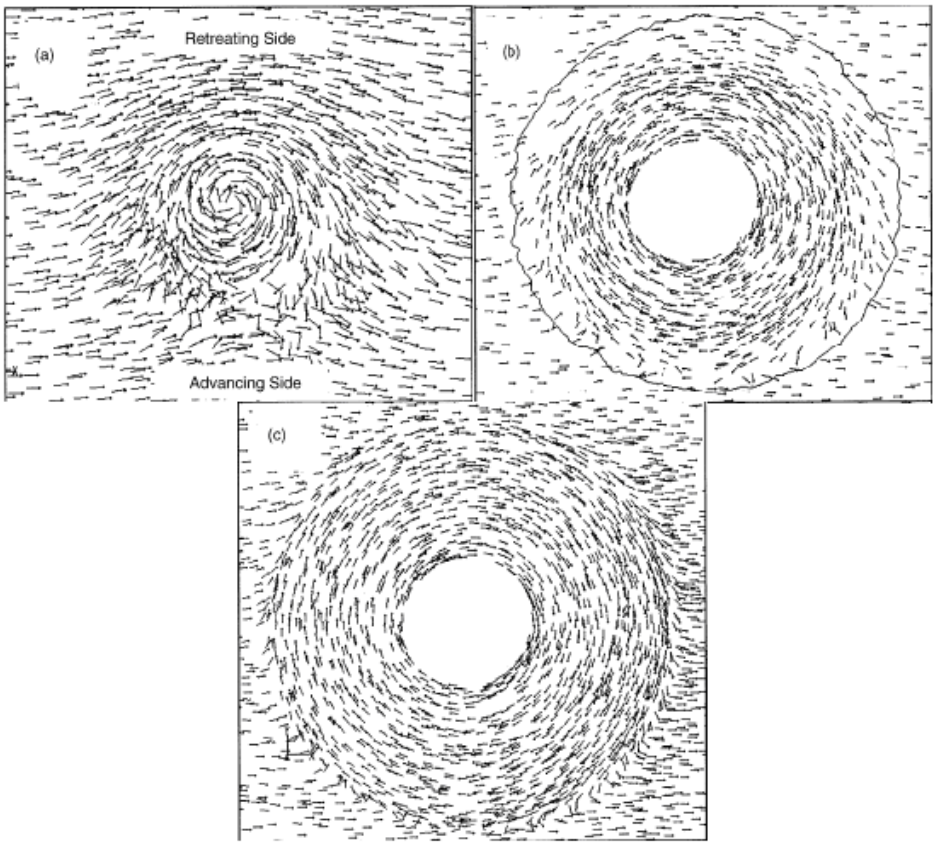

Figure 1-23 Arrow plots across the (a) z=0.1 (b) z=3.18 (c) z=6 by Colegrove and Shercliff [5]

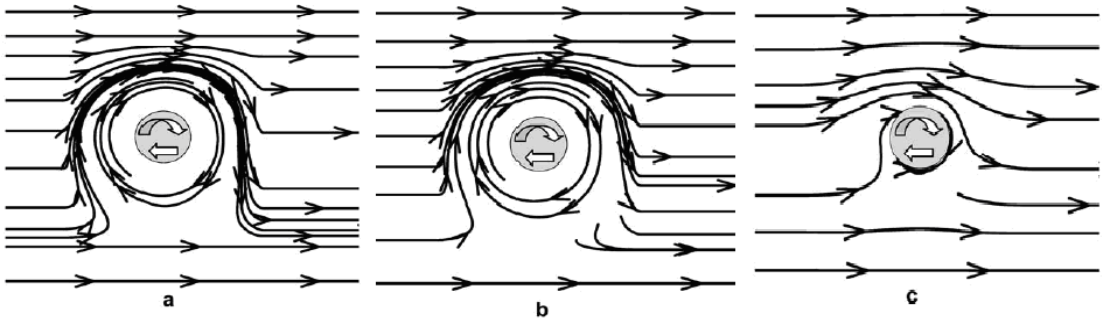

Figure 1-24 Arrow plots across the (a) z=5.72mm (b) z=4.02mm (c) z=0.64mm by Nandan et al. [58]

Figure 1-25 Particle plots from top and front view[37]

- Effects from tool condition variation

Colegrove and Shercliff[50] further updated his 2D flow models to 3D ones, which argued the benefits of Trivex geometry over Triflute. The streamline plot was used to illustrate the flow around the pin (Figure 1-26). The effects of different rake angles (-4° to 4°) were studied by Atharifar et al.[60] using a stick/slip boundary condition, which included the influence on pressure distribution, strain-rate and the velocity field. The result showed that the rake angle had large effects on the magnitude of the loads applied to the FSW tool, and some optimised rake angles were suggested for some other aluminium alloys. Another model[128] related the tool geometry with material microstructural evolution, which used a thermo-mechanical model and recommended an optimal tool geometry for improving nugget integrity.

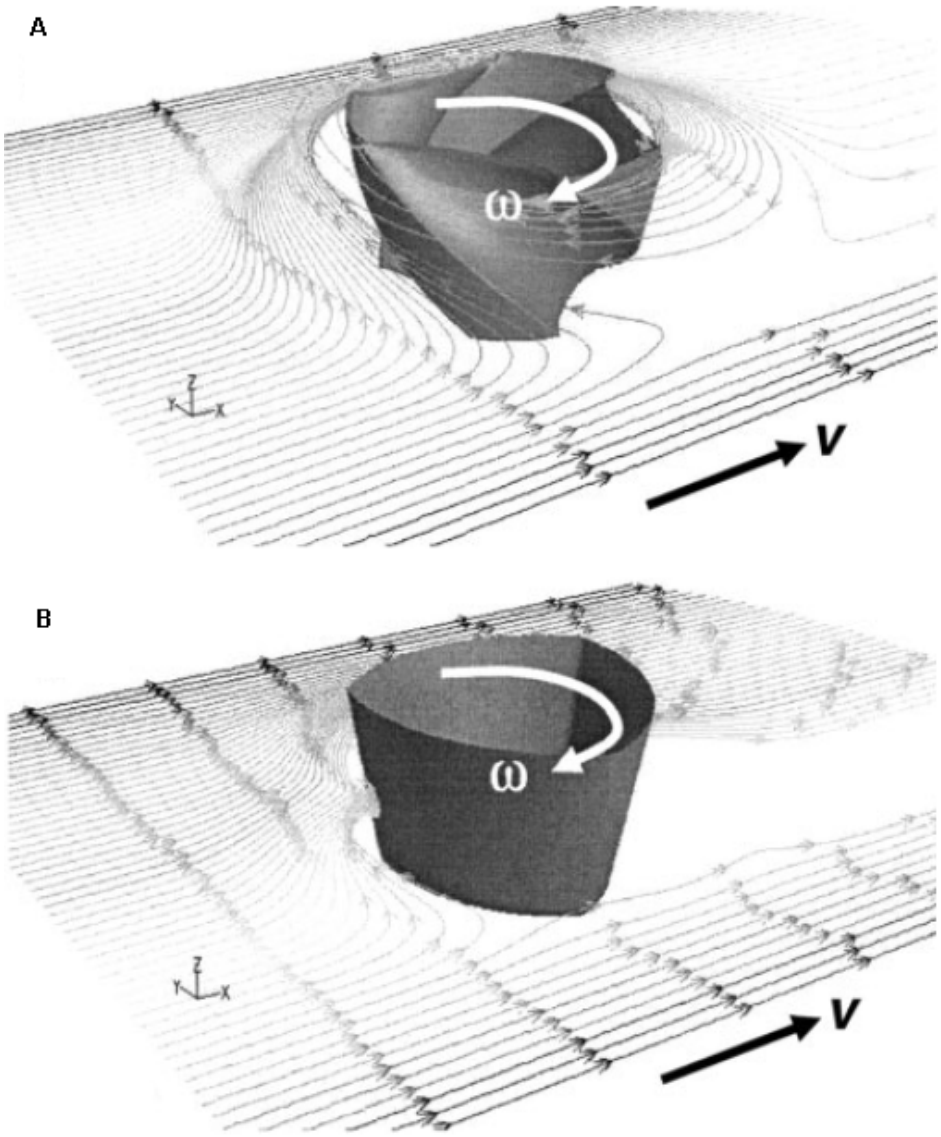

Figure 1-26 Streamlines plot of a 3D FSW flow model with a) Triflute tool and b) Trivex tool[50]

1.8.4.3 Shear layer

Some literature studied the material flow around the pin and suggested a shear layer around the pin[76,115,116]. Schmidt and Hattel[52] calculated the shear layer analytically: the shear layer was divided into three parts (Figure 1-27):

- Rotation layer: A region in the shear layer attaching to the pin, it consists of the rotation flow. The rotation flow includes the material which flows around both advancing side and retreating side of the pin.

- Transition layer: The region in the shear layer next to the rotation layer, it consists of the transition flow around the pin. The transition flow includes the material entering the region from the leading side. The transition flow volume at the retreating side is assumed to be equal to the welding flow.
- Deflection zone: This layer is outside the transition layer and is a region where the material flow is deflected rather than being swept into the main rotational flow. The material from the leading side will enter the deflection zone first then the transition zone, while material from the advancing and retreating sides will enter the deflection zone but not the transition zone.

Their work was validated with some experimental results (Figure 1-28, Figure 1-29). The shear layer method was applied to modelling work of bobbin tool FSW by Hilgert et al. [85], which was able to predict the peak temperature accurately.

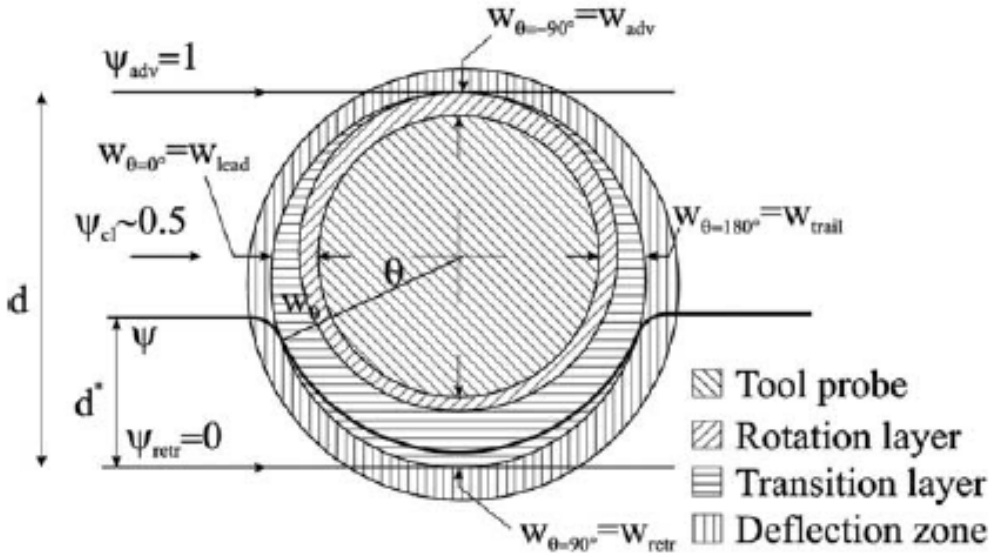

Figure 1-27 Shear layer division[115]

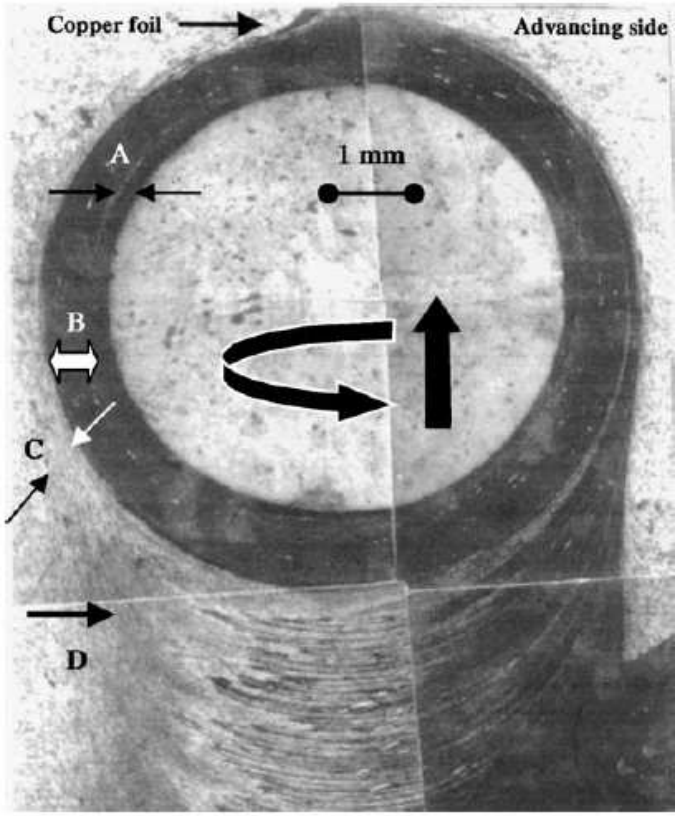

Figure 1-28 Experimental observation of shear layer[116]: Gap between tool and material; (A) Rotation zone; (B) Transitional zone; (C) Deflection zone

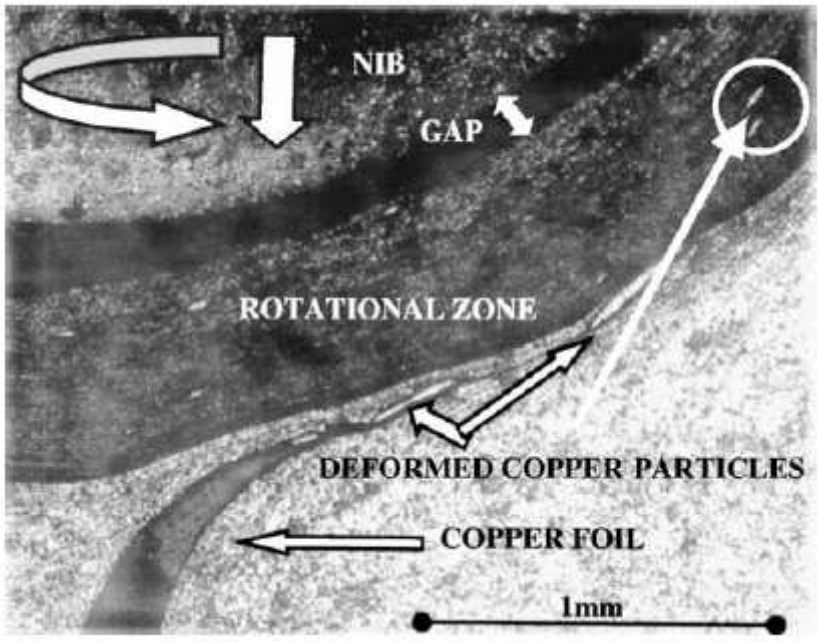

Figure 1-29 Experimental observation of shear layer[116]:copper foil is broken and gets into the rotation zone

1.8.4.4 Coupling with thermal models

The flow model is usually coupled with a thermal model so that the thermal effect on the material properties can be included. In a fully coupled model, the process loop works as follows[100]:

- The viscous dissipation and frictional heat generation is calculated at or near the material/tool interface.
- Conductive and convective heat transfer from the heat source is used to calculate the temperature distribution around the tool.
- The temperature influences the material viscosity or friction condition, which influences the heat generation.

Colegrove et al.[39] simplified this procedure by calculating the heat generation in a two-dimensional axisymmetric model then imposing it on a three-dimensional thermal model to predict the temperature field. The result from temperature field was averaged and used to update the heat flux (Figure 1-30). The calculation continued until a convergence.

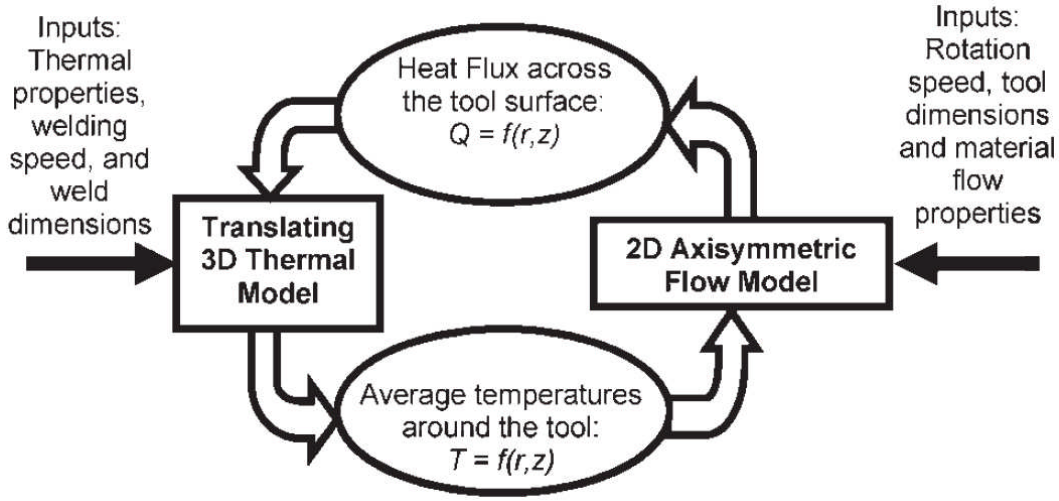

Figure 1-30 Schematic representation of coupling between a thermal and a flow model[39]

The CTH model reported in Askari et al.[108] used a fully coupled model as did Zhang et al.[372] and Li and Mackenzie[84].

1.8.4.5 Welding parameters studies

Within coupled thermal and flow models, the influences from varied welding parameters are able to be studied. Tang et al.[131] investigated the temperature distributions and included the influences from normal pressure, rotation speed, and the existence of the pin. Their results showed that high pressure and rotation speeds caused higher temperatures, but the incremental effect decreased with increasing rotation speed, which was explained by the material softening that occurs as the temperature approaches the solidus. They claimed that the tool shoulder dominated the flow pattern and heat generation. Colegrove[6] studied the material softening behaviour and the differences in terms of different rotation speeds and tool shapes (Figure 1-31). Figure 1-31(a) shows that at a low rotation speed (80rpm) large amount of material are deformed at high strain-rate but out of softening region (roughly 480-500 °C), while at higher rotation speed (200rpm) they are deformed at high temperature and strain-rate. The results also varied in terms of different pin profiles (b, c).

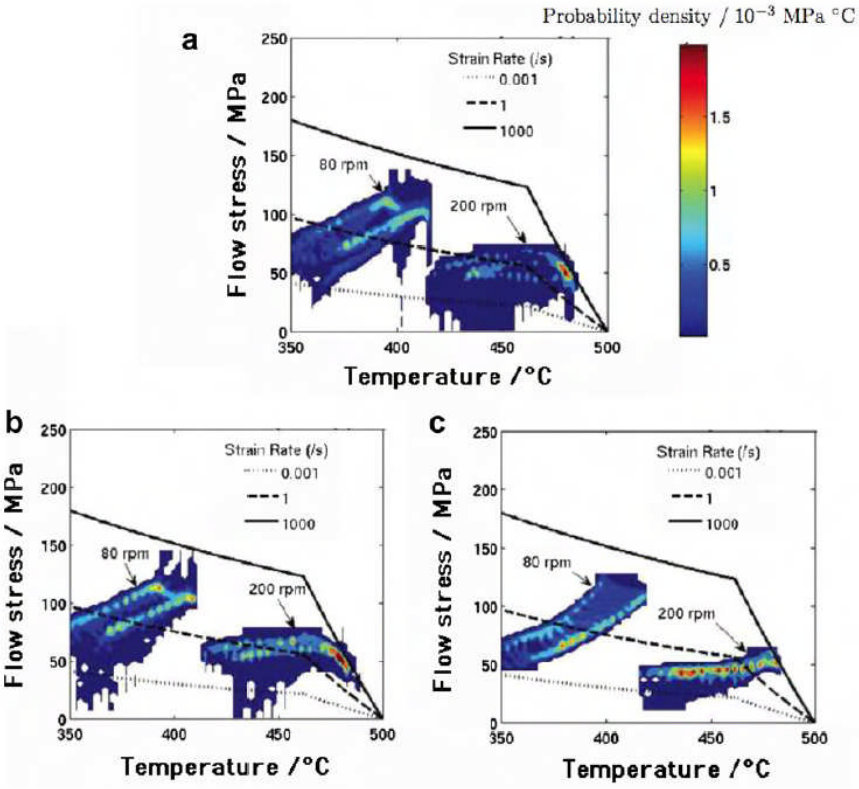

Figure 1-31 Material condition plots for: a. Triflate b. Trivex c. Cylindrical tool at 80 and 200 rpm rotation speed[6]

Long and Reynolds[89] used their models to suggest an optimum rotation speed and predict the flow pattern. Zhang and Zhang[132] investigated the influence of preheating on the FSW process, which indicated that the preheating time influenced the formation of a successful weld. Another model by Zhang and Zhang[133] explored the non-linear relationship between the maximum temperature and rotation speed.

1.8.4.6 Some difficulties in numerical modelling

The three major difficulties in numerical simulation of the FSW process are discussed as follows:

1. Numerical mesh method selection

As mentioned in section 2.2.2, the thermal models are not as sensitive to mesh methods as the flow models. The difficult part here in modelling the material flow is that when applying the Lagrangian mesh method, the material attached to the mesh is deformed due to the strain, which result in distorted elements and a failure of the model[134]. The general solution will be to use a fine mesh and remeshing of the deformed material[135]. The ALE formulation is also used by several modellers[134,136]. Guerdoux and Fourment[136] used the Eulerian formulation for the state-state analysis of the temperature distribution in FSW, and the ALE formulation with remeshing method for a transient model to have a better understanding of the deposition during the weld. Alfaro et al. [134] introduced a NEM, which kept the accuracy of the model during the mesh distortion.

2. The elastic-plastic problem

The elastic-plastic problem is caused from the principle of using the CFD method. The material is assumed to be a viscoplastic fluid instead of an elastic solid as mentioned above. This problem results in the elastic stress being ignored by the solver. A solution to this problem is the CTH code. Askari et al.[108] simulated a three-dimensional model for the FSW process by using the CTH code, which could model the FSW as an elastic-plastic problem. In CTH model, the material flow was combined with both mechanical and thermodynamic properties, and the deformation zone was distinguished by a plastically deformed layer and an elastic region. The CTH model gave good prediction of the material flow around the tool which compared favourably with the experiments, but it tended to underestimate the temperature on advancing side and overestimate it on the retreating side.

3. Investigation of porosity production

The free surface problem relates to the material adjacent to the pin[137]. In the experiments, a free space or void is sometimes left behind the welding tool in the weld[111,138] (Figure 1-32). In the models that use the CFD method the material is assumed to be in complete contact with the pin. Some success in modelling this effect has been achieved with FE models meshed with ALE formulation (Figure 1-33)[65,139]. Although these models provide useful information, they are highly sensitive to material properties and contact settings and the calculations are very time consuming. Recently He et al.[140] used a CFD code integrated with an additional porosity equation to predict the void formation. This model considered the influences from rotation, welding speed and the tool profile on the growth and distribution of porosity. A simpler prediction by Liechty and Webb[111] used a variable shear stress model to predict the potential void formation. This model assumed the void may form due to the diminishing velocities in that volume, negative pressure region, and vanishing friction at the interface (Figure 1-34). However these assumptions were based on a variable shear stress boundary condition where there was the possibility of generating zero shear stress on the tool/material interface, and the void formation was only partially predictable.

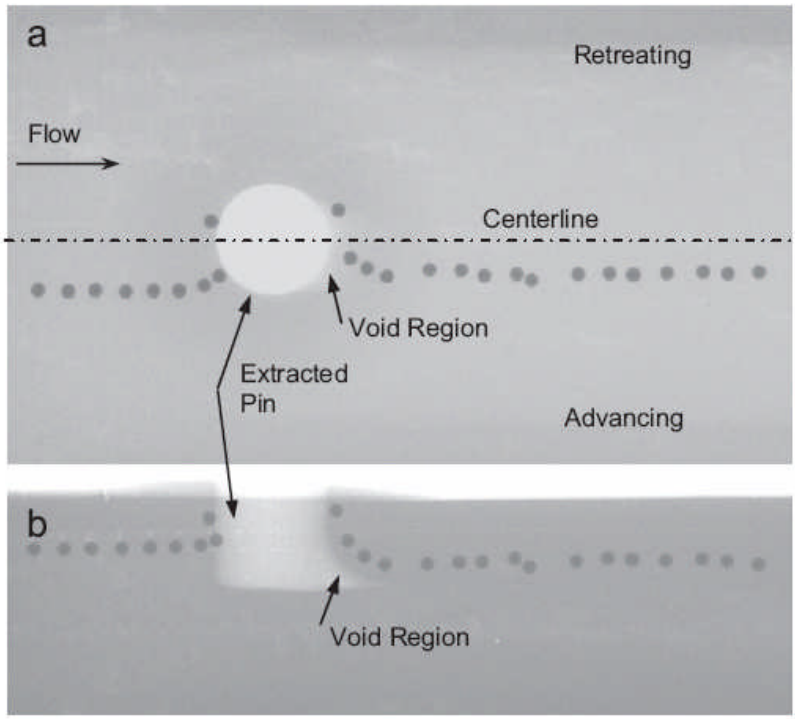

Figure 1-32 X-ray image of steel particle streamline in a stop action weld to observe the position of a void: (a) top view and (b) advancing side view[111]

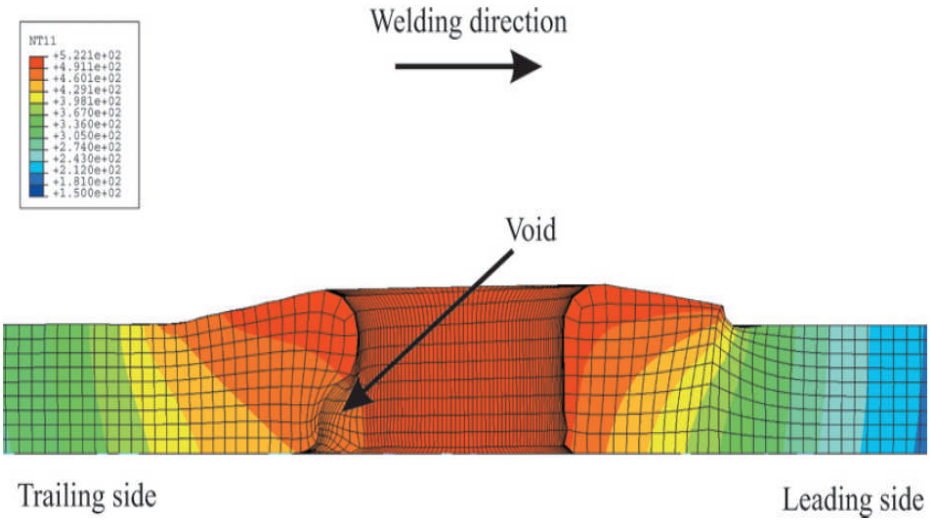

Figure 1-33 The void formation predict by a three-dimensional model[65]

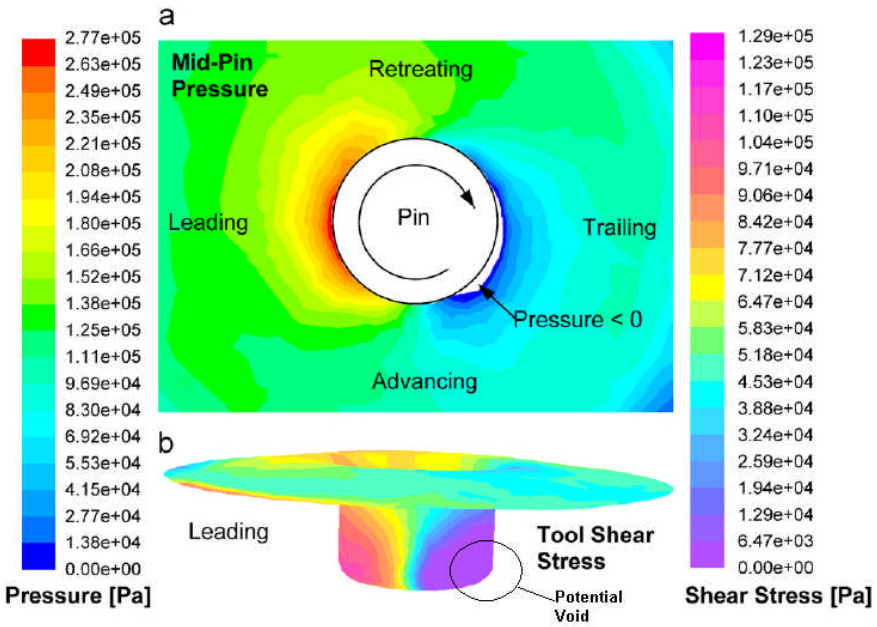

Figure 1-34 Pressure field and shear stress on the tool (a); the variable shear stress of the tool (b) and the potential void prediction[111]

1.8.5 Experimental validation

The observation of the metal flow during the FSW process is extremely difficult, however, a number of experiments have been done to study it indirectly.

1.8.5.1 Marker experiments

A common way of observing material flow in the FSW is to use markers, which do not affect the material deformation in the FSW process. The marker material includes steel or lead balls[141], contrasting aluminium alloy pins[43,142], SiC or copper foil[43,46,47,116,143,144], tungsten wire[145], and titanium powder[61]. Figure 1-35 shows the movement of an originally straight transverse marker after it has been welded: the material bulges backward in a curve and a small part of material is swept to the advancing side, which matched the prediction in the flow models by Xu et al.[45]. Figure 1-36 again shows the incoming markers being swept around the retreating side, and the flow separates at the advancing side. Figure 1-37 helps explain how the layered flow occurs: the markers are swept around the retreating side and in a layered fashion. Figure 1-28 and Figure 1-29 show the usage of materials to examine the shear layer around the pin, in which the deformed cooper foil was distributed in three zones around the pin as predicted from the shear layer model.

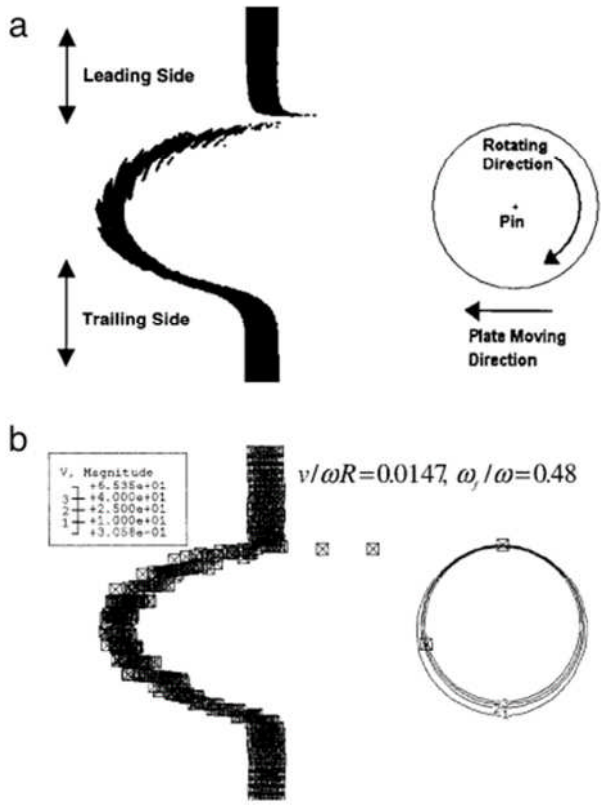

Figure 1-35 The comparison between (a) transverse copper foil and (b) and its model prediction[45]

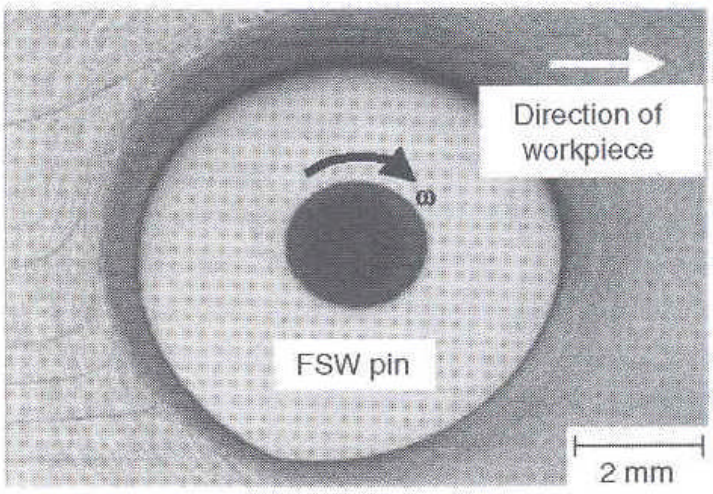

Figure 1-36 Longitudinal SiC markers[46]

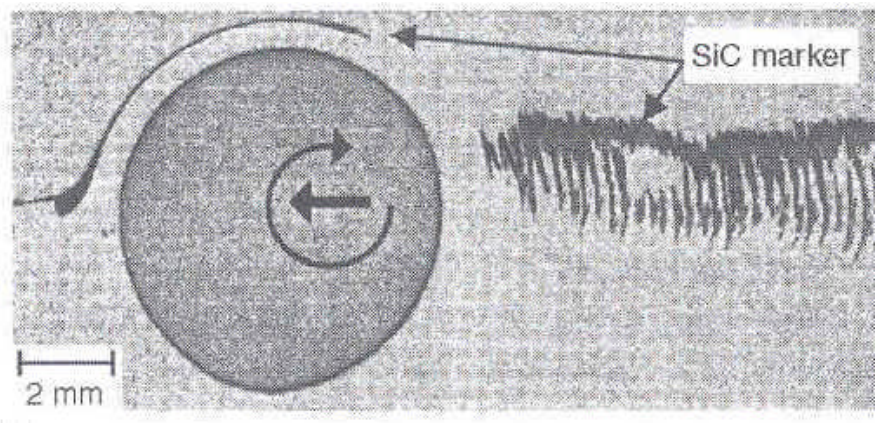

Figure 1-37 Longitudinal SiC markers[144]

1.8.5.2 Stop-action technique

A technique named 'stop-action' was applied by Colligan et al.[141] as is shown in Figure 1-38, which is formed by stopping the rotation and retracting the pin by screwing the pin out of the weld, so the material flow is left as it would had been during welding. The analysis of the longitudinal section of the exit hole shows that:

1. The material on the leading side of the pin is pushed upward and then downward when it gets closer to the pin.
2. The material filled in the tool thread rotates with the pin then swept behind the tool.
3. The 'layered' upward movement of the material behind the pin forms the 'onion ring'. It may also be influenced by the material beneath welding pin.

Chen et al.[146] conducted FSW experiments to result in the tool pin broken during the process. Their work investigated how the shear flow formed the nugget zone in the FSW weld, and included:

1. Material from the leading side was swept around the retreating side and deposited behind the tool pin (Figure 1-39). However the work did not contain any investigation about the different material from advancing side or retreating sides.
2. Figure 1-40 (a) shows the deposited material forming the weld nugget. There is a shear layer formed by the pin (c), which formed the weld nugget.

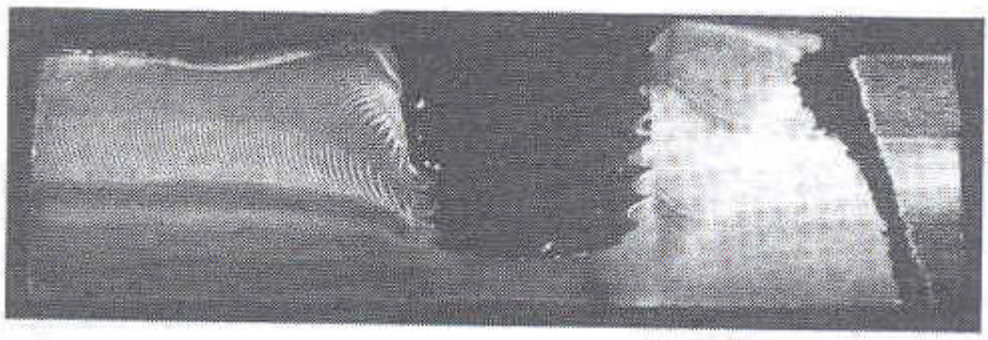

Figure 1-38 A longitudinal section of the exit hole after 'Stop-action'[141]

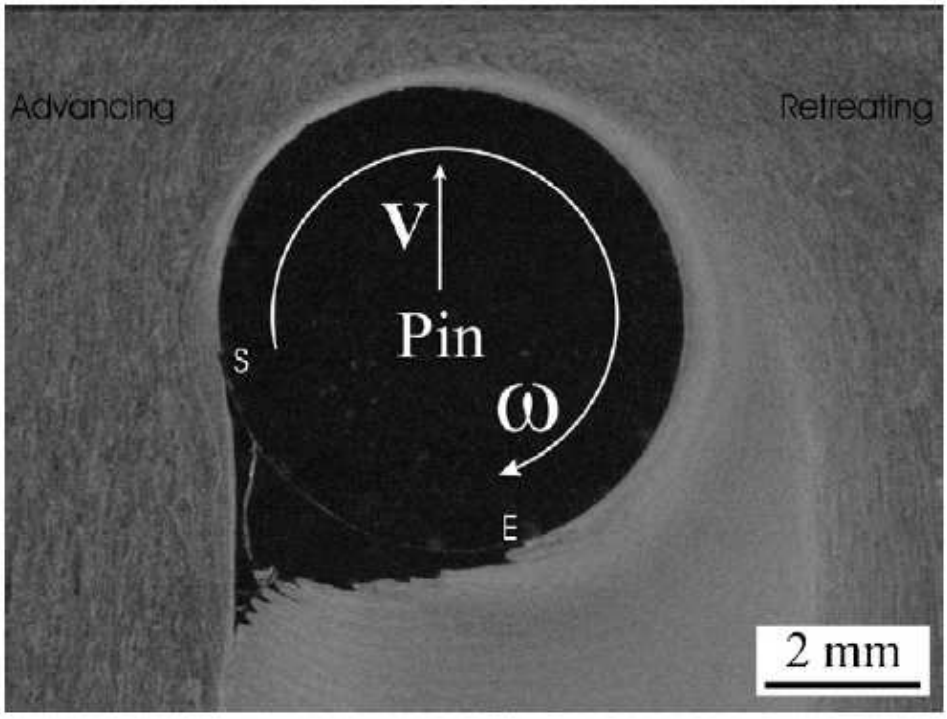

Figure 1-39 A longitudinal cross-section of the weld at the mid-plane, with a broken pin embedded[146]

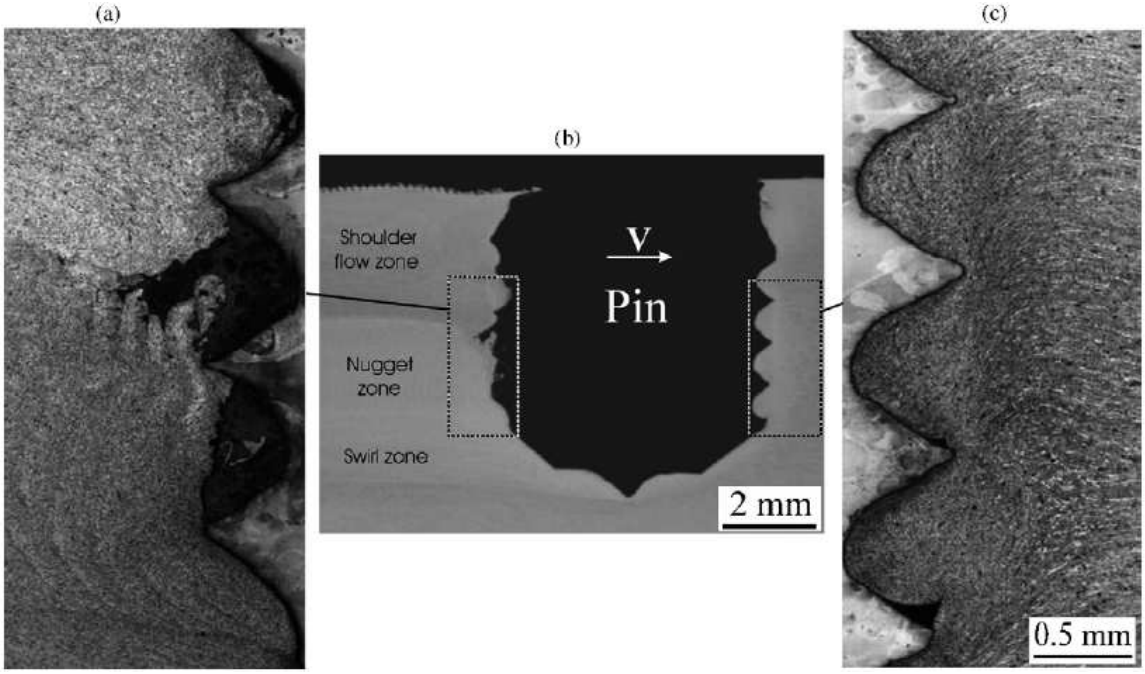

Figure 1-40 Longitudinal cross-section of the weld with a broken pin embedded, sectioning along the mid-section of the pin. (a) higher magnification micrograph of the left part of the hole (b) lower magnification micrograph (c) higher magnification micrograph of the right part of the hole[146]

1.8.5.3 Application of X-ray

The application of X-ray technique helps to analyse the deformation and distribution of the markers in the parent material without sectioning the weld. London et al.[144] used Al-20%W as the marker material, because the material can be differentiated from aluminium alloy with X-ray analysis, and it enabled a 3D monitoring of the welding deformation situation. Schneider and Nunes[145] used a Tungsten wire as a marker material then examined the deposition of the marker. The Tungsten was deformed by rotating with pin, and it was left behind the pin perpendicular to the weld direction. A computer tomography illustration of the copper foil deformed by FSW is shown in Figure 1-41. Finally copper foil was used by Schmidt et al.[115] and Dickerson et al.[143].

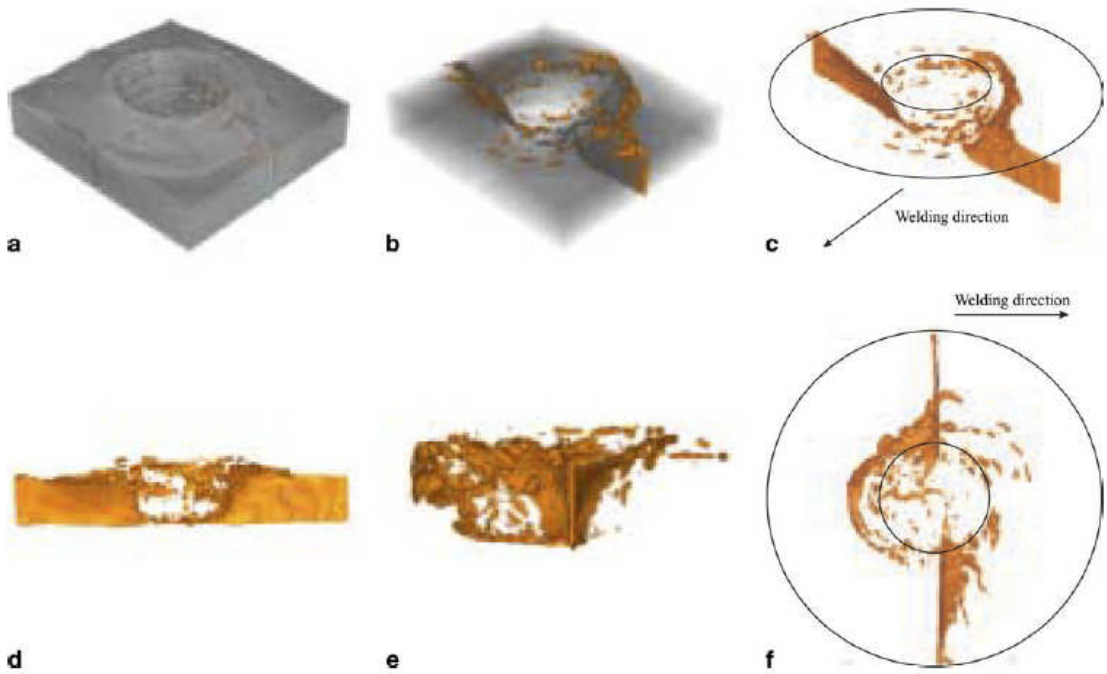

Figure 1-41 3D CT model yellow cooper foil in gray aluminium with different transparency[115]: No transparency (a); Half (b); Full (c); Front view (d); Advancing side view (e); Top view (f)

1.8.5.4 Welding other materials for visualisation purpose

McClure et al.[147] used a pin without a profile to FSW polycarbonate. Similar flow fields to aluminium alloys were found in their work. The advantage is polycarbonate is an economic material which is transparent. Liechty and Webb[121] used plasticine as an analogous material to study the flow evolution in the FSW process, which is shown to have a similar qualitative flow stress behaviour to metals.

1.9 Microstructural modelling

Early microstructural models of FSW[117,148,149] were based on a microstructural model developed by Myhr and Grong[150], in which the hardness of the material was predicted by measuring the amount of precipitate that dissolved at certain temperature for a certain time. These microstructural models used a temperature profile predicted from thermal models to calculate the amount of precipitate dissolution. As a result, the material hardness during welding and after natural aging was calculated. In another model[120] the CDRX phenomena in FSW of AA6082 was simulated and it was shown

that initial grain size was related to the Zener-Hollomon equation which enabled the calculation of the average grain size after welding.

Much more sophisticated simulations[151,152] of the evolution of precipitates in heat treatable aluminium alloys have been developed, which included the coupling with thermal models dynamically. Its methodology calculated the phase stability for metastable and equilibrium precipitates, with classical nucleation, growth, and coarsening theory. The material hardness prediction can be determined from these models.

1.10 ANN modelling of FSW

The term neural networks here mean the ANN, which use computer system to simulate human brain. Computer aided ANN are able to find out the complex relationships between multiple-channel inputs and outputs, and they have proved to be a powerful tool in the field of computer science, mathematics and engineering. Neural networks are widely applied in welding research area[35,153]. In FSW region, Fratini et al.[154] coupled a well-trained neural networks with a FE model to capture the CDRX phenomena in FSW of AA6082. The model took local values of strain, strain rate, and temperature from experiments and numerical model results as training items, to predict the average grain size under high strain rate and temperature, which are extremely hard to determine from experiment. Note that the constitutive model used for the material was the Zener-Hollomon relationship discussed in a previous section. Apart from calculating average grain size, this method can be used to predict the flow stress under high strain rate and temperature. Another neural network model by Okuyucu et al.[155] predicted the weld mechanical properties from the welding parameters, such as welding and rotation speed, which agreed well with measured data. Weiss et al.[156] created a unique HST, which combined an analytical thermal model with an ANN to predict the melting zone border shape in hybrid LB-GMA welding of aluminium alloy. Schwenk et al.[157] applied the similar method: the ANN generated a temperature field of a laser beam welding, which is used as an input for numerically simulating the welding distortions. Nandan et al.[158] applied a genetic algorithm to calculate the weld geometry in GTAW, their simplified structure for ANN is shown in Figure 1-42, which consists of three layers: input, hidden

and output. They also used the DE technique to determine some parameters in the numerical FSW model, such as the heat transfer coefficient between the workpiece and backing plate. The DE technique is introduced in the previous modelling method review.

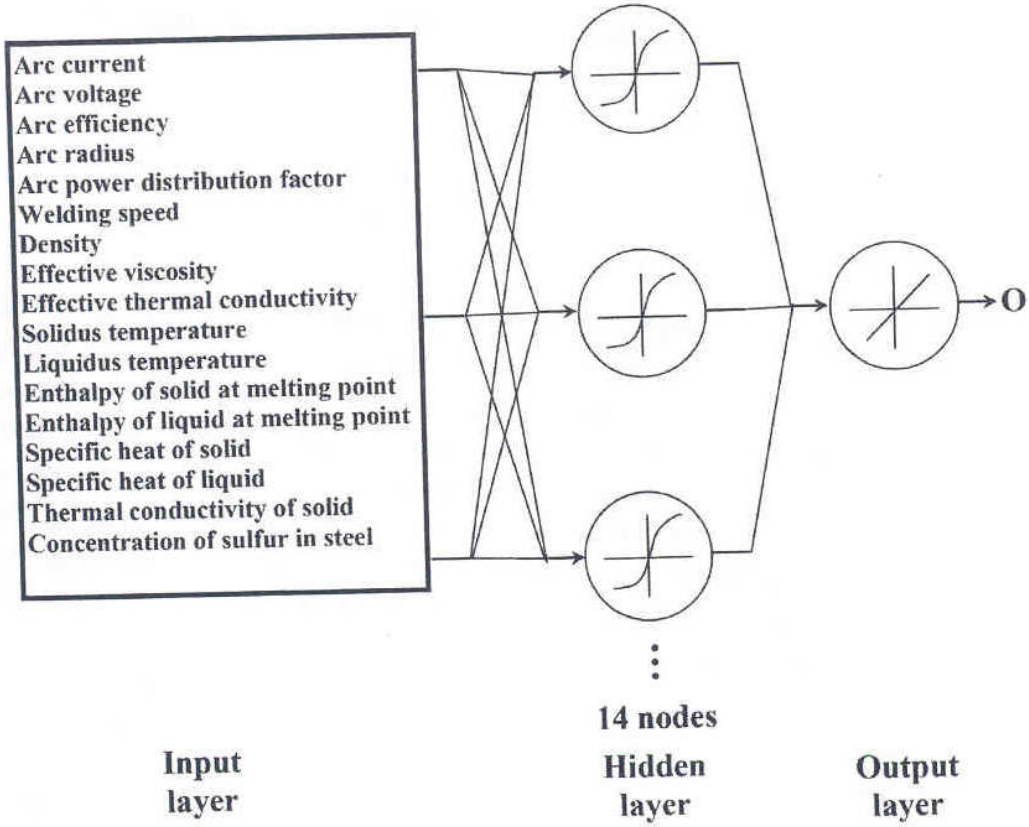

Figure 1-42 Neural network to predict the weld geometry for GTAW, the output O stands for the predicted weld geometry[158]

1.11 Conclusions and thesis outline

This chapter of the thesis introduced the modelling of FSW in two steps, which are

1. The first step of this review (from section 1.1 to 1.5) has described some of the fundamental concepts relevant to process modelling, including the physical principles and mathematical methods. It briefly introduced the conservation laws in CFD with some associated boundary conditions, the analytical methods such as the classic Rosenthal heat model and some analytical flow models, and finally numerical methods for example the finite volume method.
2. The second step of this review (from section 1.6 to 1.10) stated with some fundamental concepts of the FSW process, such as how it works, advantages and disadvantages, and the weld microstructure classification. It followed with the

introduction of the process modelling of FSW, with the discussion of the most recent works.

In conclusion, FSW is an innovative technique and the numerical modelling of FSW can help understanding and lead to process improvement. However there are still some knowledge gaps in the modelling of FSW:

1. The material constitutive behaviour under high strain-rate near solidus temperature, which is the typical condition material experiences during FSW. The material constitutive behaviour is essential for calculating both heat generation and flow behaviour so this gap needs to be filled with adequate experimental work and numerical studied based on it.
2. Methods for determining the thermal boundary condition between the workpiece and backing bar, which are either arbitrarily assigned with a constant value or adjusted with trails and error approaches[95]. A more efficient method is required for tuning the thermal boundary condition.
3. The contact condition between the welding tool and workpiece. This is very difficult to observe experimentally but very important for understanding the heat generation at tool and flow behaviour near the tool. Therefore a systematic analysis of different slip conditions is required with a numerical model.

These three main issues have been are addressed in this thesis with both experiments and new modelling methodologies:

1. Chapter 2 describes the Gleeble experiment used to investigate the constitutive behaviour of material under high strain-rate condition (up to 120 s^{-1}) near the solidus temperature, which is close to the condition material experiences during FSW. The derived new constitutive constants are also analysed by comparing with the ones found in the literature.
2. Chapter 3 and 4 introduce a hybrid modelling method which combines the weld/FSW model with an ANN model to calibrate the thermal boundary conditions between the workpiece and backing bar. This has been applied theoretically in chapter 3 and is applied to a series of FSW in chapter 4.

3. Chapter 5 studied the contact condition between the workpiece and welding tool during FSW, and its influence on the heat generation and flow behaviour.

The materials chosen for study are the typical automobile alloy 6082-T6 and common aerospace alloy 7449-T7, which are the two main industrial areas where aluminium alloys are applied.

References

1. P. A. Colegrove: 'Modelling of friction stir welding', *Thesis (Ph.D).University of Cambridge, Cambridge* 2003.

2. H. K. Versteeg: 'An Introduction to Computational Fluid Dynamics : The Finite Volume Method', 1995, Harlow, Longman Scientific & Technical.

3. P. A. Colegrove and H. R. Shercliff: 'Two-dimensional CFD [computational fluid dynamics] modelling of flow round profiled FSW [friction stir welding] tooling', *Science and Technology of Welding and Joining,* 2004, 9, 483-492.

4. FLUENT: "FLUENT User's Manual", in Release 12.1 (ed.) *FLUENT Inc.* Lebanon, NH, USA, 2006.

5. P. A. Colegrove and H. R. Shercliff: '3-dimensional CFD [computational fluid dynamics] modelling of flow round a threaded friction stir welding tool profile', *J. Mater. Process. Technol.,* 2005, 169, 320-327.

6. P. A. Colegrove and H. R. Shercliff: 'CFD modelling of friction stir welding of thick plate 7449 aluminium alloy', *Science and Technology of Welding and Joining,* 2006, 11, 429-441.

7. H. S. Carslaw and J. C. Jaeger: 'Conduction of Heat in Solids', 2nd edition, 1959, Oxford, Clarendon Press.

8. B. L. Hicks, D. J. Montgomery and R. H. Wasserman: 'On the one-dimensional theory of steady compressible fluid flow in ducts with friction and heat addition', *Journal of Applied Physics*, 1947, 18, 891-902.

9. C. A. J. Fletcher: 'Computational Techniques for Fluid Dynamics', 2nd edn, 1991, Berlin ; New York, Springer-Verlag.

10. S. V. Patankar: 'Numerical Heat Transfer and Fluid Flow', 1980, Washington; London, Hemisphere.

11. COMSOL: "Heat Transfer Module User's Guide", in *COMSOL Multiphysics*, COMSOL AB. 2005.

12. J. P. Holman: 'Heat Transfer', 6th edition, 1986, New York, McGraw-Hill Book Co.

13. Ø. Grong: 'Metallurgical modelling of welding', 2nd edn, *Book.Second Edition.Publ: London, UK; Institute of Materials;* 1997.

14. D. Rosenthal: 'Mathematical theory of heat distribution during welding and cutting', *Weld. J.*, 1941, 20, 220s-234s.

15. D. Rosenthal: 'The theory of moving sources of heat and its application to metal treatments', *Trans. ASME,* 1946, 68, 849-866.

16. O. R. Myhr and Ø. Grong: 'Dimensionless maps for heat flow analyses in fusion welding', *Acta Metallurgica*, 1990, 38, 449-460.

17. J. J. Monaghan: 'An introduction of SPH', *Computer Physics Communications,* 1988, 48, 89-96.

18. O. Kum, W. G. Hoover and H. A. Posch: 'Viscous conducting flows with smooth-particle applied mechanics', *Phys. Rev. E,* 1995, 109, 67-75.

19. J. P. Boyd: 'Chebyshev and Fourier Spectral Methods', 2nd edition, 2001, Mineola, NY, Dover Publications.

20. R. Courant: 'What is Mathematics? : An Elementary Approach to Ideas and Methods', 1941, Oxford, Oxford University Press.

21. O. C. Zienkiewicz: 'Finite Elements and Approximation', 1983, Wiley.

22. O. C. Zienkiewicz and R. L. Taylor: 'The finite element method', *Solid and Fluid Mechanics, Dynamics and Non-Linearity*, 1991, 2.

23. E. S. Oran: 'Numerical Simulation of Reactive Flow', 1987, Elsevier.

24. A. Thomas: 'Safety in numbers', *Tunnels and Tunnelling International*, 2001, 33, 31-34.

25. H. K. D. H. Bhadeshia: 'Neural networks in materials science', *ISIJ International*, 1999, 39, 966-979.

26. J. Thibault and B. P. A. Grandjean: 'A neural network methodology for heat transfer data analysis', *Int. J. Heat Mass Transfer*, 1991, 34, 2063-2070.

27. NeuroSolutions 5.07, NeuroDimension Inc., 2008.

28. S. Haykin: 'Neural Networks: A Comprehensive Foundation', 2nd edition, 1999, USA, Prentice-Hall.

29. I. Oh and C. Y. Suen: 'A class-modular feedforward neural network for handwriting recognition', *Pattern Recognit*, 2002, 35, 229-244.

30. M. Smith: 'Neural networks for statistical modeling', 1993, New York: Van Nostrand Reinhold.

31. K. V. Price: ' Differential evolution: A fast and simple numerical optimizer', Proc. Biennial Conference of the North American Fuzzy Information Processing Society - NAFIPS, 524-527, June 19-22, 1996, Berkeley, California, USA.

32. R. Storn and K. Price: 'Differential Evolution - A Simple and Efficient Heuristic for Global Optimization over Continuous Spaces', *Journal of Global Optimization*, 1997, 11, 341-359.

33. R. Storn: *Different evolution codes from UCB*, available at: http://www.icsi.berkeley.edu/~storn/code.html.

34. J. P. Boris: 'New directions in computational fluid dynamics', *Ann. Rev. Fluid Mech.*, 1989, 21, 345-385.

35. K. Andersen, G. E. Cook, G. Karsai and K. Ramaswamy: 'Artificial neural networks applied to arc welding process modeling and control', *IEEE Transactions on Industry Applications*, 1990, 26, 824-830.

36. W. M. Thomas: 'Friction stir butt welding', *Friction Stir Butt Welding International Patent Application, No. PCT/GB92 Patent Application No. 9125978.8*.

37. Z. Zhang and H. W. Zhang: 'A fully coupled thermo-mechanical model of friction stir welding', *International Journal of Advanced Manufacturing Technology*, 2008, 37, 279-293.

38. R. S. Mishra, M. W. Mahoney, and Rockwell Scientific Company: 2007, "Friction stir welding: Introduction", in Mahoney, M. W. and Mishra, R. S. (eds.) *Friction stir welding and processing*, ASM International, USA.

39. P. A. Colegrove, H. R. Shercliff and R. Zettler: 'Model for predicting heat generation and temperature in friction stir welding from the material properties', *Science and Technology of Welding and Joining*, 2007, 12, 284-297.

40. K. J. Colligan and R. S. Mishra: 'A conceptual model for the process variables related to heat generation in friction stir welding of aluminum', *Scripta Materialia*, 2008, 58, 327-331.

41. J. K. Raghulapadu, J. Peddieson, G. R. Buchanan and A. C. Nunes: 'A rotating plug model of friction stir welding heat transfer', *Heat Transfer Engineering,* 2008, 29, 321-327.

42. J. E. Gould and Z. Feng: 'Heat flow model for friction stir welding of aluminum alloys', *Journal of Materials Processing and Manufacturing Science,* 1998, **7**, 185-194.

43. A. P. Reynolds, T. U. Seidel and M. Simonsen: 'Visualization of material flow in an autogenous friction stir weld', *1st International Symposium on Friction Stir Welding,* 1999, Thousand Oaks, CA, USA.

44. P. A. Colegrove, M. Painter, D. Graham and T. Miller: '3 dimensional flow and thermal modeling of the friction stir welding process', *Proceedings of the Second International Symposium on Friction Stir Welding,* 2000, 162-169.

45. S. Xu, X. Deng, A. P. Reynolds and T. U. Seidel: 'Finite element simulation of material flow in friction stir welding', *Science and Technology of Welding and Joining,* 2001, 6, 191-193.

46. B. London, M. Mahoney, W. Bingel, M. Calabrese and D. Waldron: 'Experimental methods for determining material flow in friction stir welds', *Proceedings of the Third International Symposium on 'Friction Stir Welding',* 2001, Port Island, Kobe, Japan.

47. M. Guerra, J. C. McClure, L. E. Murr and A. C. Nunes: 'Metal flow during friction stir welding', *Proc. Friction Stir Welding and Processing,*Editor K.V. Jata, M.W. Mahoney, R.S. Mishra, TMS, 2001, 25-34.

48. H. Schmidt, J. Hattel and J. Wert: 'An analytical model for the heat generation in friction stir welding', *Modelling and Simulation in Materials Science and Engineering,* 2004, 12, 143-157.

49. P. A. Colegrove and H. R. Shercliff: 'Development of Trivex friction stir welding tool. Part 1: Two-dimensional flow modelling and experimental validation', *Science and Technology of Welding and Joining,* 2004, 9, 345-351.

50. P. A. Colegrove and H. R. Shercliff: 'Development of Trivex friction stir welding tool. Part 2: Three-dimensional flow modelling', *Science and Technology of Welding and Joining*, 2004, 9, 352-361.

51. P. A. Colegrove: 'Modelling and development of the Trivex friction stir welding tool', *Weld. World*, 2004, 48, 10-26.

52. H. Schmidt and J. Hattel: 'An analytical model for prescribing the flow around the tool probe in Friction Stir Welding', *Proceedings of a Symposium sponsored by the Shaping and Forming Committee of (MPMD) of the Minerals*, Metals and Materials Society, TMS, 205-212.

53. R. Nandan, G. G. Roy and T. Debroy: 'Numerical simulation of three dimensional heat transfer and plastic flow during friction stir welding', *Metallurgical and Materials Transactions A: Physical Metallurgy and Materials Science*, 2006, 37, 1247-1259.

54. R. Nandan, G. G. Roy, T. J. Lienert and T. Debroy: 'Numerical modelling of 3D plastic flow and heat transfer during friction stir welding of stainless steel', *Science and Technology of Welding and Joining*, 2006, 11, 526-537.

55. L. Fratini, G. Buffa, D. Palmeri, J. Hua and R. Shivpuri: 'Material flow in FSW of AA7075-T6 butt joints: Numerical simulations and experimental verifications', *Science and Technology of Welding and Joining*, 2006, 11, 412-421.

56. H. W. Zhang, Z. Zhang and J. T. Chen: '3D modeling of material flow in friction stir welding under different process parameters', *Journal of Materials Processing Technology*, 2007, 183, 62-70.

57. G. Wang, L. Zhu and Z. Zhang: 'Modeling of material flow in friction stir welding process', *China Welding (English Edition)*, 2007, 16, 63-70.

58. R. Nandan, G. G. Roy, T. J. Lienert and T. Debroy: 'Three-dimensional heat and material flow during friction stir welding of mild steel', *Acta Materialia*, 2007, 55, 883-895.

59. Z. Zhang and H. Zhang: 'Effect of process parameters on quality of friction stir welds', *Cailiao Yanjiu Xuebao/Chinese Journal of Materials Research,* 2006, 20, 504-512.

60. H. Atharifar and R. Kovacevic: 'Numerical study of the tool rake angle effect on the material flow in friction stir welding process' *ASME International Mechanical Engineering Congress and Exposition, Proceedings* 3 ,649-657.

61. R. Zettler, S. Lomolino, J. F. Dos Santos, T. Donath, F. Beckmann, T. Lippman and D. Lohwasser: 'Effect of tool geometry and process parameters on material flow in FSW of AN AA 2024-T351 alloy', *Welding in the World,* 2005, 49, 41-46.

62. P. A. Colegrove, H. R. Shercliff, and T. Hyoe: 2004, "Development of the Trivex friction stir welding tool for making lap welds", *Proceedings of the 5th International Symposium on Friction Stir Welding,* Abington, Cambridge, UK, TWI Ltd.

63. L. Hu and B. Hu: 'Numerical model of welding temperature in friction stir welding and affecting factors', *Jixie Gongcheng Xuebao/Chinese Journal of Mechanical Engineering,* 2006, 42, 235-238.

64. H. Zhang, S. B. Lin, L. Wu, J. C. Feng and S. L. Ma: 'Defects formation procedure and mathematic model for defect free friction stir welding of magnesium alloy', *Materials and Design,* 2006, 27, 805-809.

65. H. Schmidt and J. Hattel: 'A local model for the thermomechanical conditions in friction stir welding', *Modelling and Simulation in Materials Science and Engineering,* 2005, 13, 77-93.

66. C. Hamilton, S. Dymek and M. Blicharski: 'A model of material flow during friction stir welding', *Materials Characterization,* 59 (9), 2008, 1206-1214.

67. P. L. Threadgill and M. E. Nunn: 'A review of friction stir welding: Part 1: Process review', *TWI Members Report,* 760/2003, 2003, 1-31.

68. C. D. Sorensen and T. W. Nelson: ' Friction stir welding of ferrous and nickel alloys', *Proc. Friction Stir Welding and Processing,*Editor K.V. Jata, M.W. Mahoney, R.S. Mishra, TMS, 2007, 111-122.

69. R. L. Goetz and K. V. Jata: 'Modeling friction stir welding of titanium and aluminum alloys', *Proc. Friction Stir Welding and Processing,*Editor K.V. Jata, M.W. Mahoney, R.S. Mishra, TMS, 2001, 35-42.

70. W. M. Thomas, P. L. Threadgill and E. D. Nicholas: 'Feasibility of friction stir welding steel', *Science and Technology of Welding and Joining,* 1999, 4, 365-372.

71. C. G. Andersson, R. E. Andrews and G. I. Dance: 'A Comparison of Copper Canister Fabrication by the Electron Beam and Friction Stir Process', *2nd Intern. Symp. on FSW,* Gothenburg, Sweden, 2000.

72. P. L. Threadgill: 'Friction stir welds in aluminium alloys - Preliminary microstructural assessmen' *TWI Bulletin,* 1997, 28, 30-33.

73. H. R. Shercliff and P. A. Colegrove: "Process Modeling", in Mishra, R. S. and Mahoney, M. W. (eds.) *Friction stir welding and processing,* First edition, ASM International Materials Park, USA, 2007.

74. T. U. Seidel and A. P. Reynolds: 'Two-dimensional friction stir welding process model based on fluid mechanics', *Science and Technology of Welding and Joining,* 2003, 8, 175-183.

75. A. Gerlich, P. Su and T. H. North: 'Peak temperatures and microstructures in aluminium and magnesium alloy friction stir spot welds', *Science and Technology of Welding and Joining,* 2005, 10, 647-652.

76. H. R. Shercliff and P. A. Colegrove: 2002, "Modelling of friction stir welding", *Mathematical Modelling of Weld Phenomena,* vol. 6, 927-974.

77. O. Frigaard, O. Grong, B. Bjorneklett and O. T. Midling: 'Modeling of the thermal and microstructure fields during friction stir welding of aluminum alloys', *Proceedings*

of the First International Symposium on Friction Stir Welding, Thousand Oaks, California, 1999.

78. M. Song, R. Kovacevic, J. Ouyang and M. Valant: 'A Detailed Three-Dimensional Transient Heat Transfer Model for Friction Stir Welding', *ASM Proceedings of the International Conference: Trends in Welding Research*, 212-217.

79. Y. J. Chao and X. Qi: 'Thermal and thermo-mechanical modeling of friction stir welding of aluminum alloy 6061-T6', *Journal of Materials Processing and Manufacturing Science*, 1998, **7**, 215-233.

80. H. B. Schmidt and J. H. Hattel: 'Thermal modelling of friction stir welding', *Scripta Materialia*, 2008, 58, 332-337.

81. C. Hamilton, S. Dymek and A. Sommers: 'A thermal model of friction stir welding in aluminum alloys', *International Journal of Machine Tools and Manufacture*, 2008, 48, 1120-1130.

82. P. Vilaça, L. Quintino, J. F. dos Santos, R. Zettler and S. Sheikhi: 'Quality assessment of friction stir welding joints via an analytical thermal model, iSTIR', *Materials Science and Engineering A*, 2007, 445-446, 501-508.

83. J. W. Pew, T. W. Nelson and C. D. Sorensen: 'Torque based weld power model for friction stir welding', *Science and Technology of Welding and Joining*, 2007, 12, 341-347.

84. H. Li and D. Mackenzie: 'Coupled thermo-mechanical modelling of friction stir welding', *Proc. American Society of Mechanical Engineers, Pressure Vessels and Piping Division (Publication) PVP*, 193-201.

85. J. Hilgert, H. N. B. Schmidt, J. F. Dos Santos and N. Huber: 'Thermal models for bobbin tool friction stir welding', *J. Mater. Process. Technol.*, 2011, 211, 197-204.

86. J. C. McClure, W. Tang, L. E. Murr, X. Guo, Z. Feng and J. E. Gould: 'A Thermal Model of Friction Stir Welding', *Proc. ASM Proceedings of the International Conference: Trends in Welding Research*, 590-595.

87. A. Służalec: 'Thermal effects in friction welding', *International Journal of Mechanical Sciences*, 1990, 32, 467-478.

88. Z. Zhang and H. W. Zhang: 'Numerical studies of preheating time effect on temperature and material behaviours in friction stir welding process', *Science and Technology of Welding and Joining*, 2007, 12, 436-448.

89. T. Long and A. P. Reynolds: 'Parametric studies of friction stir welding by commercial fluid dynamics simulation', *Science and Technology of Welding and Joining*, 2006, 11, 200-208.

90. A. Needleman: 'Material Rate Dependence and Mesh Sensitivity in Localization Problems.', *Computer Methods in Applied Mechanics and Engineering*, 1988, 67, 69-85.

91. Y. S. Touloukian: 'Thermal Conductivity: Non Metallic Solids', 1970, New York, Plenum.

92. Y. S. Touloukian: 'Specific Heat: Non Metallic Solids', 1970, New York, Plenum.

93. Q. Shi, T. Dickerson and H. R. Shercliff: 'Thermomechanical FE modeling of friction stir welding of Al-2024 including tool loads', *Proceedings of 4th International Friction Stir Welding Symposium*, Park City, UT, USA, 2003.

94. M. Z. H. Khandkar, J. A. Khan and A. P. Reynolds: 'Prediction of temperature distribution and thermal history during friction stir welding: Input torque based model', *Science and Technology of Welding and Joining*, 2003, 8, 165-174.

95. A. Simar, J. Lecomte-Beckers, T. Pardoen and B. De Meester: 'Effect of boundary conditions and heat source distribution on temperature distribution in friction stir welding', *Science and Technology of Welding and Joining*, 2006, 11, 170-177.

96. Q. Shi, T. Dickerson and H. R. Shercliff: 'Thermo-mechanical Analyses of Welding Aluminium Alloy with TIG and Friction Stir Welding', *Proc. ASM Proceedings of the International Conference: Trends in Welding Research*, 247-252.

97. J. A. Schneider and A. C. Nunes Jr.: ' Thermo-mechanical processing in friction stir welds', *TMS Annual Meeting ,* 2003, 43-51.

98. Z. Zhang, Y. Liu, J. Chen and H. Zhang: 'Material flow patterns in friction stir welding', *Hanjie Xuebao/Transactions of the China Welding Institution,* 2007, 28, 17-21.

99. Z. Zhang and H. Zhang: 'Effect of welding parameters on mixing of materials in nugget zone of friction stir welds', *Jinshu Xuebao/Acta Metallurgica Sinica,* 2007, 43, 321-326.

100. P. Dong, F. Lu, J. K. Hong and Z. Cao: 'Coupled thermomechanical analysis of friction stir welding process using simplified models', *Science and Technology of Welding and Joining,* 2001, 6, 281-287.

101. D. Jacquin, B. De Meester, A. Simar, D. Deloison, F. Montheillet and C. Desrayaud: 'A simple Eulerian thermomechanical modeling of friction stir welding', *J. Mater. Process. Technol.,* 2011, 211, 57-65.

102. H. Schmidt and J. Hattel: 'Modelling heat flow around tool probe in friction stir welding', *Science and Technology of Welding and Joining,* 2005, 10, 176-186.

103. Z. Zhang and J. T. Chen: 'The simulation of material behaviors in friction stir welding process by using rate-dependent constitutive model', *Journal of Materials Science,* 2008, 43, 222-232.

104. M. Assidi, L. Fourment, S. Guerdoux and T. Nelson: 'Friction model for friction stir welding process simulation: Calibrations from welding experiments', *Int. J. Mach. Tools Manuf.,* 2010, 50, 143-155.

105. C. M. Sellars and W. J. M. Tegart: 'Hot workability', *Int. Met. Rev.,* 1972, **17**, 1-24.

106. T. Long, T. U. Seidel, W. Tang and A. P. Reynolds: 'A friction stir welding model using computational fluid dynamics', *Hot Deformation of Aluminum Alloys III, TMS Annual Meeting* , 2003, 299-312.

107. G. R. Johnson and W. H. Cook: 'A constitutive model and data for metals subject to large strains, high strain rates and high temperatures', *Seventh International Symposium on Ballistics,* 1983, The Hague, The Netherlands.

108. A. Askari, S. Silling, B. London and M. Mahoney: 'Modeling and analysis of friction stir welding processes', *Proc. Friction Stir Welding and Processing,* 2001, 43-54.

109. H. Schmidt and J. Hattel: ' A local model for the thermomechanical conditions in friction stir welding', *Proc. Friction Stir Welding and Processing III - Proceedings of a Symposium sponsored by the Shaping and Forming Committee of (MPMD) of the Minerals, Metals and Materials Society, TMS*, San Francisco, CA, USA, 2005, 225-232.

110. A. Moal and E. Massoni: 'Finite element simulation of the inertia welding of two similar parts', *Engineering Computations,* 1995, 12, 497-512.

111. B. C. Liechty and B. W. Webb: 'Modeling the frictional boundary condition in friction stir welding', *International Journal of Machine Tools and Manufacture,* 2008, 48 (12-13) , 1474-1485.

112. H. -. Zhang, Z. Zhang, J. Bie, L. Zhou and J. -. Chen: 'Effect of viscosity on material behavior in friction stir welding process', *Transactions of Nonferrous Metals Society of China (English Edition),* 2006, 16, 1045-1052.

113. J. -. Ponthot: 'An extension of the radial return algorithm to account for rate-dependent effects in factional contact and visco-plasticity', *Journal of Materials Processing Technology,* 1998, 80-81, 628-634.

114. M. B. Stewart, G. P. Adams, A. C. Nunes and P. Romine: 'A combined experimental and analytical modeling approach to understanding friction stir-welding', *Developments in Theoretical and Applied Mechanics,* 1998, 472.

115. H. N. B. Schmidt, T. L. Dickerson and J. H. Hattel: 'Material flow in butt friction stir welds in AA2024-T3', *Acta Materialia,* 2006, 54, 1199-1209.

116. M. Guerra, C. Schmidt, J. C. McClure, L. E. Murr and A. C. Nunes: 'Flow patterns during friction stir welding', *Materials Characterization,* 2002, 49, 95-101.

117. P. Heurtier, C. Desrayaud and F. Montheillet: 'A thermomechanical analysis of the friction stir welding process', Proc. Materials Science Forum, 1537-1542.

118. W. J. Arbegast: 'A flow-partitioned deformation zone model for defect formation during friction stir welding', *Scripta Materialia,* 2008, 58, 372-376.

119. A. Simar, T. Pardoen and B. De Meester: 'Effect of rotational material flow on temperature distribution in friction stir welds', *Science and Technology of Welding and Joining,* 2007, 12, 324-333.

120. G. Buffa, L. Fratini and R. Shivpuri: 'CDRX modelling in friction stir welding of AA7075-T6 aluminum alloy: Analytical approaches', *Journal of Materials Processing Technology,* 2007, 191, 356-359.

121. B. C. Liechty and B. W. Webb: 'The use of plasticine as an analog to explore material flow in friction stir welding', *Journal of Materials Processing Technology,* 2007, 184, 240-250.

122. J. M. McGlaun, S. L. Thompson, L. N. Kmetyk and M. G. Elrick: 'A brief description of the three-dimensional shock wave physics code CTH', *A Brief Description of the Three-Dimensional Shock Wave Physics Code CTH,* 1990, .

123. P. Ulysse: 'Three-dimensional modeling of the friction stir-welding process' *Mach. Tools Manuf.,* 2002, 42 (14), 1549-1557.

124. S. Xu and X. Deng: 'Two-and three-dimensional finite element models for the friction-stir welding process', *4th International Symposium on Friction Stir Welding Park City, USA,* 2003.

125. J. Cho, S. H. Kang, H. N. Han and K. H. Oh: 'Modeling friction stir welding process of aluminum alloys', *Metals and Materials International,* 2008, 14, 247-258.

126. P. A. Colegrove and H. R. Shercliff: ' Development of Trivex friction stir welding tool Part 1 - Two-dimensional flow modelling and experimental validation', *Science and Technology of Welding and Joining*, 2004, 9 (4) , 345-351.

127. H. W. Zhang, Z. Zhang and J. T. Chen: 'The finite element simulation of the friction stir welding process', *Materials Science and Engineering A,* 2005, 403, 340-348.

128. G. Buffa, J. Hua, R. Shivpuri and L. Fratini: 'Design of the friction stir welding tool using the continuum based FEM model', *Materials Science and Engineering A,* 2006, 419, 381-388.

129. S. W. Xu and X. M. Deng: 'A three-dimensional model for the friction stir welding process', *Proceedings of the 21st Southeastern Conference on Theoretical and Applied Mechanics XXI,* 2002, 699-704.

130. T. De Vuyst and L. D'Alvise: 'Material flow around a friction stir welding tool: Development of a thermo-fluid code', *Welding in the World*, 2007, 51, 37-43.

131. W. Tang, X. Guo, J. C. McClure, L. E. Murr and A. Nunes: 'Heat input and temperature distribution in friction stir welding', *Journal of Materials Processing and Manufacturing Science,* 1998, 7, 163-172.

132. Z. Zhang and H. W. Zhang: 'Numerical studies on effect of axial pressure in friction stir welding', *Science and Technology of Welding and Joining,* 2007, 12, 226-248.

133. Z. Zhang and H. W. Zhang: 'Numerical studies on controlling of process parameters in friction stir welding', *Journal of Materials Processing Tech.,* 2008.

134. I. Alfaro, L. Fratini, E. Cueto, F. Chinesta and F. Micari: Proc. AIP Conference Proceedings, 203-208.

135. R. Radovitzky and M. Ortiz: 'Lagrangian finite element analysis of Newtonian fluid flows', *International Journal for Numerical Methods in Engineering*, 1998, 43, 607-619.

136. S. Guerdoux and L. Fourment: Proc. AIP Conference Proceedings, 185-190.

137. A. Huerta and W. K. Liu: 'Viscous flow with large fee surface motion', *Computer Methods in Applied Mechanics and Engineering*, 1988, 69, 277-324.

138. S. Hirasawa, S. Hirano, M. Haneda and T. Tomimura: 'Analysis of flow and temperature distribution during friction stir welding', Proc. Proceedings of the ASME Heat Transfer/Fluids Engineering Summer Conference 2004, HT/FED 2004, 929-934.

139. L. Fourment, S. Guerdoux, M. Miles and T. Nelson: 'Numerical simulation of the friction stir welding process using both lagrangian and arbitrary lagrangian eulerian formulations', *5th FSW Symposium, Metz, France*, 2004.

140. Y. He, D. E. Boyce and P. R. Dawson: 'Three-dimensional modeling of void growth in friction stir welding of stainless steel', Proc. AIP Conference Proceedings, 25-34.

141. K. Colligan: 'Material flow behavior during friction stir welding of aluminum', *Welding Journal (Miami, Fla)*, 1999, 78, 229-s.

142. Y. Zhao, S. Lin, F. Qu and L. Wu: 'Influence of pin geometry on material flow in friction stir welding process', *Materials Science and Technology*, 2006, 22, 45-50.

143. T. L. Dickerson, H. R. Shercliff and H. N. B. Schmidt: 'A weld marker technique for flow visualization in friction stir welding', *Fourth International Friction Stir Welding Symposium, Park City, USA*, 2004.

144. B. London, M. Mahoney, W. Bingel, M. Calabrese, R. H. Bossi and D. Waldron: 'Material flow in friction stir welding monitoredwith Al-SiC and Al-W composite marker', *Proceedings of Symposia 2003 TMS Annual Meeting San Diego, California*, 2003.

145. J. A. Schneider and A. C. Nunes Jr.: 'Thermo-mechanical processing in friction stir welds', Proc. TMS Annual Meeting, 43-51.

146. Z. W. Chen, T. Pasang and Y. Qi: 'Shear flow and formation of Nugget zone during friction stir welding of aluminium alloy 5083-O', *Materials Science and Engineering A*, 2008, 474, 312-316.

147. J. C. McClure, E. Coronado, S. Aloor, B. M. Nowak, L. E. Murr and A. C. Nunes Jr.: 'Effect of Pin Tool Shape on Metal Flow During Friction Stir Welding', *Proc. ASM Proceedings of the International Conference: Trends in Welding Research*, 257-261.

148. M. J. Russell and H. R. Shercliff: 'Analytical modeling of microstructure development in friction stir welding', *Proceedings, 1st Int. Symposium on Friction Stir Welding, Thousand Oaks, California, USA*, 1999.

149. T. Hyoe, P. A. Colegrove and H. R. Shercliff: 'Anther 7000 series microstructural research (FSW)', *Proceedings of the TMS 2003 Annual Meeting on Friction Stir Welding and Processing II*, 2003.

150. O. R. Myhr and Ø. Grong: 'Process modelling applied to 6082-T6 aluminium weldments-I. Reaction kinetics', *Acta Metallurgica Et Materialia*, 1991, 39, 2693-2702.

151. A. Sullivan, J. D. Robson, H. R. Shercliff and G. McShane: 'Microstructural research on 7000 series Aluminium aloys (FSW)', *Proceedings of the Thermec 2006*, 2006.

152. J. D. Robson, N. Kamp and A. Sullivan: 'Microstructural modelling for friction stir welding of aluminium alloys', *Materials and Manufacturing Processes*, 2007, 22, 450-456.

153. G. Wang and T. W. Liao: 'Automatic identification of different types of welding defects in radiographic images', *NDT and E International*, 2002, 35, 519-528.

154. L. Fratini and G. Buffa: 'Continuous dynamic recrystallization phenomena modelling in friction stir welding of aluminium alloys: A neural-network-based

approach', *Proceedings of the Institution of Mechanical Engineers, Part B: Journal of Engineering Manufacture*, 2007, 221, 857-864.

155. H. Okuyucu, A. Kurt and E. Arcaklioglu: 'Artificial neural network application to the friction stir welding of aluminum plates', *Materials and Design*, 2007, 28, 78-84.

156. D. Weiss, K. H. Christensen, and J. K. Kristensen: 2007, "Computerised calibration of thermal welding models", in Cerjak, H., Bhadeshia, H. and Kozeschnik, E. (eds.) *Mathematical modelling of weld phenomena 8*, TU Graz, 469-484.

157. C. Schwenk, Rethmeier M, and D. Weiss: 2007, "Rapid generation of temperature fields for simulation of welding distortion", in Cerjak, H., Bhadeshia, H. and Kozeschnik, E. (eds.) *Methematical modelling of weld phenomena 8*, TU Graz, 835-846.

158. R. Nandan, S. Mishra, and T. Debroy: 2007, "Tailoring fusion and friction stir welds using a transport phenomena based reliable and efficient model and a genetic algorithm", in Cerjak, H., Bhadeshia, H. and Kozeschnik, E. (eds.) *Mathematical modelling of weld phenomena 8*, TU Graz, 485-510.

CHAPTER 2

Experiments on Materials Constitutive Properties and Application to Friction Stir Welding Process Models

2.1 Introduction

During the process modelling of FSW using CFD method, one of the most important inputs is the material flow stress which determines the viscous heat generation. The material flow stress characterisation has been studied in several studies on hot workability[1-4]. McQueen[5] explained how materials are strain-hardened to a steady state condition during hot working, where the work hardening is balanced by recovery and dynamic recrystallization[6,7]. To describe this procedure precisely, the materials constitutive equations are established from the experimental results of hot work.

The Zener-Holloman equation[8] is one of these constitutive equations which calculate the material flow stress from the strain-rate and temperature:

$$Z = \dot{\varepsilon} \exp(Q/(RT)) = A[\sinh(\alpha\sigma)]^n \qquad \text{Eq. 2-1}$$

where $\dot{\varepsilon}$ is the strain-rate, Q is the activation energy, R is the gas constant, T is the temperature, σ is the flow stress, and n, α and A are the material constants. The Zener-Holloman equation was used to describe the material flow evolution during FSW, such as Colegrove et al.[9] on modelling of FSW on three aluminium alloys and Nandan et al.[10] on mild steel. In addition, an empirical softening regime was applied by some researchers[9,11-14] at temperatures approaching the solidus. This includes a critical loss of flow strength from an arbitrarily defined softening temperature T_m to the solidus temperature T_s, as shown in Figure 2-1.

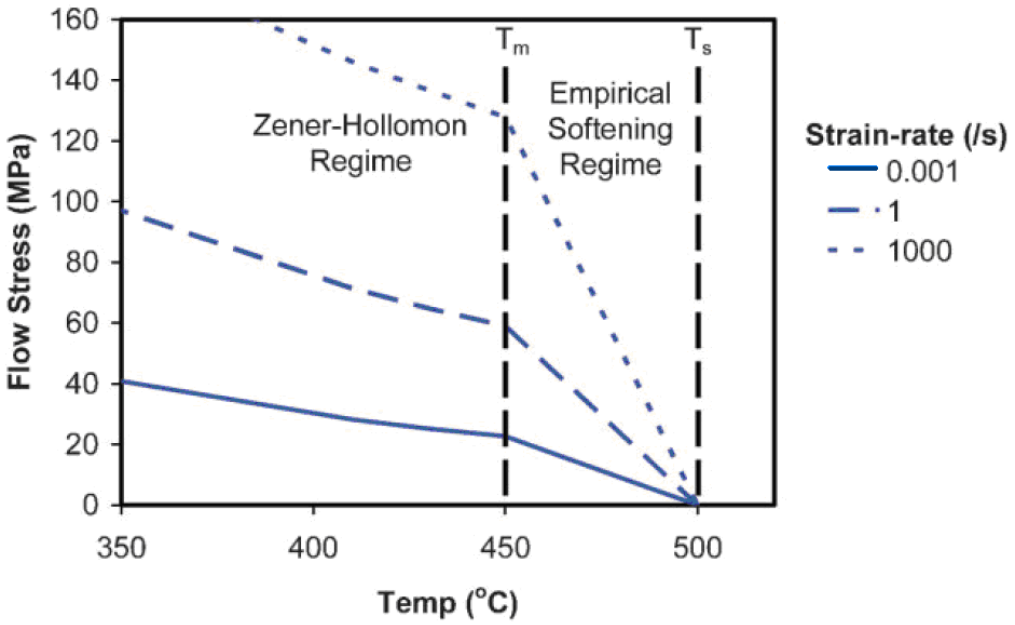

Figure 2-1: Constitutive behaviour curves for aluminium alloy 7449, fitted to the Zener-Holloman law[9], with an empirical softening regime

The material constants applied in the FSW models are normally found from literature based on experimental investigations. However the literature about the material's flow stress at high temperature and high strain-rate particularly near the solidus temperature is very rare. The objective of the present study is to analyse the results from the Gleeble experiments, and derive a new set of Zener-Holloman material constants for aluminium alloys 6082-T6 and 7449-T7 over a wide range of strain-rates and temperatures. Due to the fact that the Zener-Holloman constitutive behaviour can well represent the material flow stress over wide ranges of temperature and strain rate, the discovered material constants were applied in the FSW models described in subsequent chapter in this thesis.

2.2 Methodologies

2.2.1 Material properties

The Gleeble experiment was performed with the Gleeble® 3800 machine[24] at Technische Universität Berlin Germany. The Gleeble® 3800 machine is a complete, fully integrated hydraulic servo system capable of 20 tons of static force in both tension and compression. The specimens for the Gleeble test were cylindrical: 9.6 mm in

diameter with a length of 15 mm for 6082, and 10 mm in diameter with a length of 15 mm for 7449, as show in Figure 2-2(a). The chemical compositions of the two alloys investigated are given in Table 2-1.

	Cu	Mg	Si	Fe	Mn	Zn	Cr	Ti	Al
6082-T6	0.04	0.74	0.87	0.28	0.51	0.01	<0.01	0.02	Bal.
7449-T7	1.80	2.03	0.05	0.08	<0.01	8.36			Bal.

Table 2-1: Nominal composition (in wt.%) of aluminium alloys 6082-T6 and 7449-T7

A direct resistance heating system was used to take the samples to the predefined temperature with the rate of approximately 5 K per second, and K type thermocouples were resistance welded to the sample to observe and control the temperature of the sample, as shown in Figure 2-2(b). A cement was used to aid attachment of the thermocouple for the high temperature samples. To lubricate the sample surface in contact with the anvils, graphite foils were pasted with a nickel based anti-seize & lubricating compound, as shown in Figure 2-3. The test temperatures for aluminium alloy 6082-T6 were 673, 723, 753, 773, 818 and 838 K, where the last value is 10 K lower than the solidus value of 848 K. The test temperatures for aluminium alloy 7449-T7 were 673, 723, 753, and 768 K, where the last value is 5 K lower than solidus value of 773. The specimens were deformed at average true stain-rates of 1, 10, 50, and 100 sec^{-1} for both 6082-T6 and 7449-T7. The strain-rates were approximate because the deformation velocity is fixed by the machine. The strain-rate is a function of this value, however it is not linearly dependent. During a test, the specimen was rapidly heated to the desired temperature, held for 30 seconds for equilibrium, compressed to the desired strain and held for 5 seconds, after which the sample was naturally cooled. The comparison of a sample before and after compression is shown in Figure 2-4. The Gleeble machine recorded the force and displacement to calculate the true stress and strain. The barrelling of the samples was determined and was within a tolerable range.

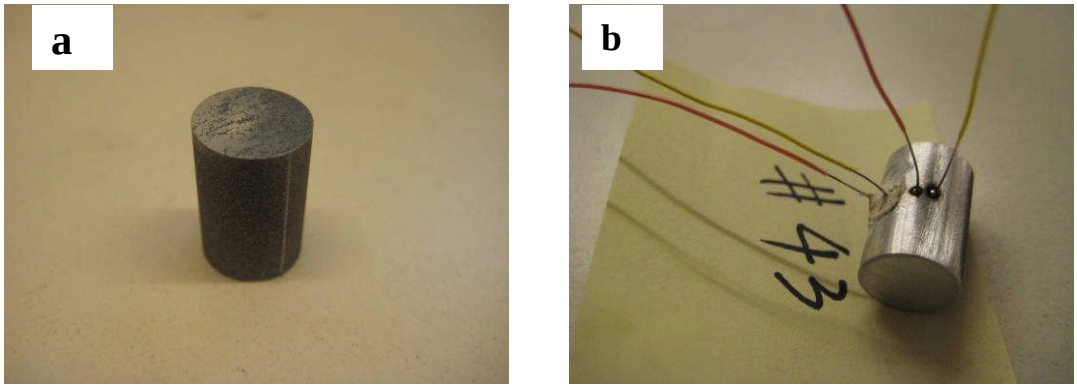

Figure 2-2: a) One of the 7449 samples; b) Thermocouples welded to a sample. Note for high temperature tests a cement was used to aid attachment of the thermocouple.

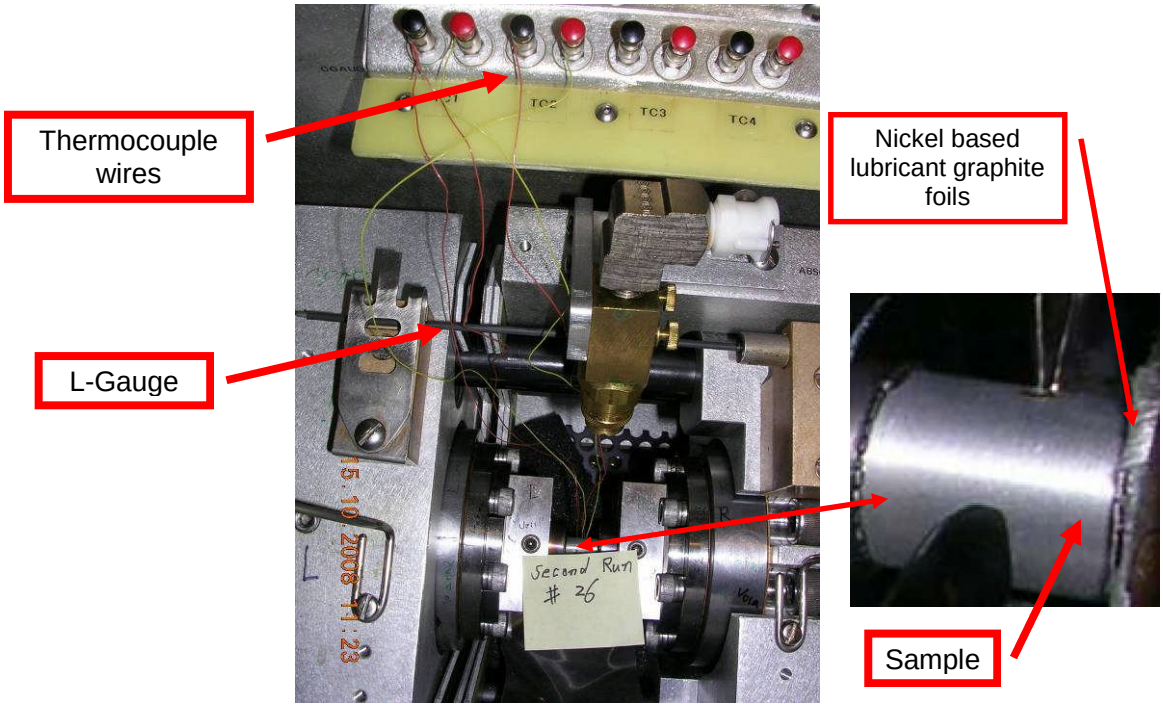

Figure 2-3: Sample clamped in the middle of Gleeble machine, including the thermocouples for observing and controlling the temperature, the L-gauge for measuring the displacement and the sample with nickel based lubricant graphite foils to avoid the compressed sample sticking to the machine.

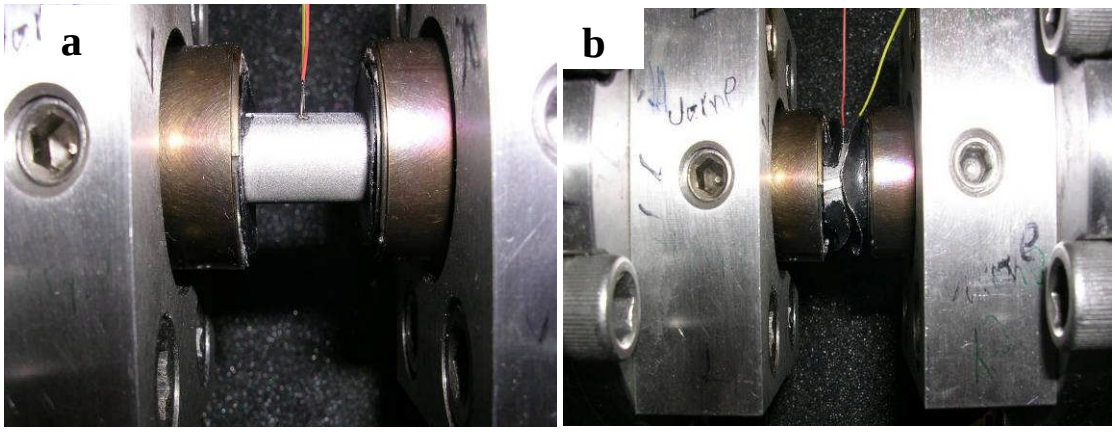

Figure 2-4: Sample mounted in Gleeble® 3800 machine (a) before and (b) after compression.

2.2.2 Find materials constants

During the compression, the deformation velocity of the sample was kept approximately constant by the machine which resulted in variation of the strain-rate. In this case, both the strain-rate and stress values were averaged for each test condition. The averaging of the strain-rate and flow stress, and the reading of experimental temperature are introduced in Appendix A1.

For both materials, the corresponding Zener-Holloman material constants Q, n, α and A were found by using a conventional curve fitting method, which included the following steps:

1. Select a range of activation energies Q based around values found by other researchers.
2. For each value of Q, the Zener-Holloman parameter Z was calculated from the equation:

   $$Z = \dot{\varepsilon} \exp(Q/RT) \qquad \text{Eq. 2-2}$$

   which used experimental values of temperature and strain-rate.
3. From the value Z and flow stress, find the corresponding material constants n, α and A by carrying out curve fitting on the following equation:

   $$\sigma = \sinh^{-1}\left[(Z/A)^{\frac{1}{n}} \right] \Big/ \alpha \qquad \text{Eq. 2-3}$$

   The Origin software package was used for this purpose.

4. During the curve fitting, the coefficient of determination R^2, which represents the quality of the curve fitting was recorded for each Q value. The value Q that maximised R^2 (close to 1) was found. This defined the activation energy (Q) and the corresponding constants n, α and A.

The Zener-Holloman material constants were used to plot the flow stress against temperature and strain-rate, and the plot was compared with ones from the literature, in order to investigate the variations.

2.3 Results

2.3.1 Material constants

The 6082-T6 experimental results and corresponding curve fit of the derived flow stress vs. temperature and strain-rate given in Figure 2-5(a), which indicates that the curve fitting method worked for 6082-T6. The error bars (showing the difference between the two readings) are also included for some test conditions where two trials were conducted. Each of the values in Figure 2-5 has the numerical value of strain-rate next to them. The results show that there was a close match between the experimental and the Zener-Holloman equation values for strain-rate up to 50 s^{-1}. The match with the high strain-rate values (100 s^{-1}) was poorer, particularly for those of high temperature. Note however that the actual strain-rate of the experiments deviated from the desired value for some tests, e.g. high temperatures and strain-rates. This exacerbated the difference with the curve fit for these values. There may also be influences from the errors in the measurements/calculations or the noise in the experiments, which will be discussed later.

The results for 7449-T7 are shown in Figure 2-5(b). Interestingly, the slope with temperature changes above 723 K, particularly at high strain-rates. Using the standard curve fitting method will result in overpredicting the flow stress at high temperature and strain-rate. To predict the curves more accurately an additional term was added to the Zener-Holloman equation to describe the material flow stress when the temperature is less than 723 K.

$$\sigma = \frac{1}{\alpha} \cdot a\sinh(x) - \frac{723 - T}{50} \cdot \left(k \cdot \ln\left(\dot{\varepsilon}\right) + m\right), (T < 723K) \qquad \text{Eq. 2-4}$$

where *k* and *m* are additional constants. Hence the standard Zener-Holloman constant are found from the temperature values above 723 K. The modified equation 2-4 was then applied to the experimental values at 673 K. The additional term reduces the flow stress linearly with temperature below 723 K and exponentially with strain-rate. The effect of this additional term at low strain-rates is negligible. This modified equation is purely empirical and has no physical basis. As shown in Figure 2-5(b), the modified flow curves are close to the experimental results, when the modified Zener-Holloman equation was applied. As a summary, the derived Zener-Holloman constants for 6082-T6 and 7449-T7 are given in Table 2-2, including the additional terms for 7449-T7.

Materials	Q (J/mol)	A (s^{-1})	n	α (MPa)	k	m
6082-T6 aluminium	1.68E+05	3.02E+11	4.71	2.4E-02	n/a	n/a
7449-T7 aluminium	1.40E+05	5.03E+11	5.17	0.7E-02	6.99	2.14

Table 2-2: The derived Zener-Holloman constants for 6082-T6 and 7449-T7

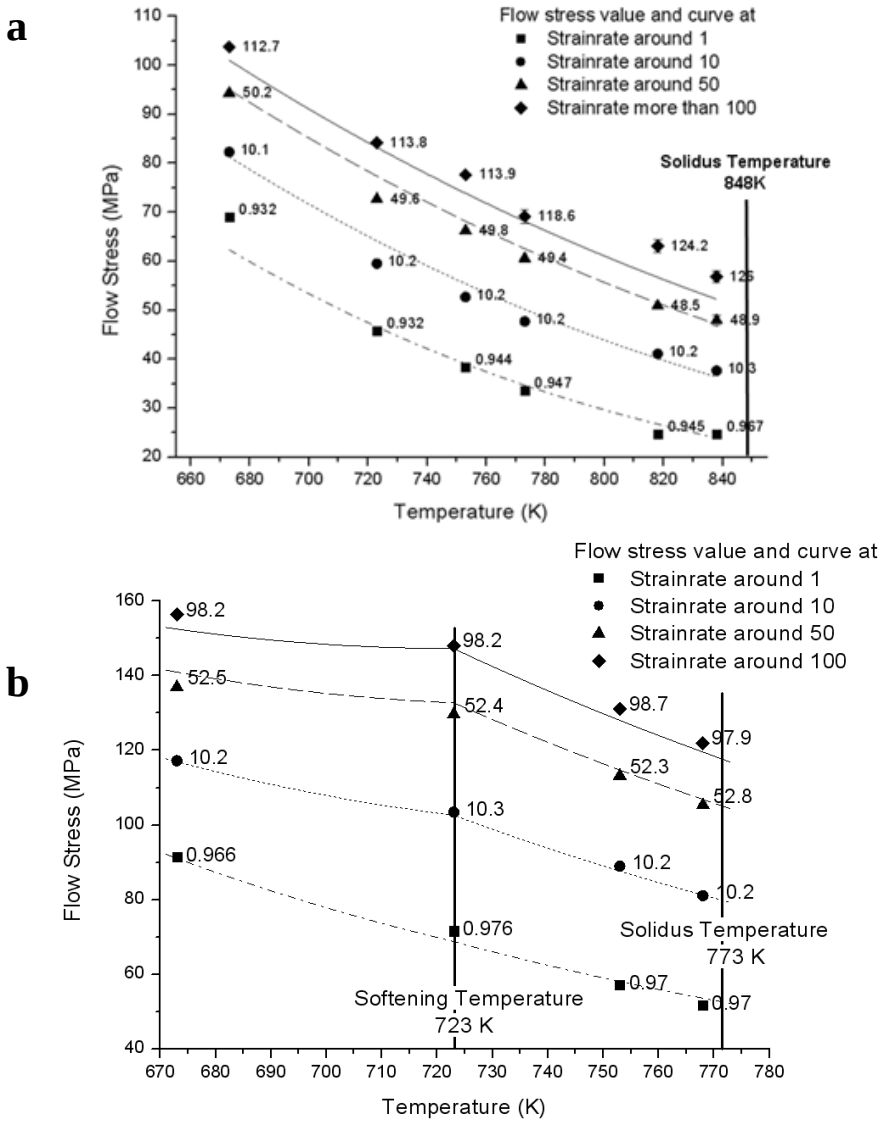

Figure 2-5: Predicted material flow stress for (a) 6082-T6 and (b) 7449-T7. Note the solidus temperatures are given for both materials and the temperature at which the slope of the flow strength changes (723 K) is shown for 7449-T7.

2.3.2 Flow stress curves

The derived material constants were input into the Zener-Holloman equation, and plotted against the temperature and strain-rate, to study the difference between from ones from the literature, particularly for temperatures near the solidus. Figure 2-6 shows a comparison of the flow stress between the experimental results and ones by Sheppard and Jackson[1] for 6082-T6. The flow stress curves based on the results from this study are not significantly different from ones found in the literature[1]. The comparison shows that the Zener-Holloman curves with new material constants predicts a lower flow stress

in the high temperature regime, but greater flow stress at lower temperature. The region with the lowest discrepancies is around 550 to 600 K for strain-rate between 1 to 100 s^{-1}. The maximum difference between the curves is about 20 MPa for 848 K and strain-rate at 100 s^{-1}, and for lower strain-rate the difference will be slightly less. The difference between the curves at lower temperature is smaller, the maximum value is about 12 MPa for 500 K and strain-rate at 100 s^{-1}, and similarly for lower strain-rate the difference is less.

For 7449-T7, the curves comparison is shown in Figure 2-7, which shows that there are large discrepancies between curves from the new Zener-Holloman constants and the ones found in the literature[9]. The curves with the new constants produce much higher flow stress in the low temperature regime, however the flow stress reduced dramatically as the temperature approached the solidus 773 K. At the solidus temperature, the discrepancy between the curves is smaller when the strain-rate is lower. For instance, the difference between the curves of 100 s^{-1} at solidus temperature is nearly 30 MPa, while of 1 s^{-1} at solidus temperature is only about 5 MPa. The reduction in flow stress with the new curves is greater when the strain-rate is high.

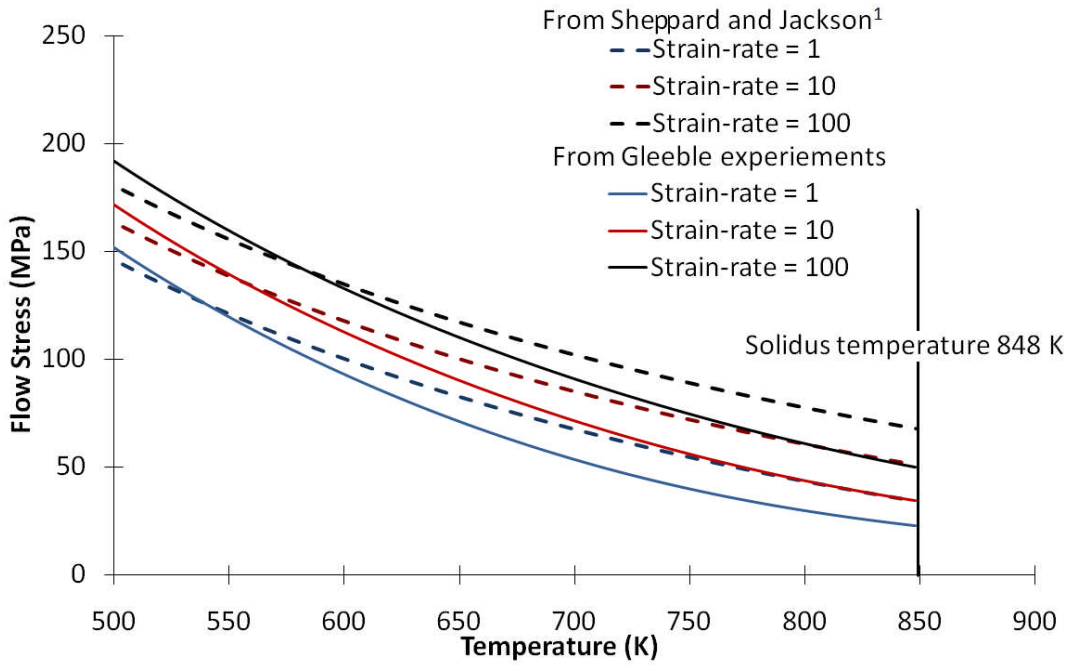

Figure 2-6: Comparison of 6082-T6 flow stress curves between using determined Zener-Holloman constants and those from Sheppard and Jackson[1], note a line indicating the solidus temperature 848 K is included

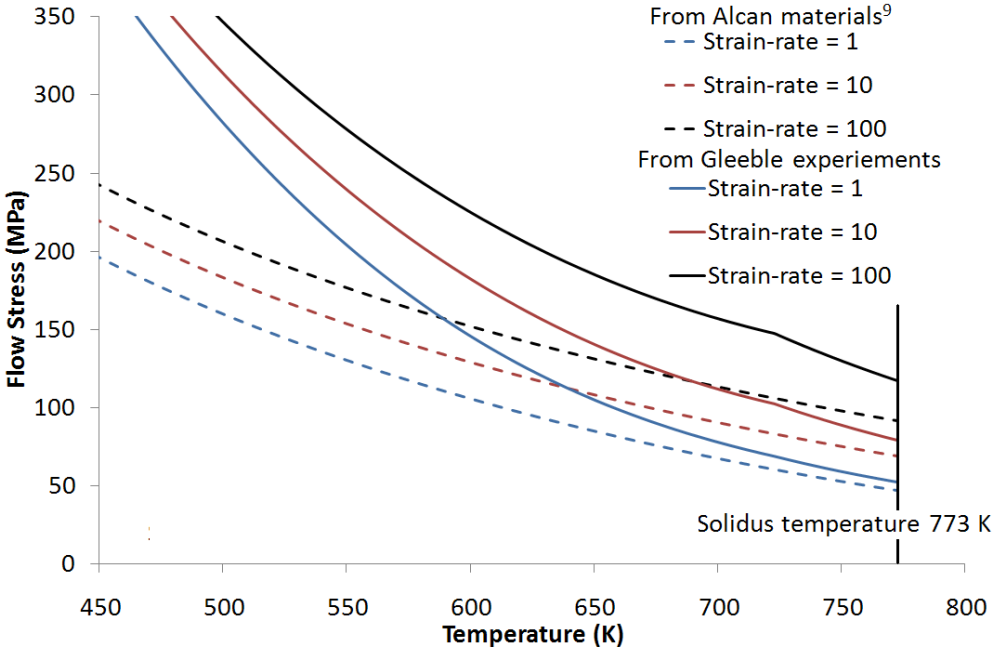

Figure 2-7: Comparison of 7449-T7 flow stress curves between using determined Zener-Holloman constants and using ones from Alcan material[9], note a line indicating the solidus temperature 773 K is included

2.3.3 Noise in the results

As an example, four stress verses strain plots for 6082-T6 are shown in Figure 2-8. The large differences between the curves indicate that noise exists in the system, and the noise level changes as the deformation condition changes. Figure 2-8(a) and (b) are at two similar low strain-rates but different temperatures. The material exhibits more noise at higher temperature, particularly at a lower strain regime (from 0.02 to 0.2), but the noise get less significant as the strain increased. This may because of the balancing between the work hardening and softening within the material. This indicates there are thermal influences on the noise of the results. The test condition for results in Figure 2-8(c) is taken under the highest test temperature condition, 10 K lower than solidus, and by comparing to Figure 2-8(b) it indicates increasing the test temperature closer to solidus, the noise in the system will increase, particularly for low strains. Figure 2-8(b) and (d) are curves under same temperature but different strain-rate, and the large difference between the curves indicates that the strain-rate will contribute more significantly than the temperature.

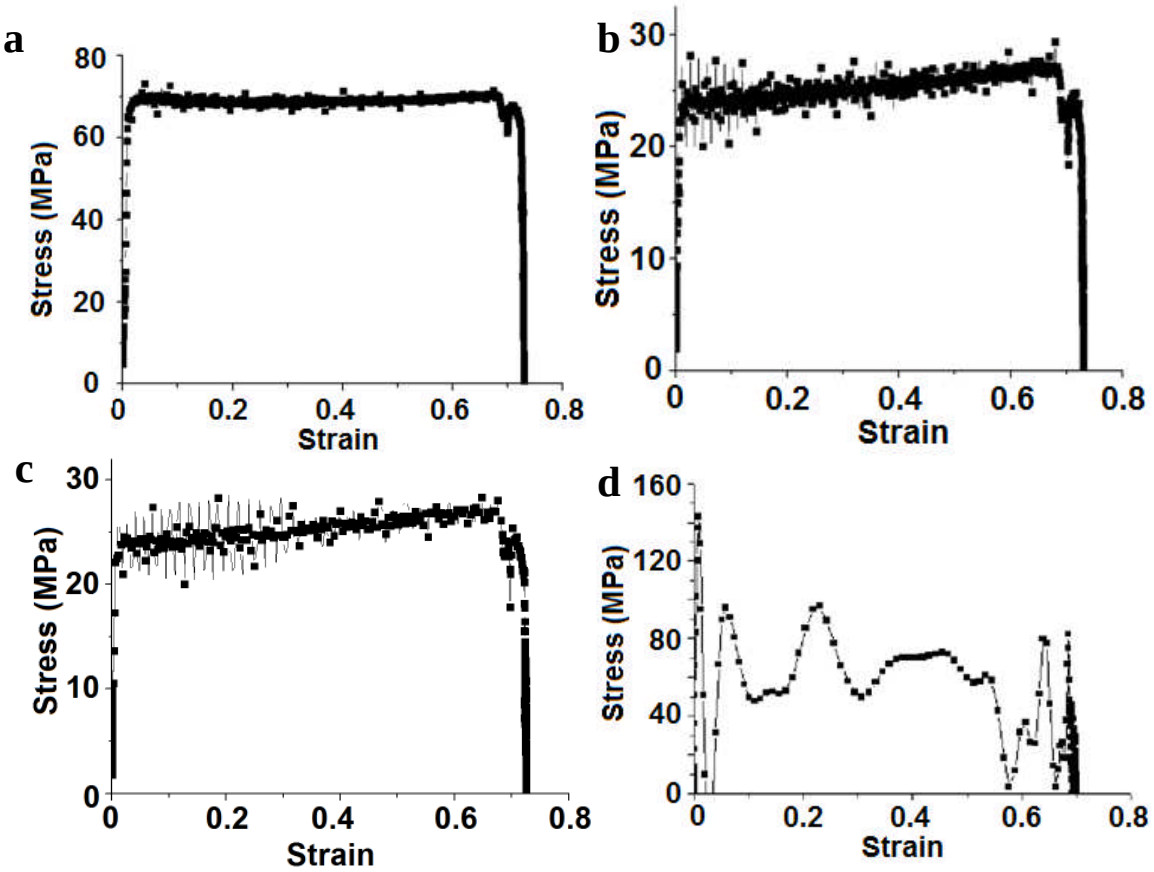

Figure 2-8: Plots of stress vs. strain for Gleeble tests of 6082-T6 with deformation conditions at: a) 673K, 0.932 s^{-1}; b) 818K, 0.945 s^{-1} c) 848K, 0.916 s^{-1} and d) 818K, 123.8 s^{-1}

2.4 Discussion

The novel aspect of the work is that the test was done at high strain-rates (up to 120 s^{-1}) and near the solidus temperature for both materials, which has not been accomplished by other researchers. The experimental material results for 6082-T6 showed a reduction of flow stress with increasing temperature, however no rapid softening regime occurred as the temperature approached the solidus. One of the determined Zener-Holloman constants, the activation energy Q (168000 J/mol) suggests that the activation energy values described in the literature by Sheppard and Jackson[1] (143890 J/mol) and Li et al.[26] (153000 J/mol) were underestimated, which may be due to the higher temperatures used in these experiments. At high temperatures the Zener-Holloman equation with material constants from this study predicts less flow stress compared to the ones used the constants from Sheppard and Jackson[1]. However it is important to note that the

comparison depends on the range of temperature and strain-rate values used to determine the fitting constants. As explained in Sheppard and Jackson[1], the experimental temperature used to determine the fitting constants was between 533 and 693 K. In this region the match with the new experimental values is very close. Outside this region, where the curves from Sheppard and Jackson[1] need to be extrapolated the comparison is poorer.

For 7449-T7, one major finding was the flow stress curves changed slope around 723 K. The fact that the slope changed around 723 K was an artefact of the experimental values of temperature used in this study, i.e. further experiments around 723 K are required to determine how the slope changes. There is no reason for this apparent change in the flow behaviour. Further experiments need to be carried out to populate more data for a better understanding.

When comparing the new curves with those in the literature based on data from Alcan[9], the discovered activation energy (140000 J/mol) is higher than the one (134158.4 J/mol) found in literature[9]. However there was a significant difference between the flow stress predictions, particularly at low temperatures. The curves derived from the Alcan experiments[9] were determined at lower temperatures than those in the current study. This would explain the poor match between the two curves at low temperature and would suggest that the new equations give a poor prediction of the flow stress when extrapolating values at low temperatures.

The noise in the Gleeble results is found to be relative to both the test temperature and strain-rate. The noise increases as the temperature and/or strain-rate increases, but the strain-rate has a greater influence. A higher noise can be observed at the start stage of each test, particularly for higher strain-rate, and this may be due to the initial impact load of the Gleeble test. A slight increase in the stress value over the duration of the experiment is observed in Figure 2-8(b) and (c), but the reason is unclear. Finally the high level of noise in the high temperature, high strain-rate condition can help explain the scatter in the results in the high temperature and strain-rate regime of the flow curves in Figure 2-5.

2.5 Conclusions

In this study, the Gleeble experiments were conducted to understand the constitutive behaviour of 6082-T6 and 7449-T7 alloys under high strain-rates and near solidus temperatures. A new set of Zener-Holloman constants was found for 6082-T6 and a modified equation was derived for 7449-T7. The modified equation for 7449-T7 is empirical and needs to be further studied with experimental/physical study. The extrapolation of the adjusted normal Zener-Holloman curve to lower temperature also needs some further experimental validation. The new parameters were used in the modelling work presented in the subsequent chapters. The outcomes of this study are:

1. No rapid softening regime was discovered for either material at temperatures approaching the solidus. However a slight reduction was observed in the 7449-T7 flow stress, which could be due to complete dissolution of precipitates.
2. Noise existed in the Gleeble experimental results. As the experimental temperature and strain-rate increased, the noise level increased. The strain-rate had a greater effect on the noise.
3. Comparing the new Zener-Holloman curves with those found in the literature, there is a close prediction for 6082-T6, particularly at low temperatures where the experimental regimes used to derive the curves overlapped. There was a poorer match for 7449-T7 which was more pronounced at low temperatures.

References

1. T. Sheppard and A. Jackson: 'Constitutive equations for use in prediction of flow stress during extrusion of aluminium alloys', *Materials Science and Technology*, 1997, 13, 203-209.

2. H. Li, Z. Li, F. Guo, L. Meng and X. Liang: 'Constitutive equation model for hot deformation of Al-Cu-Mg-Ag alloy', *Tezhong Zhuzao Ji Youse Hejin/Special Casting and Nonferrous Alloys*, 2008, 28, 823-826.

3. P. Zhao, G. Ren, Z. Shen and C. Xu: 'Influence of hot compressive deformation conditions of 6061 aluminum alloy on flow stress and research on its constitutive

equation', *Suxing Gongcheng Xuebao/Journal of Plasticity Engineering*, 2007, 14, 130-133.

4. Y. Yi, J. Yang and Y. Lin: 'Flow stress constitutive equation of 7050 aluminum alloy during hot compression', *Cailiao Gongcheng/Journal of Materials Engineering*, 2007, 4, 20-22, 26.

5. H. J. McQueen and N. D. Ryan: 'Constitutive analysis in hot working', *Materials Science and Engineering A*, 2002, 322, 43-63.

6. H. J. McQueen, W. A. Wong and J. J. Jonas: 'Discussion of dynamic recovery during hot working', *Acta Metallurgica*, 1967, 15, 586-588.

7. B. Verlinden, P. Wouters, H. J. McQueen, E. Aernoudt, L. Delaey and S. Cauwenberg: 'Effect of different homogenization treatments on the hot workability of aluminium alloy AA2024', *Materials Science and Engineering A*, 1990, 123, 229-237.

8. C. M. Sellars and W. J. M. Tegart: 'Hot workability', *Int. Met. Rev.*, 1972, 17, 1-24.

9. P. A. Colegrove, H. R. Shercliff and R. Zettler: 'Model for predicting heat generation and temperature in friction stir welding from the material properties', *Science and Technology of Welding and Joining*, 2007, 12, 284-297.

10. R. Nandan, G. G. Roy, T. J. Lienert and T. Debroy: 'Three-dimensional heat and material flow during friction stir welding of mild steel', *Acta Materialia*, 2007, 55, 883-895.

11. T. U. Seidel and A. P. Reynolds: 'Two-dimensional friction stir welding process model based on fluid mechanics', *Science and Technology of Welding and Joining*, 2003, 8, 175-183.

12. T. Long, T. U. Seidel, W. Tang and A. P. Reynolds: ' A friction stir welding model using computational fluid dynamics', Proc. TMS Annual Meeting, 2003, 299-312.

13. P. A. Colegrove, H. R. Shercliff and T. Hyoe: 'Development of the Trivex™ friction stir welding tool for making lap welds', *Proceedings of the 5th International Symposium on Friction Stir Welding,* 2004, Metz, France.

14. P. A. Colegrove and H. R. Shercliff: 'CFD modelling of friction stir welding of thick plate 7449 aluminium alloy', *Science and Technology of Welding and Joining,* 2006, 11, 429-441.

15. G. R. Johnson and W. H. Cook: 'A constitutive model and data for metals subjected to large strains, high strain rates and high temperatures', *Proceedings of the Seventh International Symposium on Ballistics,* 1983, 541-547.

16. A. Askari, S. Silling, B. London and M. Mahoney: ' Modeling and analysis of friction stir welding processes', *Friction Stir Welding and Processing,* 2001, 43-54.

17. H. Schmidt and J. Hattel: ' CFD modelling of the shear layer around the tool probe in Friction Stir Welding ' *Proc. Friction Stir Welding and Processing III - Proceedings of a Symposium sponsored by the Shaping and Forming Committee of (MPMD) of the Minerals, Metals and Materials Society, TMS,* 2005, 225-232.

18. H. Schmidt and J. Hattel: 'A local model for the thermomechanical conditions in friction stir welding', *Modelling and Simulation in Materials Science and Engineering,* 2005, 13, 77-93.

19. A. Moal and E. Massoni: 'Finite element simulation of the inertia welding of two similar parts', *Engineering Computations,* 1995, 12, 497-512.

20. B. C. Liechty and B. W. Webb: 'Modeling the frictional boundary condition in friction stir welding', *International Journal of Machine Tools and Manufacture,* 2008, 48(12-13), 1474-1485.

21. J. Ponthot: 'An extension of the radial return algorithm to account for rate-dependent effects in factional contact and visco-plasticity', *Journal of Materials Processing Technology,* 1998, 80-81, 628-634.

22. H. Zhang, Z. Zhang, J. Bie, L. Zhou and J. Chen: 'Effect of viscosity on material behavior in friction stir welding process', *Transactions of Nonferrous Metals Society of China (English Edition)*, 2006, 16, 1045-1052.

23. Z. Zhang and J. T. Chen: 'The simulation of material behaviors in friction stir welding process by using rate-dependent constitutive model', *Journal of Materials Science*, 2008, 43, 222-232.

24. Gleeble 3800, http://www.gleeble.com/3800.htm, Dynamic Systems Inc.

25. J. P. Holman: 'Heat Transfer', 6th edition, 1986, New York, McGraw-Hill Book Co.

26. X. Li, J. Chen and H. Zhang: 'Constitutive model for hot deformation of 6082 aluminum alloy', *Zhongguo Youse Jinshu Xuebao/Chinese Journal of Nonferrous Metals*, 2008, 18, 1769-1774.

CHAPTER 3

Development of a Hybrid Thermal Model for a Simple Welding Process

3.1 Introduction

Determining the power input and the thermal boundary conditions for process models is difficult, since it is sensitive to many environmental conditions such as the contact condition, pressure with the backing bar and the local temperature. This problem also exists in the process modelling of FSW.

In previous FSW modelling work, Simar[1] assumed there was no heat loss at the bottom of the workpiece, by adopting an adiabatic boundary condition, which resulted in a significant over-prediction of temperature. Khandkar[2] simplified the heat loss with a convective heat transfer coefficient, and the resulting model was able to predict an accurate peak temperature, but failed to predict the cooling slope. Other researchers[1-3] included the backing bar in their models by applying a contact gap conductance to represent the imperfect contact at the interface. The governing equation is given by

$$Q = k(T_W - T_B) \qquad \text{Eq. 3-1}$$

where Q is the heat flux from workpiece to the backing bar, T_W is the temperature at the workpiece and T_B is the temperature at the backing bar. Colegrove et al.[3] applied a higher constant contact gap conductance to the area under the tool, and the area that had been welded. A lower one was applied to the unwelded area which gave a good prediction of thermal profile. Khandkar[2] stated that models that included the backing plate and contact gap conductance were able to produce a better prediction of the temperature, and a variable contact gap conductance was more representative of the real situation. Simar[1] used a contact gap conductance based on varying normal pressure which led to a better prediction of temperature, and Shi et al.[4] applied a temperature dependent contact gap conductance. The investigation of the problem can be described as an Inverse Heat Conduction Problem (IHCP)[5], where the thermal boundary conditions are calculated from outputs such as the experimental temperature history.

One way of solving the IHCP is to solve the problem with an ANN. This is a numerical modelling technique that simulates the structure and functions of biological neural network[6]. The ANN model is a geometric combination of artificial neurons which processes information with a connectionist approach to computation. It is capable of altering its internal structure and data based on external information that travels through the network during the learning stage, to investigate complex relationships between inputs and outputs or to find patterns in data.

ANN methods have been combined with numerical models to investigate boundary conditions in thermal models. Examples are found in Sablani[7] and Sreekanth et al.[5], who used an ANN to investigate the heat transfer coefficients between solid particles and a fluid.

One important factor to consider when using an ANN is applying the best topology. Three topologies commonly used for ANN are:

1. The network (MLP)[8], which is a layered feed-forward network typically trained with static back-propagation. The MLP method can be applied to most cases, however it needs a large amount of data for training.
2. The generalized feed-forward network (GFF)[8], which allows data to flow over one or more layers. The GFF can normally solve problems as effectively as the MLP network but with less training data, but it requires longer time for training.
3. The modular feed-forward network (MFF)[9], which is a geometric combination of several parallel MLP structures. The advantage of the MFF network is it requires less training data.

To adjust the weights in the ANN model, the BP algorithm is commonly used. Two gradient descent methods are used: the simpler momentum method and the LM which uses a higher-order algorithm. More details including a graphic description of the ANN topologies, BP algorithm and gradient descent methods are described in the literature review.

This chapter is to establish the thermal boundary conditions by using a hybrid ANN numerical heat transfer model. This will be used to determine:

1. Whether the ANN model is capable of predicting a single constant heat transfer coefficient or gap conductance;
2. Whether the ANN model is able to predict more complex boundary conditions, such as variable gap conductance;
3. The most effective method of inputting the thermal profile data into the neural network;
4. The most effective ANN and topology and gradient descent method;
5. How the type of complex boundary condition affects the ANN's ability to predict the boundary conditions.

3.2 ANN development method

3.2.1 Method of implementing the ANN

A generalized diagram in Figure 3-1 shows the two stages of using an ANN model to predict the boundary conditions:

1. The supervised learning stage: The thermal data will be used to train the neural network. Note both inputs and outputs are collected from the numerical model.
2. The testing stage: This is used to test the effectiveness of the ANN model developed in the step 1. There are two ways of implementing this test. Firstly it can be done theoretically. In this case 'test conditions' can be generated by the thermal model. The test thermal curves are input to the ANN, and the power input and thermal boundary conditions are predicted. These predicted values are then compared against the values from the model. Alternatively, experimental thermal data may be used as the input in the predicting stage, and the ANN is used to find the equivalent heat input and thermal boundary conditions. This is demonstrated in the next chapter. During this study, both inputs and desired outputs are collected from the numerical model. Note, when implemented using experimental data, the inputs will be abstracted from thermocouple data.

This basic strategy will not change during all the studies of ANN, but the learning algorithm, transfer function and structure of the hidden layers will be altered to determine which provides the best prediction. The commercial software package NeuroSolutions[10] was used to implement the neural network. Note the welding speed is not included in the ANN model because it is a *known* parameter in a welding experiment.

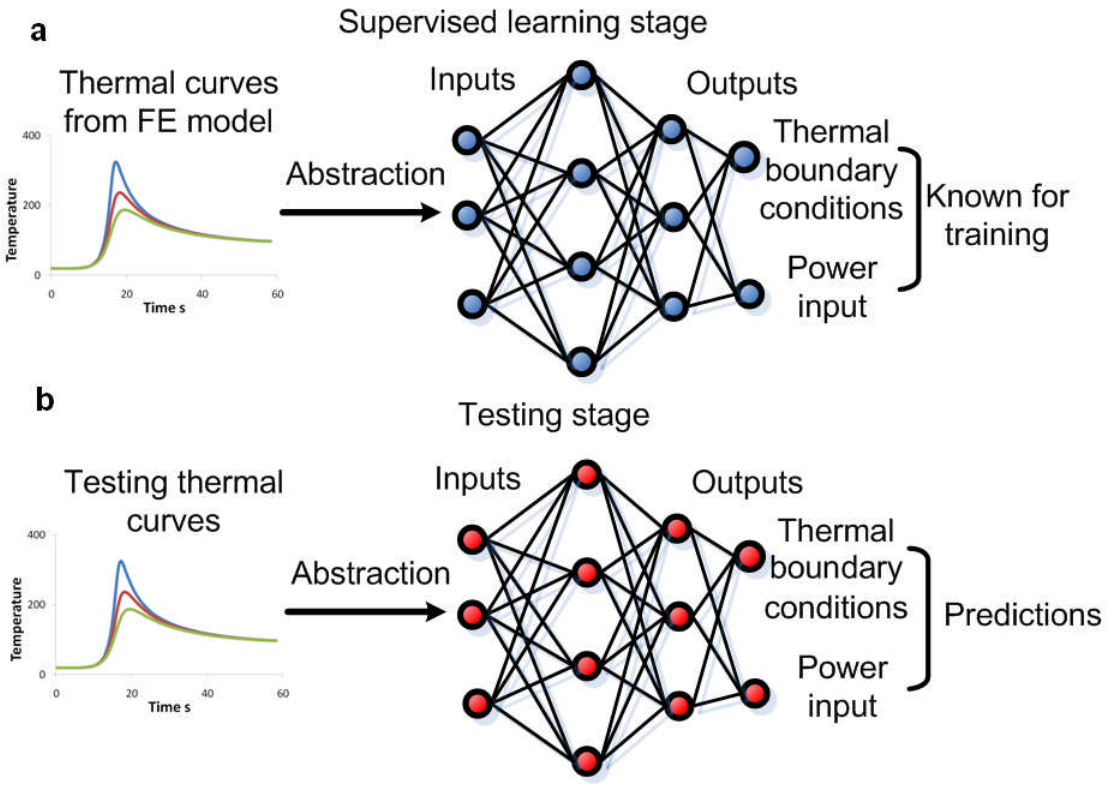

Figure 3-1: Two stages of how an ANN model processes:
a) the supervised learning stage; b) the testing stage

3.2.2 Inputting the thermal profiles into the ANN

From the previous section, one of the key requirements is a method of inputting the thermal data into the ANN. Theoretically, thermal profiles collected from the numerical model can be input directly into the ANN, but it is very inefficient, which makes it necessary to investigate methods of abstracting the thermal profile. The major abstracting methods used in this modelling work are illustrated by the thermal profile in Figure 3-2, and include:

1. The ‘9 input method’ which uses the peak temperature; the cooling slope which is the slope of the line between the peak temperature and the temperature at half this value; and the integral of temperature against time. The time over which the temperature is integrated equals the length of plate divided by the travel speed. This is done at distances of 10, 15 and 20 mm from the centreline of the heat source.
2. The ‘6 input method’ which is the same as the ‘9 input’ method but excludes the cooling slope.
3. The ‘4 input method’ which is based on the ‘6 input’ method but excludes the thermal data from the point 15 mm from the centreline.
4. The ‘2 input method’ which is based on the ‘4 input’ method but excludes the thermal data from the point 20 mm from the centreline
5. The ‘five point temperatures method’ where five temperature points from the thermal curve are selected to represent the curve itself. The first point is the peak temperature and the remaining 4 are at time coordinates of 40, 55, 70 and 85 seconds. All the models developed in this chapter used a travel speed of 0.0066 m/s (400 mm/min), so the times selected capture the peak temperature as well as 4 points on the ‘tail’ which indicates the rate of cooling.

Note that not all these methods are applied for each model type in the proceeding sections.

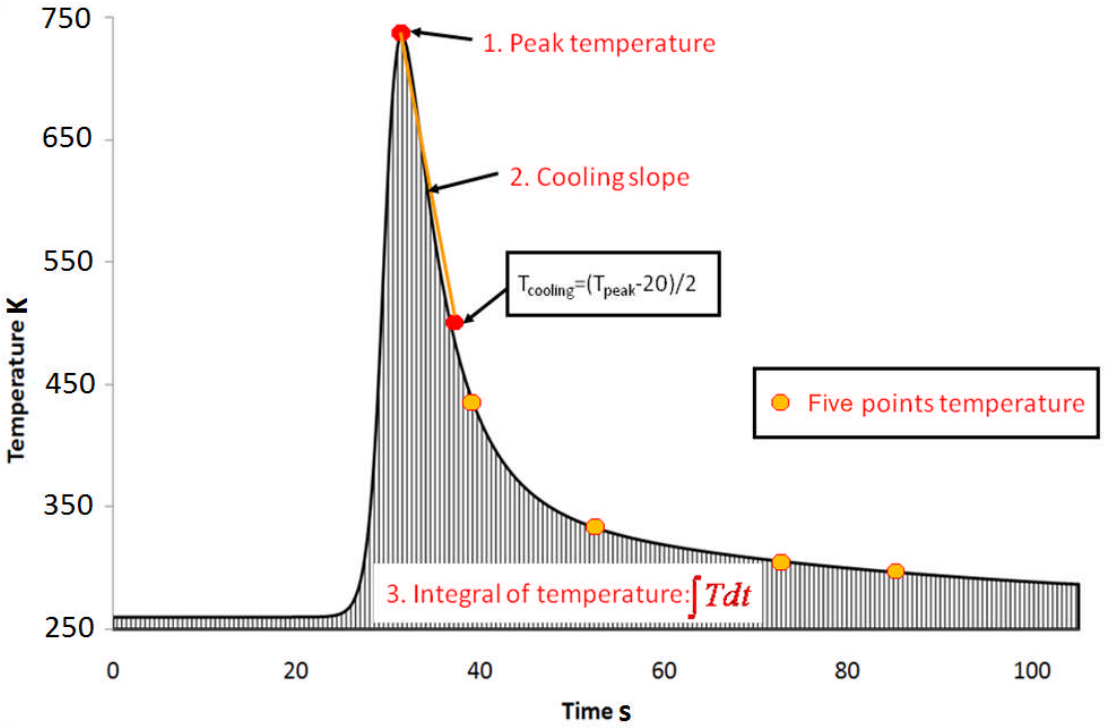

Figure 3-2: Methods of abstracting a thermal profile, including main features used the methods

Each ANN model is assessed by calculating the MRE which is defined as:

$$MRE = \frac{1}{N}\sum_{i=1}^{N}\left|\frac{Y_i - D_i}{D_i}\right| \qquad \text{Eq. 3-2}$$

where Y_i is the neural network output and D_i is the desired value.

In the first stage of developing the modelling technique, the hybrid ANN model was used to predict the convective heat transfer coefficients for a model, where the backing bar was excluded (see Appendix B1 and B2), i.e. the heat loss from the backing bar was represented with a convective heat transfer coefficient. Several different model types were attempted, including MLP, GFF and MFF networks. The ANN models in Appendix B were partially successful. One of the important findings from this works was the importance of selecting appropriate training values which is described in Appendix B.2.6.

It was found that the inclusion of the backing bar improved the model's predictive performance. Therefore much greater effort was spent on developing these model models which are reported in the next section.

3.3 Single contact gap conductance model

3.3.1 Numerical model description

In this section the ANN technique was applied to the heat transfer models with a steel backing plate and a gap conductance with the aluminium workpiece material to determine whether the ANN model can predict this type of boundary condition. A FE thermal model with backing plate was constructed with COMSOL multiphysics, as shown in Figure 3-3. The model is steady state and symmetric along the welding axis. The geometry is shown in the diagram. The heat flux distribution is applied with a radius of 15 mm. The equation of the Gaussian distributed heat flux is given by

$$Q_G = Q \cdot \frac{\exp\left(\frac{-\left(x^2+y^2\right)}{R_{heating}{}^2}\right)}{\left(1-\exp\left(-\frac{1}{9}\right)\right)\cdot\pi\cdot R_{heating}{}^2} \qquad \text{Eq. 3-3}$$

where Q_G is the Gaussian heat flux (W/m^2) distribution, Q is the power input, x and y are the coordinate geometry, and $R_{heating}$ describes the distribution of the heat which is set to a constant value of 5 mm, i.e. the model is not used to predict the distribution of heat. The detailed derivation procedure of this equation is given in Appendix A2. The welding speed is 400 mm/min and is fixed. The thermal properties of the materials used for the models in this report are given in Table 3-1.

Item	Material	Thermal Conductivity (W/(m^{2}K))	Specific Heat (kJ/kgK)	Density (kg/m^3)
Workpiece	Aluminium Alloy2024	121[11]	0.875[12]	2780[11]
Backing bar	Carbon Steel	40[13]	0.465[13]	7833[13]

Table 3-1: Material properties used in FE model

The convective heat loss coefficient from the top surface has a fixed value[14] of 10 W/(m^{2}K). The convective heat loss[3] at the bottom of the steel backing plate is 1000 W/(m^{2}K). The heat loss from the workpiece to the backing bar is represented with a gap conductance and is the subject of this investigation, as well as the heat input.

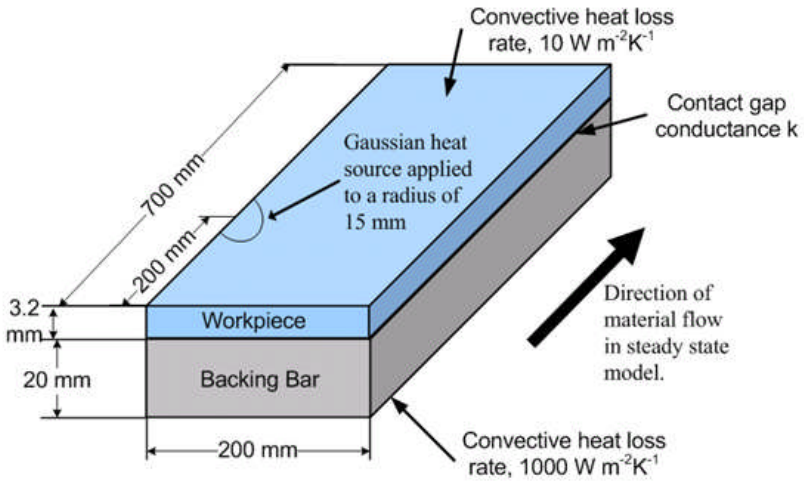

Figure 3-3: FE model geometry and boundary conditions of the single contact gap conductance model

3.3.2 ANN methodology

Five power input values and six contact gap conductance k values (Table 3-2) formed thirty training combinations. The gap conductance values were chosen around typical gap conductance values of 1000 to 10000 W/(m^{2}K) from literature[2]. For each combination of power input and contact gap conductance, different thermal profiles were obtained from the FE model along three lines parallel to the welding axis of distances of 10, 15 and 20 mm from the weld centreline. Note that many of these combinations resulted in unrealistically high temperatures. The focus of this work is on the method and not the numerical values of temperature. The values used for testing the different ANN models are shown in Table 3-3.

30 combinations for training	
Q (W)	k (W/(m^{2}K))
2852	500
5705	1000
8557	2000
11410	3000
14262	5000
	7500

Table 3-2: Data used for training the single gap conductance model

4 groups of values for testing	
Q (W),	k (W/(m^{2}K))
7131,	2500
9508,	6000
4754,	1500
12361,	14000

Table 3-3: Data used for testing the single gap conductance model

A total of eighteen combinations of ANN topologies and abstracting methods were used for the investigation and are summarised in Table 3-4.

New	Abstracting methods				
ANN topologies	Five point temperatures	9 input	6 input	4 input	2 input
MLP, momentum	n/a	6-4-3	6-4-3	6-4-3	6-4-3
MLP, LM	9-6-3	6-4-3	6-4-3	6-4-3	6-4-3
MFF, LM	5-5-5	5-5-5	5-5-5	5-5-5	5-5-5
GFF, LM	n/a	6-4-3	6-4-3	6-4-3	6-4-3

Table 3-4: The numbers of hidden layers for different ANN topologies and thermal curve abstracting methods applied in the study of the single contact gap conductance model

3.3.3 Results and discussion

The detailed results are shown in Appendix C1 and an overall comparison of the prediction qualities is shown in Figure 3-4. The error bars indicate the 95% confidence interval of the mean. It shows the quality of the five point temperature is not acceptable, which is also the reason why only two ANN models were tested. The 9, 6 and 4 input methods are able to give similarly good predictions of the results, indicating that the additional information provided by the 9 input method is not helpful for improving the prediction comparing to the 4 input method. Moreover the reduction to 2 inputs resulted in a higher MRE due to the lack of information. In terms of the ANN topologies, Figure 3-4 shows that the momentum method (MLP, momentum) gives much higher MREs than the LM method. The higher order LM method is able to handle plateaus in the

responses, which occur when the contact gap conductance value is high. Therefore the three topologies with LM method have a much lower MRE. The MRE with the 4 input method is slightly lower than either the 6 or the 9 input methods. Therefore the 4 inputs which include the peak temperature and integral of temperature vs. time at two locations provides sufficient information to predict the power and the heat loss to the backing bar. The differences between the three ANN topologies that used the LM method were marginal.

To illustrate how the average MRE is calculated, the predicted results of 4 input method with MLP topology is given in Table 3-5, in which the MREs for all the test values are calculated and an averaged MRE value is mathematically calculated based on these numbers. The MREs for all the test values are small. This means the ANN model is able to find the *Q* and *k* values accurately for all the testing cases. In order to understand the influence of the discrepancies in the predicted *Q* and *k*, the predicted values are inputted back into FE models and the corresponding thermal profiles are generated to compare with the original ones. The visual comparison of the one with the lowest MRE is shown in Figure 3-5(a), and the highest one in Figure 3-5(b). As shown in the plots, a good match is found, which indicates that the ANN model is able to predict the contact gap conductance boundary condition in a FE model. Note that the model temperature predictions are unrealistic, and the purpose of the model is to illustrate the technique.

Desired *Q* (W)	Desired *k* (W/(m^{2}K))	Desired *Q* (W)	Desired *k* (W/(m^{2}K))	MRE
7131	2500	7258	2503	0.96%
9508	6000	9382	6009	0.74%
4754	1500	4591	1491	2.00%
12361	4000	12563	4015	1.02%
			Average	1.18%

Table 3-5: Results from 4 input model with MFF topology and LM BP applied to the single contact gap conductance model

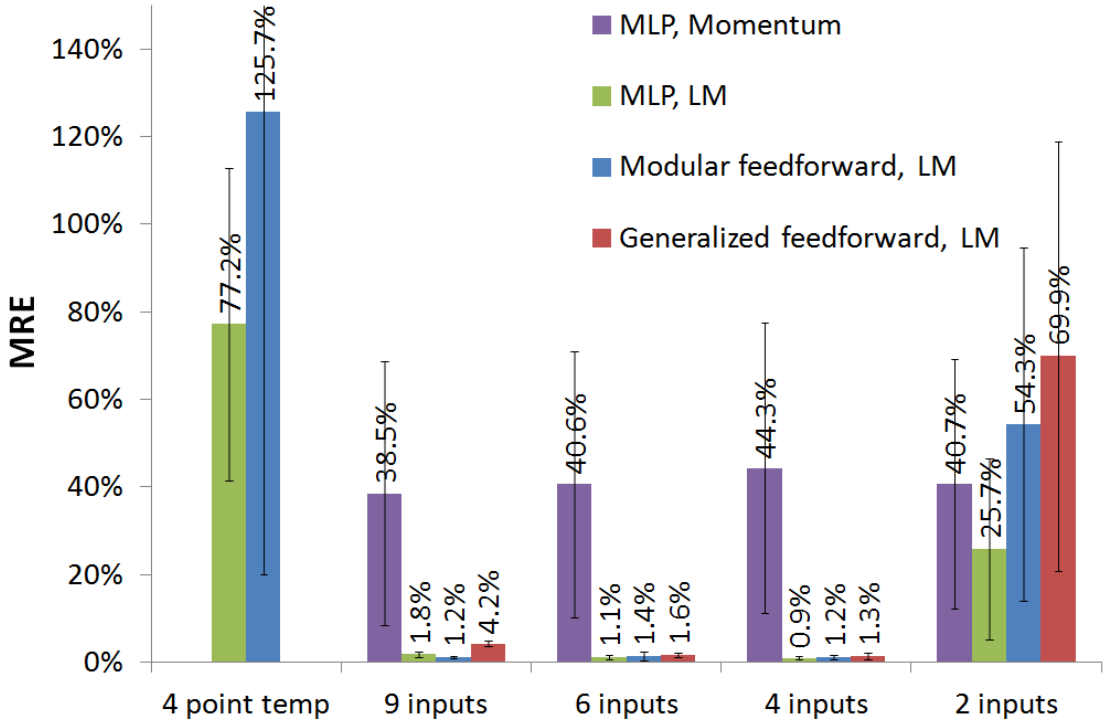

Figure 3-4: Comparison of MRE values with error bars that shows 95% confidence interval of the mean from different ANN validation results for the single contact gap conductance model

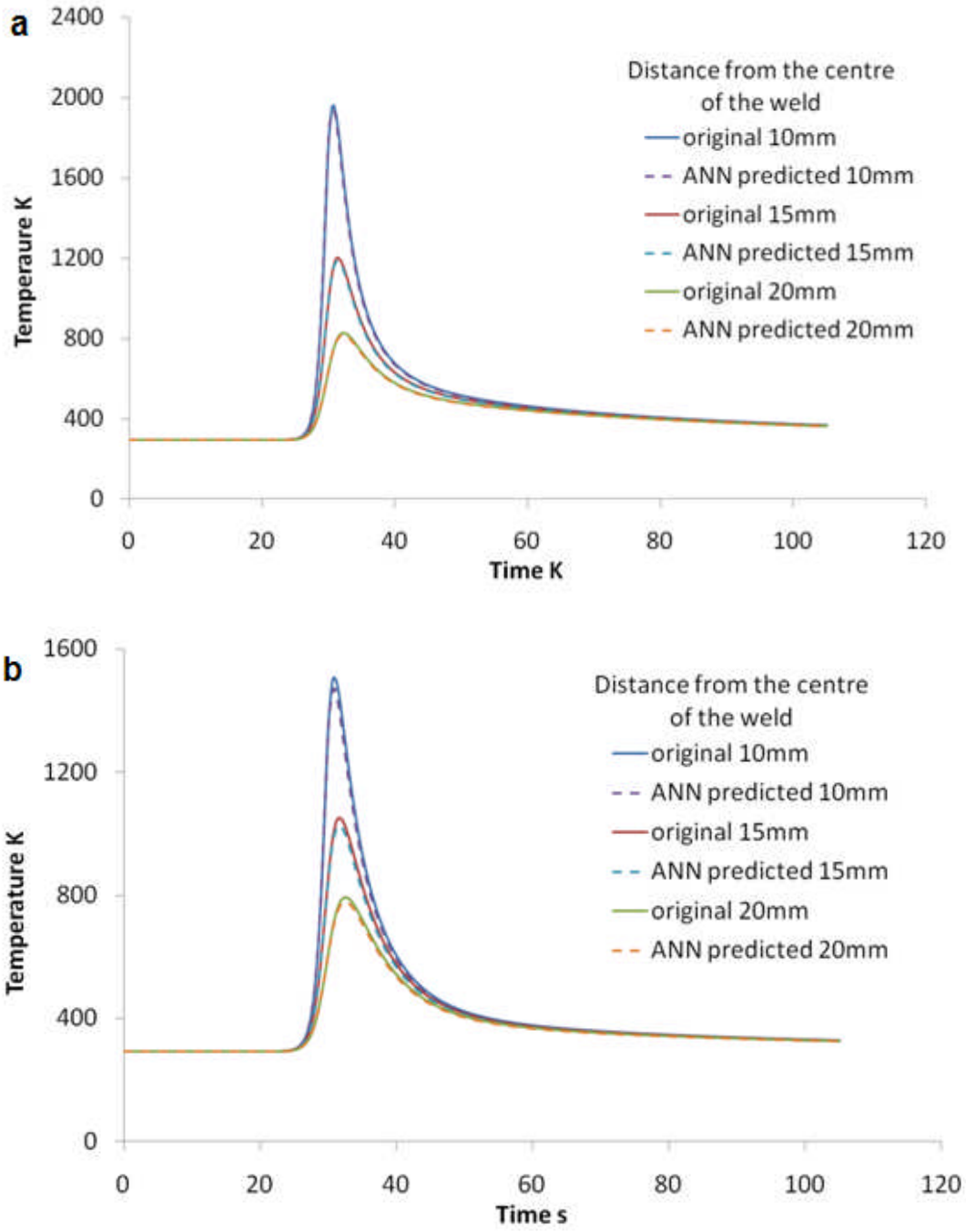

Figure 3-5: Comparison between the original thermal profiles and the curves from the FE model predicted values using ANN for test conditions of (a) Q= 9508 W, and k = 6000 W/(m^{2}K); and (b) Q= 4754 W, and k = 1500 W/(m^{2}K). The results are from the 4 input method model with MFF topology and LM BP method applied to the single contact gap conductance model.

3.4 Double constant contact gap conductance model

3.4.1 Numerical model description

As the ANN technique is capable of analysing a problem with a single constant contact gap conductance, a more complex situation is studied. The regions where the different contact gap conductances were applied are shown in Figure 3-6. The interface between aluminium alloy workpiece and steel backing plate is separated into two areas: a lower one in the far-field which is under the region which is not welded, and a higher one under the region which is welded. A similar approach was used by Colegrove et al.[3] in a model of the FSW process.

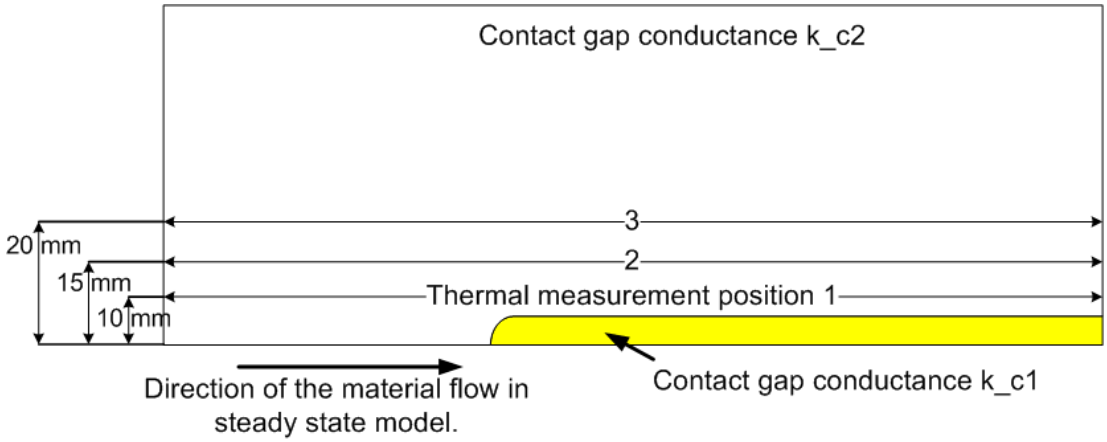

Figure 3-6: Regions where the two contact gap conductances are applied

3.4.2 ANN methodology

Three power input values and four contact gap conductance values for k_c1 and k_c2 were selected to construct the training data set, forming forty-eight combinations (Table 3-6). The conditions used for testing the model are shown in Table 3-7, and the four ANN types used to represent the data are shown in Table 3-8. Note that the 4 and 9 input methods were chosen because of their success in representing the single contact gap conductance model. In addition, only the LM gradient descent method was used because this proved more successful than the momentum method in the previous section.

48 combinations for training		
Q (W)	k_c1 ($W/(m^2K)$)	k_c2 ($W/(m^2K)$)
5714	500	10
9508	2000	100
14262	5000	300
	8000	500

Table 3-6: Data used for training the double contact gap conductance model

4 groups of values of testing		
Q (W),	k_c1 ($W/(m^2K)$),	k_c2 ($W/(m^2K)$)
7606,	3000,	400
11410,	1000,	200
13311,	7000,	50
7131,	2500,	250

Table 3-7: Data used for testing the double contact gap conductance model

ANN types	Abstracting methods	
	4 input	9 input
MFF, LM	5-5-5	5-5-5
GFF, LM	9-6-6	9-6-6

Table 3-8: The numbers of hidden layers for different ANN topologies and thermal curve abstracting methods applied in the study of the double contact gap conductance model

3.4.3 Results and discussion

The detailed results are included in Appendix C2, and the average MRE for the different model types is listed in Figure 3-7. The plot shows that the 4 input method with GFF gives the best prediction among all methods applied, and the comparison of the original and predicted values are given in Table 3-9, which also shows how the MRE of 9.97% was predicted. The predicted power input and thermal boundary condition values are

applied to the FE models to find the corresponding thermal profiles which were compared to the thermal profiles from the original values in Figure 3-8.

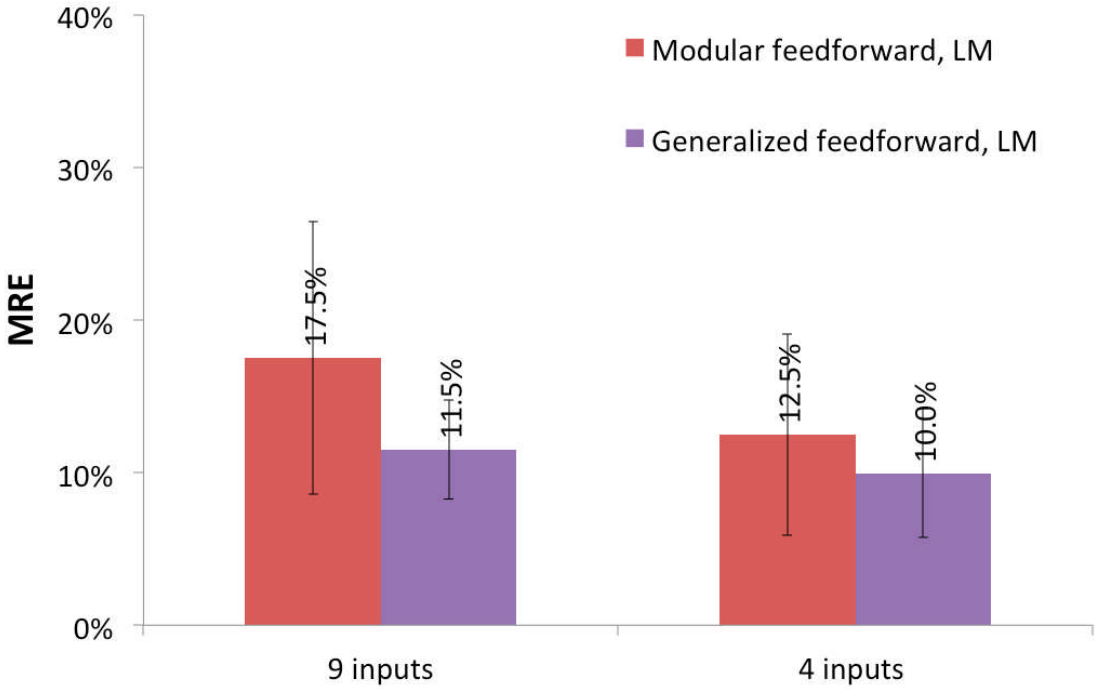

Figure 3-7: Comparison of MRE values with error bars from different ANN validation results for the double contact gap conductance model

Test values			Values predicted from ANN			MRE
Q (W)	k_c1 (W/(m^{2}K))	k_c2 (W/(m^{2}K))	Q (W)	k_c1 (W/(m^{2}K))	k_c2 (W/(m^{2}K))	
7606	3000	400	6922	3020	426	8.20%
11410	1000	200	12382	944	164	15.9%
13311	7000	50	13910	7293	44	10.0%
7131	2500	250	6474	2525	246	5.74%
					Average	9.97%

Table 3-9: Results from 4 input model with GFF topology and LM BP applied to the double contact gap conductance model

As shown in Figure 3-7, the 4 input method gave better predictions than the 9 input method, which indicates the additional input data over-trained the ANN model. Due to the fact that this study was more complex than the one in section 3.3, the GFF and MFF topologies were used, as the more complex ANN structure can provide a better. In

section 3.3, the averaged MRE between 4 and 9 input were very close, but in this case the results of the 4 input method were slightly better. Making conclusions from these results is complicated by the size of the error bars, i.e. whether the perceived benefit of using 4 inputs is real, or this is only true for the particular conditions being tested. Unlike section 3.3, the GFF method was able to give better predictions.

One conclusion that is absolutely clear, is compared to the single constant gap conductance model in section 3.3, the prediction quality in this study is poorer. The reason for this is because of the increasing complexity of the boundary condition. In the previous case, the thermal boundary condition was governed by one overall constant value, while in this case the thermal boundary condition layer was geometrically split into two areas. As shown in Figure 3-6, the closest thermal measuring position 1 is controlled predominantly by k_c1, while the other two are more influenced by k_c2. However according to the training and testing data in Table 3-6 and Table 3-7, the magnitude of k_c2 value was much smaller than k_c1, hence the influence would not be as large as k_c1. Under this circumstance, both the peak temperature, cooling slope and integral of temperature are dynamically balanced by the three input parameters. This results in a significant increase in complexity indicating it is more difficult for the ANN to give an accurate prediction.

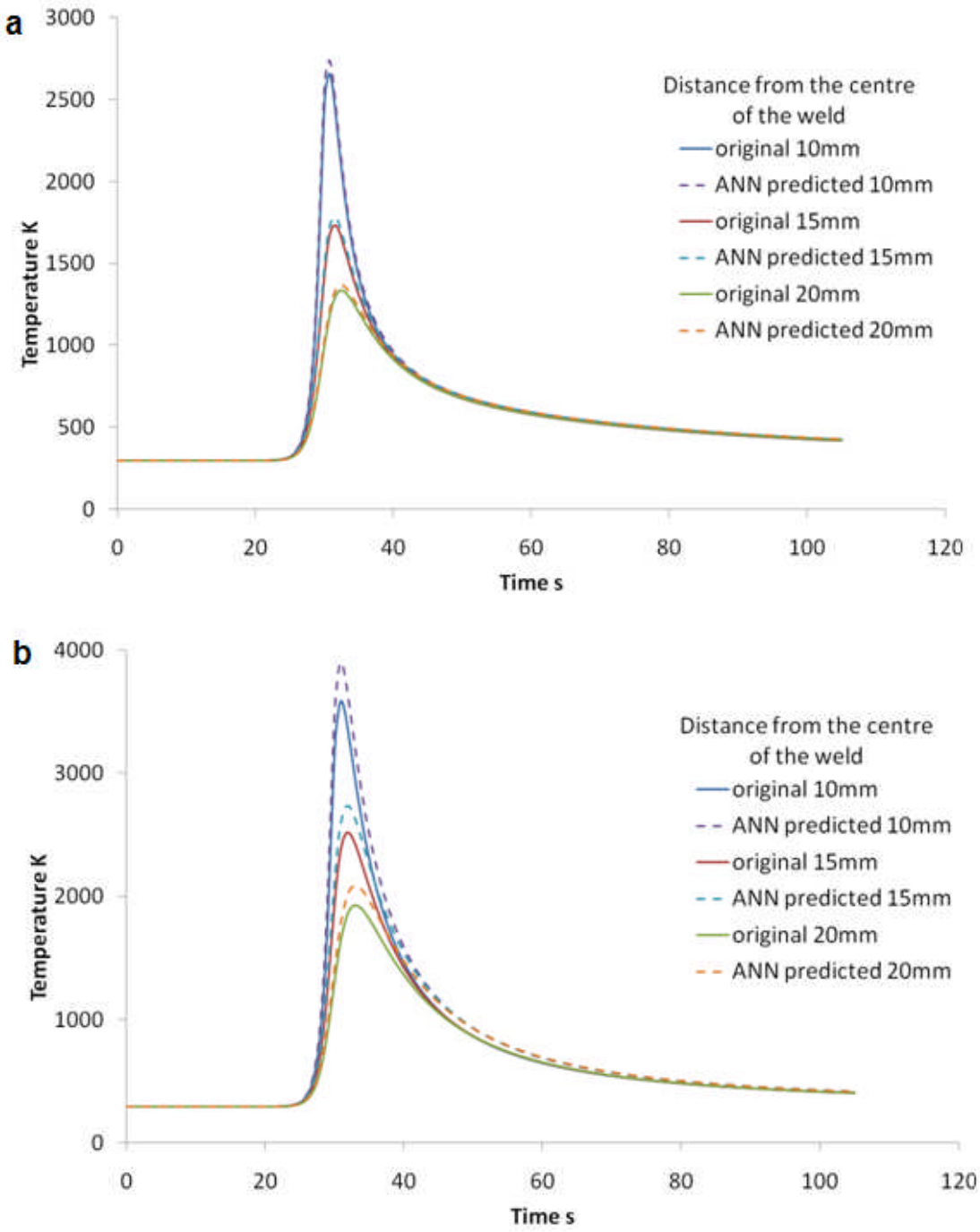

Figure 3-8: Comparison between the original thermal profiles and the curves from the FE model predicted values using ANN for test conditions of (a) Q= 7131 W, k_c1 = 2500 W/(m^2K) and k_c2 = 250 W/(m^2K); and (b) Q= 11410 W, k_c1 = 1000 W/(m^2K) and k_c2 = 200 W/(m^2K). The results are from the 4 input method model with GFF topology and LM BP method applied to the double contact gap conductance model.

3.4.4 Improving the ANN prediction

To improve the prediction quality of the double contact gap conductance model, a second stage prediction method was used. The first stage is the one that has just been implemented and provides the first estimate of the power Q_1, and the two gap conductances, k_c1_1 and k_c2_1. The second stage involved obtaining seven more training data sets from

1. Q_1, k_c1_1 and k_c2_1.
2. ±10% Q_1, k_c1_1 and k_c2_1.
3. Q_1, ±10% k_c1_1 and k_c2_1.
4. Q_1, k_c1_1 and ±10% k_c2_1.

These points are shown diagrammatically in Figure 3-9. When these new data points were added to the original 48, the prediction quality was improved dramatically, as is illustrated by the results in Table 3-10. Note that these results were obtained with the 4 input abstracting method and the GFF topology. A couple of other ANN methodologies were implemented in the section stage, such as only training the ANN with the seven new values. The one reported proved to be the most successful. The improved predictions can be seen in the plot of the thermal profiles which are shown in Figure 3-10. The new data values provide more training data around the region of interest facilitating the improved ANN model predictions.

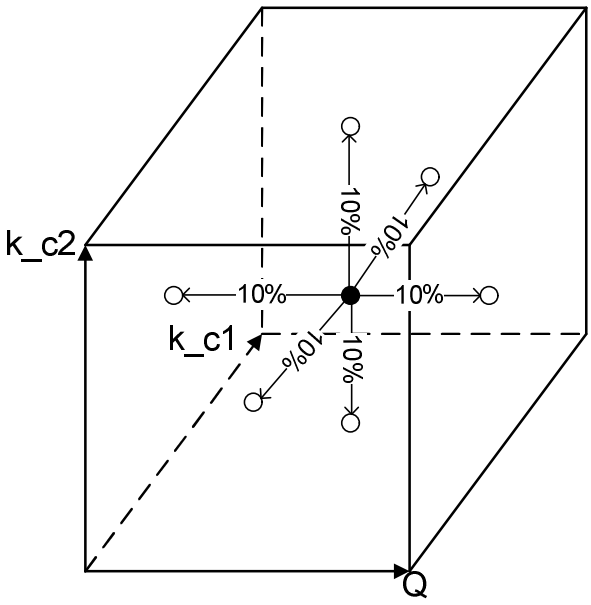

Figure 3-9: Diagram of parameters shifting for narrowing method

Test values			Values predicted from ANN			MRE
Q (W)	k_c1 ($W/(m^2K)$)	k_c2 ($W/(m^2K)$)	Q (W)	k_c1 ($W/(m^2K)$)	k_c2 ($W/(m^2K)$)	
7606	3000	400	7581	2973	401	0.78%
11410	1000	200	11388	1001	200	0.22%
13311	7000	50	13197	6997	51	1.49%
7131	2500	250	7116	2481	251	0.70%
					Average	0.80%

Table 3-10: Results from applying the second stage improvement for the original results from the 4 input method model with GFF topology and LM BP method applied to the double contact gap conductance model.

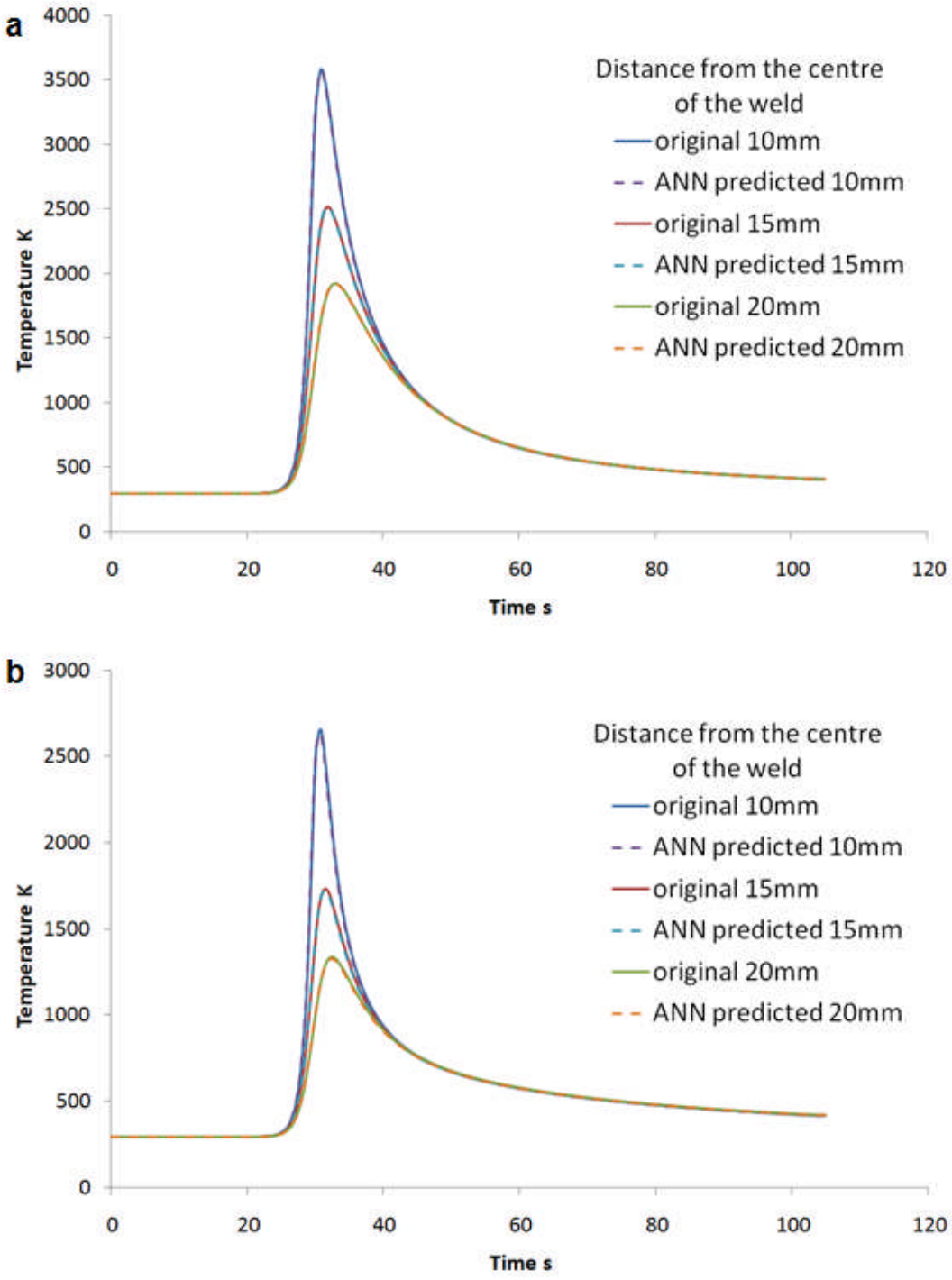

Figure 3-10: Comparison between the original thermal profiles and the curves from the ANN predicted values for test conditions of (a) Q= 11410 W, k_c1 = 1000 W/(m^{2}K) and k_c2 = 200 W/(m^{2}K); and (b) Q= 7131 W, k_c1 = 2500 W/(m^{2}K) and k_c2 = 250 W/(m^{2}K). The results are from the 4 input method model with GFF topology and LM BP method applied to the double contact gap conductance model.

3.5 Temperature dependent contact gap conductance model

3.5.1 Background and FE model description

The model used in this section is identical to that used for the double constant gap conductance model apart from the temperature dependent contact gap conductance. As discussed previously, another method of modelling the contact with the backing bar is with the temperature dependent contact gap conductance. This method was used by Shi et al.[4], and the calibrated curve obtained from this work is shown in Figure 3-11(a).

Rather than using a look-up table of values, an exponential curve was used to represent this data:

$$k = a \cdot \exp(b \cdot T) \qquad \text{Eq. 3-4}$$

where k is the contact gap conductivity, T is the local temperature in Kelvin, a and b are constants to be determined by the ANN technique. As shown in Figure 3-11(a), a numerical curve fitting method was applied to find initial values for these constants, which gave values of 22.2 W/(m^{2}K) for a and 0.0107 K^{-1} for b.

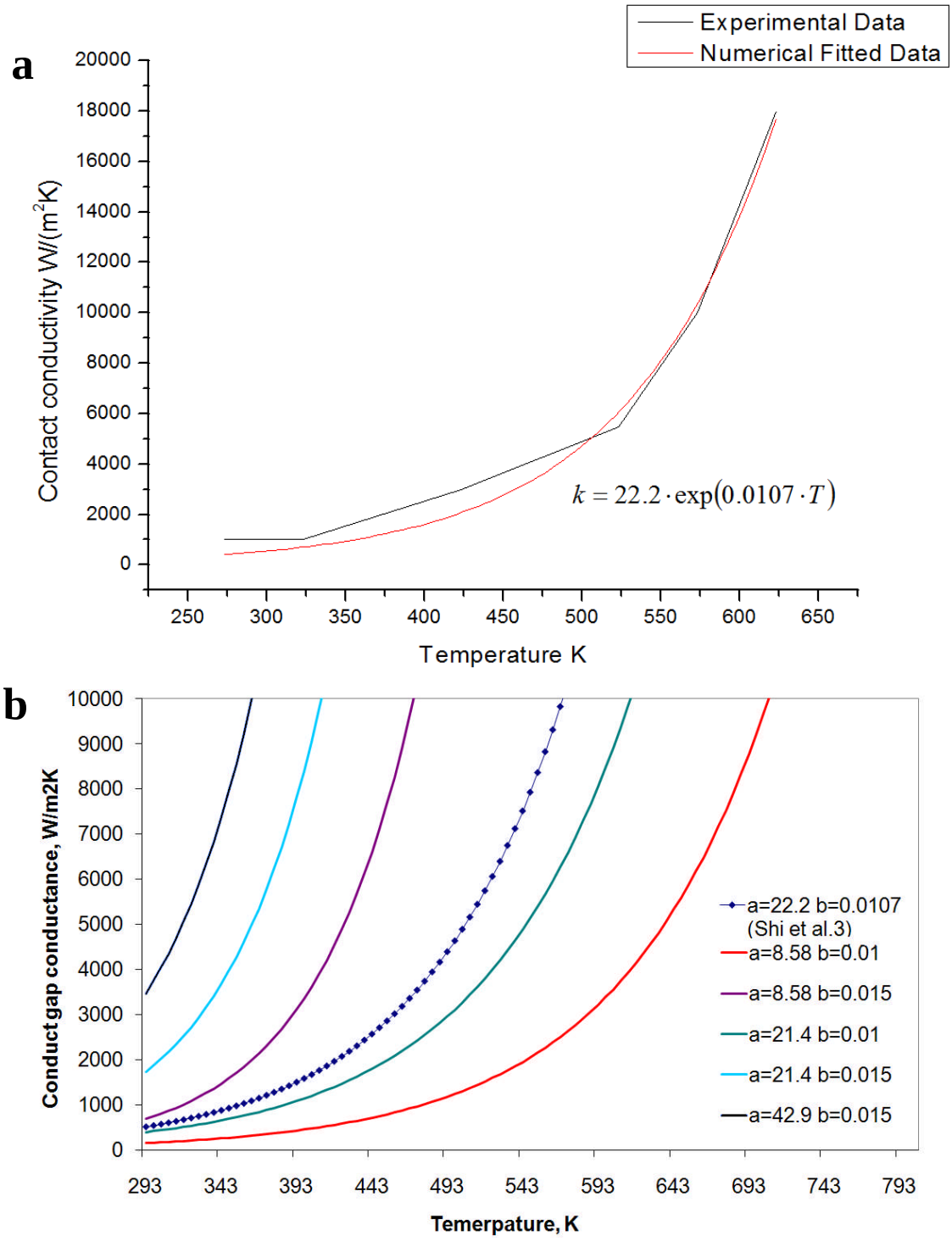

Figure 3-11: (a) Numerical curve fitting to find initial values, (b) diagram showing example of contact conductance curves which cover the range used in the training data

The training values used for the ANN are shown in Table 3-11, which form 48 combinations. The effect of altering a and b on the contact conductance for some select

values is shown in Figure 3-11(b). As shown in Figure 3-11(b), the curves plotted for chosen a and b values are not only able to consist of the data range from Shi et al.[4], but are sufficiently wide to give a large variation in contact gap conductance with temperature. The data used for testing the ANN model are shown in Table 3-12, and the ANN methods and model types implemented with the technique are shown in Table 3-13.

48 combinations for training		
Q (W)	a (W/(m^{2}K))	b (K^{-1})
1902	8.58	0.005
3803	21.4	0.01
5705	38.6	0.012
	42.9	0.015

Table 3-11: Data used for training the temperature dependent contact gap conductance model

4 groups of values for testing		
Q (W),	a (W/(m^{2}K)),	b (K^{-1})
2377,	12.9,	0.014
2852,	21.4,	0.011
4754,	30.0,	0.008
5229,	23.6,	0.006

Table 3-12: Data used for testing the temperature dependent gap conductance model

ANN types	Abstracting methods		
	4 input	6 input	9 input
MFF, LM	5-5-5	5-5-5	5-5-5
MFF, LM	9-6-6	9-6-6	9-6-6
GFF, LM	9-6-6	9-6-6	9-6-6
MLP, LM	9-6-6	9-6-6	9-6-6

Table 3-13: The numbers of hidden layers for different ANN topologies and thermal curve abstracting methods applied in the study of the temperature dependent contact gap conductance model

3.5.2 Results and discussion

The detailed results of applying an ANN to investigate the temperature dependent contact gap conductance model are shown in Appendix C3. The comparison of average MRE for the different ANN models is shown in Figure 3-12. With this more complex thermal boundary condition, the ANN was able to offer a reasonable prediction of the thermal profile, but it was not as good as the single contact gap conductance model in section 3.3. Note that the error bars for each of the results are large, making conclusions difficult. Nevertheless in the group of 4 input method, the average MRE is around 15% for all ANN topologies. As the training information increased from 4 input to 6 and 9 inputs, the performance of the ANN with MLP structure worsened, which indicates the MLP method may be over-trained. The opposite occurs for the GFF and MFF topologies when the training information is increased. This shows that in case of GFF and MFF, additional training data benefit the prediction quality. Also no improvement is discovered by increasing the hidden nodes from 5-5-5 to 9-6-6 in the 9 input group.

The one with the best match was the 9 input method with GFF topology, and the results are given in Table 3-14. The visual comparison between the predicted and original values is given in Figure 3-13. The best prediction quality MRE is 2.39%, which is shown in Figure 3-13(a), while the poorest one is 12.3% shown in Figure 3-13(b).

Test values			Values predicted from ANN			MRE
Q (W)	a (W/(m^{2}K))	b (K^{-1})	Q (W)	a (W/(m^{2}K))	b (K^{-1})	
2377	12.86	1.40E-02	2110	10.1	1.45E-02	12.3%
2852	21.44	1.10E-02	2517	19.9	1.12E-02	7.00%
4754	30.02	8.00E-03	5094	35.7	8.01E-03	8.75%
5229	23.59	6.00E-03	5364	23.7	5.75E-03	2.39%
					Average	7.62%

Table 3-14: Results from 9 input model with GFF topology and LM BP applied to the temperature dependent contact gap conductance model

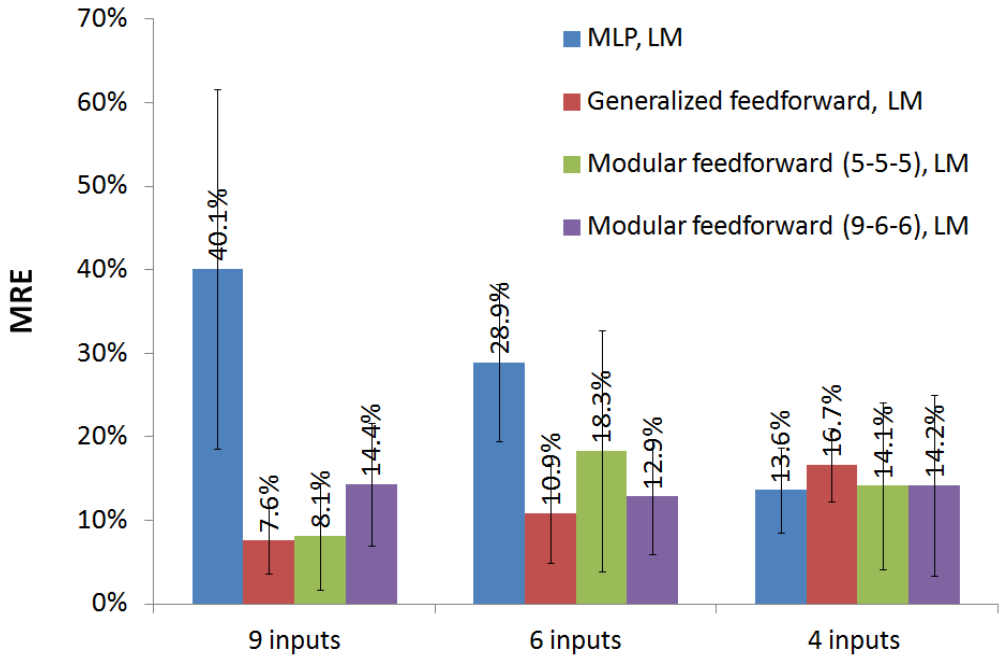

Figure 3-12: Comparison of MRE values with error bars from different ANN validation results for the temperature dependent contact gap conductance model

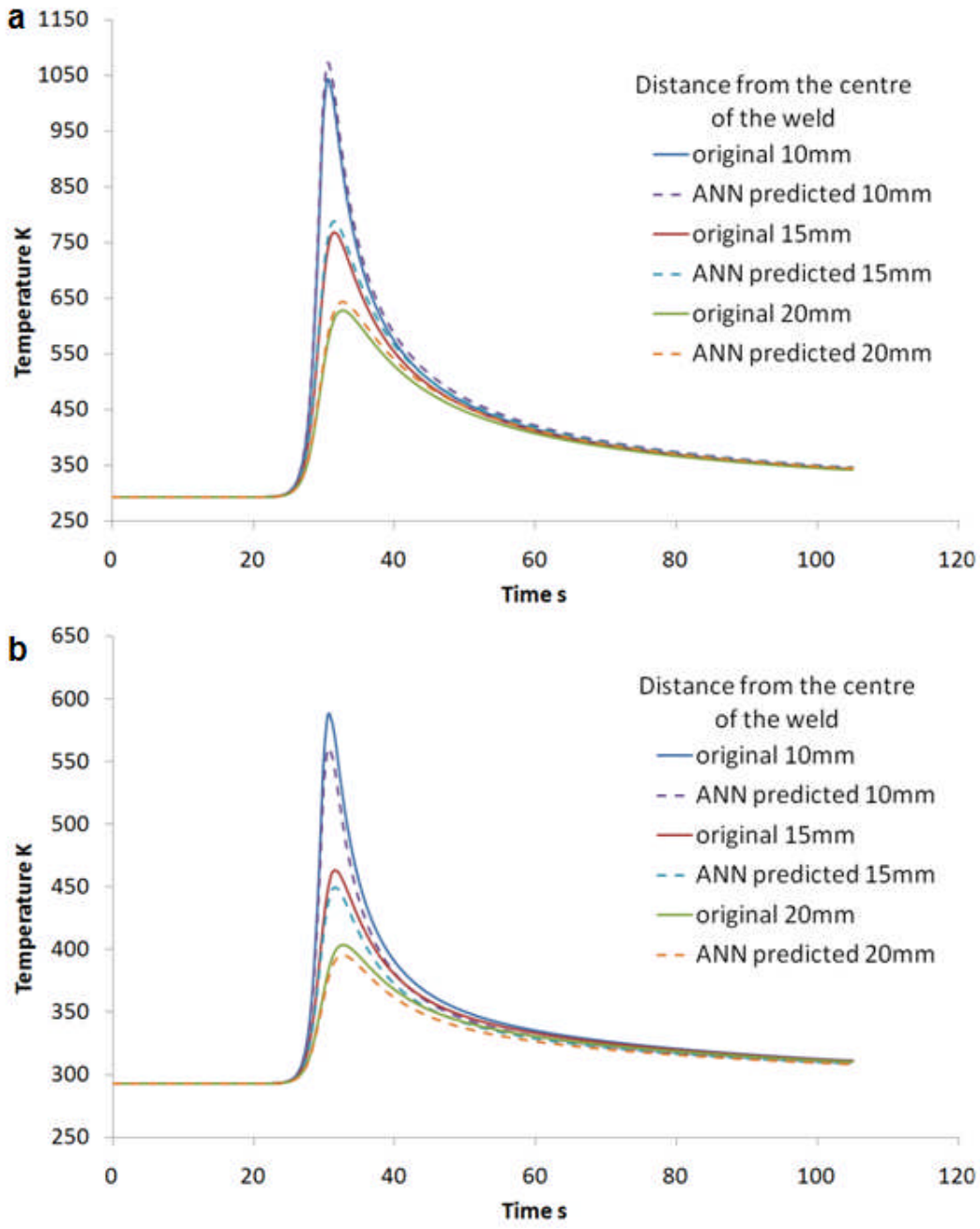

Figure 3-13: Comparison between the original thermal profiles and the curves from the FE model predicted values using ANN for test conditions of (a) Q= 5229 W, a = 23.59 K^{-1} and b = 6E-3 W/(m^2K); and (b) Q= 2337 W, a = 12.86 W/(m^2K) and b = 1.4E-2 K^{-1}. The results are from the 9 input method model with GFF topology and LM BP method applied to the temperature dependent contact gap conductance model.

3.5.3 Improving the ANN prediction

The same method, which was described in section 4.4, for improving the model accuracy was applied to the temperature dependent contact gap conductance model. The results shown in Table 3-15 which were implemented for the 9 input GFF model and demonstrate a significant improvement in prediction quality. This is reflected in the improved MRE of 0.93%. The improved results are validated as shown in Figure 3-14. The new training set with more data around the region of interest was able to provide a much better prediction.

Test values			Values predicted from ANN			MRE
Q (W)	a ($W/(m^2K)$)	b (K^{-1})	Q (W)	a ($W/(m^2K)$)	b (K^{-1})	
2377	12.86	1.40E-02	2369	12.7	1.41E-02	1.14%
2852	21.44	1.10E-02	2869	21.8	1.10E-02	1.18%
4754	30.02	8.00E-03	4732	29.9	8.00E-03	0.43%
5229	23.59	6.00E-03	5217	23.9	5.99E-03	0.97%
					Average	0.93%

Table 3-15: Results from applying the second stage method improvement for the original results from the 9 input method model with GFF topology and LM BP method applied to the temperature dependent contact gap conductance model.

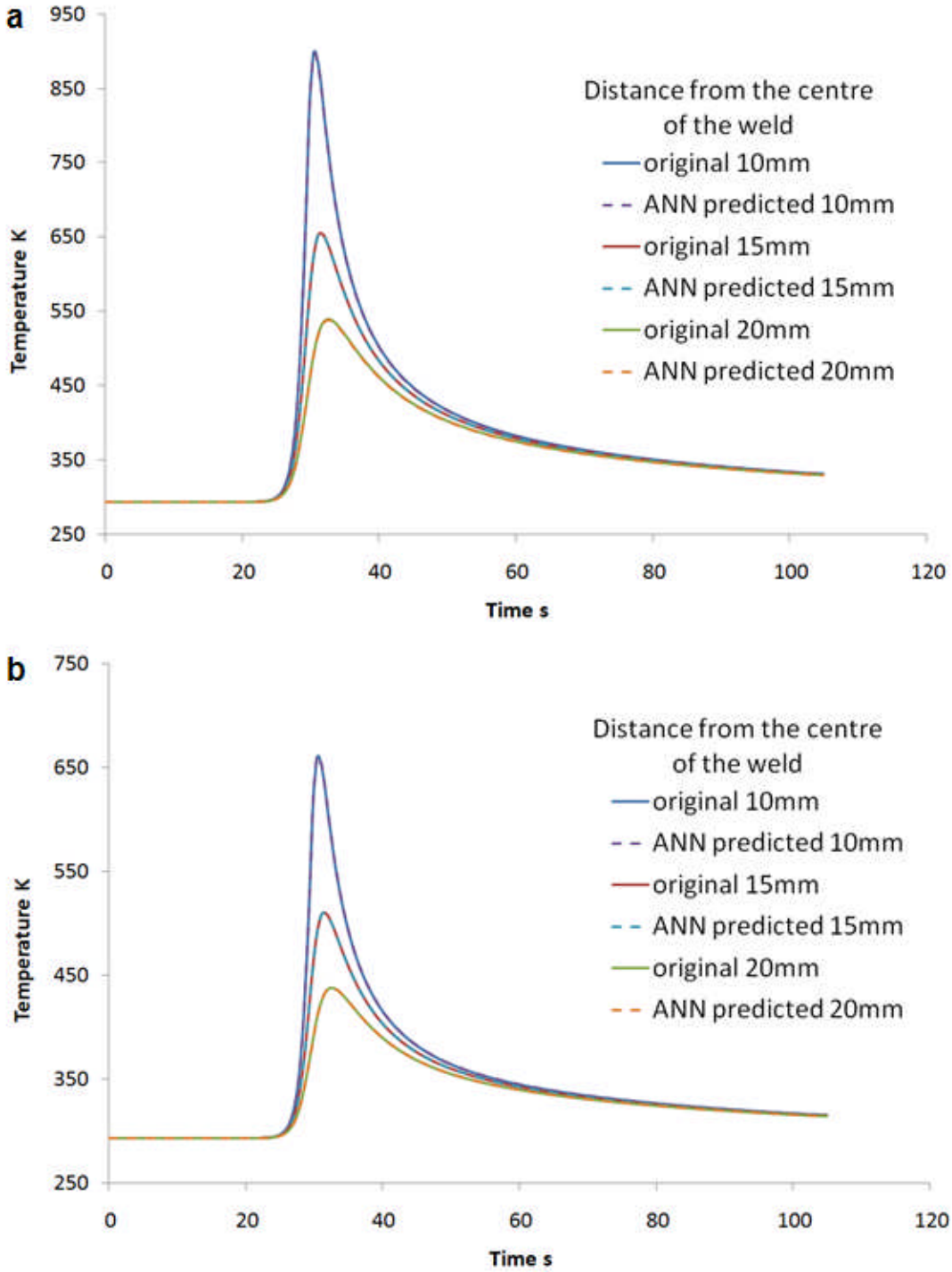

Figure 3-14: Comparison between the original thermal profiles and the curves from the ANN predicted values for test conditions of (a) Q= 4754 W, a = 30.02 K^{-1} and b = 8E-3 $W/(m^2K)$; and (b) Q= 2852 W, a = 21.44 $W/(m^2K)$ and b = 1.1E-2 K^{-1}. The results are from the 9 input method model with GFF topology and LM BP method applied to the temperature dependent contact gap conductance model.

3.6 Conclusions

This study successfully demonstrated that by combining the ANN model with an FE model, it is possible to find accurate power and thermal boundary conditions from the abstracted temperature history. The following are the main findings from this work:

1. The selection of the training data range is found to be of essential importance for applying the ANN techniques.
2. The FE model with a single contact gap conductance will require the 4 input method for training the ANN model properly. The 4 input method includes the peak temperature and the integral of temperature vs. time at two locations (10 and 20 mm away from the centreline).
3. The FE model with double contact gap conductances boundary required the same 4 input method for training, however due to the increasing complexity of the thermal boundary condition, the prediction quality was poorer.
4. Significantly more training data is required for the temperature dependent contact gap conductance model; the 9 input method was used in this case. The inputs also included the slope of the cooling part in the thermal profile at three locations. In addition, the accuracy of the prediction was similar to the double contact gap conductance model.
5. The predicted results can be improved by implementing a second stage ANN which provides additional training data around the region of interest.
6. The importance of the topology of the ANN has been studied, which showed that the LM method was more accurate than the momentum method.
7. While the MLP topology proved adequate for the single contact gap conductance model, the GFF topology proved the most successful for the more complex double and temperature dependent contact gap conductance models.

In the next section this technique will be applied to a process model for FSW.

References

1. A. Simar, T. Pardoen and B. De Meester: 'Effect of rotational material flow on temperature distribution in friction stir welds', *Sci. Technol. Weld. Joining*, 2007, 12, 324-333.

2. M. Z. H. Khandkar, J. A. Khan and A. P. Reynolds: 'Prediction of temperature distribution and thermal history during friction stir welding: Input torque based model', *Sci. Technol. Weld. Joining*, 2003, 8, 165-174.

3. P. A. Colegrove, H. R. Shercliff and R. Zettler: 'Model for predicting heat generation and temperature in friction stir welding from the material properties', *Sci. Technol. Weld. Joining*, 2007, 12, 284-297.

4. Q. Shi, T. Dickerson and H. R. Shercliff: 'Thermomechanical FE modeling of friction stir welding of Al-2024 including tool loads', *Proc. 4th Int. Friction Stir Welding Sym., Park City, Utah, USA*, May 2003.

5. S. Sreekanth, H. S. Ramaswamy, S. S. Sablani and S. O. Prasher: 'A neural network approach for evaluation of surface heat transfer coefficient', *J. Food Process. Preserv.*, 1999, 23, 329-348.

6. M. Smith: 'Neural networks for statistical modeling', *New York: Van Nostrand Reinhold*, 1993.

7. S. S. Sablani: 'A neural network approach for non-iterative calculation of heat transfer coefficient in fluid-particle systems', *Chem. Eng. Proc.: Proc. Intensification*, 2001, 40, 363-369.

8. S. Haykin: 'Neural Networks: A Comprehensive Foundation', 2nd edition, 1999, USA, Prentice-Hall.

9. I. Oh and C. Y. Suen: 'A class-modular feedforward neural network for handwriting recognition', *Pattern Recognit*, 2002, 35, 229-244.

10. NeuroSolutions 5.07, NeuroDimension Inc., 2008.

11. Y. S. Touloukian: 'Thermal Conductivity: Non Metallic Solids', New York, Plenum, 1970.

12. Y. S. Touloukian: 'Specific Heat: Non Metallic Solids', 1970, New York, Plenum.

13. J. P. Holman: 'Heat Transfer', 6th edition, New York, McGraw-Hill Book Co., 1986.

14. Y. J. Chao and X. Qi: 'Thermal and thermo-mechanical modeling of friction stir welding of aluminum alloy 6061-T6', *Journal of Materials Processing and Manufacturing Science*, 1998, 7, 215-233.

15. J. Thibault and B. P. A. Grandjean: 'A neural network methodology for heat transfer data analysis', *Int. J. Heat Mass Transfer*, 1991, 34, 2063-2070.

16. COMSOL 3.3, COMSOL Multiphysics, 2005.

CHAPTER 4

Hybrid Modelling of 7449-T7 Friction Stir Welds

4.1 Introduction

The previous section showed how a process model can be linked to ANN models to find the unknown boundary coefficients. Such models are called 'hybrid models' due to the combination of the two model types. Some researchers have applied similar concepts such as Sablani[1] and Sreekanth et al.[2] in their analysis of the heat transfer between the solid particles and a fluid. The general procedure for developing a hybrid model is[1]:

1. Obtaining a group of temperature versus time curves from analytic or numerical thermal models.
2. Train the ANN model using the outputs from the thermal model as inputs, while using the inputs of the thermal model as outputs to the ANN model.
3. Once the ANN has been trained, experimental thermal data is input into the trained ANN to find the corresponding boundary conditions.

ANN models have also been applied to welding processes. Weiss et al.[3] applied a hybrid modelling technique to calibrate a model of hybrid LB-GMA aluminium welding. A similar, but slightly different approach was used by Kumar and DebRoy[4] who combined a genetic algorithm with a process model for arc welding to predict weld results such as the penetration, weld pool length and peak temperature from welding parameters and material thermal properties.

The main purpose of this study is to investigate the thermal boundary condition using a hybrid model of the FSW process. This will be applied to a series of welds produced with the 'Flexi-stir' FSW machine which is used to analyse the phase changes which occur during welding with synchrotron radiation. Previously, ANN techniques were used to predict the thermal boundary conditions in a simple FE thermal model. This section uses the hybrid model to investigate the complex heat transfer between the workpiece and backing bar during FSW. The study investigates different methods for inputting the thermal data into the ANN as well as different ANN topologies.

4.2 Friction stir welding experiments

The experimental FSW work was performed on 3.2 mm thick 7449-T7 plates at HZG (formerly GKSS Forschungszentrum). Travel speeds of 2, 3, 4, 5, 6 and 8 mm/s with a rotation speed of 1300 rpm were used for the welds. The workpiece and the thermocouple positions are shown in Figure 4-1(a). The thermal profiles from the retreating and advancing side were averaged and calibrated to input into the trained ANN model for validation. The average temperature difference between both sides was 13 K. The FSW process used displacement control, and the welding tool dimensions are shown in Figure 4-1(b).

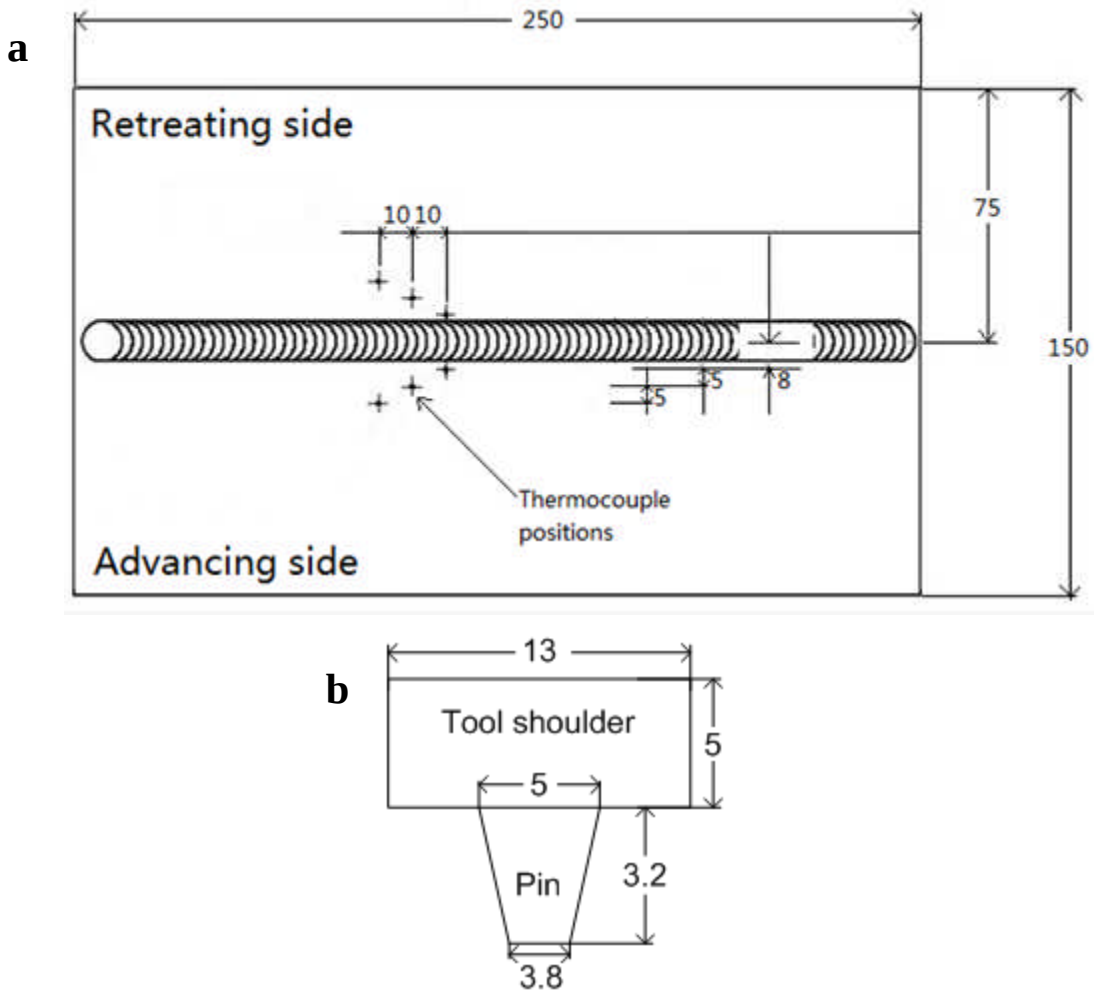

Figure 4-1: a) The welding plate and thermocouple positions and b) dimensions of the tool (units: mm)

4.3 Structure of the hybrid model

The hybrid modelling procedure is represented in Figure 4-2, which consists of the following steps:

1. Construct the FSW process model and ANN training model.
2. Applying 48 groups of hypothetical boundary condition values to the FSW process model, and obtain the corresponding thermal data.
3. Abstract the thermal data so that the characteristics of the thermal curves can be represented by key data values.
4. Train the ANN models with the data values from step 3. Note that during training the thermal data are inputs and the boundary condition values are outputs.
5. Abstract the experimental thermal data using the same method that was used for the model data and input into the trained ANN. Obtain the predicted boundary condition values.
6. Enter the predicted boundary conditions into the FSW process model, and obtain the corresponding thermal data.
7. Compare the predicted thermal data with experimental thermal data from step 5 to validate the method for finding the boundary conditions.

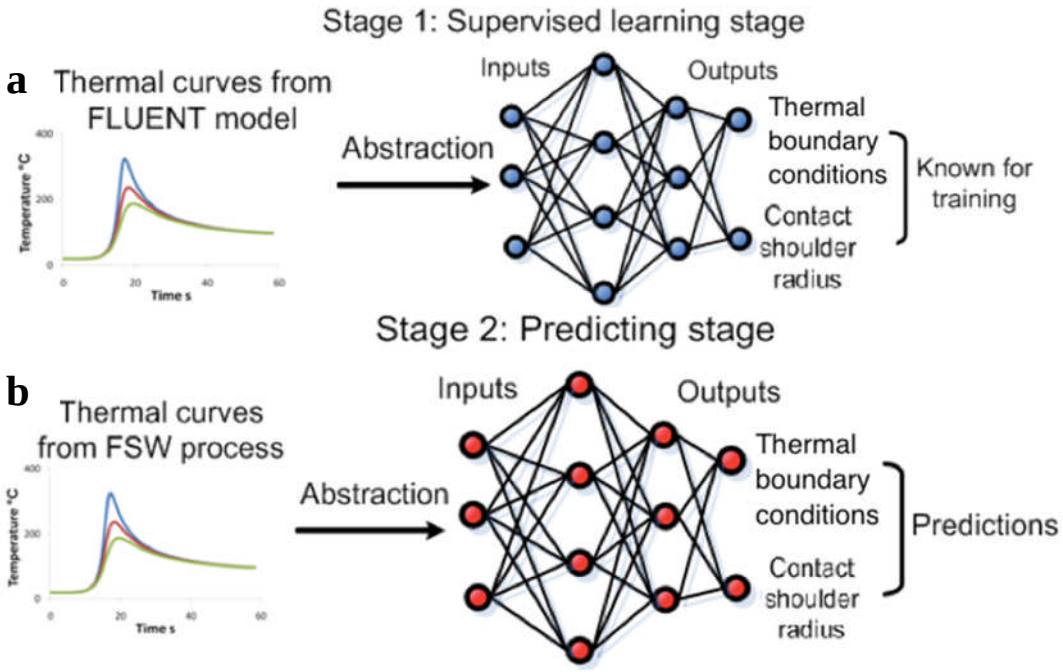

Figure 4-2: The working structure of FSW hybrid model, including (a) the learning stage and (b) the predicting stage

4.4 Friction stir welding model development

4.4.1 Model dimensions and solver type

The FSW process model is a three-dimensional fully coupled model developed with FLUENT CFD solver and is similar to those developed by Colegrove and Shercliff[5]. The deforming material is modelled as a highly viscous fluid. The boundary conditions in the model are used to represent the unique characteristics of the 'Flexi-stir' machine[6] developed at HZG (former GKSS Forschungszentrum Geesthacht). Note that a thin copper backing bar is used underneath the tool to allow the synchrotron radiation to pass through the workpiece to the target. The geometry is as shown in Figure 4-3(a) and (b), and the material properties used in the model are shown in Table 4-1.

Material name	Density ($kg \cdot m^{-3}$)	Specific heat ($J \cdot Kg^{-1} \cdot K^{-1}$)	Thermal conductivity ($W \cdot m^{-1} \cdot K^{-1}$)
7449-T7 aluminium workpiece[7]	2840	860	154
Copper backing bar[8]	8954	383	386
Backing bar steel (0.5% C steel) at 150°C [8]	7833	465	40
H13 tool steel (5% chrome) at 300°C[8]	7833	460	36

Table 4-1: Thermal properties of the materials used in the FSW process model

Since the material movement in the area far away from the welding tool is negligible, the workpiece is divided into a liquid aluminium region adjacent to the tool in which the momentum and heat equations are solved, and a solid aluminium region in the far field in which only the heat equation is solved. The model is solved in the steady-state mode, which was found suitable for all travel speeds with the procedure described in Grong[9]. This strategy results in a more rapid solution than a full transient simulation. Note that the limited size of the model does slightly affect the temperatures in the far field, particularly for the low travel speeds.

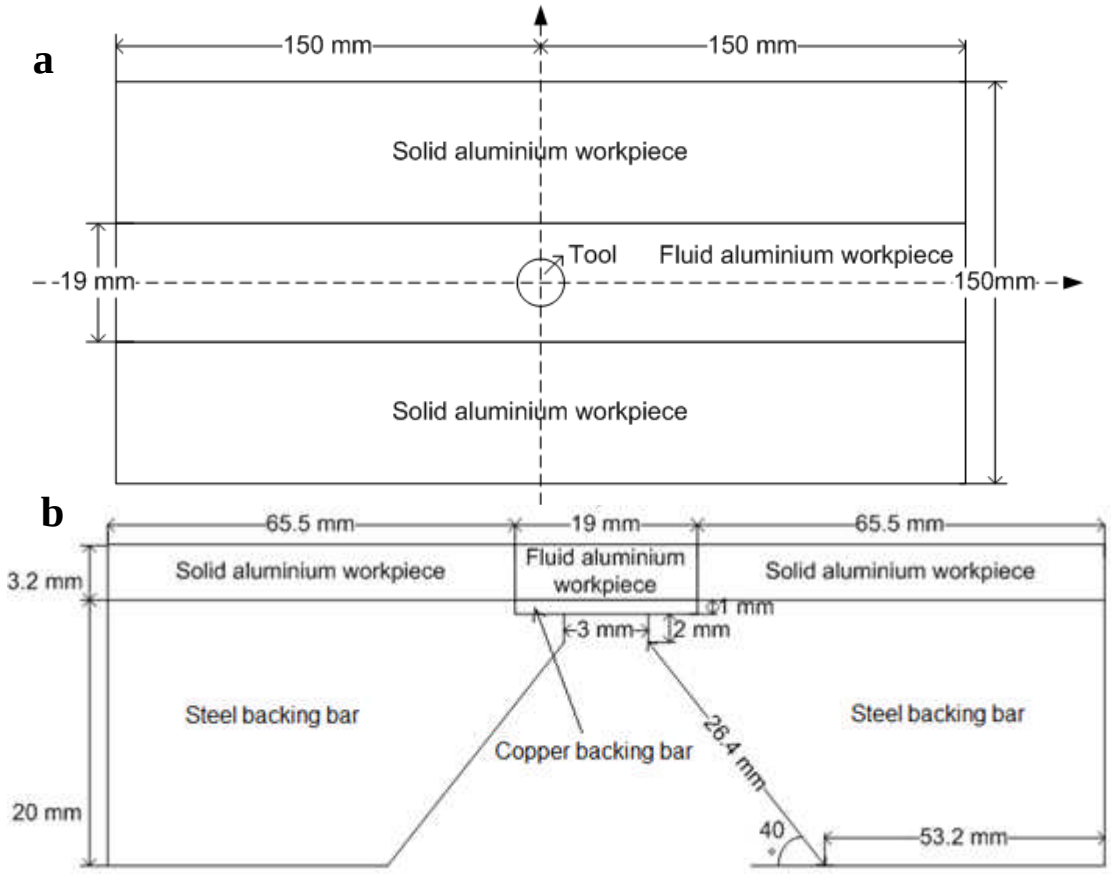

Figure 4-3: Diagram of the geometry used of the FLUENT model; a) top-view and b) side view

4.4.2 Model thermal boundary conditions

To model the imperfect contact between the aluminium workpiece and the backing bars, temperature dependent contact gap conductance boundary conditions were applied. According to Figure 4-3, there were three interfacial boundaries which needed to be determined: the boundary condition between aluminium workpiece and copper backing bar k_1, the aluminium workpiece and the steel backing bar k_2 and the copper and steel backing bars k_3. An experimental investigation of the contact gap conductance by Yuncu[10] showed that the values between aluminium and steel, and copper and steel were similar and approximately a quarter of the value between copper and aluminium. Both aluminium and copper are softer and more ductile compared to steel, which leads to a better contact condition. As stated previously a temperature dependent contact gap conductance between the aluminium workpiece and steel backing bar was used by Shi et al.[11] and Rohsenow[12]. Although discrete values in the form of a lookup table were

used, the values approximate an exponential curve. The justification for this approach can be seen in the experimental values in Figure 4-4. In the far field both the temperature and interfacial pressure are low which leads to a low contact gap conductance. Near the tool, both the temperature and pressure increase leading to an exponential increasing contact gap conductance. Therefore the temperature dependent contact gap conductance values in the hybrid model are represented by:

$$k_2 = k_3 = a \cdot \exp(b \cdot T) = \frac{1}{4} k_1 \qquad \text{Eq. 4-1}$$

where T is the temperature at the interface between the workpiece and backing bar in Kelvin, and a and b are constants to be determined with the hybrid model.

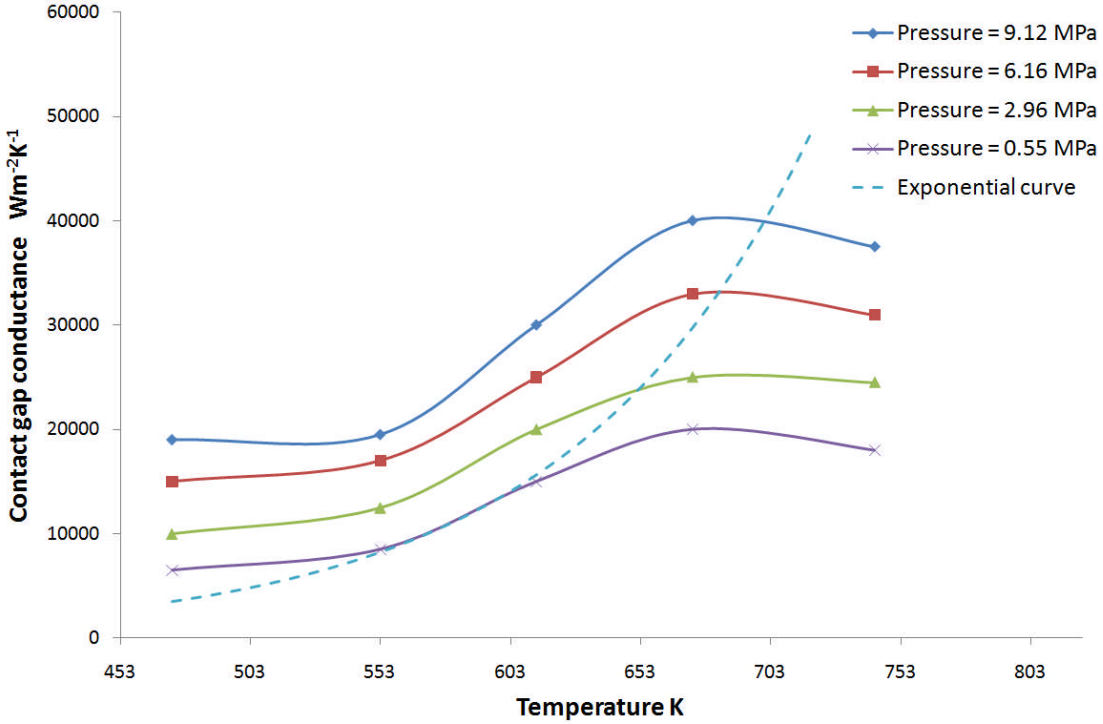

Figure 4-4: Near the tool both the pressure and temperature increase which leads to an exponential relationship with the temperature (if pressure is not modelled)[13]

The remaining thermal boundary conditions in the model are simpler. The convective heat loss through the bottom of the steel backing bars had a constant value of 1000 W/m^{2}K suggested by Colegrove et al.[14]. Khandkar et al.[15] found that the temperature of the workpiece was insensitive to this value. The convective heat loss from the top surface of aluminium workpiece is 10 W/m^{2}K suggested from experimental analysis done by Chao and Qi[16].

4.4.3 Material flow stress property

Describing the material flow behaviour is one of the essential parts for modelling the FSW process. Different constitutive laws have been applied to FSW models, including the Johnson-Cook model used by Askari et al.[17] and Schmidt et al.[18,19], the Norton-Hoff law applied by Moal et al. [20] and Liechty et al.[21], and the von Mises law applied by Zhang er al.[22] and Zhang et al.[23]. However this work uses the Zener-Holloman law proposed by Sellars and Tegart[24], which is widely used for aluminium alloys[25,26]. Previous work[27] has demonstrated that the following relationship can be fit to experimental results from Gleeble experiments:

- When $T < T_m$

$$Z = \dot{\varepsilon} \cdot \exp\left(\frac{Q}{R \cdot T}\right) \qquad \text{Eq. 4-2}$$

$$x = \left(\frac{Z}{A}\right)^{1/n} \qquad \text{Eq. 4-3}$$

$$\sigma = \frac{1}{\alpha} \cdot a\sinh(x) - \frac{720 - T}{50} \cdot \left(k \cdot \ln(\dot{\varepsilon}) + m\right) \quad \text{When } T \leq 720 \qquad \text{Eq. 4-4}$$

$$\sigma = \frac{1}{\alpha} \cdot a\sinh(x) \text{ , when } T > 720 \text{ K} \qquad \text{Eq. 4-5}$$

where $\dot{\varepsilon}$ is the strain-rate (s^{-1}), Q is the activation energy equalling 140000 J/mol, R is the gas constant (J/kg·K), σ is the flow stress, A, n, α, k and m are the material constants equalling to 5.026e11 s^{-1}, 5.167, 6.910E-03 MPa^{-1}, 6.991 and 2.137 respectively. T_s is the material solidus temperature equalling to 773 K. As the temperature approaches the solidus, a rapid softening regime was implemented like that implemented by Colegrove et al.[14]. This avoided overpredicting the heat generation as the temperature approaches the solidus. When T is greater than the arbitrarily set softening temperature T_m (753 K) the flow strength is linearly reduced to zero at the solidus.

- When $T \geq T_m$

$$Z' = \dot{\varepsilon} \cdot \exp\left(\frac{Q}{R \cdot T_m}\right) \qquad \text{Eq. 4-6}$$

$$x' = \left(\frac{Z'}{A}\right)^{1/n} \qquad \text{Eq. 4-7}$$

$$\sigma = \frac{1}{\alpha} \cdot a\sinh(x') \cdot \frac{T - T_s}{T_m - T_s} \qquad \text{Eq. 4-8}$$

The resulting Zener-Holloman curves for the 7449-T7 are shown in Figure 4-5.

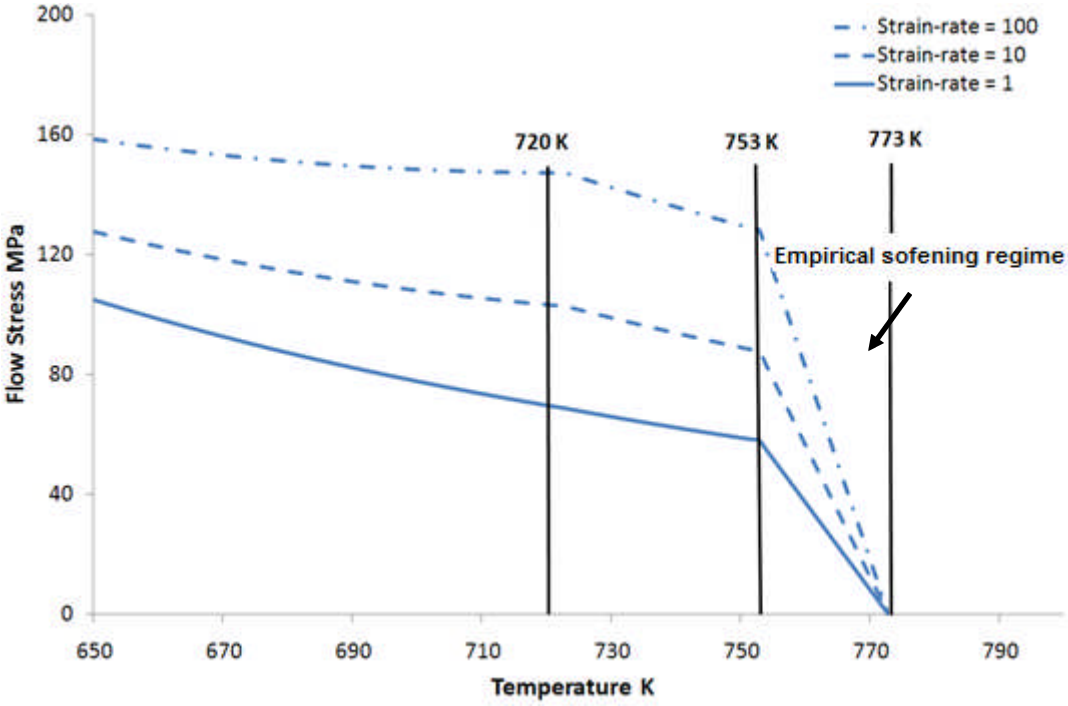

Figure 4-5: Predicted material flow stress for 7449-T7 aluminium alloy[27]

Note that the experimental results in the chapter 2 showed that no rapid softening regime exists for this aluminium alloy. The rapid softening regime has been included because it avoids the problem of overpredicting the temperature. The next chapter describes an alternative modelling approach where there is no material softening, but slip is used at the interface.

4.4.4 Model heat generation and heat flow

The equations for describing the heat and mass flow are described elsewhere in Colegrove et al.[14]. The model assumes a sticking condition between the workpiece and the tool. A concept used by Colegrove et al.[14] is the CSRR, which assumed that during the FSW process only a fraction of the shoulder is fully in contact with the workpiece material and generates heat. This was used because there is usually an imperfect contact condition between the shoulder and the material during FSW, i.e. the shoulder does not

fully contact the workpiece material. In addition, there is likely to be slip between the tool and the workpiece material in the real weld and the reduced shoulder contact radius helps to compensate for this effect. Since the shoulder contact radius has a direct impact on the heat generation, it is one of the adjustable parameters in the hybrid model.

4.5 ANN model development

4.5.1 Abstracting the thermal curves

As described previously, one of the key requirements of the hybrid model is abstracting the thermal curves before inputting them into the ANN. The abstracting methods used in this study are shown in Figure 4-6 and described below:

1. The first one called the '9 input' method uses: the peak temperature; the cooling slope which is the slope of the line between the peak temperature and the temperature at half this value; and the integral of temperature against time. The time over which the temperature is integrated varies for the different travel speeds, and equals the length of plate divided by the travel speed. This is done at distances of 8, 13 and 18 mm from the weld centreline, which correspond to the location of the thermocouples in the experiments (see Figure 4-1(a)).

2. The second type is the '6 input' method which is the same as the '9 input' method but excludes *either* the peak temperature, integral of temperature or cooling slope, i.e. there are three variants – one which excludes the peak temperature, one which excludes the integral of temperature and one which excludes the cooling slope.

3. The last one is the '4 input' method and is based the '6 input' methods but excludes the thermal data from the point 13 mm from the centreline. Once again there are three variants.

The different abstracting methods are summarised in Table 4-2.

Abstracting Method	Parameters	Thermocouple positions – distance (mm) from weld centreline
9 input	Peak temperature, integral of temperature, and cooling slope	8, 13 and 18
6 input-p-i	Peak temperature, and integral of temperature	8, 13 and 18
6 input-p-c	Peak temperature, and cooling slope	8, 13 and 18
6 input-i-c	Integral of temperature, and cooling slope	8, 13 and 18
4 input-p-i	Peak temperature, and integral of temperature	8 and 18
4 input-p-c	Peak temperature, and cooling slope	8 and 18
4 input-i-c	Integral of temperature, and cooling slope	8 and 18

Table 4-2: Summary of abstracting method used for the hybrid ANN models

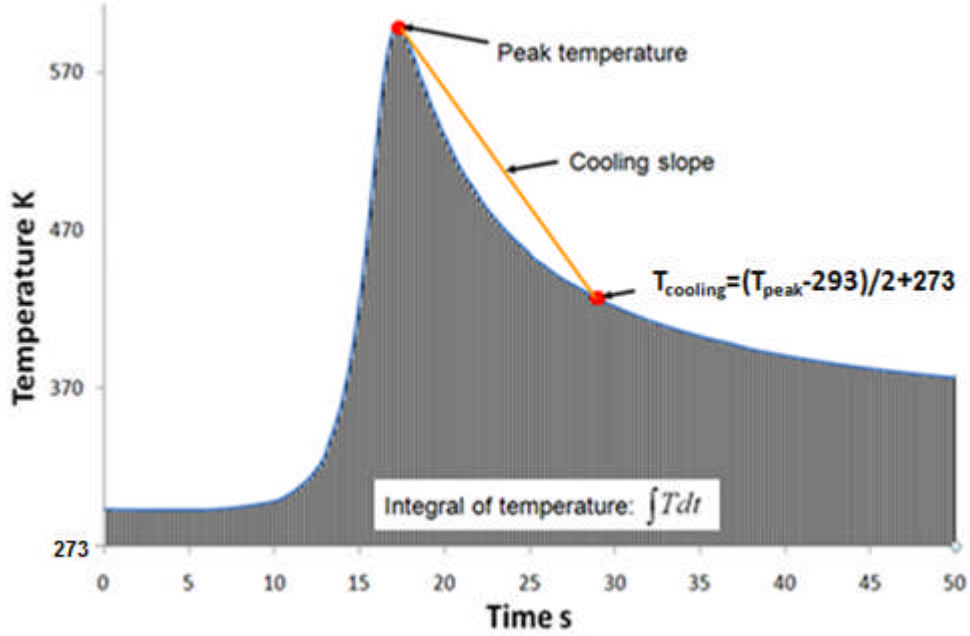

Figure 4-6: Method of abstracting a thermal profile

4.5.2 Applied ANN model components

The fundamental components of the ANN model, are the ANN topology, transfer function and training algorithm[28]. The overall applied transfer function is the sigmoid equation. The BP algorithm is used throughout the study with the LM gradient descent

method, which is a high-order adaptive method suitable for analyzing the complex boundary conditions in the process model. There are three ANN topologies which have been applied during the study:

1. MLP network,
2. GFF network,
3. MFF network.

4.5.3 Training data set

To train the hybrid model, three CSRR values and four values of the backing bar constants *a* and *b* were used, giving forty-eight combinations. The applied values are shown in Table 4-3.

48 combinations of values for training		
CSRR	a (W $m^{-2}K^{-1}$)	b (K^{-1})
43.2%	8	0.005
55.4%	21	0.01
75.7%	38	0.012
	43	0.015

Table 4-3: The training data used for the hybrid model

4.5.4 Analysis of results

To compare the predicted thermal profiles from the hybrid model, with the experimental curves the MRE is found from:

$$MRE = \frac{1}{N}\sum_{i=1}^{N}\left|\frac{Y_i - X_i}{X_i}\right| \qquad \text{Eq. 4-9}$$

where X_i and Y_i are the abstracted peak temperature, integral of temperature and cooling slope from the model and experiments respectively.

4.6 Results and discussion

4.6.1 Topology and abstraction method investigation

Table 4-4 gives the MRE for the different abstracting methods, travel speeds and ANN topologies. The average prediction qualities with the error bars indicating the 95% confidence interval of the mean are calculated by averaging across the different travel speeds for each abstracting method and ANN topology and are shown in Figure 4-7. By comparing both the averaged MRE including the spread in the mean, the plot indicates that the 4 input-i-c abstracting method with the integral of temperature and cooling slope had the lowest MRE of the seven abstracting methods. This indicates that the additional information from 6 and 9 input methods such as the peak temperature at more locations did not improve but reduced the prediction quality. Of the three topologies, the GFF topology provided the lowest overall MRE. The MLP topology performed particularly poorly on the 9 input method, which may be a result of excessive data and over-training. Moreover the MFF topology gave poor predictions as the amount the training data reduced, which can be observed for some of the 4 input methods. It is important to note however that for each results the error bar are large, so some of these conclusions may change with more data points. The predicted CSRR and boundary conditions for the different travel speeds are shown in Table 4-5 for the 4 input-i-c abstracting method with GFF ANN topology.

9 input								
Topology	2 mm/s	3 mm/s	4 mm/s	5 mm/s	6 mm/s	8 mm/s	MRE	95%
MLP	21.91%	1.63%	6.51%	3.48%	19.03%	13.73%	11.05%	6.75%
GFF	3.75%	6.99%	12.79%	2.32%	2.46%	13.19%	6.92%	4.00%
MFF	4.04%	7.64%	5.66%	10.87%	2.34%	11.77%	7.05%	3.00%
6 input-p-i								
Topology	2 mm/s	3 mm/s	4 mm/s	5 mm/s	6 mm/s	8 mm/s	MRE	95%
MLP	4.94%	9.40%	3.55%	8.75%	2.37%	7.47%	6.08%	2.31%
GFF	3.75%	9.43%	7.57%	3.87%	2.27%	10.82%	6.28%	2.78%
MFF	4.04%	8.71%	3.54%	2.27%	2.35%	12.81%	5.62%	3.39%
6 input-p-c								
Topology	2 mm/s	3 mm/s	4 mm/s	5 mm/s	6 mm/s	8 mm/s	MRE	95%
MLP	9.34%	1.46%	6.57%	3.20%	13.84%	4.01%	6.40%	3.66%
GFF	3.73%	9.54%	4.98%	3.05%	16.54%	3.17%	6.84%	4.27%
MFF	4.11%	7.46%	12.83%	1.67%	2.56%	13.96%	7.10%	4.22%
6 input-i-c								
Topology	2 mm/s	3 mm/s	4 mm/s	5 mm/s	6 mm/s	8 mm/s	MRE	95%
MLP	3.18%	7.57%	12.77%	10.92%	9.85%	1.22%	7.59%	3.63%
GFF	10.08%	1.96%	12.66%	4.98%	2.46%	1.16%	5.55%	3.80%
MFF	9.24%	6.76%	12.39%	5.81%	12.06%	13.86%	10.02%	2.62%
4 input-p-i								
Topology	2 mm/s	3 mm/s	4 mm/s	5 mm/s	6 mm/s	8 mm/s	MRE	95%
MLP	3.30%	8.59%	4.97%	11.77%	2.38%	10.13%	6.86%	3.08%
GFF	3.99%	9.82%	4.76%	7.20%	2.43%	4.96%	5.53%	2.09%
MFF	4.01%	13.17%	10.79%	10.93%	19.85%	12.72%	11.91%	4.08%
4 input-p-c								
Topology	2 mm/s	3 mm/s	4 mm/s	5 mm/s	6 mm/s	8 mm/s	MRE	95%
MLP	3.52%	1.90%	12.85%	3.98%	2.32%	21.54%	7.69%	6.32%
GFF	1.39%	8.39%	12.47%	3.35%	5.52%	10.20%	6.89%	3.37%
MFF	4.02%	13.87%	12.45%	13.19%	2.24%	13.33%	9.85%	4.21%
4 input-i-c								
Topology	2 mm/s	3 mm/s	4 mm/s	5 mm/s	6 mm/s	8 mm/s	MRE	95%
MLP	2.94%	1.46%	6.57%	3.20%	13.84%	4.01%	5.34%	3.60%
GFF	3.34%	1.93%	5.61%	3.18%	2.35%	2.01%	3.07%	1.10%
MFF	3.74%	2.41%	11.06%	5.68%	2.35%	1.84%	4.51%	2.80%

Table 4-4: MRE for the different abstracting methods, travel speeds and ANN topologies

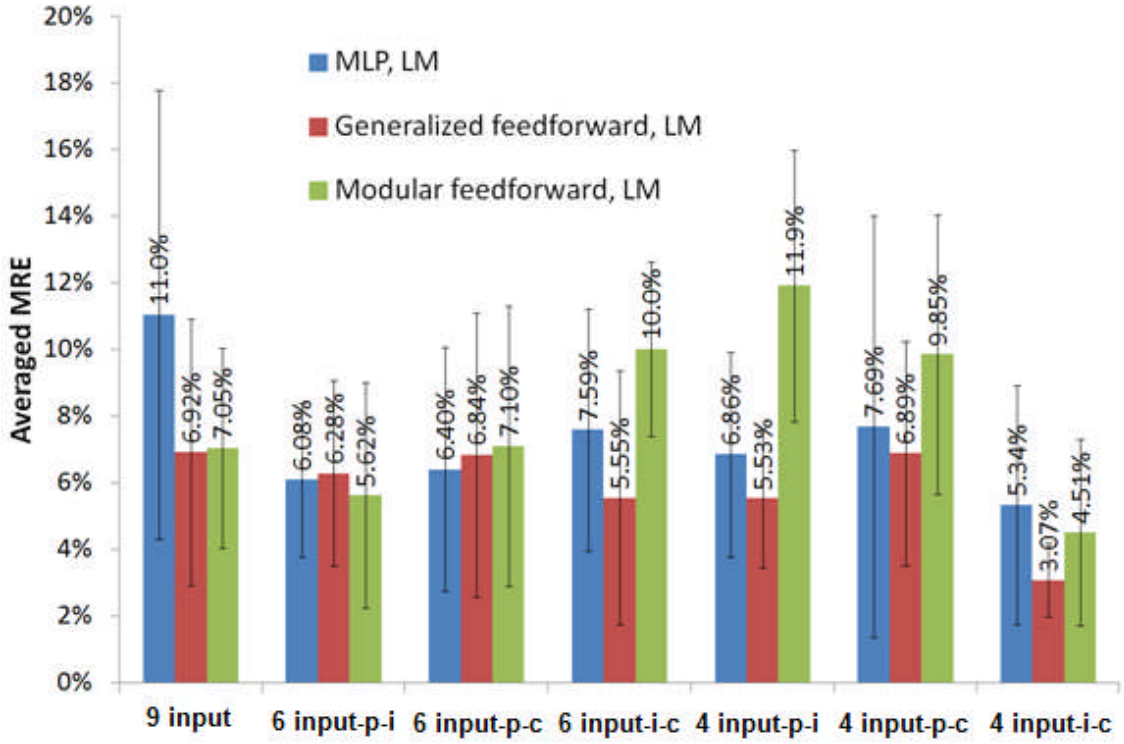

Figure 4-7: Average MRE for the different abstracting methods and ANN topologies. Note that the different abstracting methods are defined in Table 4-4

The visual comparisons between the experimental measurements and those from the 4 input-i-c are shown in Figure 4-8. The comparisons show that all the predicted curves were able to give good predictions in the thermal cycles, particularly the peak temperature. In most cases the hybrid models are able to give accurate predictions of the cooling slopes. Although there are some discrepancies with the peak temperature and integral of temperature for the slowest speed weld (2 mm/s), the thermal curves from the other models are well matched with the experimental ones. This shows that the hybrid models are able to predict the complex heat transfer phenomenon in the FSW process.

The predicted contact gap conductances from the parameters in Table 4-5 are shown in Figure 4-9. The visual comparisons and the predicted values in Table 4-5 suggest that the thermal boundary condition performance and the CSRR are not independent of each other. For instance, the 5 mm/s case has a larger contact gap conductance, at the same time its CSRR value is also higher at level 70.86%. Hence the larger CSRR, which results in more heat being generated, is balanced by a higher contact gap conductance

which increases the heat loss. The situation is also complicated by variations in the welding process. These issues are investigated in greater depth in the next section.

Travel Speed	CSRR	a (W $m^{-2}K^{-1}$)	b (K^{-1})
2 mm/s	63.9%	43.5	4.56E-03
3 mm/s	43.2%	44.9	4.54E-03
4 mm/s	74.7%	44.6	4.46E-03
5 mm/s	70.9%	6.32	1.04E-02
6 mm/s	75.7%	6.06	4.91E-03
8 mm/s	51.9%	6.56	5.20E-03
Average values	63.4%	25.3	5.67E-03

Table 4-5: The predicted hybrid results and averaged results

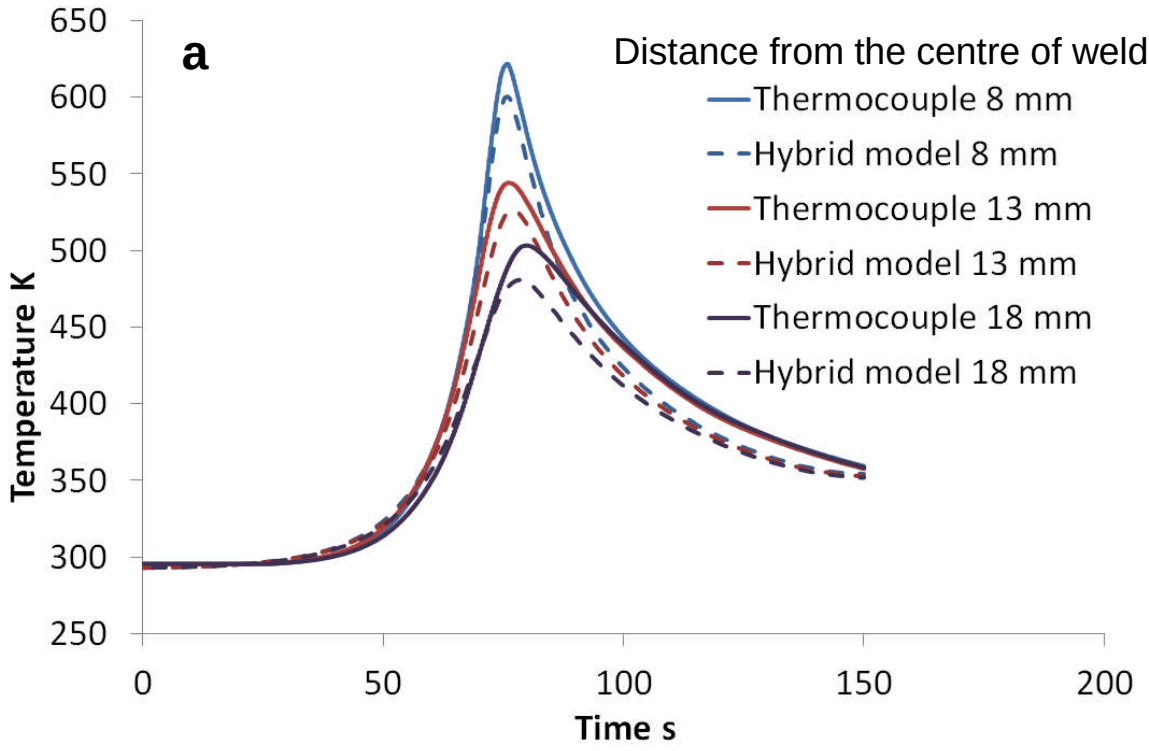

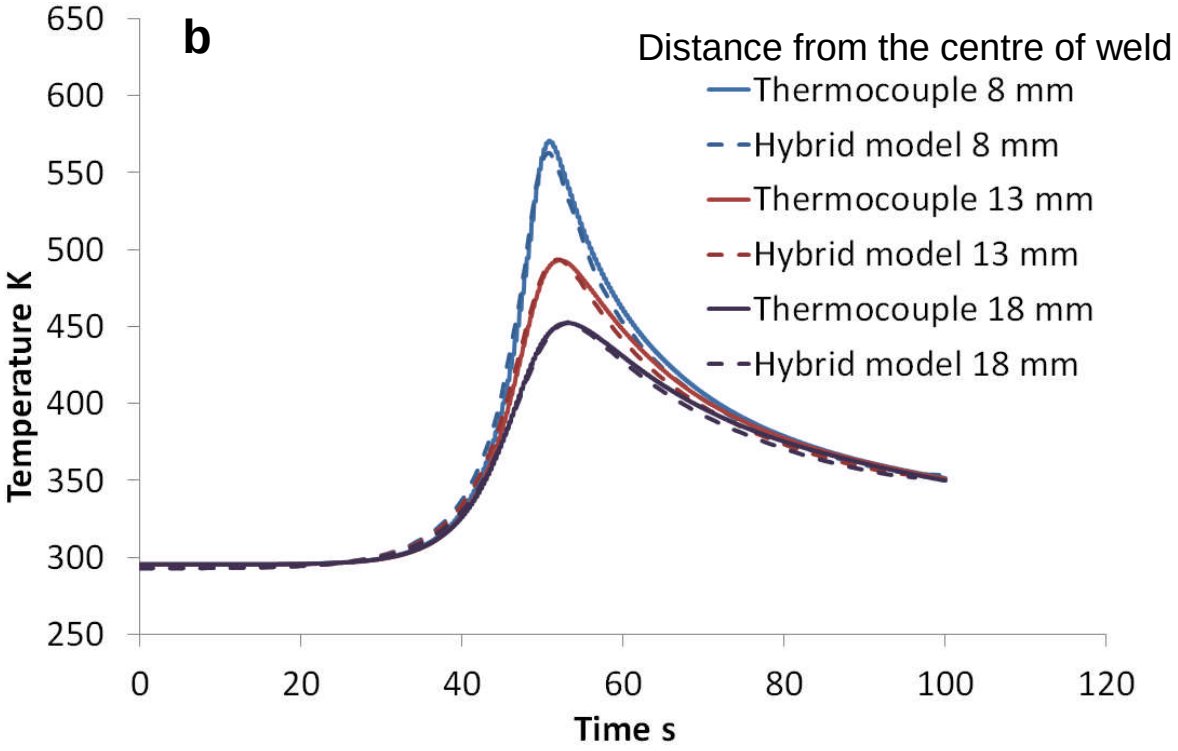
b
Distance from the centre of weld
Thermocouple 8 mm
Hybrid model 8 mm
Thermocouple 13 mm
Hybrid model 13 mm
Thermocouple 18 mm
Hybrid model 18 mm
Temperature K
650
600
550
500
450
400
350
300
250
0
20
40
60
80
100
120
Time s

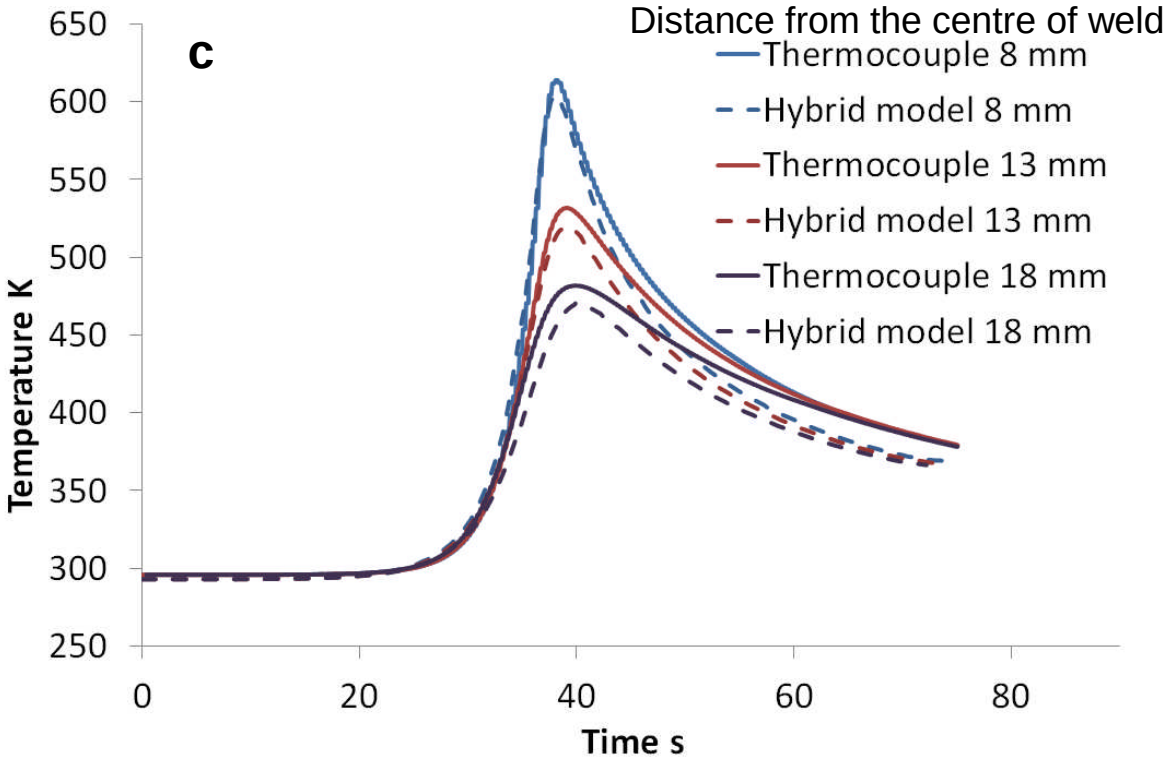
c
Distance from the centre of weld
Thermocouple 8 mm
Hybrid model 8 mm
Thermocouple 13 mm
Hybrid model 13 mm
Thermocouple 18 mm
Hybrid model 18 mm
Temperature K
650
600
550
500
450
400
350
300
250
0
20
40
60
80
Time s

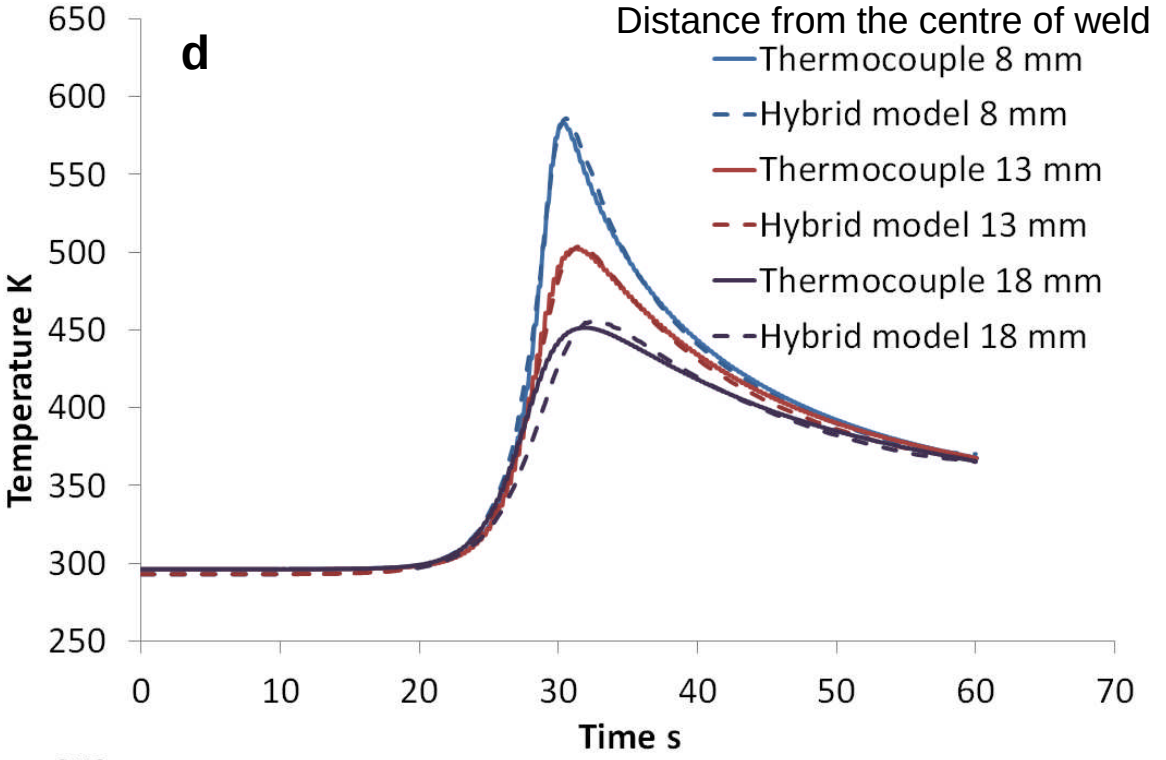
d
Distance from the centre of weld
Thermocouple 8 mm
Hybrid model 8 mm
Thermocouple 13 mm
Hybrid model 13 mm
Thermocouple 18 mm
Hybrid model 18 mm
Temperature K
650
600
550
500
450
400
350
300
250
0
10
20
30
40
50
60
70
Time s

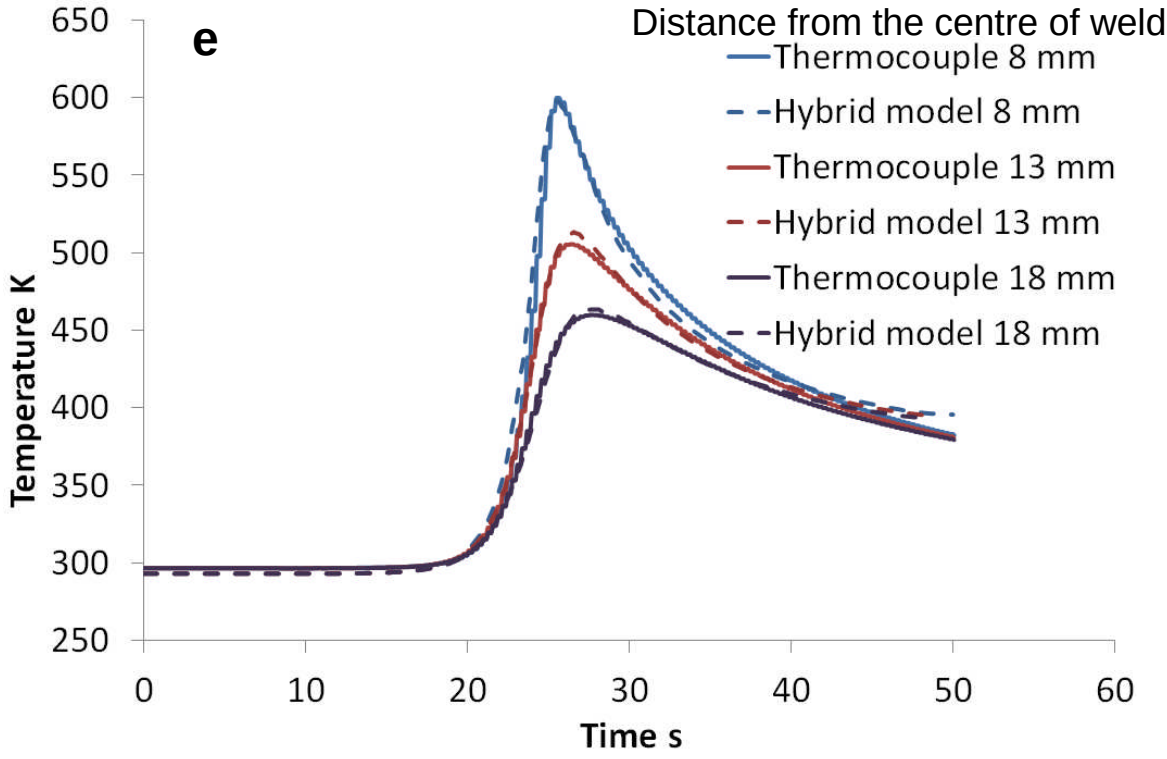
e
Distance from the centre of weld
Thermocouple 8 mm
Hybrid model 8 mm
Thermocouple 13 mm
Hybrid model 13 mm
Thermocouple 18 mm
Hybrid model 18 mm
Temperature K
650
600
550
500
450
400
350
300
250
0
10
20
30
40
50
60
Time s

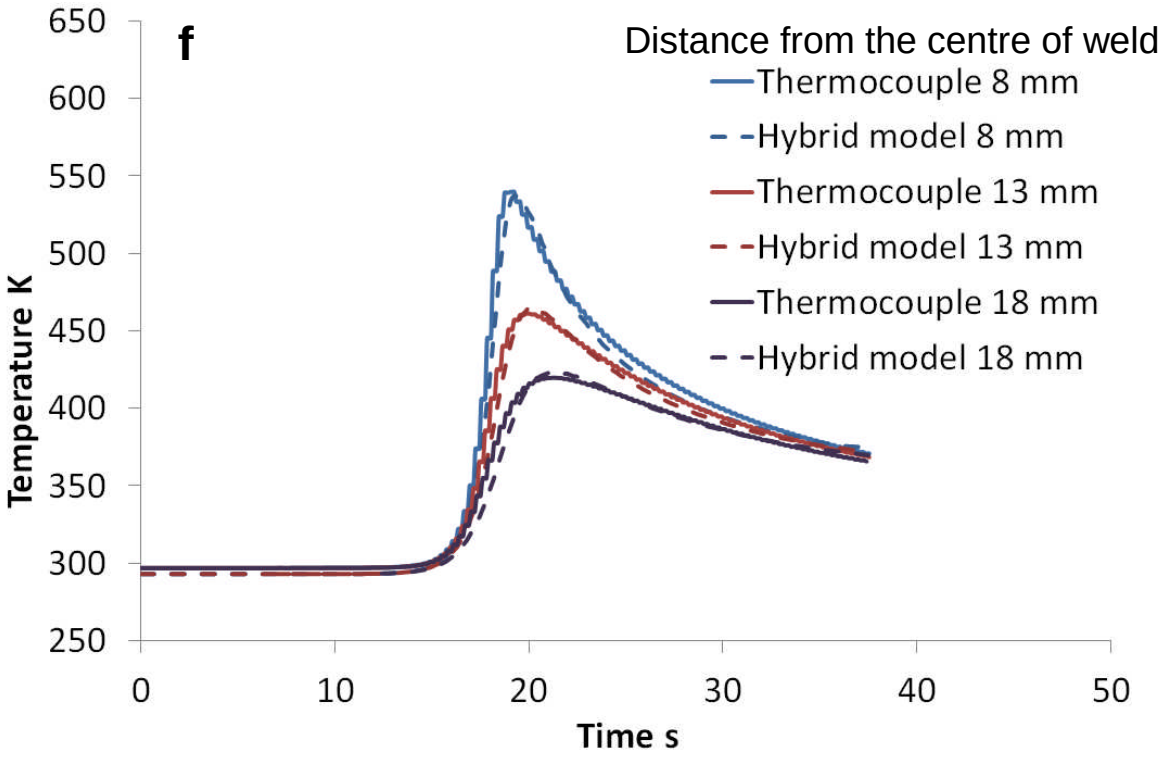

Figure 4-8: Comparison between hybrid model and experimental thermal profiles for travel speeds of a) 2 mm/s, b) 3 mm/s, c) 4 mm/s, d) 5 mm/s, e) 6 mm/s, and f) 8 mm/s

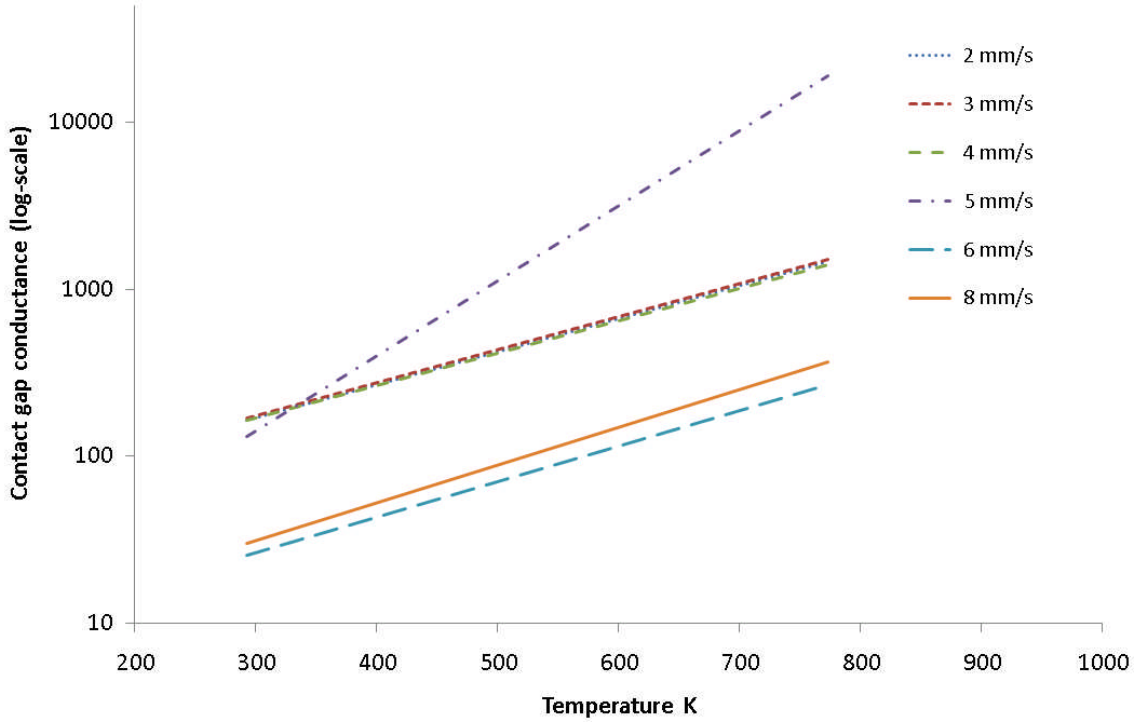

Figure 4-9: Predicted contact gap conductance vs. temperature. Note unit of the contact gap conductance is W/(m^{2}K)

The time taken to train the different hybrid models is shown in Table 4-6. Although the times are short compared with that required solving the FLUENT model, it is nevertheless worth noting that the GFF topology is the most time consuming due to its complicated structure. The preferred 4 input method takes considerably less time than the 9 input method and the 170 seconds required with the GFF topology is not considered onerous.

Temperature dependent models (unit: s)			
	MLP, LM	GFF, LM	MFF, LM
9 input	64	1011	204
6 input	43	330	146
4 input	34	170	120

Table 4-6: The training time consumption for each types of model

4.6.2 Investigation into variable fitting constants

Colegrove et al.[14] has shown that it is possible to find a universal set of fitting constants that suit all welding parameters. The previous section found that the fitting constants depended on the travel speed. These values are now averaged across the travel speeds and applied to each of the welds, and the quality of the fit is determined. The average values are shown in Table 4-5. The averaged CSRR value is very close to the one discovered by Colegrove and Shercliff[7].

The comparison plots are shown in Figure 4-10 and the numerical discrepancies between the modelling and experimental results are shown in Table 4-7. The predictions for the 2, 5 and 8 mm/s welds (Figure 4-10(a), (d) and (f)) are reasonably good with the difference in the peak temperature being less than 16 K. The 4 and 6 mm/s models (Figure 4-10(c) and (e)) have under-predicted the experimental results, while the 3 mm/s model (Figure 4-10(b)) has over-predicted the experimental results.

Travel speed	Peak temperature discrepancies	Imprint of stir region into plate
2 mm/s	- 16 K	0.21 mm
3 mm/s	26 K	0.105 mm
4 mm/s	- 32 K	0.325 mm
5 mm/s	- 12 K	0.20 mm
6 mm/s	- 39 K	0.27 mm
8 mm/s	10 K	0.20 mm

Table 4-7: Discrepancy in the peak temperature (positive means over-prediction and negative under-prediction) between the experimental and predicted thermal curves with averaged fitting coefficients, and measured imprint of the stir region into the plate

One of the reasons for variability in thermal measurements between nominally identical welding conditions is the plunge depth or the plunge force (depending on whether the FSW machine works in force or displacement control). Tang et al.[29] has shown that the temperature increases with plunge depth. The Flexi-stir machine used displacement control and different values were used for different welding conditions. To understand the variation in displacement between the welds, the imprint of each weld into the plate was measured as shown in Figure 4-11. Note that considerable deformation occurs under the weld due to the copper backing bar used for Flexi-stir machine (see Figure 4-3). The imprints were measured on both sides of the weld stir region, and the values averaged. These values are summarised in Table 4-7.

The results show that where there was a good temperature prediction, (2, 5 and 8 mm/s) the imprint depth is approximately 0.20 ± 0.01 mm. For 3 mm/s weld, the temperature was over-predicted by the model and the imprint was only 0.105 mm. This indicates that during the welding process, the tool position was higher compared to those with an imprint of 0.2 mm. Hence the contact between the shoulder and the material was poorer, leading to less heat generation. This was also reflected in a lack of fusion defect for this weld.

For the 4 and 6 mm/s models, the temperature values were under-predicted by the model. The imprint depths were 0.325 and 0.27 mm, for these welds indicating that the tool plunged further into the material. This leads to better contact with the material and a greater heat generation. Hence the model underpredicted the temperature.

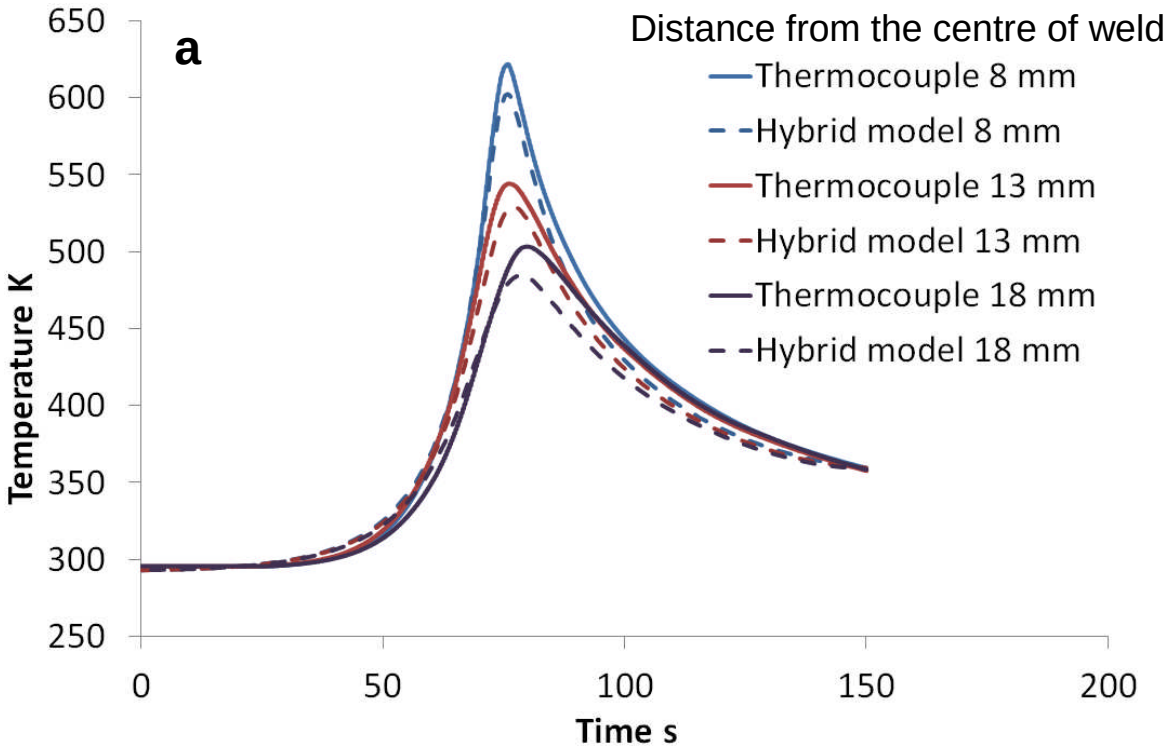

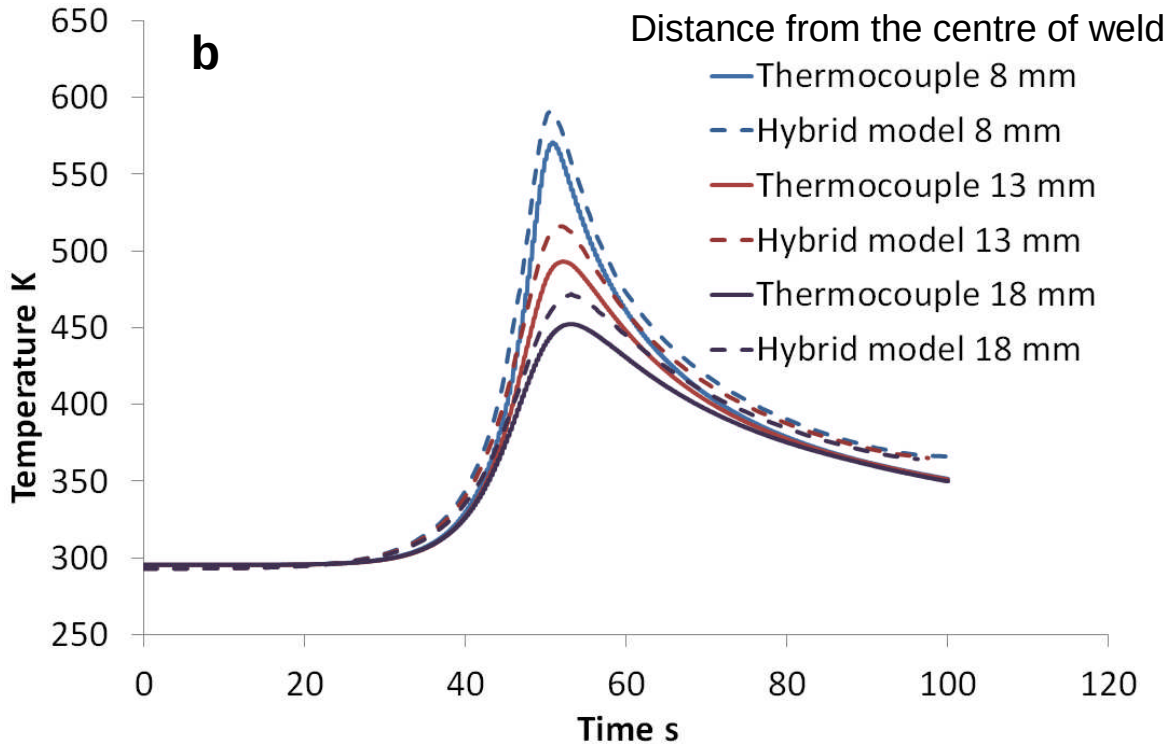

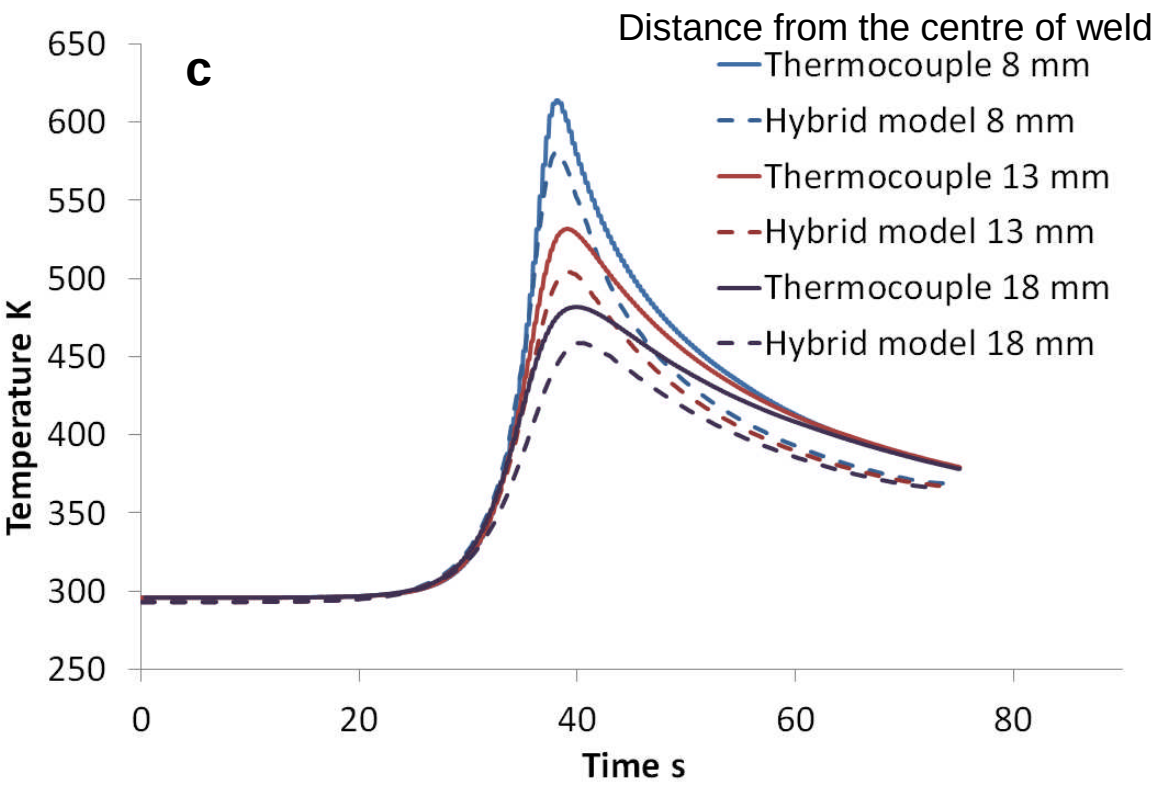
c
Distance from the centre of weld
Thermocouple 8 mm
Hybrid model 8 mm
Thermocouple 13 mm
Hybrid model 13 mm
Thermocouple 18 mm
Hybrid model 18 mm
Temperature K
650
600
550
500
450
400
350
300
250
0
20
40
60
80
Time s

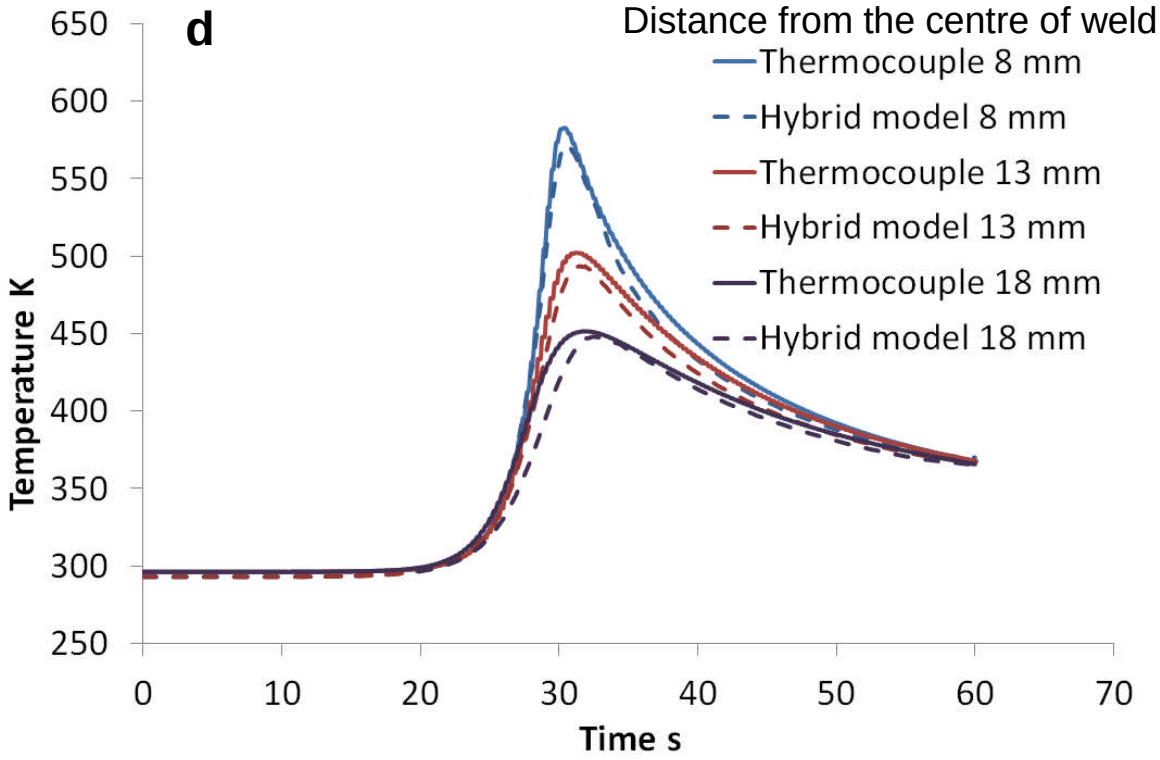
d
Distance from the centre of weld
Thermocouple 8 mm
Hybrid model 8 mm
Thermocouple 13 mm
Hybrid model 13 mm
Thermocouple 18 mm
Hybrid model 18 mm
Temperature K
650
600
550
500
450
400
350
300
250
0
10
20
30
40
50
60
70
Time s

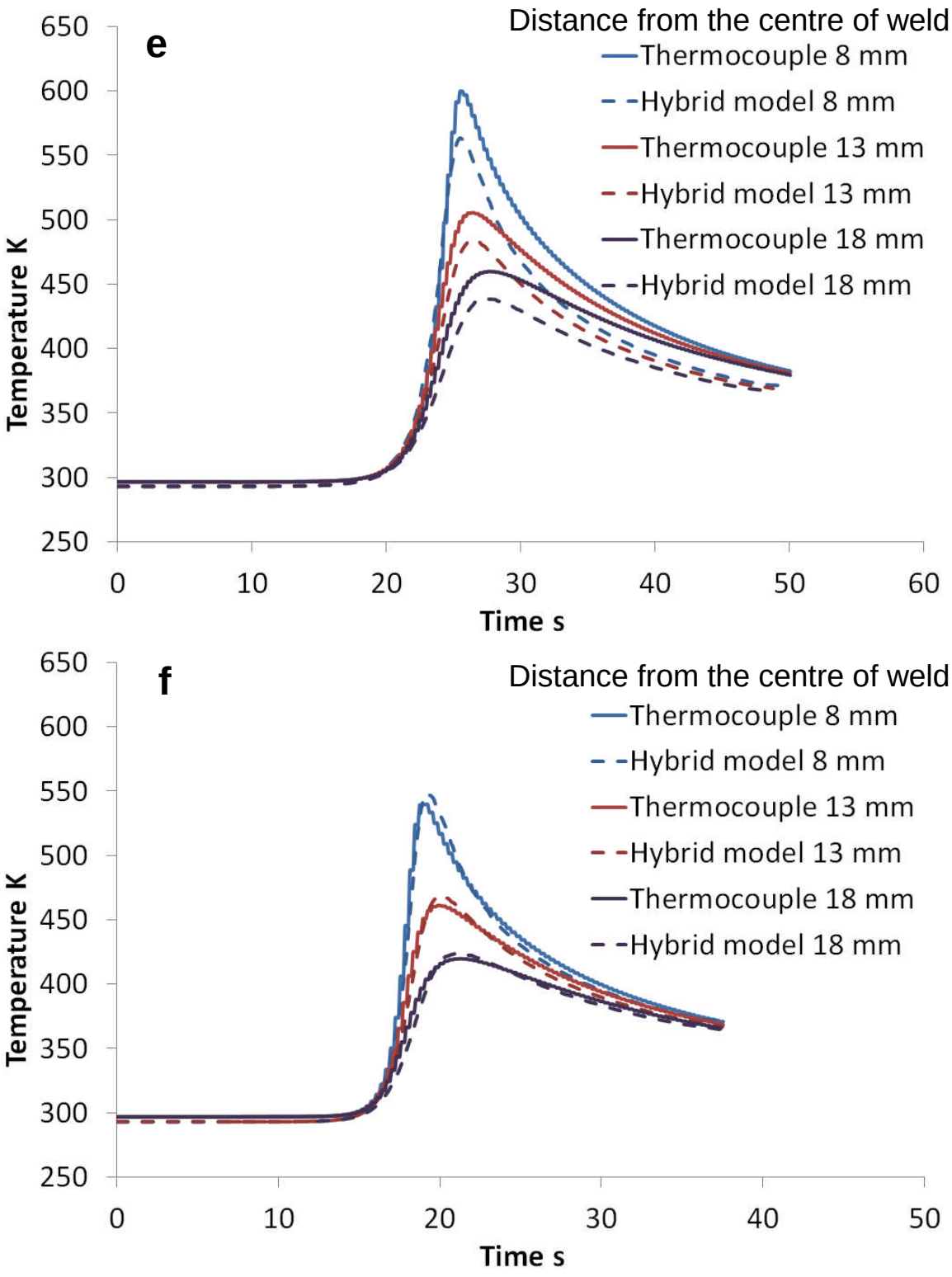

Figure 4-10: Comparison between hybrid model using averaged coefficients and experimental thermal profiles for travel speeds of a) 2 mm/s, b) 3 mm/s, c) 4 mm/s, d) 5 mm/s, e) 6 mm/s, f) 8 mm/s

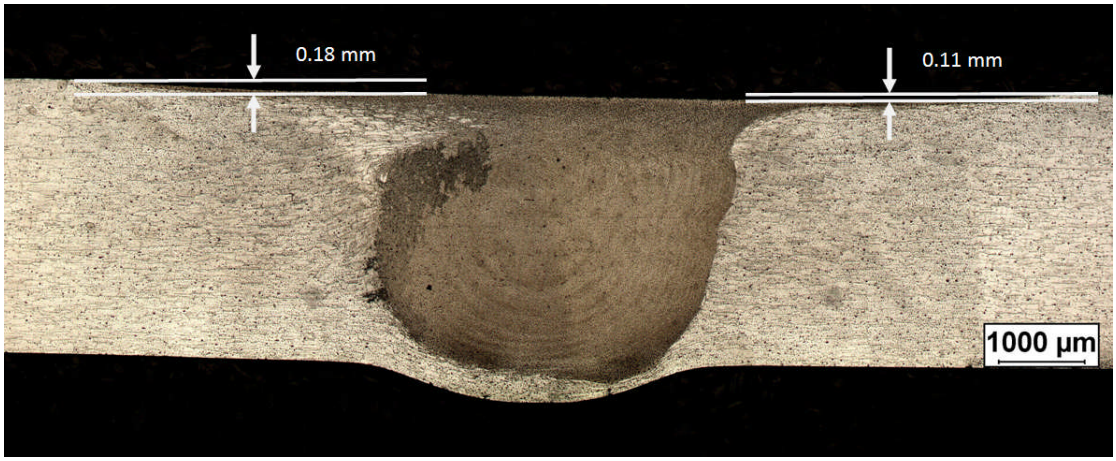

Figure 4-11: Measurement of the imprint of the FSW tool into the workpiece material. This particular macro is from the 3 mm/s travel speed weld

4.7 Conclusions

A hybrid model of FSW was developed by combining a process model with an ANN model. The technique was used to investigate the thermal boundary condition at the interface between the workpiece and backing bar, as well as the CSRR. It was demonstrated that:

- The hybrid model was able to predict suitable values for temperature dependent thermal boundary condition parameters and the CSRR.
- A GFF topology for the ANN with 4 abstracted inputs based on the integrated temperature and the cooling slope gave the best prediction of the experimental values.
- The analysis indicated that the CSRR and the thermal boundary conditions were not independent of each other. Hence a high CSRR could be balanced by a high heat loss to the backing bar.
- Although the initial analysis indicated that it was not possible to find a universal set of fitting parameters for these welds, further analysis indicated that the variability could be explained with variation in the plunge depth which was reflected in the weld imprints.

References

1. S. S. Sablani: 'A neural network approach for non-iterative calculation of heat transfer coefficient in fluid-particle systems', *Chemical Engineering and Processing: Process Intensification,* 2001, 40, 363-369.

2. S. Sreekanth, H. S. Ramaswamy, S. S. Sablani and S. O. Prasher: 'A neural network approach for inverse heat transfer problems', *American Society of Mechanical Engineers National Heat Transfer Conference Baltimore MD 1997,* 2005, .

3. D. Weiss, K. H. Christensen, and J. K. Kristensen: 'Computerised calibration of thermal welding models' *Mathematical modelling of weld phenomena 8,* 469-484, 2007.

4. A. Kumar and T. DebRoy: 'Neural network model of heat and fluid flow in gas metal arc fillet welding based on genetic algorithm and conjugate gradient optimisation', *Science and Technology of Welding and Joining,* 2006, 11, 106-119.

5. P. A. Colegrove and H. R. Shercliff: 'Experimental and numerical analysis of aluminium alloy 7075-T7351 friction stir welds', *Science and Technology of Welding and Joining,* 2003, 8, 360-368.

6. Sheikhi S., Zettler R., Beyer M., Roos A., Loitz H., dos Santos J.F.: Vorrichtung zum Reibrührschwei-ßen: 102005029882.6 (DE), and Vorrichtung und Verfahren zum Reibrührschweißen: 102005029881.8 (DE), Patent Applications (‘FlexStir’) 2005.

7. P. A. Colegrove and H. R. Shercliff: 'CFD modelling of friction stir welding of thick plate 7449 aluminium alloy', *Science and Technology of Welding and Joining,* 2006, 11, 429-441.

8. J. P. Holman: 'Heat Transfer', 6th edition, 1986, New York, McGraw-Hill Book Co.

9. Ø. Grong: 'Metallurgical modelling of welding', *Book.Second Edition.Publ: London SW1Y 5DB, UK; Institute of Materials; 1997.ISBN 1-86125-036-3*.

10. H. Yüncü: 'Thermal contact conductance of nominaly flat surfaces', *Heat Mass Transfer*, 2006, 43, 1-5.

11. Q. Shi, T. Dickerson and H. R. Shercliff: 'Thermomechanical FE modeling of friction stir welding of Al-2024 including tool loads', *Proceedings of 4th International Friction Stir Welding Symposium*,Park City, Utah, USA, 2003.

12. W. M. Rohsenow and J. P. Hartnett: *Handbook of Heat Tranfer*, 1973.

13. D. Zhu, L. Zhang, J. Pei, G. Zhang and R. Wei: 'Experiment research on the thermal contact conductance during the solid plastic forming', *Suxing Gongcheng Xuebao/Journal of Plasticity Engineering*, 2008, 15, 92-96.

14. P. A. Colegrove, H. R. Shercliff and R. Zettler: 'Model for predicting heat generation and temperature in friction stir welding from the material properties', *Science and Technology of Welding and Joining*, 2007, 12, 284-297.

15. M. Z. H. Khandkar, J. A. Khan and A. P. Reynolds: 'Prediction of temperature distribution and thermal history during friction stir welding: Input torque based model', *Science and Technology of Welding and Joining*, 2003, 8, 165-174.

16. Y. J. Chao and X. Qi: 'Thermal and thermo-mechanical modeling of friction stir welding of aluminum alloy 6061-T6', *Journal of Materials Processing and Manufacturing Science*, 1998, **7**, 215-233.

17. A. Askari, S. Silling, B. London and M. Mahoney: ' Modeling and analysis of friction stir welding processes', Friction Stir Welding and Processing, 2001, 43-54.

18. H. Schmidt and J. Hattel: ' CFD modelling of the shear layer around the tool probe in Friction Stir Welding', *Friction Stir Welding and Processing III - Proceedings of a Symposium sponsored by the Shaping and Forming Committee of (MPMD) of the Minerals*, Metals and Materials Society, TMS, 2005, 225-232.

19. H. Schmidt and J. Hattel: 'A local model for the thermomechanical conditions in friction stir welding', *Modelling and Simulation in Materials Science and Engineering,* 2005, 13, 77-93.

20. A. Moal and E. Massoni: 'Finite element simulation of the inertia welding of two similar parts', *Engineering Computations*, 1995, 12, 497-512.

21. B. C. Liechty and B. W. Webb: 'Modeling the frictional boundary condition in friction stir welding', *International Journal of Machine Tools and Manufacture 48* (12-13), pp. 1474-1485.

22. H. Zhang, Z. Zhang, J. Bie, L. Zhou and J. Chen: 'Effect of viscosity on material behavior in friction stir welding process', *Transactions of Nonferrous Metals Society of China (English Edition),* 2006, 16, 1045-1052.

23. Z. Zhang and J. T. Chen: 'The simulation of material behaviors in friction stir welding process by using rate-dependent constitutive model', *Journal of Materials Science,* 2008, 43, 222-232.

24. C. M. Sellars and Tegart, W. J. Mc. G.:' Hot Workability', *International Metals Review*, 1972, 17, 1-24.

25. R. Carmona, Q. Zhu, C. M. Sellars and J. H. Beynon: 'Controlling mechanisms of deformation of AA5052 aluminium alloy at small strains under hot working conditions', *Materials Science and Engineering A,* 2005, 393, 157-163.

26. V. M. Sample, G. L. Fitzsimons and A. J. DeArdo: 'Dynamic softening of copper during deformation at high temperatures and strain rates', *Acta Metallurgica,* 1987, 35, 367-379.

27. H. Wang, P. Colegrove, H. M. Mayer, L. Campbell, and R. D. Robson: *Advanced Materials Research,* 2010, vol. 89-91, 615.

28. M. H. Hassoum: 'Fundamentals of artificial neural networks', *Mit Press, Cambridge,* 1995.

29. W. Tang, X. Guo, J. C. McClure, L. E. Murr and A. Nunes: 'Heat input and temperature distribution in friction stir welding', *Journal of Materials Processing and Manufacturing Science,* 1998, **7**, 163-172.

CHAPTER 5

Friction Stir Welding Models with Stick and Slip Boundary Conditions

5.1 Introduction

One of the major issues in the process modelling of the FSW is determining the contact condition at the interface between the workpiece and welding tool. The experiments by Valberg and Malvik[1] showed that within the extrusion process which has similar characteristics to FSW, the contact is incomplete, which meant that both sticking and slipping conditions existed on the die. North et al.[2] proved that during FSW of some high strength aluminium alloys, the peak temperature may reach the solidus, which will lead some materials into the liquid phase weakening the contact and resulting in slipping of the workpiece material, against the tool.

Some modelling work[3-5] applied slip boundary condition to models, to investigate the partially sticking/slipping phenomenon during the process. Palm et al.[3] calculated a friction coefficient from the material yield stress and temperature to determine the frictional heat generation. Vilaça et al.[4] also applied a friction coefficient at the shoulder interface to work out the temperature at the shoulder surface. In the fluid dynamics based modelling work by Colegrove and Shercliff[5], the slip boundary condition was determined from the local wall shear stress at the tool interface. The model results were used to select a better welding pin profile. Schmidt et al.[6] used a dimensionless slip rate to calculate the relative velocity of the material at the tool interface, and the value was used to find out the slip condition at the interface. The material's yield stress was used to find the heat generation. Schmidt and Hattel[7] applied a value of friction coefficient on a fully contacted tool shoulder. Although the simulation was close to the reality, it was difficult to find a universal constant to implement this imperfect contact. Hamilton et al.[8] improved the slip factor method by Nandan et al.[9] to calculate the peak temperature during the FSW. Liechty and Webb[10] compared a stick model and a slip model with variable shear stress, which came to the conclusion that the slip model can predict much

better results than the stick one, particularly when the slip model assumed that the maximum velocity of the interface material was 9% of the local rotational speed.

The objective of this work is to investigate the influence of applying slip and stick boundary conditions to a FSW process model. The different models compare the heat generation, temperature and material flow around the tool. The FSW process has many unknowns, which are difficult to calculate and/or determine. Therefore this section investigates a series of boundary conditions and their effect on the heat generation and temperature and comments are made as to whether such conditions are likely to exist in practice.

5.2 Methodology

5.2.1 Material properties

Two types of aluminium alloy materials were studied in this work, 6082-T6 and 7449-T7, and the thermal properties of the materials used in the FSW model are shown in Table 4-1. This includes the workpiece aluminium alloys, the backing bar steel and the welding tool steel. Constant values of thermal conductivity have been used.

Material name	Density ($kg \cdot m^{-3}$)	Specific heat ($J \cdot kg^{-1} \cdot K^{-1}$)	Thermal conductivity ($W \cdot m^{-1} \cdot K^{-1}$)
7449-T7 aluminium workpiece	2840	860	154
6082-T6 aluminium workpiece	2710	894	172
Backing bar steel (0.5% C steel) at 150°C	7833	465	40
H13 tool steel (5% chrome) at 300°C	7833	460	36

Table 5-1: Thermal properties[11,12] of the materials used in the FSW process model

One of the most important factors in the model is the constitutive law used to describe flow stress of the workpiece material. This work uses the Zener-Holloman law proposed by Sellars and Tegart[19], and the corresponding material constants are from previous experimental work in chapter 2 of this thesis that involved Gleeble testing. In all cases the effective viscosity (μ) of the deforming material is calculated from

$$\mu = \frac{\sigma}{3 \cdot \bar{\dot{\varepsilon}}} \qquad \text{Eq. 5-1}$$

The viscosity is a key input parameter to the CFD flow simulation. The effective viscosity is implemented in FLUENT using a User Defined Function (UDF).

5.2.2 FSW model

The model used for researching different interface boundary conditions is a three-dimensional fully coupled process model, developed with the FLUENT CFD solver, and is similar to one developed by Colegrove and Shercliff[20]. This model was able to predict heat generation and the resulting thermal field from the tool and plate dimensions, materials thermal properties and material constitutive behaviour. This model was experimentally validated against a series of welding experiments performed at HZG. The work presented in this chapter uses this same experimentally validated model as the basis for the investigation into stick and slip boundary conditions. The workpiece geometry, tool size and boundary conditions are identical to this model. The essential details are repeated here. In order to have a more rapid solution for analysis, a steady state model was developed. The geometry of the model is demonstrated in Figure 5-1. As shown in Figure 5-1(a) and (b), the aluminium workpiece is divided into two parts:

1. The liquid aluminium region in the centre area, in which both the momentum and heat equations are solved

2. The solid aluminium regions in the area far away from the welding tool. Since the material flow is negligible, only the heat equation is solved.

The dimensions of the welding tool are shown in Figure 5-1(c), and tool profile was not included in this modelling work.

The concept of the contact gap conductance was used to describe the heat transfer between the workpiece and the backing bar due to the imperfect contact. Two areas of contact gap conductance are included in the model. As shown in Figure 5-2, the centre light blue area is defined as the welded area which has a higher contact gap conductance (25000 $Wm^{-2}K^{-1}$) due to the softened material and normal pressure from the tool during

the welding process; alternatively the light yellow area has a lower value (200 $Wm^{-2}K^{-1}$) since the contact condition here is poorer since the material in this region is not processed against the backing bar by the shoulder. The backing bar in the area coloured white was not modelled, so the heat loss is represented by a convective heat transfer coefficient which is equal to 100 $Wm^{-2}K^{-1}$. A vacuum backing bar was used in this area in the experiments upon which this model was based[20]. The heat loss from the top and side of the workpiece to the environment was described as convectional with a coefficient of 10 $Wm^{-2}K^{-1}$. The heat loss from the bottom of the backing bar to the welding table was also simplified as convectional with a coefficient of 1000 W $m^{-2}K^{-1}$, and the side of the backing bar was set to an adiabatic condition.

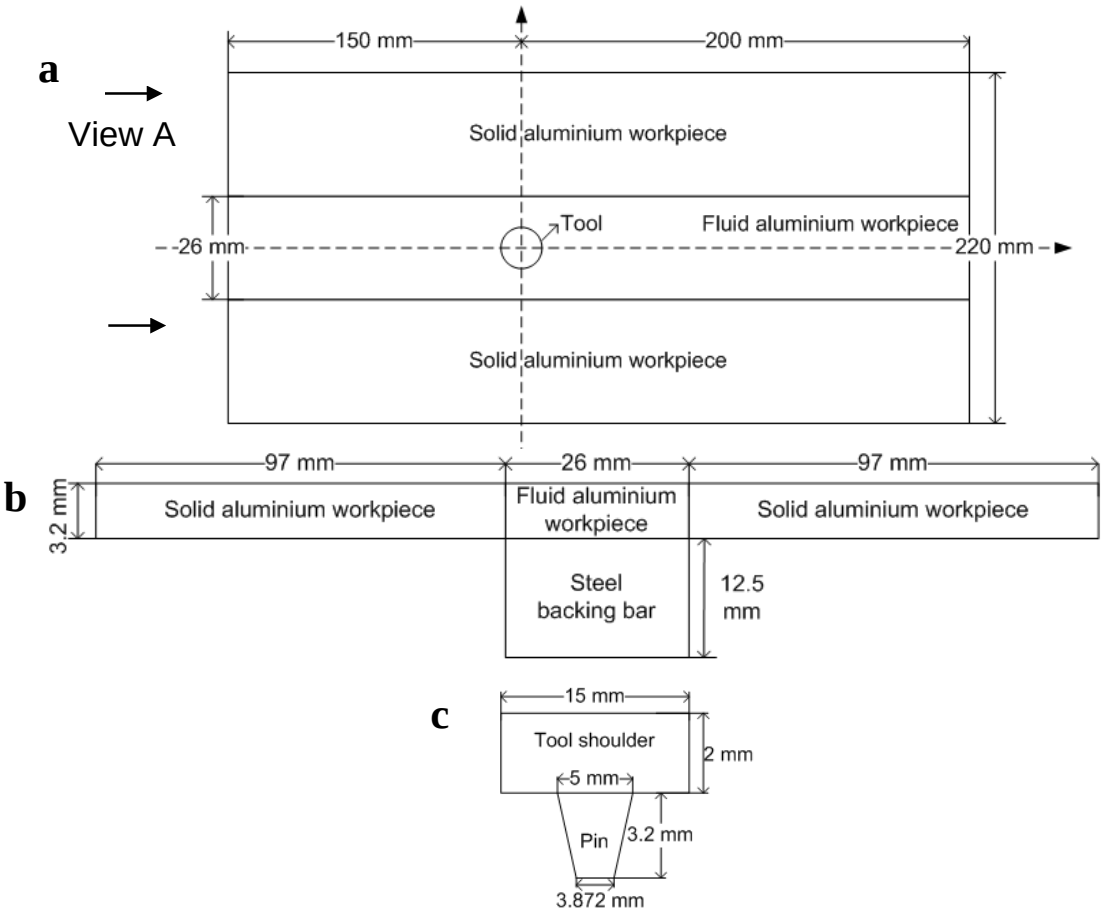

Figure 5-1: Diagram of the geometry used for the FLUENT model: a) top-view and b) end view (view A from (a)) and c) the welding tool

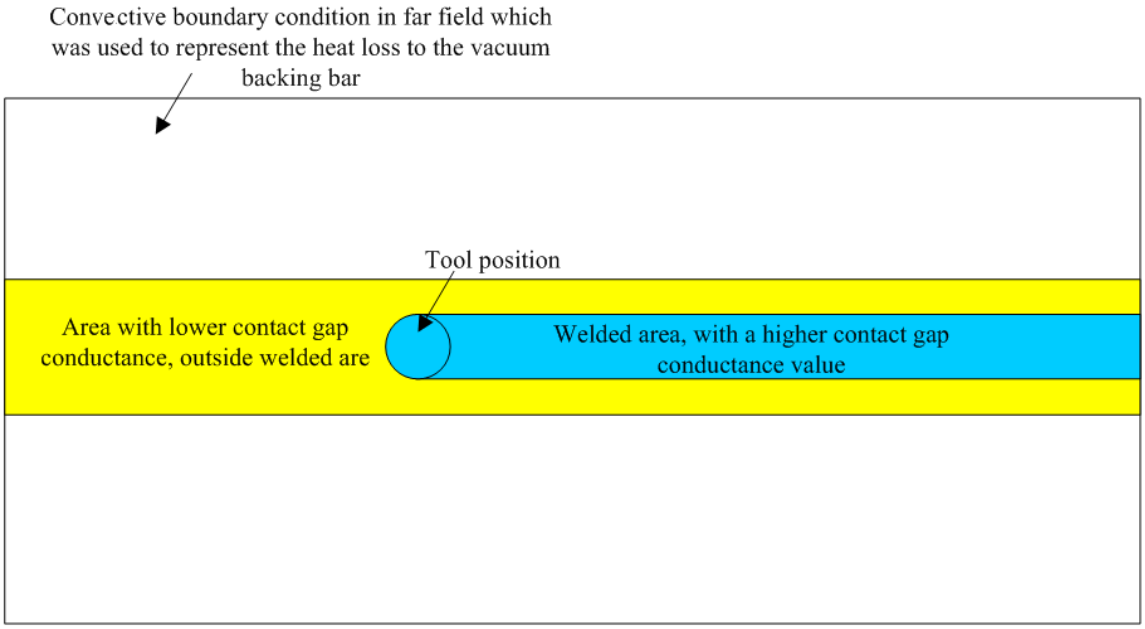

Figure 5-2: Top view of the boundary conditions used between the workpiece and backing bar

5.2.3 Interface boundary conditions

Two types of boundary conditions were applied at the interface between the workpiece and welding tool: stick and slip. The slip boundary condition was implemented with a slip coefficient θ, which was used by Schmidt et al.[6]. The slip coefficient is the ratio of the speed of the workpiece material at the tool interface to the rotational speed of the tool. It was assumed uniform over the surface of the tool, which was in contact with the workpiece material. The flow field was calculated from the slip coefficient with the velocity of material (in unit of m/s) at the tool interface defined as:

$$\frac{2\omega \cdot r \cdot \pi \cdot \theta}{60} \qquad \text{Eq. 5-2}$$

where r is the radius and ω is the rotation speed of the tool in unit of rpm.

The viscous heat generation in both the stick and slip models is given by:

$$S_h = \nabla \cdot (\tau \cdot v) \qquad \text{Eq. 5-3}$$

where S_h is the viscous heat generation, v is the velocity, τ is the stress tensor given by

$$\tau = \mu\left(\nabla v + \nabla v^T\right) \qquad \text{Eq. 5-4}$$

where μ is the viscosity calculated from flow stress and strain-rate as shown in equation 5-1.

The amount of viscous heat generation is obviously smaller with the slip model due to the different flow field, which results from using the slip coefficient. In the slip model, the frictional heat generation was given by governed by the slip velocity multiplied by the wall shear stress:

$$q = \frac{(1-\theta)\cdot 2\cdot \omega \cdot r \cdot \pi}{60} \cdot \sigma_{wall} \qquad \text{Eq. 5-5}$$

where θ is the slip coefficient, ω is the rotation speed in rpm, r is the local radius and σ_{wall} is the magnitude of the shear stress at the interface. Unlike many models which implement a slip boundary condition, the shear stress was calculated from the flow prediction, i.e. the slip coefficient at the wall was used to calculate the flow field which was used to calculate the wall shear stress. Once again this was implemented in FLUENT using a user sub-routine. As the thermal and flow field were coupled, it was necessary to iterate the solution until convergence was achieved. It should be noted that the temperature affects the flow strength of the material, which affects both the viscous heat generation and wall shear stress, which both affect the material temperature. Note that one issue encountered during FSW flow modelling is the generation of excessive heat as will become apparent in this analysis. Some authors have addressed this issue with a factor for thermal efficiency[22]. While it is clear how this applies in arc welding where there are radiation losses, it is not clear how such a term may applied in FSW where all thermal losses are accounted for. Hence no efficiency term was used in the current modelling work.

5.2.4 Model types

The FSW process has many unknowns, which are difficult to calculate and/or determine. Therefore this section investigates a series of boundary conditions and their effect on the heat generation and temperature and comments are made as to whether such conditions are likely to exist in practice.

To compare the influence of stick and slip boundary conditions, 8 different model types were investigated, which are summarised in Table 5-2. Apart from the model type 7 and 8, the conditions were applied to both 6082-T6 and 7449-T7. A travel speed of 8 mm/s was used for all welds with a rotation speed of 400, 600, 800 and 1200 rpm. In some of the model types, the CSRR method was applied, which assumed reduced shoulder contact with the workpiece material. This was used in the previous chapter. As stated in Colegrove et al.[12] the reasons for including the CSRR with a stick model are twofold:

1. Firstly there is often incomplete contact between the shoulder of the FSW tool and the workpiece material.
2. A slip condition may exist between the workpiece material and the tool. Since determining the slip conditions is difficult, it was expedient to include any such effects within a single adjustable parameter: the CSRR.

This section aims to investigate this parameter in greater depth and in particular to compare models where it is and is not included.

The different model types are summarised as follows:

1. Model type 1 was a full stick condition model. The heat generation was 100% viscous and it was used to investigate the amount of heat generation without taking into account softening or slip. There was full contact between the deforming material and the shoulder (CSRR = 100%).
2. Model type 2 was full stick with softening, to find out the reduction in heat generation by applying the softening regime to the constitutive behaviour. There was full contact with the shoulder.
3. Model type 3 applied a slip boundary condition which was adjusted so that the heat generation was identical to the equivalent model type 2 where softening occurred. The material strain-rate and deformation region around the welding tool was investigated to find the difference between stick (model type 2) and slip (model type 3) models.
4. Model type 4 was a stick condition model where the CSRR was applied. The CSRR selected was 68.4%, which was identical to the value used by Colegrove and Shercliff[20]. This model was compared to model type 1 to find the heat generation reduction by applying the CSRR.

5. Model type 5 was identical to model type 4, however the softening regime was included in the material constitutive behaviour to further limit the heat generation. It is important to note that this model type was identical to the one used by Colegrove et al.[12] to predict the heat generation in FSW. The model was experimentally validated in this publication.
6. Model type 6 was similar to model type 5, however a slip condition was used instead of material softening. The heat generation was adjusted so that it was the same as model type 5, and the model was used to investigate the difference between stick and slip boundary conditions.
7. Model type 7 was only applied to 7449-T7, and the same boundary conditions as those applied to the 6082-T6 model type 3 were used. This model type was used to determine the differences between the two materials.
8. Model type 8 was only applied to 7449-T7, and the same boundary conditions as those applied to the 6082-T6 model type 6 were used. This model type was used to determine the differences between the two materials.

Model type	Contact condition	CSRR	Softening	Comment
1	Stick	100%	No	
2	Stick	100%	Yes	
3	Slip	100%	No	Heat input matches equivalent model type 2
4	Stick	68.4%	No	
5	Stick	68.4%	Yes	
6	Slip	68.4%	No	Heat input matches equivalent model type 5
7	Slip	100%	No	Only applied to 7449-T7. The slip coefficient is set so that it is identical to 6082-T6 model type 3.
8	Slip	68.4%	No	Only applied to 7449-T7. The slip coefficient is set so that it is identical to 6082-T6 model type 6.

Table 5-2: The summary of the model types applied in investigating the differences between the slip and stick boundary conditions

5.2.5 Comparison to experimental results

The slip boundary condition was applied to a 7449-T7 FSW process model described in chapter 4, to investigate whether the slip boundary condition is suitable for real welds. Model type 6 was applied. The CSRR and temperature dependent contact gap conductance variables applied were the ones demined in chapter 4, for each travel speed. The travel speeds for validating were 2, 3, 4, 5, 6 and 8 mm/s.

Similar to the models used in the rest part of this chapter, the heat generation in this model consists of viscous and slip. One small difference between this model and the one described previously is heat flow between the workpiece material and the pin had to be turned off due to a bug in the FLUENT software. This is a minor difference and it is not expected to have a significant effect on the result.

5.2.6 Analysis methods

To better understand how the material behaved with the various models, a streamline plot was generated along the centreline half way through the thickness (mid-plate 1.6 mm from the bottom of workpiece) and at the top of the workpiece plate (top-plate 3.2 mm from the bottom of workpiece). A diagram in Figure 5-3, shows a streamline travelling from the left of the workpiece, around the rotating welding tool and to the right. The ‘streamline 1’ from mid-plate and top-plate were used for analysis since they represent how the material flow behaves near the welding tool.

The deformation region for each model was found. This was defined as the area in the mid-plate where the material strain-rate value exceeded 2 s^{-1}. This strain-rate value is arbitrary and was selected to show the region where the strain-rate was significant. Note that behaviour of the material in a fluid flow model is different to the real material because the elastic properties are ignored. The area calculated excluded that of the pin.

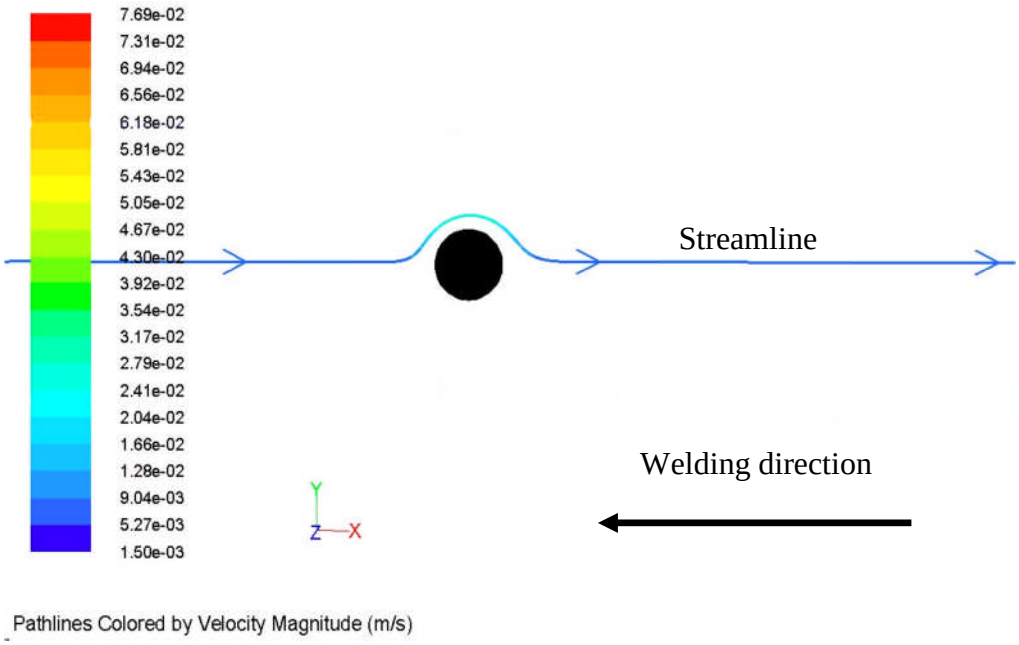

Figure 5-3: The diagram shows a streamline travelling past the modelling tool (the black object in the middle of the graph) at the mid-plate (1.6 mm from bottom of workpiece).

5.3 Results

A summary of the results is contained in Appendix D. For the stick models, the heat generation was purely viscous, and for slip models it was a combination of viscous and frictional. Graphs of the results are shown in the subsequent sections. It was not possible to find an equivalent slip model for all conditions, particularly for model type 3 with 7449-T7 and high rotation speeds. This was because the corresponding stick model had a low heat generation could not be matched with the lowest heat generation with the slip condition, i.e. even a slip coefficient of 0 did not produce the desired heat generation. The comparison of the results and analysis of each model type are given in the following sections.

5.3.1 Heat generation and slip conditions

Figure 5-4(a) shows the heat generation for model types 1, 2 and 3 as a function of the rotation speed. For 6082-T6, the heat generation of model type 1 and 2 are the same at a rotation speed 400 RPM, and as the rotation speed increases, the heat generation in model type 2 reached a plateau while model type 1 kept increasing. For 7449-T7, as the rotation speed increased, the heat generation in model type 1 increased, while the heat generation in model type 2 was mostly constant, as shown in Figure 5-4. The

continuous increase in the heat generation of model type 1 was because there was no softening in the material's constitutive behaviour (see Table 5-2). When applying the softening regime model type, the heat generation reached a plateau at high rotation speeds, which is similar to the real welds[12]. The reason for the plateau is well described in Colegrove and Shercliff[20], and is because of the limitation imposed by the solidus temperature where softening is included in the material's constitutive behaviour, i.e. increasing the rotation speed increases the amount of material softening and does not cause any additional heat generation. The lower flow strength of 6082-T6 compared to 7449-T7 is seen in the comparison of the heat generation with model type 1, i.e. much more heat is generated due to the greater flow strength. Where the heat generation is limited by the solidus temperature (model type 2), the model that used 6082-T6 showed greater heat generation due to the higher solidus temperature of this alloy.

Figure 5-4(b) gives the slip coefficients and the viscous and slip heat generation distribution for method 3. For 6082-T6, the slip coefficient reduced as the rotation speed increased, from nearly 1 to 0.125. The slip heat increased, and the viscous heat generation reduced. For 7449-T7, only one slip condition was solved which was for a rotation speed of 400 RPM, and the reason for which was described previously. With this condition, the slip coefficient was low (due to the high flow strength of the material) so most of the heat generation occurred at the surface due to the slip.

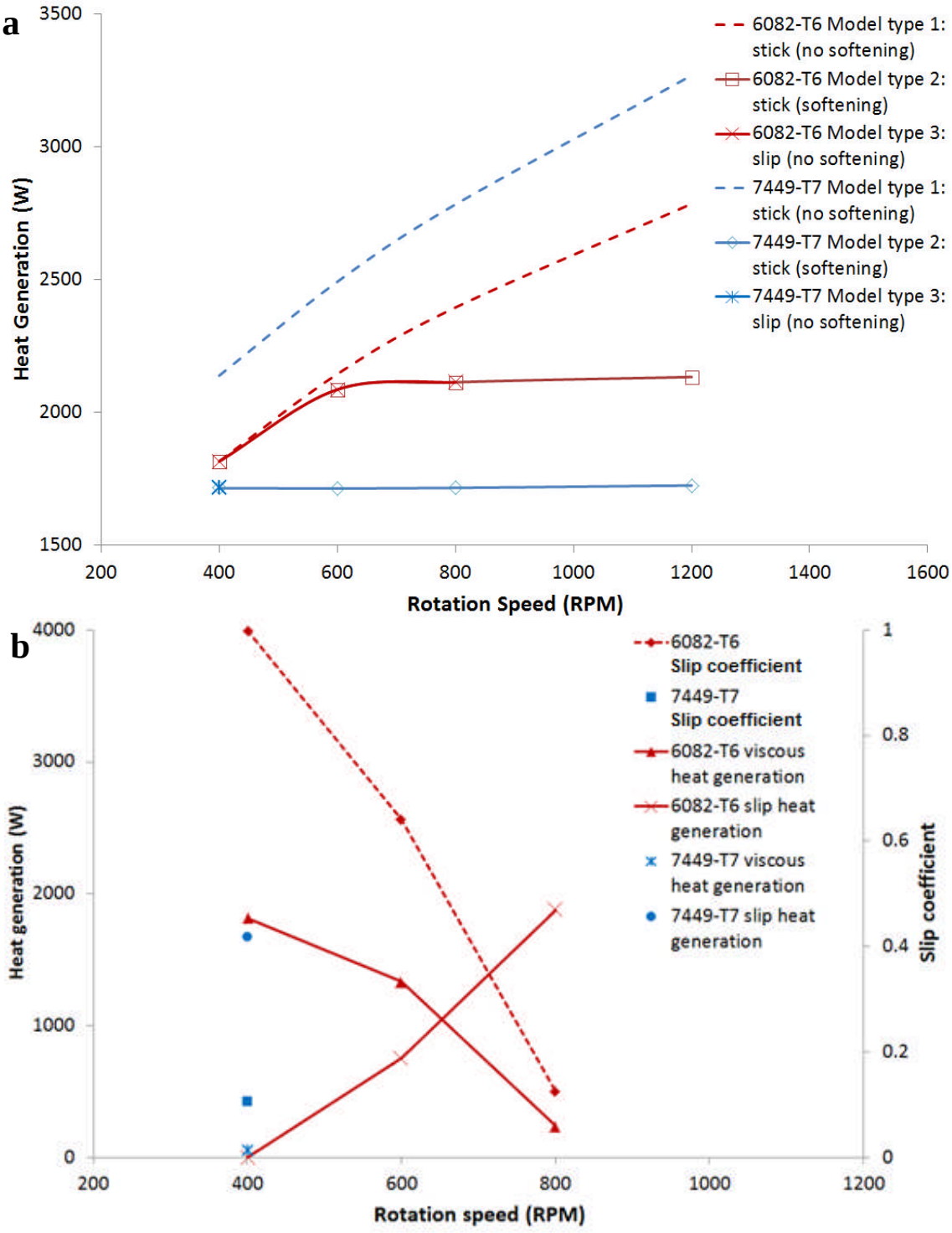

Figure 5-4: a) The total heat generation in model type 1, 2 and 3. Note that the heat generation for model type 3 is the same as model type 2 except where model type 3 could not be solved, and b) slip coefficient and distribution of heat for materials 6082-T6 and 7449-T7, with rotation speeds of 400, 600, 800 and 1200 RPM

Figure 5-5(a) shows the comparison of heat generation for model type 4 and 5. The use of the CSRR for these models resulted in a much lower total heat generation than the previous model types. For 6082-T6, the heat generation from model types 4 and 5 show very close agreement and increase as the rotation speed increased. At a rotation speed of 1200 RPM, the heat generation in model type 4 was slightly higher. For 7449-T7, as the rotation speed increases, the heat generation in model type 4 rises continuously, while the heat generation in model type 5 increased up to a rotation speed of 600 RPM and later became slightly lower, as shown in Figure 5-5. A plateau was reached in model type 5 with 7449-T7 as the rotation speed increased, due to the limitation in the material constitutive behaviour. However no plateau was observed in model type 5 with 6082-T6, and it indicates that apart from the 1200 RPM rotation speed the 6082-T6 was deformed without any softening (see Figure 5-5).

By comparing to the experimental results from Colegrove and Shercliff[20], for 6082-T6 the heat generation in model type 5 is most realistic, while the heat generation in model type 4 will overpredict the experimental values, as shown in Figure 5-6 most of the temperatures are over the solidus as the rotation speed passes 800 RPM.

Figure 5-5(b) gives the slip coefficients and the viscous and slip heat generation distribution with method 6. For 6082-T6, the slip coefficient was approximately 1 for the three lower rotation speeds and reduced to 0.62 at a rotation speed of 1200 RPM. The corresponding slip heat generations almost did not change until the rotation speed was set to 1200 RPM in which the slip heat increased significantly. The viscous heat generation increased from 400 to 800 RPM due to the higher rotation speed, but reduced dramatically beyond 1200 RPM due to the slip. For 7449-T7, three slip condition models were solved. Both the slip coefficient and viscous heat generation reduced as the rotation speed increased, while the slip heat generation increased.

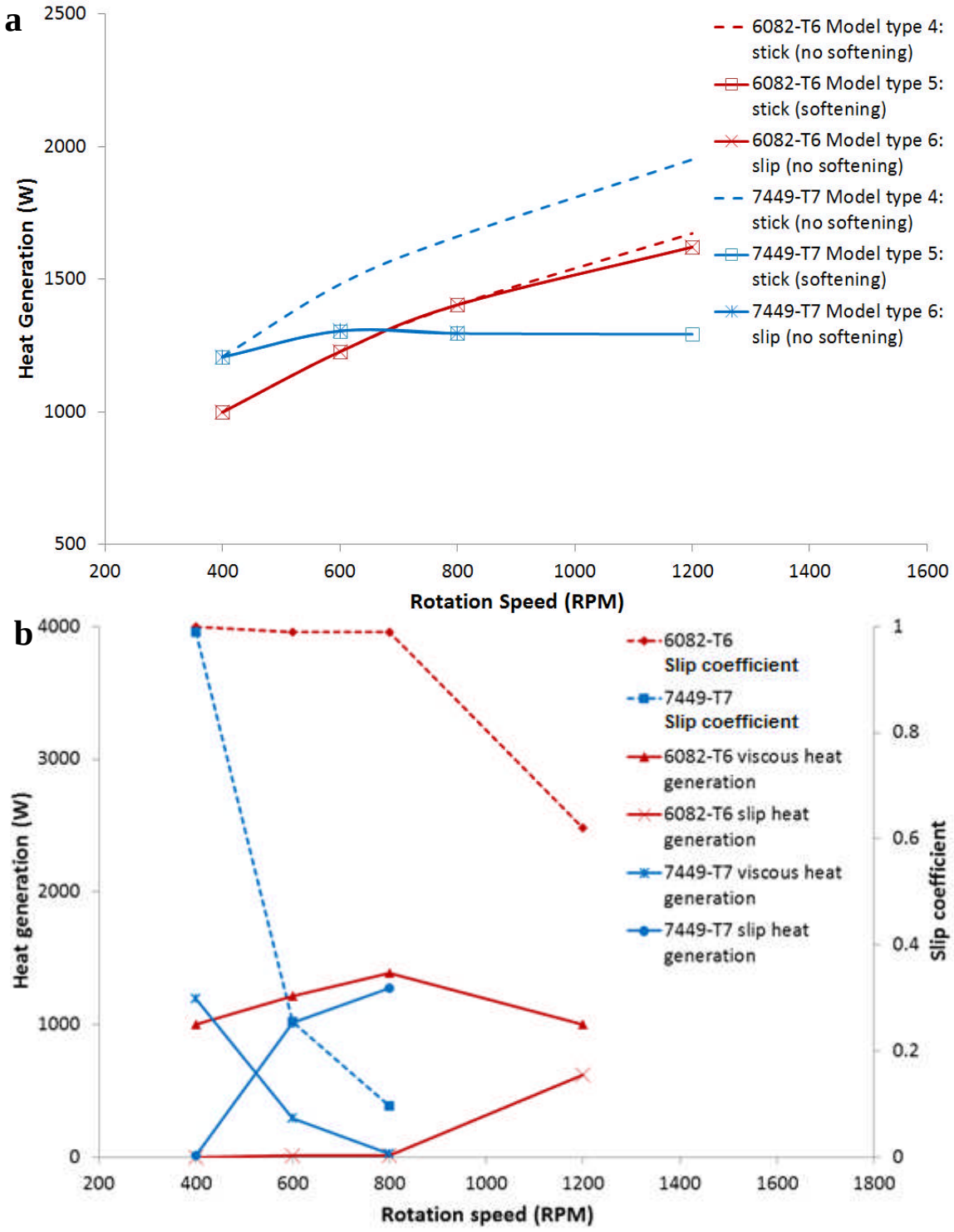

Figure 5-5: a) The total heat generation in model type 4, 5 and 6, note the filled markers represent the results for model type 6, and b) slip coefficient and distribution of heat for materials 6082-T6 and 7449-T7, with rotation speeds of 400, 600, 800 and 1200 RPM

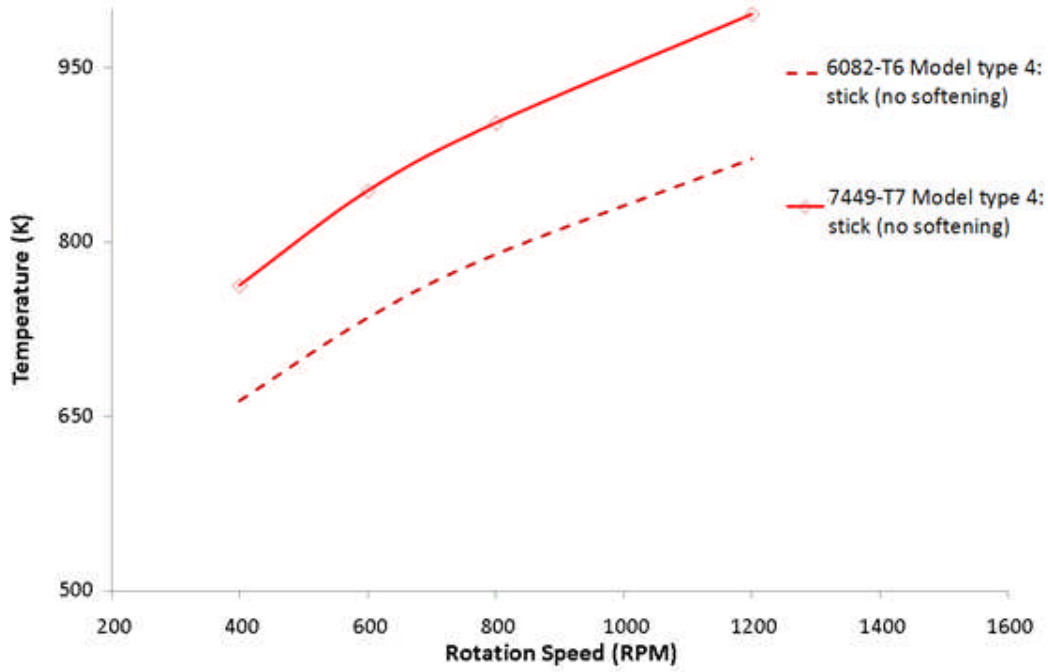

Figure 5-6: The peak temperature in model type 4 of 6082-T6 and 7449-T7, with rotation speeds of 400, 600, 800 and 1200 RPM

5.3.2 Comparisons between models that have full contact with the shoulder (model types 2 and 3)

5.3.2.1 6082-T6 models

The temperature plots for the mid-plate and top-plate streamlines are shown in Figure 5-7 for 6082-T6. Since the heat generations are the same, the temperature curves between the stick and slip models are mostly identical, apart from some discrepancies for the higher rotation speed in Figure 5-7(c) between the top-plate curves, and the reason for this will be explained later. The temperature values in the mid-plate curves are slightly lower than ones from the top-plate, and the temperature rises up as the rotation speed increases but not dramatically. This is due to the fact that applying softening regime in model type 2 restricts the peak temperature within the solidus, which is 848 K for 6082-T6.

Figure 5-8 gives the strain-rate comparisons, which show that the strain-rate values in the top-plate are much larger than ones in mid-plate, since the top-plate is adjacent to the rotating shoulder. For Figure 5-8(a), the strain-rate plots are identical because the

slip coefficient is 0.999 which means the boundary is almost a stick condition. The strain-rate plots from Figure 5-8(b) and (c) indicate that applying a slip boundary condition will significantly reduce the strain-rate. The results from the models that used a rotation speed of 600 RPM in Figure 5-8(b) show that the stick model top-plate strain-rate values are around 4800 s^{-1}, particularly in the middle of the curve. However in the corresponding slip model the strain-rate values are less than 3000 s^{-1}. In the stick model mid-plate the strain-rate values are around 100 s^{-1}, but ones from the slip condition are no more than 50 s^{-1}. Hence when the rotation speed is 600 RPM, the slip condition reduces the strain-rate nearly 50%. The reduction of strain-rate gets even more obvious as the rotation speed increases. In Figure 5-8(c), the stick model top-plate has the strain-rate values are more than 5000 s^{-1}, while the strain-rate values in the corresponding slip model are about 1000 s^{-1}. In the stick model mid-plate the strain-rate values are slightly more than 200 s^{-1}, but ones from the slip condition are no more than 20 s^{-1}. The strain-rate value with the slip condition is lower than the one from the 600 RPM models because the slip coefficient at 800 RPM (0.125) is lower than one at 600 RPM (0.64). In the 800 RPM case, the slip condition reduces the strain-rate nearly 80%, because of the lower slip coefficient.

In order to analyse the deformation region of each model, strain-rate clips have been applied at the middle of the plate around welding tool. The limiting value of the strain-rate clip is 2 s^{-1}. The area of the deformation region sizes are given in Figure 5-9(a). For 400 RPM models, because the slip model is nearly a stick condition, the deformation area is identical. For 600 and 800 RPM, the deformation areas in slip conditions are approximately 3% and 7% less respectively, compared to the stick models. Hence there is very little difference in the area deformed between the stick and slip models. The visual shapes of the deformation regions are illustrated in Figure 5-10. In the stick models, the material around the tool is deformed more uniformly. In the slip models more material is deformed on the retreating side. This is seen particularly in the 800 RPM case, because the low slip coefficient, the majority of the high strain-rate material is on the retreating side. As has been demonstrated in Figure 5-8, the magnitude of the strain-rate with slipping models is much lower. Therefore material movement around

the tool is more difficult, which may be one of the reasons for the greater deformation on the retreating side of the slip models.

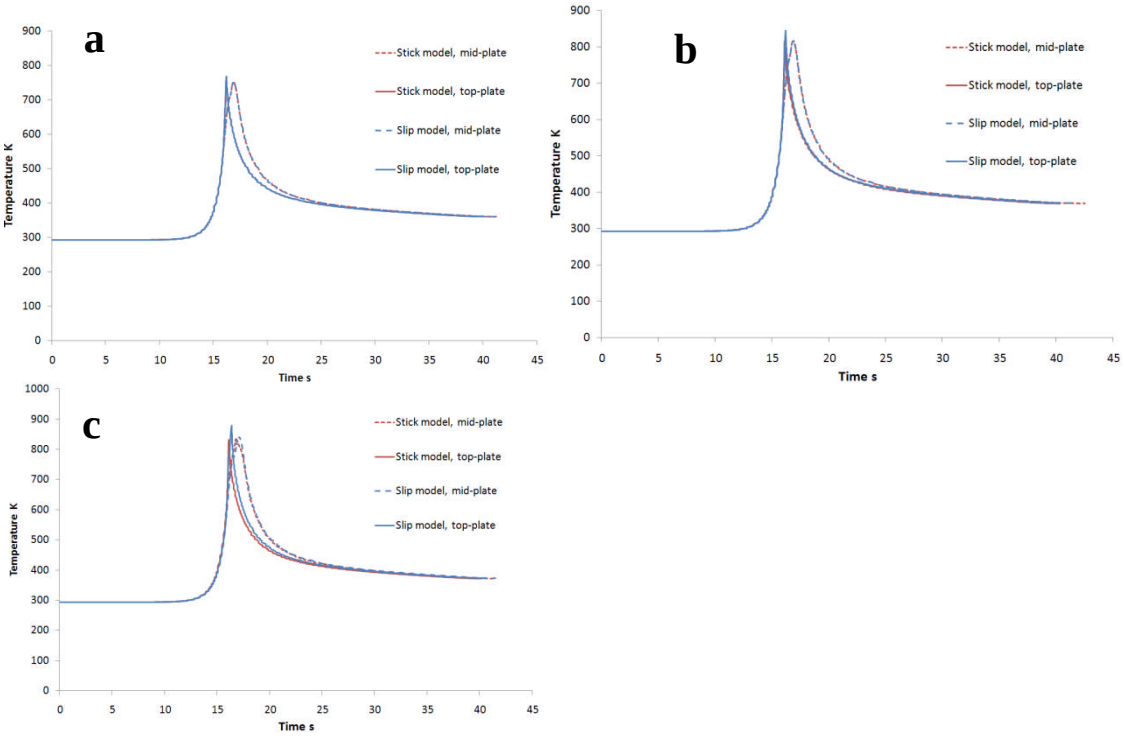

Figure 5-7: The temperature streamline plots of 6082-T6 models that use model types 2 and 3 with different rotation speeds of (a) 400 RPM, (b) 600 RPM and (c) 800 RPM, from mid-plate (1.6 mm from bottom of workpiece) and top-plate positions (3.2 mm from bottom of workpiece)

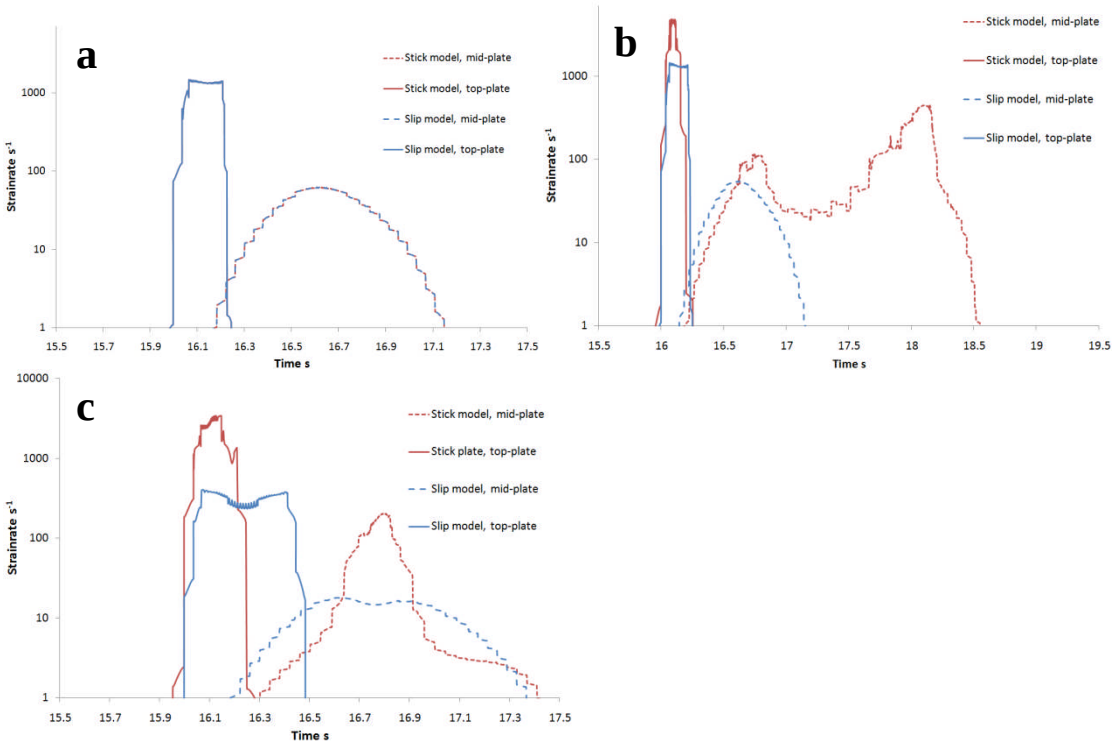

Figure 5-8: The strain-rate streamline plots of 6082-T6 models that use model type 2 and 3 with different rotation speeds of (a) 400 RPM, (b) 600 RPM and (c) 800 RPM, from mid-plate (1.6 mm from bottom of workpiece) and top-plate positions (3.2 mm from bottom of workpiece). Note the x-axis is taken from 15.5 to 17.5 second (19.5 for (b)) for a better observation of the curves, and the y-axis is in logarithmic scale

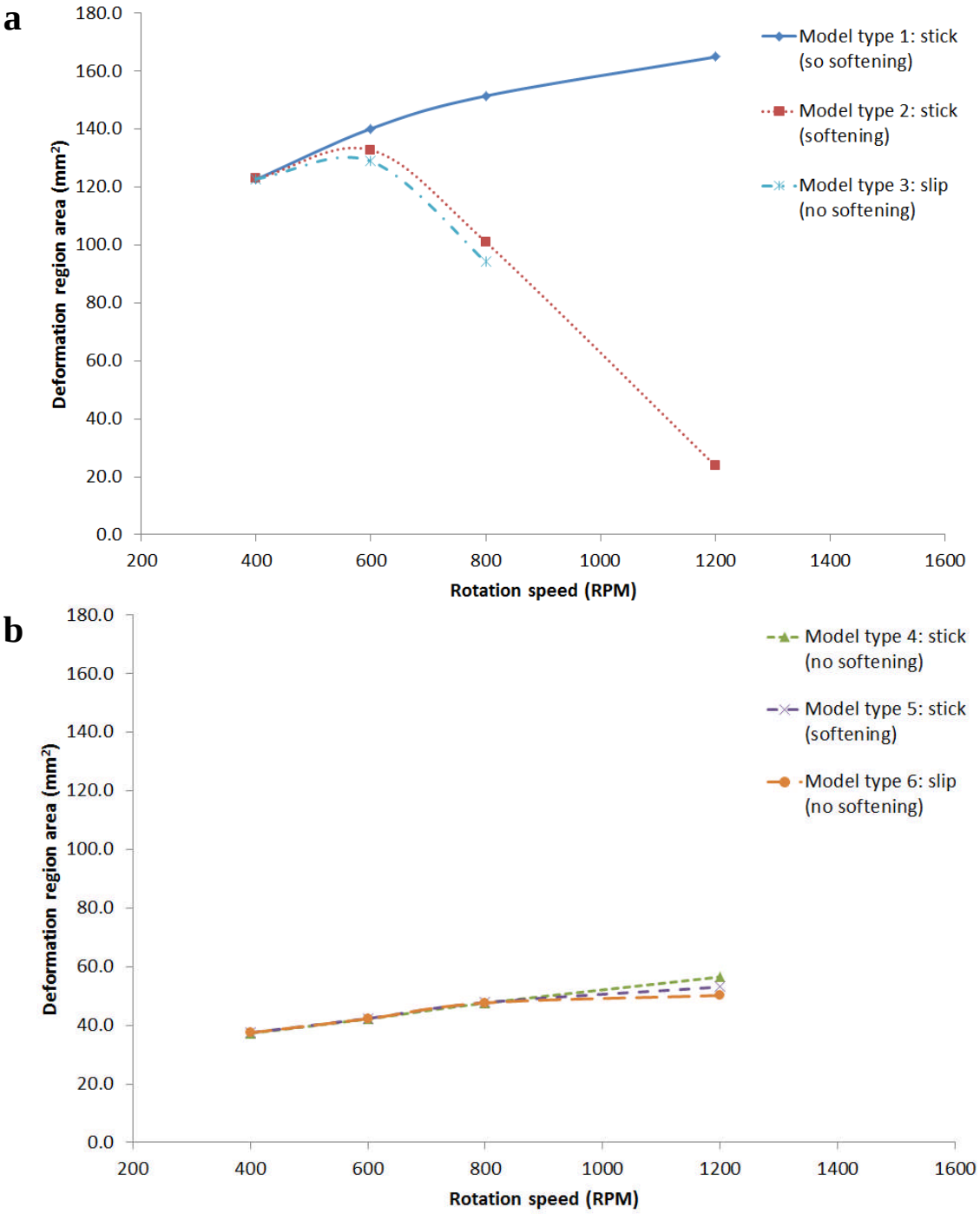

Figure 5-9: The deformation area plots vs. rotation speed for (a) model type 1, 2 and 3, and (b) model type 4, 5 and 6 in 6082-T6

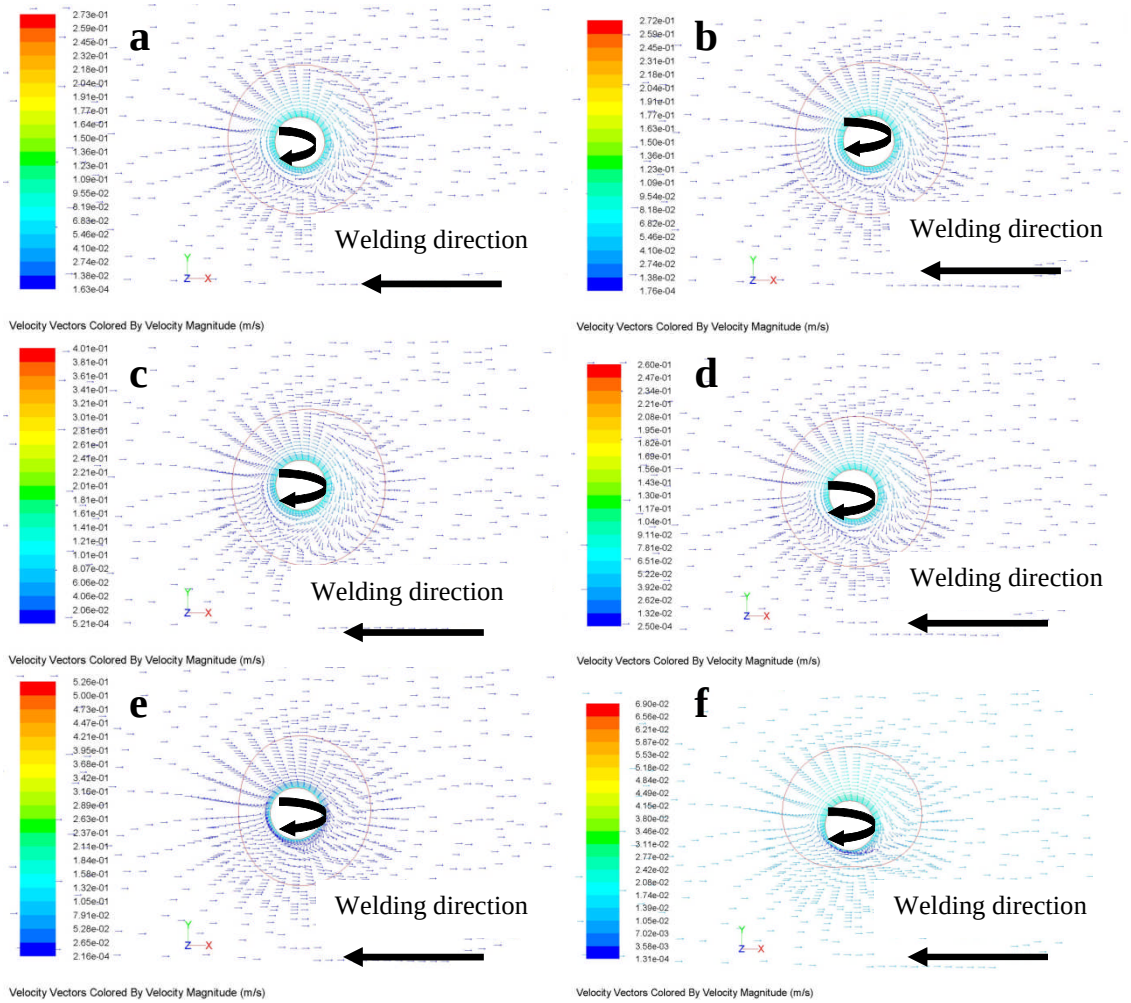

Figure 5-10: Velocity vectors and deformation regions on the mid-plate in 6082-T6 models with rotation speed and model type of (a) 400 RPM model type 2, (b) 400 RPM model type 3, (c) 600 RPM model type 2, (d) 600 RPM model type 3, (e) 800 RPM model type 2 and (f) 800 RPM model type 3. The tool rotation and welding directions are illustrated in the figures. Note the red boundary showing the deformation region size is for a strain-rate equal to 2 s^{-1}

5.3.2.2 7449-T7 models

As the 7449-T7 has been shown to be a harder material, only the lowest rotation speed of 400 RPM enabled a match between the model type 2 and 3, and the slip coefficient was very low (0.105). The temperature plots in Figure 5-11 show some discrepancies between the thermal curves although the power inputs are calculated to be the same. The reason for this is because in the slip model, most of the heat flux is generated at the shoulder interface rather than viscous heat generation (see Figure 5-12). In the model

type 2 (stick model) the temperature is limited by the solidus (773 K) due to the softening regime in the constitutive behaviour. The far field temperature plots in Figure 5-13 show that the temperature curves are very close which indicates the heat generation calculation is correct. This case represents that under low slip coefficient, since most of the friction heat is produced in the shoulder interface, the streamline temperature plot at the top-plate in slip model may be higher than the one from the corresponding stick model. As mentioned previously, this issue happened with the 800 RPM of 6082-T6 model.

As shown in Figure 5-14, the strain-rate in the top-plate from stick model is more than 2500 s^{-1}, and in the slip model it is about 460 s^{-1}. The strain-rate in the mid-plate from stick model is slight than 200 s^{-1}, and in the slip model it is about 16 s^{-1}. The strain-rate is reduced about 80% by introducing the slip condition. This ratio is close to the one from 800 RPM in 6082-T6 model, because their slip coefficient is very close. A comparison between the two materials is undertaken later in this chapter. A comparison between the deformation regions for the stick and slip models for 7449-T7 is shown in Figure 5-15. Unlike the 6082-T6 models, both the stick and slip models are deformed more on the retreating side, and the deformation area in the stick model is 52% smaller than one in slip model, as shown in Figure 5-16(a). In the slip model, there is also a low strain-rate region on the retreating side underneath the shoulder.

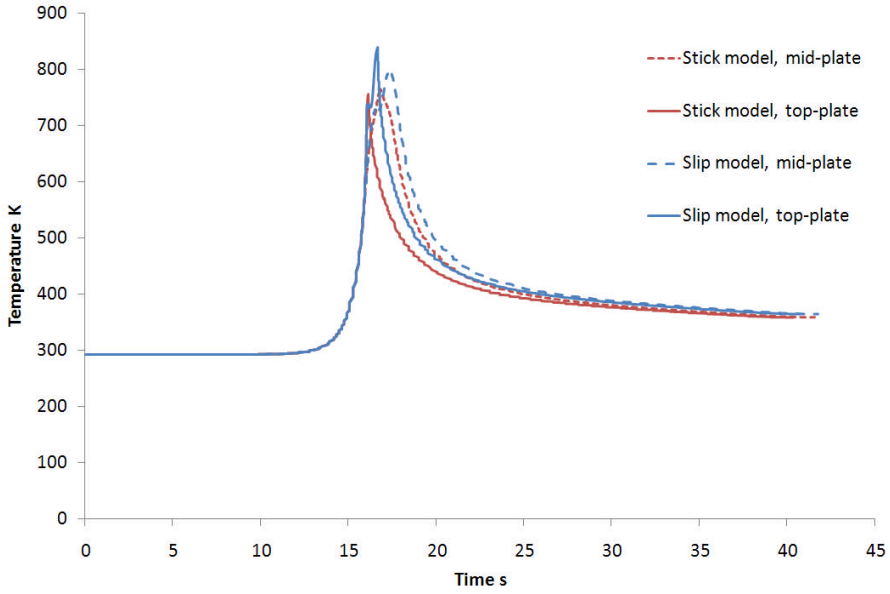

Figure 5-11: The temperature streamline plot of 7449-T7 models that use model types 2 and 3 with rotation speed 400 RPM, from mid-plate (1.6 mm from bottom of workpiece) and top-plate positions (3.2 mm from bottom of workpiece)

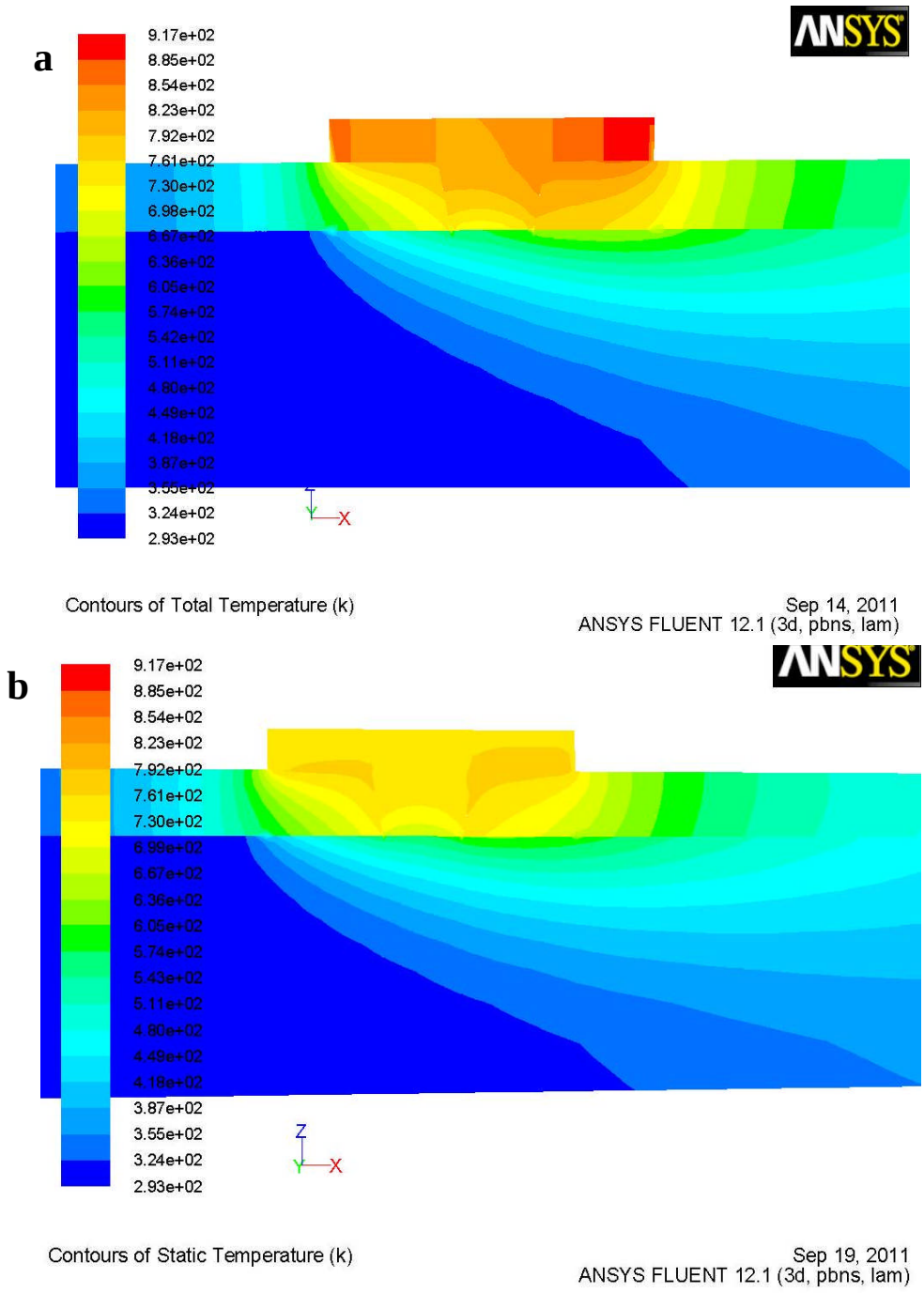

Figure 5-12: The temperature plot of 7449-T7 models with rotation speed 400 RPM for (a) model type 3 and (b) model type 2, this is the cross section along the welding direction.

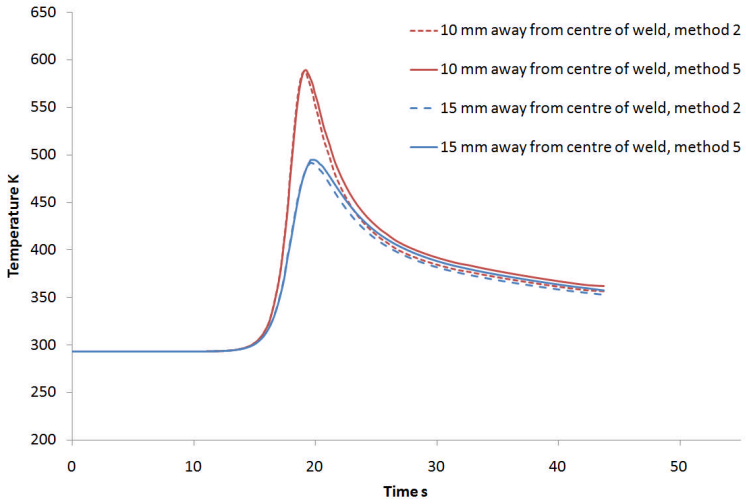

Figure 5-13: The temperature line plot of 7449-T7 models with rotation speed 400 RPM, the plot lines are 10 and 15 mm away from the centre of weld in model type 2 and 3

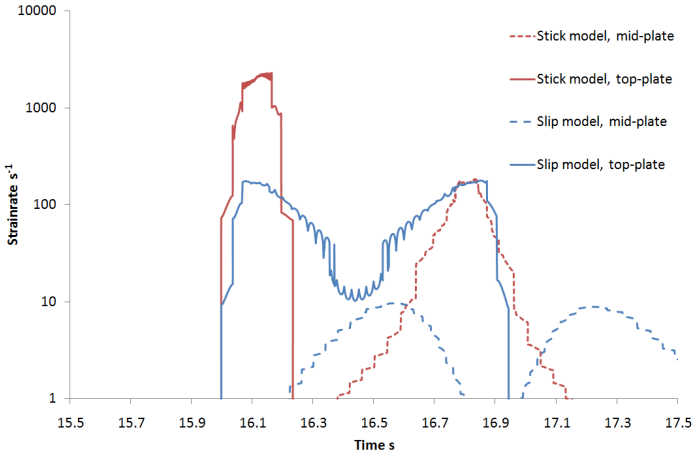

Figure 5-14: The strain-rate streamline plots of 7449-T7 models that use model types 2 and 3 with different rotation speeds of 400 RPM, from mid-plate (1.6 mm from bottom of workpiece) and top-plate positions (3.2 mm from bottom of workpiece). Note the x-axis is taken from 15.5 to 17.5 second for a better observation of the curves, and y-axis is in logarithmic scale

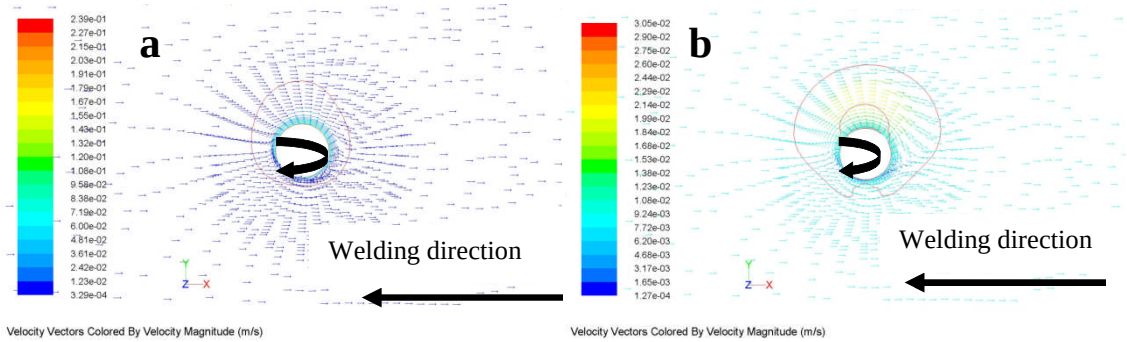

Figure 5-15: Velocity vectors and deformation regions on the mid-plate in 7449-T7 models with rotation speed and model type of (a) 400 RPM model type 2 and (b) 400 RPM model type 3. The tool rotation and welding directions are illustrated in the figures. Note the red boundary of deformation region is with the strain-rate that equals to $2s^{-1}$

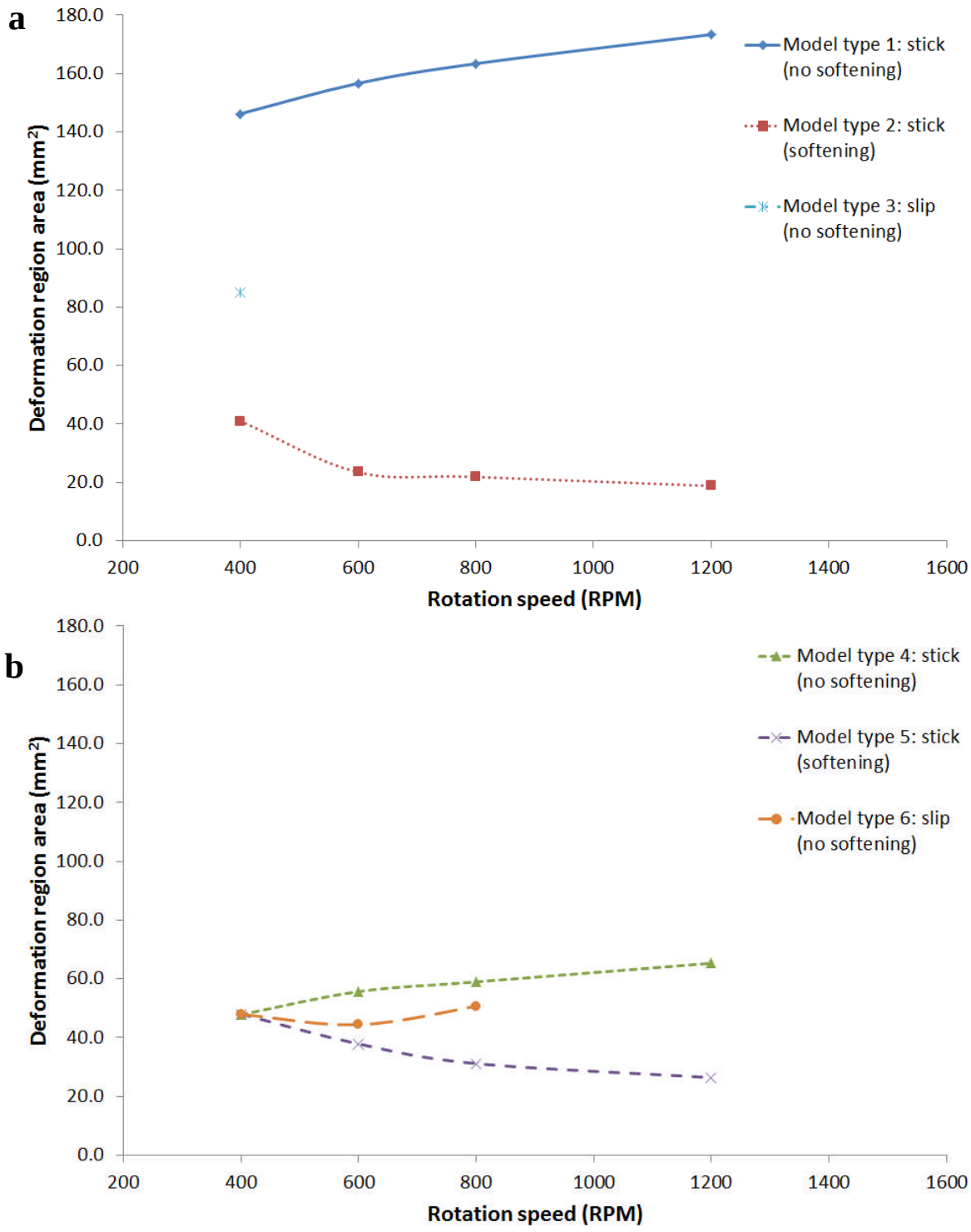

Figure 5-16: The deformation area plots vs. rotation speed for (a) model type 1, 2 and 3, and (b) model type 4, 5 and 6 in 7449-T7

5.3.3 Comparisons between models that use a CSRR (model types 5 and 6)

In model type 5 and 6, the CSRR was 68.4% which limited the heat generation, and makes it easier to find matching heat generations between the stick and slip models in both 6082-T6 and 7449-T7 cases. As shown in Appendix D, only the 7449-T7 stick model with 1200 RPM rotation speed did not find a slip model with the same heat generation.

5.3.3.1 6082-T6 models

As shown in Figure 5-17, the temperature curves between the stick and slip models are mostly identical. The temperature values in the mid-plate curves are slightly lower than ones from the top-plate, and the temperature increased as the rotation speed increased. These changes in temperature reflect the changes in power which were observed in Figure 5-5(a).

Figure 5-18 shows the strain-rate comparisons between different model conditions. In 400, 600 and 800 RPM cases, the slip coefficients are 0.999, 0.99 and 0.99 respectively, the slip coefficient is very high and the models are basically a stick condition. In these cases, the strain-rate curves for the stick and slip models are almost identical. As shown in Figure 5-18(d), in the top-plate of the 1200 RPM model, the stick model produced about 7000 s^{-1} while the slip model does 4000 s^{-1}. In the mid-plate of the 1200 RPM, the strain-rate in the stick model is about 300 s^{-1}, while the slip model is about 200 s^{-1}. The reduction ratio is about 40%, which is a reflection of the slip coefficient which is 0.62.
The area of the deformation region sizes are given in Figure 5-9(b). For 400, 600 and 800 RPM models, because the slip models are nearly in stick condition, the deformation areas are identical. For 1200 RPM model, the deformation areas for the slip conditions are approximately 6% less than the stick one. The visual shapes of the deformation regions are illustrated in Figure 5-19. Since the strain-rate field in 400, 600 and 800 RPM are identical, the visual deformation regions are identical. However in 1200 RPM case, as shown in Figure 5-19(g) and (h), slightly more materials is deformed behind the welding tool in the stick model, while the high strain-rate materials are more uniformly distributed in the slip condition.

5.3.3.2 7449-T7 models

In the comparison of model type 5 and 6 for 7449-T7 models, the introduction of the CSRR, enable equivalent slip models (model type 6) to be found for three rotation speeds. The resulting temperature plots are given in Figure 5-20, which show that the temperature increases as the rotation speeds rises from 400 to 600 and 800 RPM. The temperature differences between the mid-plate and top-plate are small. Most of the temperature curves of corresponding stick and slip models are identical, apart from the 800 RPM case. As discussed previously, due to the low slip coefficient and softening regime in the stick condition, there are some slight discrepancies between thermal curves in the stick and slip model, as shown in Figure 5-20(c).

The resulting strain-rate curves are shown in Figure 5-21. Since with a rotation speed of 400 RPM, the slip coefficient is 0.99 which means the slip model is basically in a stick condition, the strain-rate curves are identical between the stick and slip, as shown in Figure 5-21(a). For 600 and 800 RPM, the strain-rate is largely reduced by including the slip condition. In Figure 5-21(b) top-plate, the strain-rate is reduced from 3000 s^{-1} to 1000 s^{-1}, and in the mid-plate the reduction is from 400 s^{-1} to 50 s^{-1}. The reduction ratio is approximately 67% in top-plate and 87% in mid-plate. In Figure 5-21(c) top-plate, the strain-rate is reduced from 4000 s^{-1} to 500 s^{-1}, and in the mid-plate the reduction is from 720 s^{-1} to 20 s^{-1}. The reduction ratio is approximately 87% in top-plate and 97% in mid-plate. The increase in the reduction ratio is due to the reduction of slip coefficient from 0.255 in 600 RPM model to 0.096 in 800 RPM model.

As discussed previously, for 7449-T7 models the deformation areas in stick models are smaller than ones in the slip models as shown in Figure 5-16(b). In the 400 RPM case the deformation area are the same for stick and slip models; in the 600 RPM case the deformation area in stick model is 15% less; and in the 800 RPM case the deformation area in stick model is 38% less. The visual deformation region graphs in Figure 5-22 show that in both stick and slip cases more material is deformed on the retreating side of the weld. In the slip model of 800 RPM, because of the low slip coefficient, there is a low strain-rate region near the advancing side of the pin underneath the shoulder.

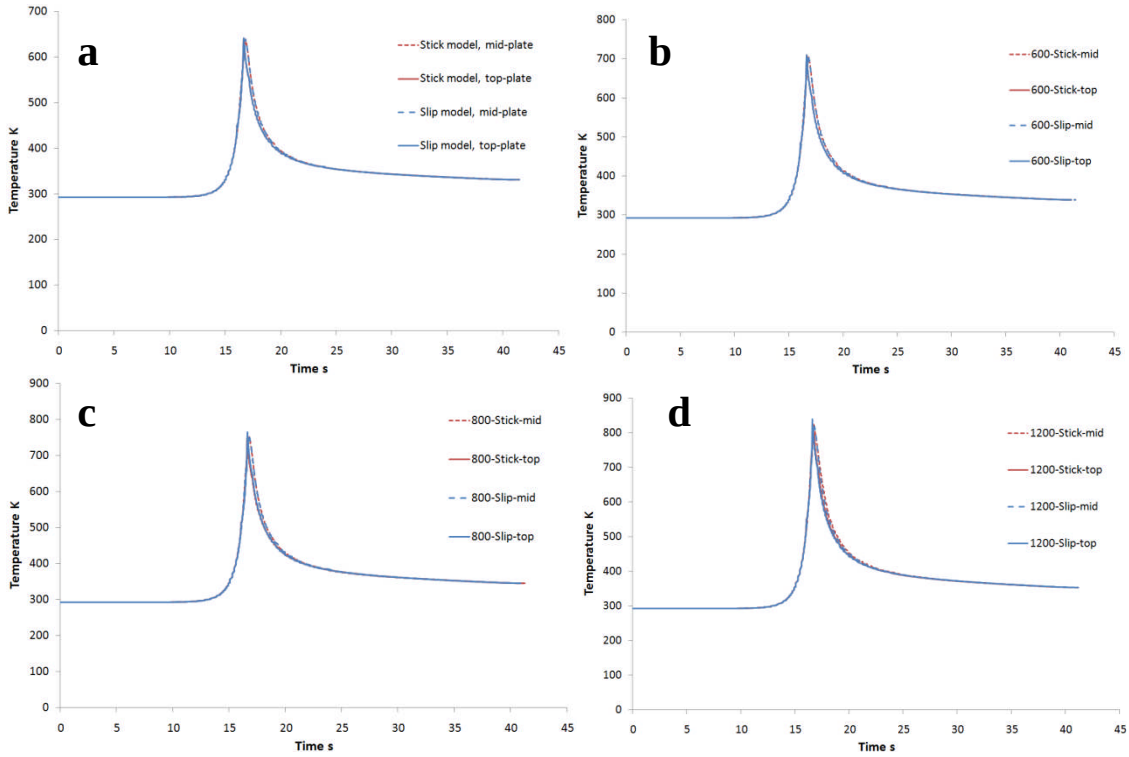

Figure 5-17: The temperature streamline plots of 6082-T6 models that use model types 5 and 6 with different rotation speeds of (a) 400 RPM, (b) 600 RPM, (c) 800 RPM and (d) 1200 RPM, from mid-plate (1.6 mm from bottom of workpiece) and top-plate positions (3.2 mm from bottom of workpiece)

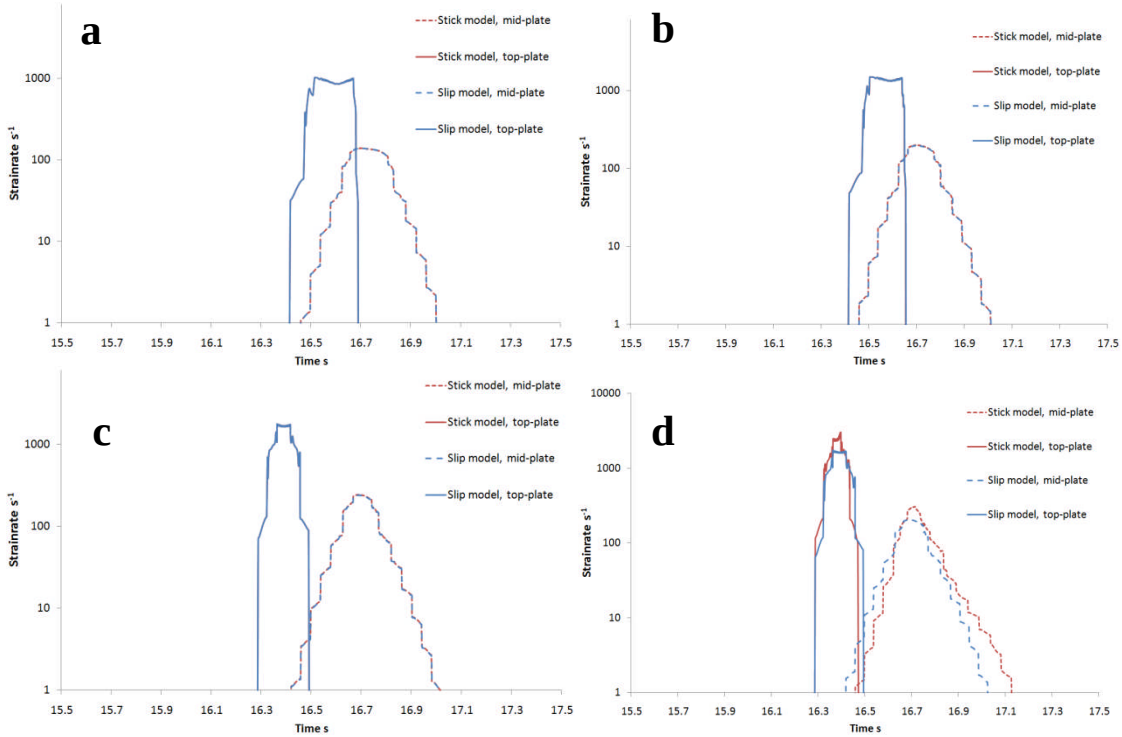

Figure 5-18: The strain-rate streamline plots of 6082-T6 models that use model types 5 and 6 with different rotation speeds of (a) 400 RPM, (b) 600 RPM, (c) 800 RPM and (d) 1200 RPM, from mid-plate (1.6 mm from bottom of workpiece) and top-plate positions (3.2 mm from bottom of workpiece). Note the x-axis is taken from 15.5 to 17.5 second for a better observation of the curves, and the y-axis is in logarithmic scale

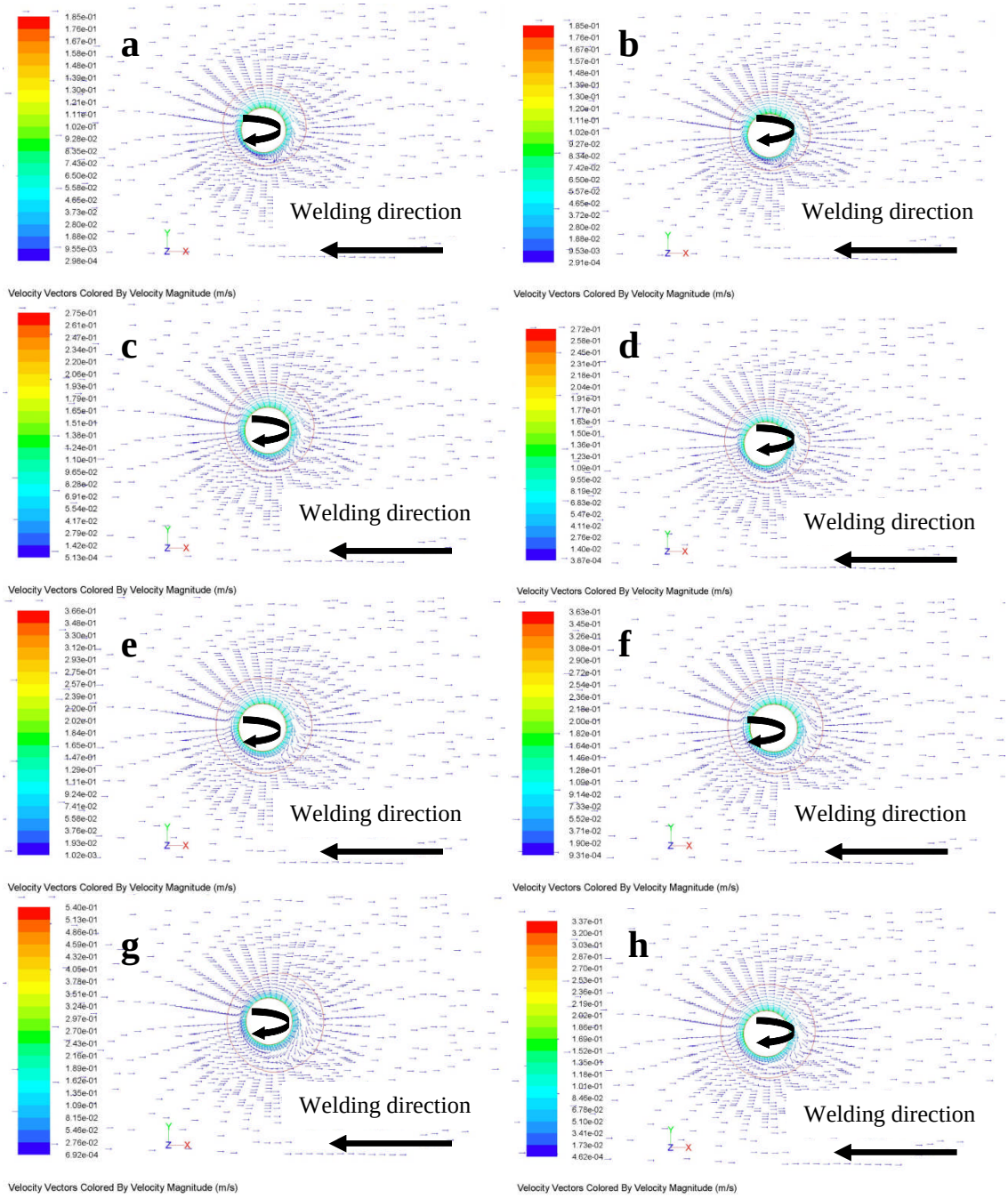

Figure 5-19: Velocity vectors and deformation regions on the mid-plate in 6082-T6 models with rotation speed and model type of (a) 400 RPM model type 5, (b) 400 RPM model type 6, (c) 600 RPM model type 5, (d) 600 RPM model type 6, (e) 800 RPM model type 5, (f) 800 RPM model type 6, (g) 1200 RPM model type 5 and (h) 1200 RPM model type 6. The tool rotation and welding directions are illustrated in the figures. Note the red boundary of the deformation region is with a strain-rate that equals to 2 s^{-1}

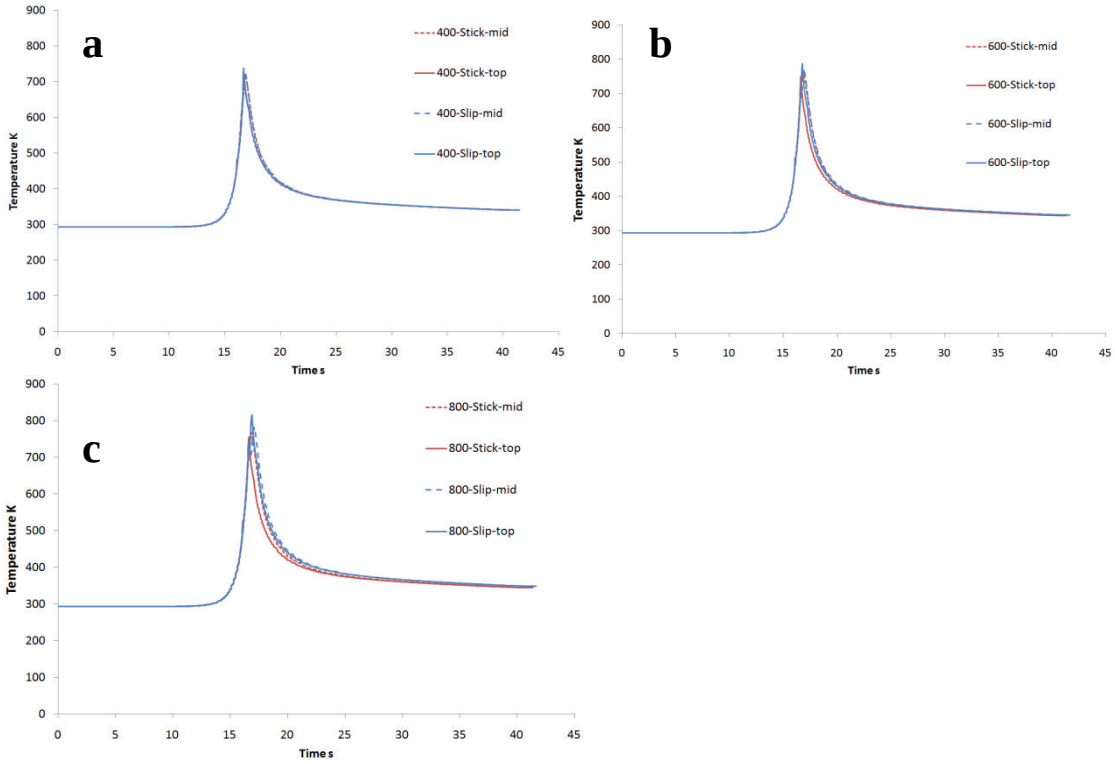

Figure 5-20: The temperature streamline plots of 7449-T7 models that use model types 5 and 6 with different rotation speeds of (a) 400 RPM, (b) 600 RPM and (c) 800 RPM, from mid-plate (1.6 mm from bottom of workpiece) and top-plate positions (3.2 mm from bottom of workpiece)

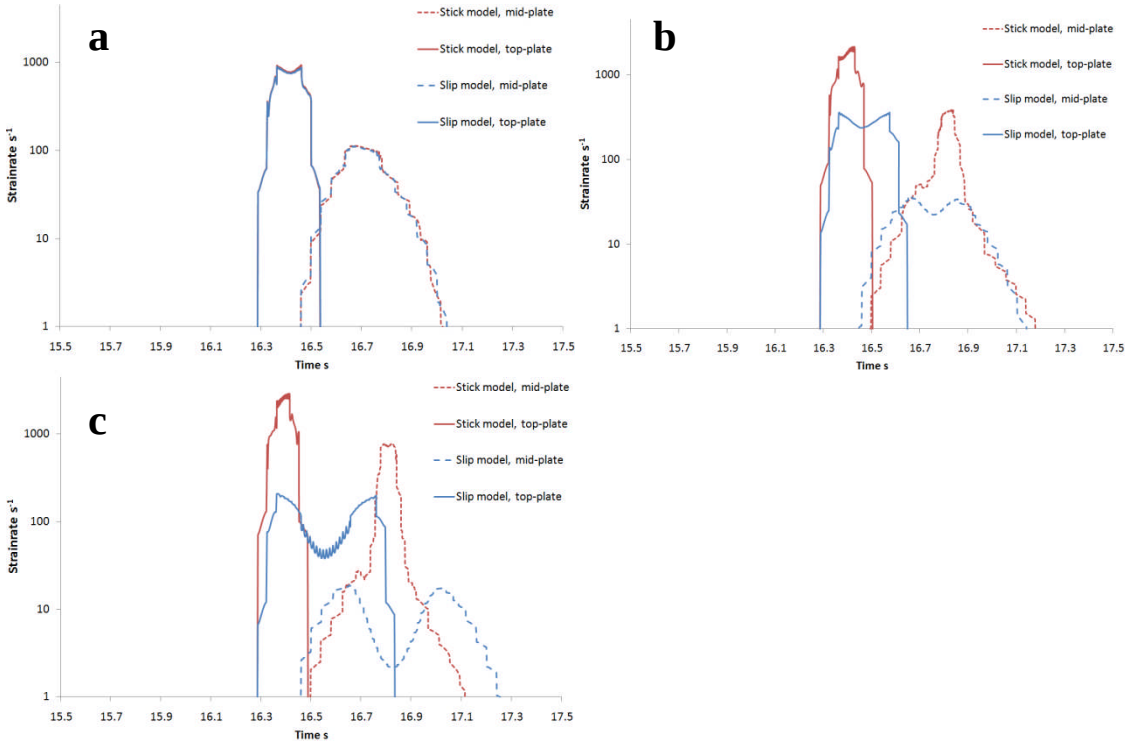

Figure 5-21: The strain-rate streamline plots of 7449-T7 models that use model types 5 and 6 with different rotation speeds of (a) 400 RPM, (b) 600 RPM and (c) 800 RPM, from mid-plate (1.6 mm from bottom of workpiece) and top-plate positions (3.2 mm from bottom of workpiece). Note the x-axis is taken from 15.5 to 17.5 second for a better observation of the curves

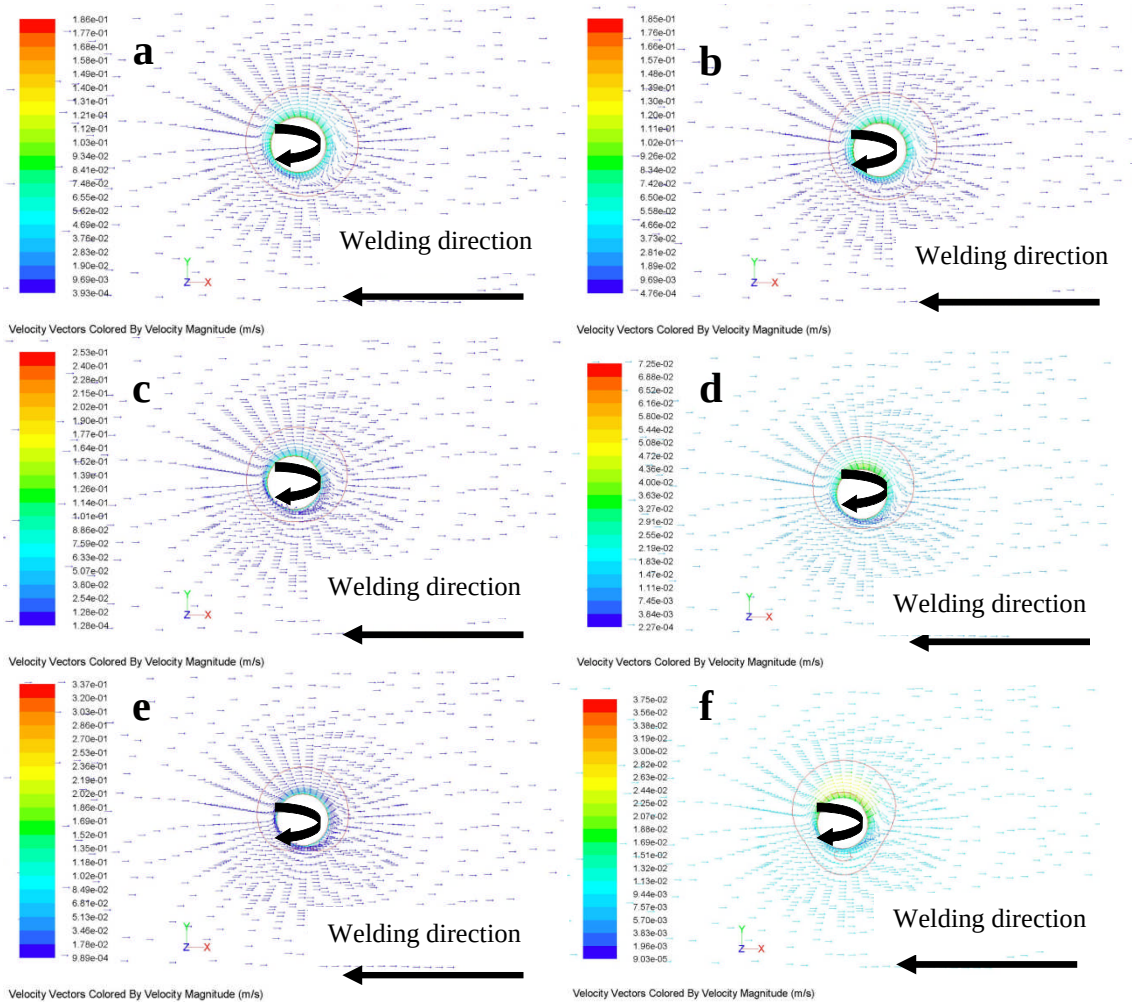

Figure 5-22: Velocity vectors and deformation regions on the mid-plate in 7449-T7 models with rotation speed and model type of (a) 400 RPM model type 5, (b) 400 RPM model type 6, (c) 600 RPM model type 5, (d) 600 RPM model type 6, (e) 800 RPM model type 5 and (f) 800 RPM model type 6. The tool rotation and welding directions are illustrated in the figures. Note the red boundary of the deformation region is with the strain-rate that equals to 2 s^{-1}

5.3.4 The model type 7 and 8

To investigate the influence of the material properties with a slip boundary condition, model type 7 and 8 were applied with the same boundary conditions as 6082-T6 models in model type 3 and 6 respectively, apart from the material properties and constitutive behaviour equations.

For the model type 7, a number of streamline plots of temperature and strain-rate were generated at the mid-plate and top-plate, as shown in Figure 5-23 and Figure 5-24. The temperature plots indicate that with the same settings, the 7449-T7 models generate more heat than 6082-T6. The reason is that 7449 is a harder material and more viscous heat will be generated due to the high flow stress.

As shown in Figure 5-24, the strain-rate plots at mid-plate and top-plate are virtually identical, because of the same setting on the boundary condition. The deformation region areas in model type 7 are all larger than ones in 6082-T6 models (see Figure 5-25).

In model type 8, the streamline plots of temperature and strain-rate were also generated at the mid-plate and top-plate, as shown in Figure 5-27 and Figure 5-28. The temperature results in the 7449-T7 models are also higher than ones from 6082-T6 models, although all the peak temperatures have reduced due to the introduction of the CSRR. The strain-rate curves at the top-plate are also roughly identical because of the same boundary setting at the model, and the peak values of the 7449-T7 strain-rate at the mid-plate are slightly lower. This may be because of the higher temperature in the local area which leads to lower strain-rate, although it is not significant. The deformation region areas in model types 7 are larger than the corresponding ones in 6082-T6 models (see Figure 5-25 and Figure 5-26), but the deformation shapes are very similar, as shown in Figure 5-29. The material is deformed uniformly around the tool.

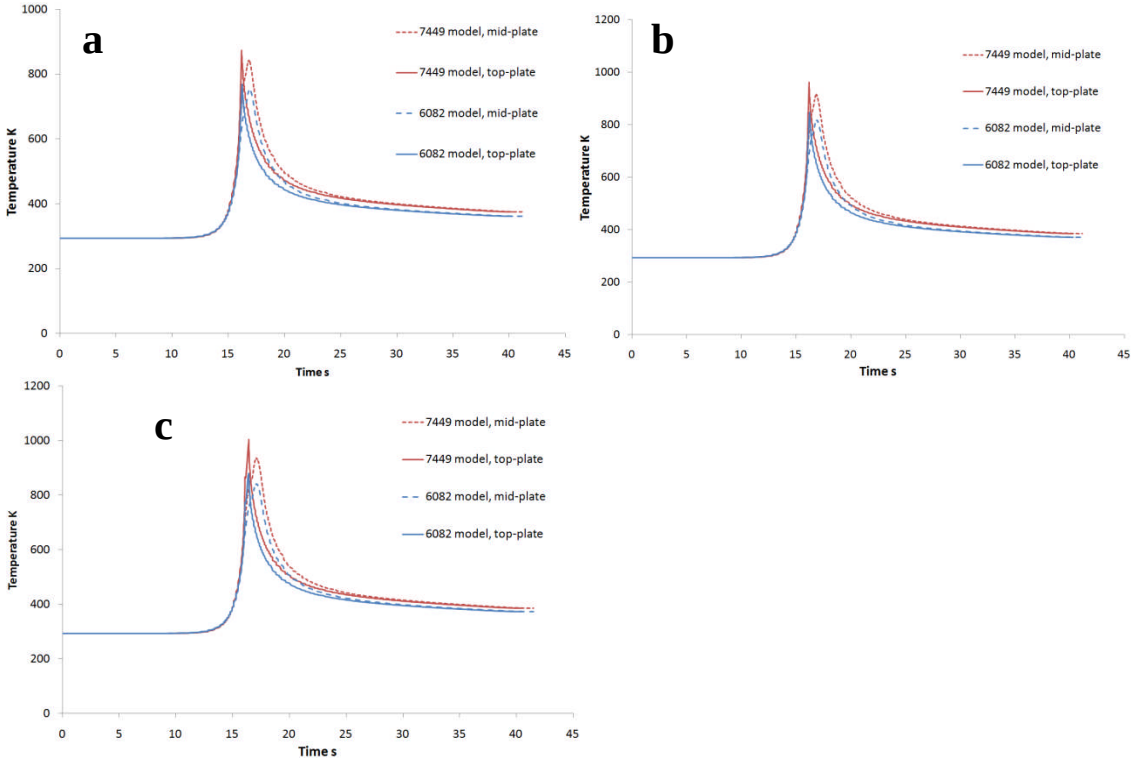

Figure 5-23: The temperature streamline plots of 7449-T7 models that use model type 7 with different rotation speeds of (a) 400 RPM, (b) 600 RPM and (c) 800 RPM, from mid-plate (1.6 mm from bottom of workpiece) and top-plate positions (3.2 mm from bottom of workpiece)

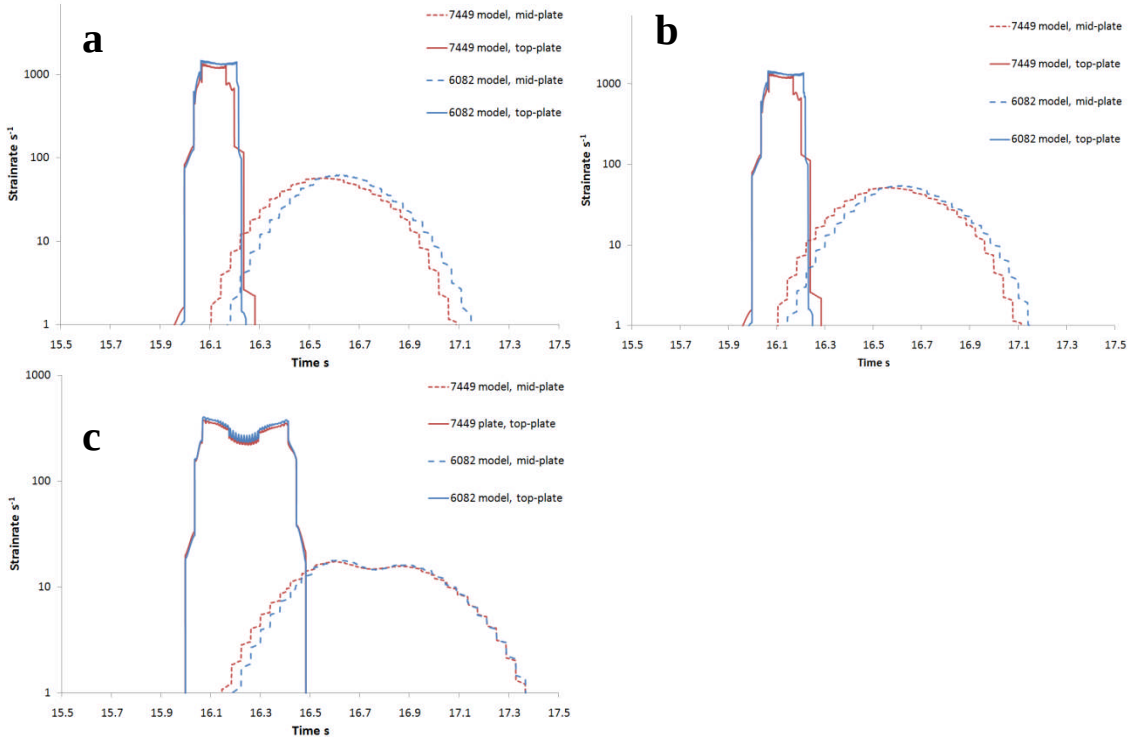

Figure 5-24: The strain-rate streamline plots of 7449-T7 models that use model types 7 with different rotation speeds of (a) 400 RPM, (b) 600 RPM and (c) 800 RPM, from mid-plate (1.6 mm from bottom of workpiece) and top-plate positions (3.2 mm from bottom of workpiece). Note the x-axis is taken from 15.5 to 17.5 second for a better observation of the curves, and the y-axis is in logarithmic scale

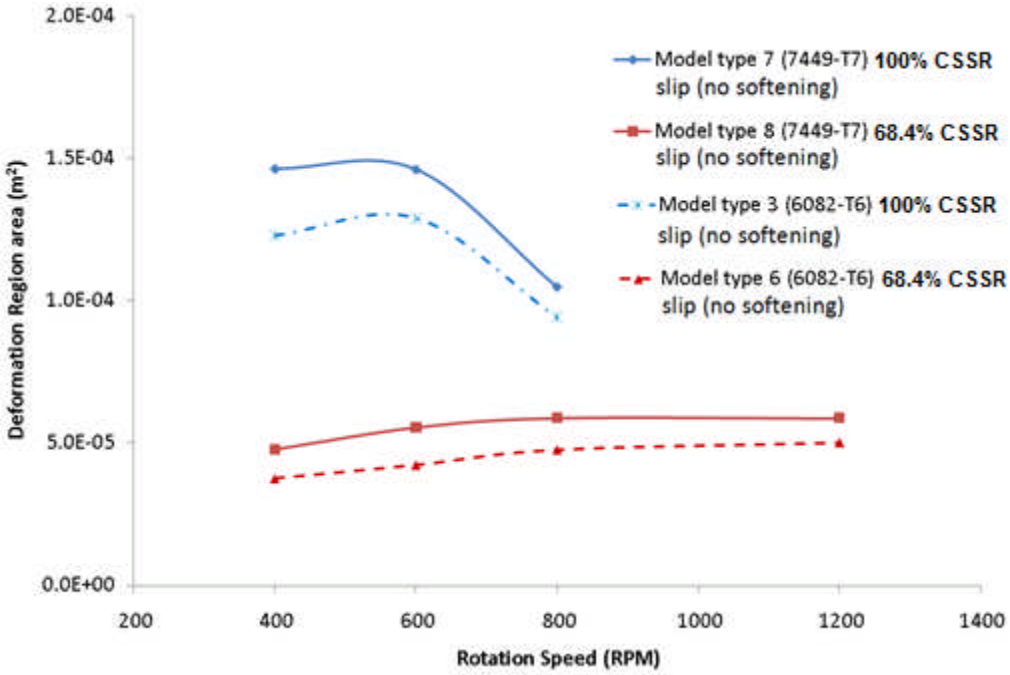

Figure 5-25: The deformation regions area comparison plot between the model type 7, 8 and their corresponding 6082-T6 models

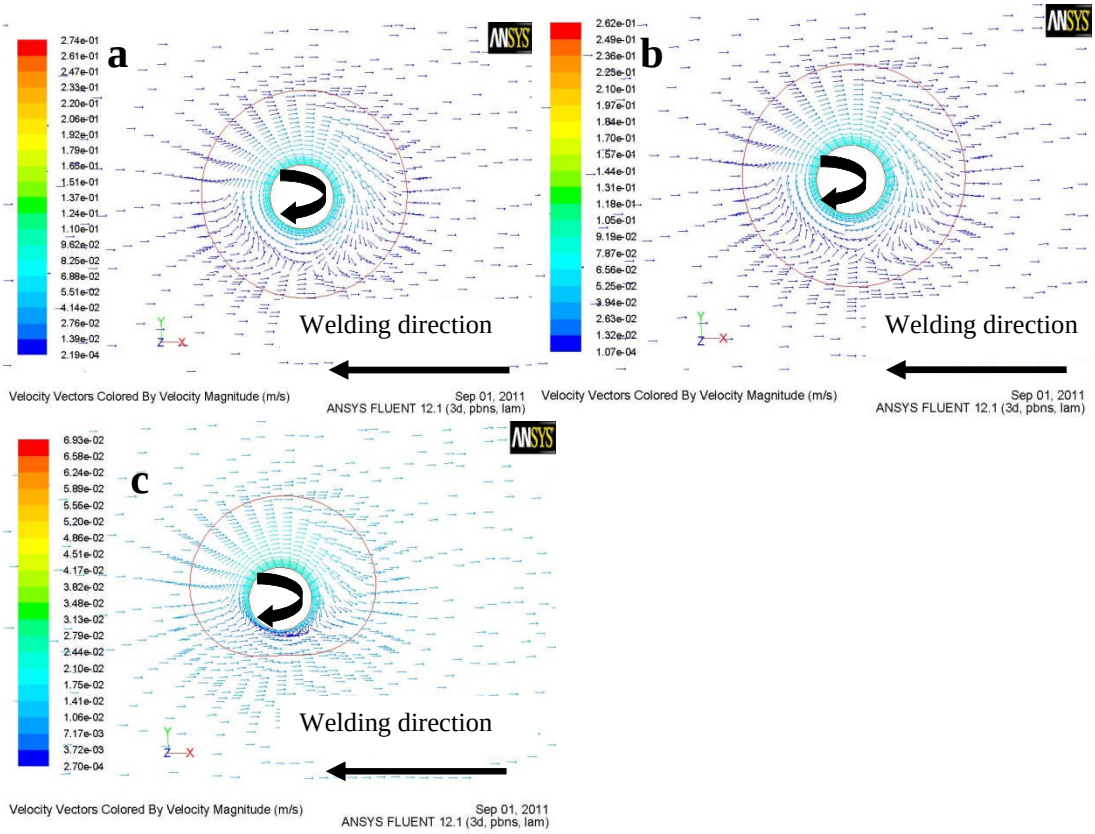

Figure 5-26: Velocity vectors and deformation regions on the mid-plate in 7449-T7 models with model type 7 and rotation speeds of (a) 400 RPM, (b) 600 RPM and (c) 800 RPM. The tool rotation and welding directions are illustrated in the figures. Note the red boundary of the deformation region is with a strain-rate that equals to 2 s^{-1}

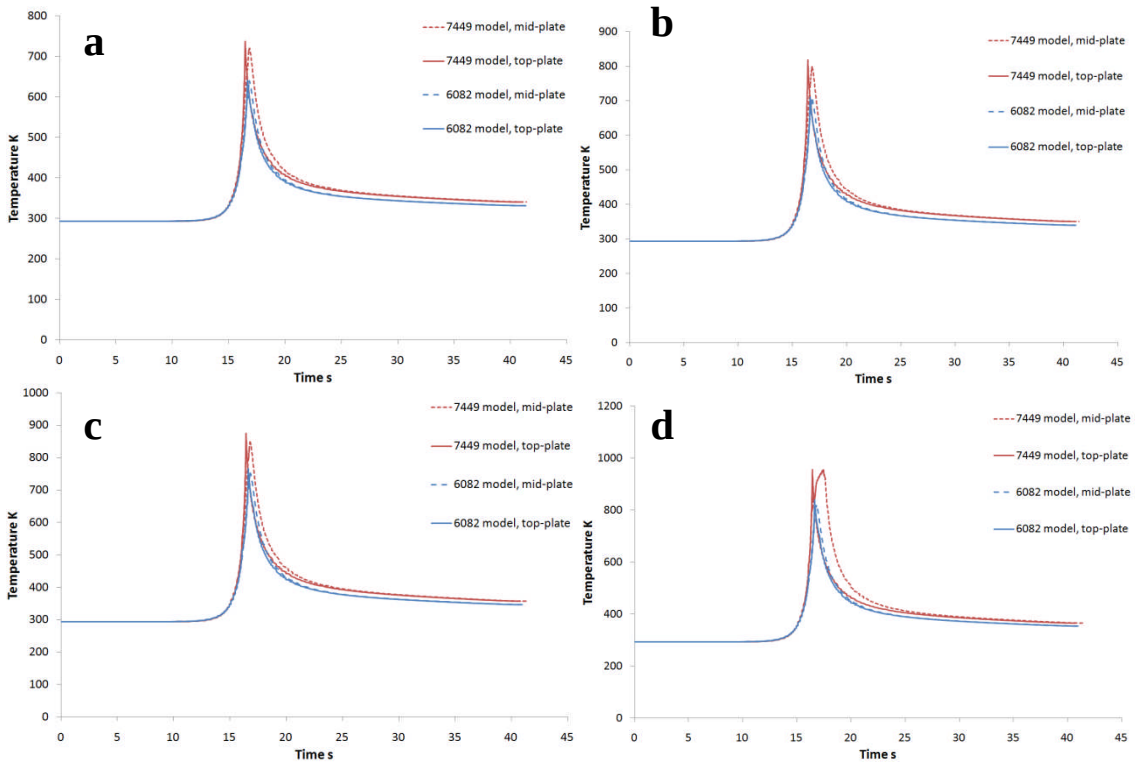

Figure 5-27: The temperature streamline plots of 7449-T7 models that use model types 8 with different rotation speeds of (a) 400 RPM, (b) 600 RPM, (c) 800 RPM and (d) 1200 RPM, from mid-plate (1.6 mm from bottom of workpiece) and top-plate positions (3.2 mm from bottom of workpiece)

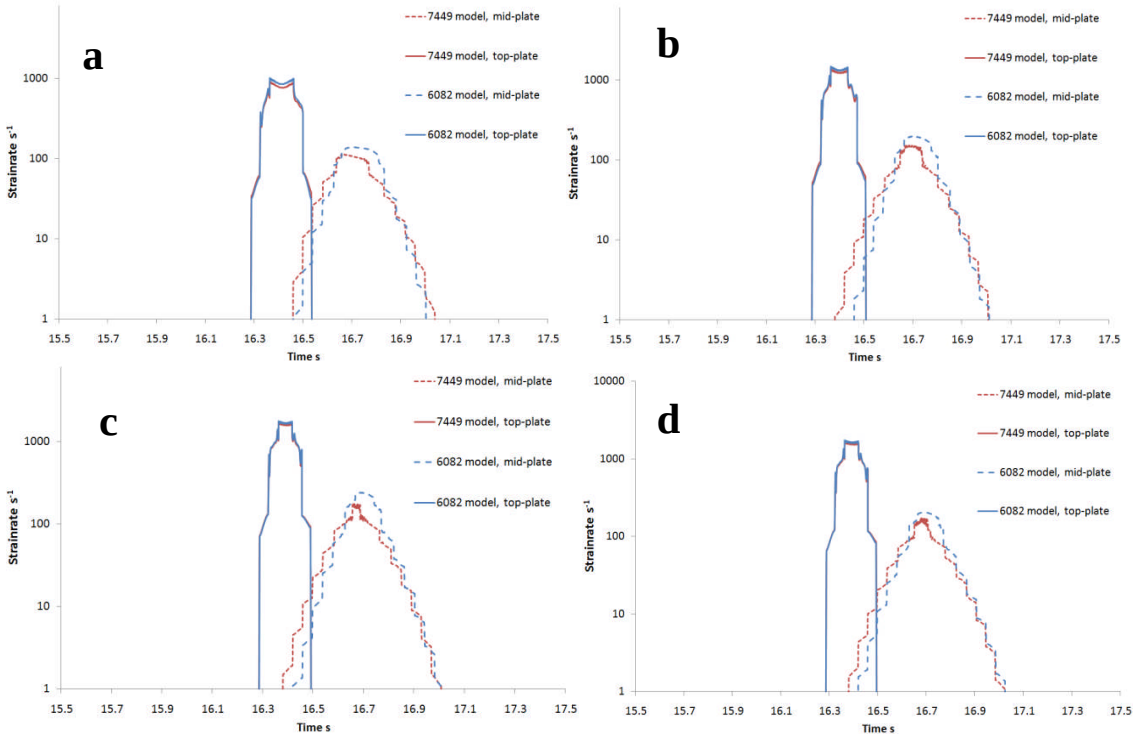

Figure 5-28: The strain-rate streamline plots of 7449-T7 models that use model types 8 with different rotation speeds of (a) 400 RPM, (b) 600 RPM, (c) 800 RPM and (d) 1200 RPM, from mid-plate (1.6 mm from bottom of workpiece) and top-plate positions (3.2 mm from bottom of workpiece). Note the x-axis is taken from 15.5 to 17.5 second for a better observation of the curves, and the y-axis is in logarithmic scale

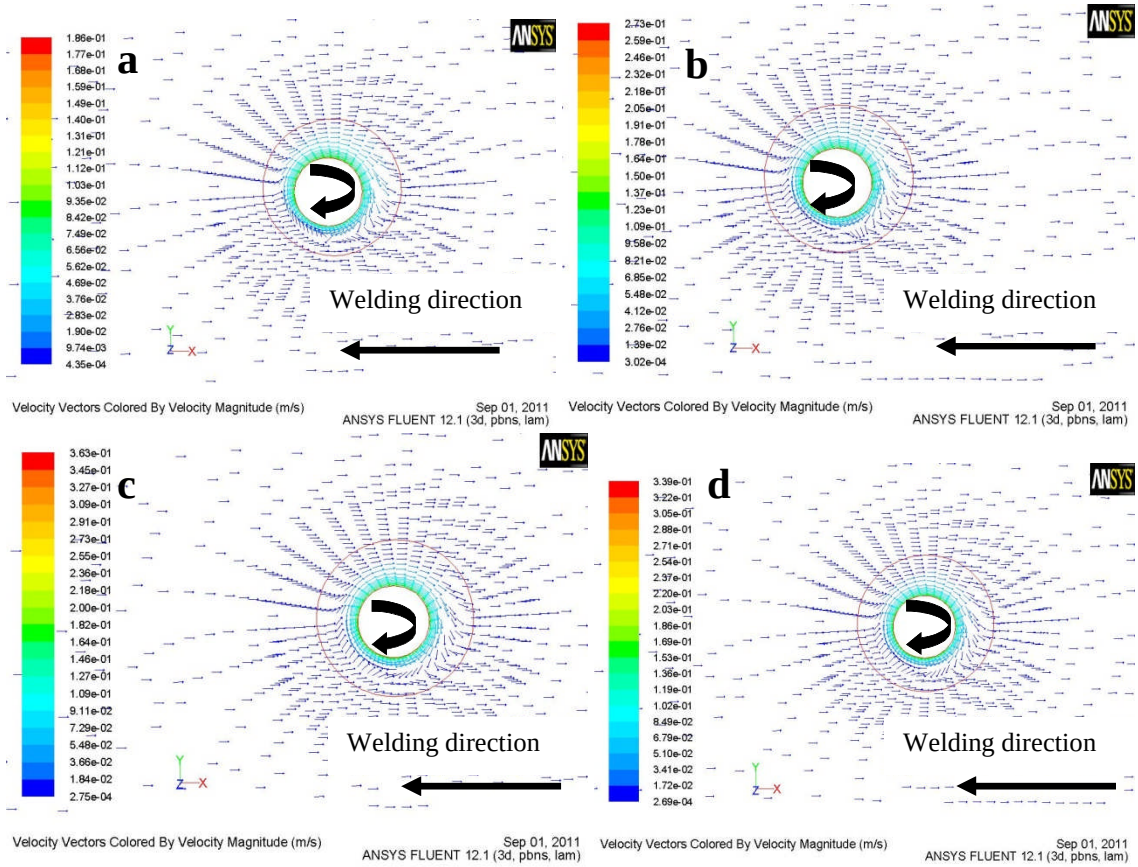

Figure 5-29: Velocity vectors and deformation regions on the mid-plate in 7449-T7 models with model type 8 and rotation speeds of (a) 400 RPM, (b) 600 RPM, (c) 800 RPM and (d) 1200 RPM. The tool rotation and welding directions are illustrated in the figures. Note the red boundary of the deformation region is with a strain-rate that equals to 2 s^{-1}

5.3.5 Comparisons with the experimental results

Six travel speeds were applied with the slip condition to seek matching conditions compared to the experimental results; however a matching condition with the slip model was only found with the 8 mm/s travel speed. The reason for this is that the rotation speed is too high, which generates a large amount of heat despite the CSRR being used and the slip coefficient being reduced to a low level. For 8 mm/s, the calculated slip coefficient is 0.099, the viscous heat is 1.90 W and the slip heat is 729.5 W.

The thermal profile comparison between the experimental results, the slip model and the corresponding stick model is given in Figure 5-30. The heat generation in the stick model is purely viscous and equals 659.5 W. The comparison indicates that even though

a close value is found, the temperature in the slip model is still slightly larger than the ones from the experiment and stick models. However both the slip coefficient and the viscous heat generation are both very low.

The streamline plots were done in the mid-plate for stick and slip model to find the differences in the flow behaviour, in terms of the temperature and strain-rate. The temperature comparison plot in Figure 5-31 indicates temperature in the slip model is higher, which is because the heat generation in the slip model is higher. The strain-rate comparison is similar to those shown previously in section 5.3.3.2, and shows that although the slip model generates more heat, the strain-rate value in the stick model is much greater. There is a reduction in the strain-rate in the middle of the curve of the slip model, while no such reduction is observed in the stick model. The high strain-rate area is larger in the slip model, which shows from the end of the curves when the slip curve starts to be larger than the stick one. This can also be seen from the deformation region in the mid-plate around the tool as shown in Figure 5-33, which shows that the deformation region in the stick model (21 mm^2) is smaller than the one in the slip model (39.4 mm^2). Figure 5-33 also shows that the material with higher strain-rate is more concentrated at the retreating side in the stick model, while in the slip model the deformed material distributes in both sides and there is a low strain-rate part inside area, which is the same from Figure 5-22(f) under a similar condition.

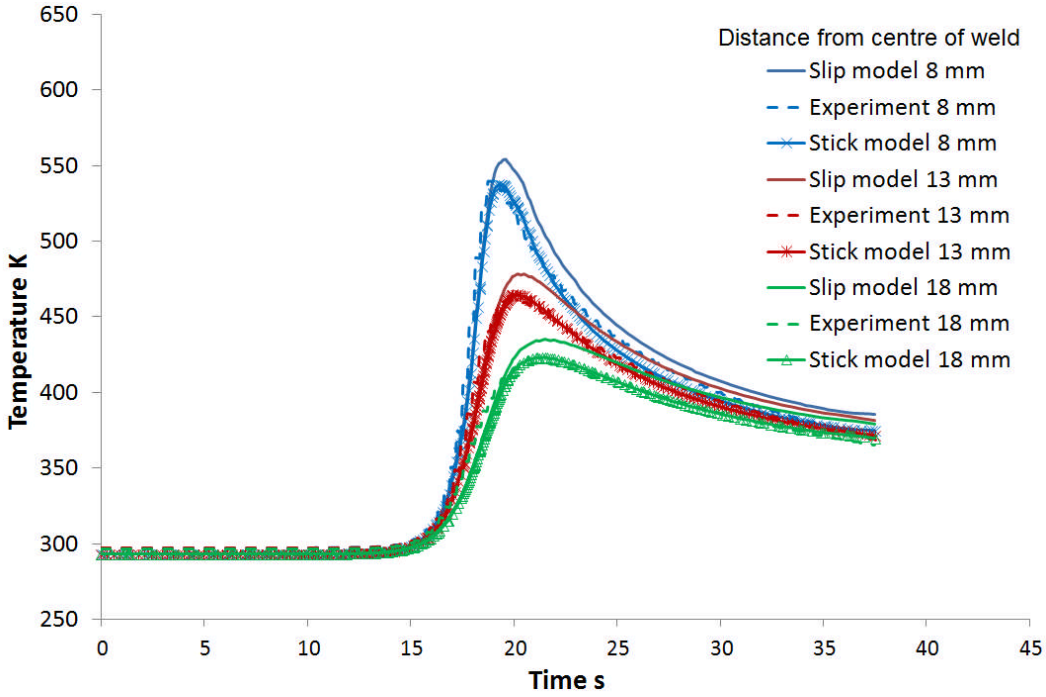

Figure 5-30: Temperature comparisons between the slip, stick models and experimental results for 7449-T7 FSW process model with 1300 RPM rotation speed and 8 mm/s travel speed

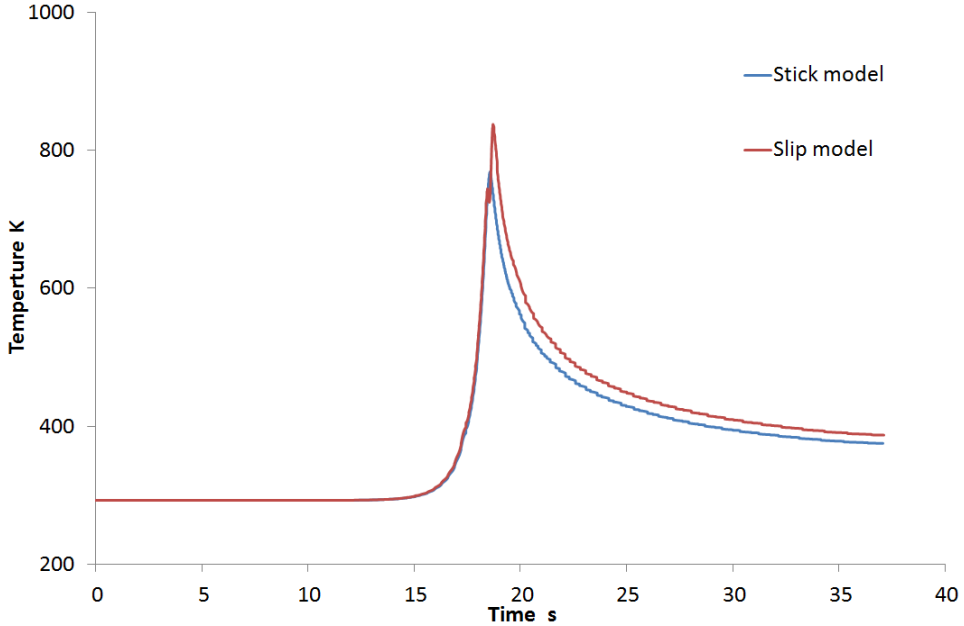

Figure 5-31: The temperature streamline plots of 7449-T7 process models use model types 6 with stick and slip boundary conditions, from mid-plate (1.6 mm from bottom of workpiece)

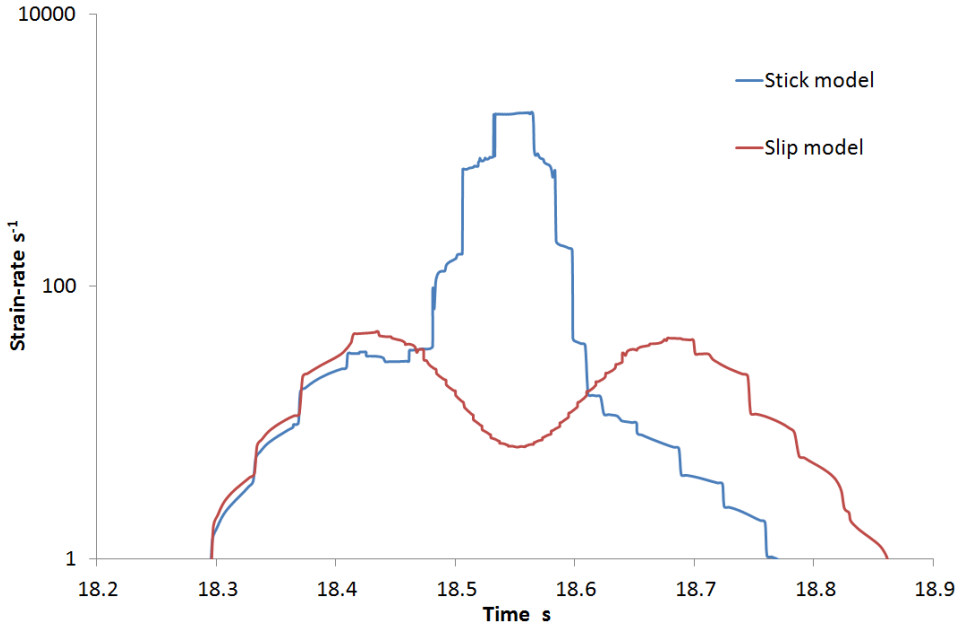

Figure 5-32: The strain-rate streamline plots of 7449-T7 process models use model types 6 with stick and slip boundary conditions, from mid-plate (1.6 mm from bottom of workpiece). Note the x-axis is taken from 18.2 to 18.9 second for a better observation of the curves, and the y-axis is in logarithmic scale

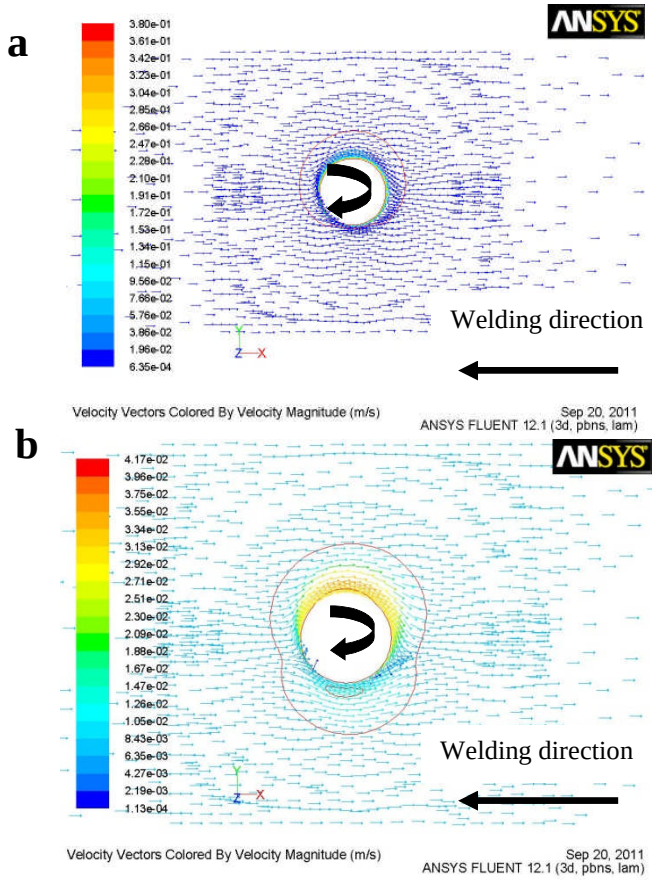

Figure 5-33: Velocity vectors and deformation regions on the mid-plate in 7449-T7 FSW process models with model type 6 and rotation speeds of 1300 RPM, under (a) stick and (b) slip conditions. The tool rotation and welding directions are illustrated in the figures. Note the red boundary of the deformation region is with a strain-rate that equals to 2 s^{-1}

5.4 Discussion

From an overview of the 6082-T6 and 7449-T7 results, it is clear that implementing a slip boundary condition is able to reduce the heat generation in both materials, and capture the reduction in heat generation which can also be represented with a reduction in the flow strength near the solidus temperature. The reduction in heat generation is a consequence of the strain-rate sensitivity of the material. Hence greater slip reduces the material strain-rate which reduces the flow stress. The constitutive laws used in this work indicate that as the strain-rate reduces, the strength reduces to the yield value, at that temperature. Therefore the minimum heat generation that can be obtained with the slip model occurs when the slip coefficient equals 0. As the heat generation with this

type of model can exceed that from the stick model that includes softening (model type 2). It was not always possible to find an equivalent slip model, for all conditions.

With the same parameters, the heat generation with the harder 7449-T7 is greater than that for the softer 6082-T6 (see Figure 5-4). This suggests that lower rotation speeds should be used for this harder material to avoid overheating the material. The different flow strengths made comparing the two materials difficult. Nevertheless when applying the same slip boundary conditions (e.g. Figure 5-24 and Figure 5-28) the strain-rate predictions were virtually identical. This indicates that the flow is dominated by the velocity at the surface rather than the material properties. The main difference between the two materials was the size of the deformation area which was lower with the 7449-T7 (Figure 5-25). The deformation may be dominated by the rate at which the flow strength increases with distance from the tool, which will be dependent on the material properties and heat flow. This phenomenon has been discussed in a paper by Schmidt and Hattel[7]. In addition, it was noted however that while the deformation region size with the slip boundary conditions was lower with 6082-T6 it was slightly larger with 7449-T7. The reason for the difference is unclear although it may also be related to the rate of the flow strength increase with distance from the tool.

While a uniform slip coefficient is used in these models, this is unlikely to exist in practice. Indeed, the slip coefficient near the pin may be much higher than that on the periphery of the shoulder, i.e. more slip occurs on the shoulder than the pin. This is reflected in typical macrosections which often demonstrate little deformation underneath the periphery of the shoulder. Under these conditions:

1. The shear stress between the tool and workpiece material may well be below the yield value.
2. No/minimal deformation of the material occurs.
3. Dry rubbing contact occurs, i.e. such as that which exists in friction welding and linear friction welding during phase 1, i.e. asperity contact[23].

Therefore the procedure for describing the slip boundary conditions in this chapter may only partially represent the conditions that exist in practice.

To validate the modelling method a slip model was developed to represent the Flexi-stir welds described in chapter 5. The high rotation speeds of the experiment meant that a slip model could be created for only the highest travel speed. The strain-rate in the model was much smaller than the one in the stick model, due to the very low slip coefficient. The deformation region in the stick model was significant smaller than the one in the slip model, and the material was more uniformly distributed on the advancing and retreating sides.

5.5 Conclusions

In this study, eight different model types were developed to compare stick and slip boundary conditions, large and small CSRR and 6082-T6 and 7449-T7 materials. The outcomes of the study were:

1. Due to the fact that 7449-T7 is harder material than 6082-T6, lower rotation speeds are more appropriate. This is because to solidus temperature is more readily reached which limits the heat generation.
2. For both 6082-T6 and 7449-T7 models, applying the slip boundary condition can reduce the strain-rate dramatically. This has been used to capture the effect of softening of temperatures approaching the solidus.
3. The slip boundary condition also reduced the heat generation compared with the stick model. In the model developed there is a limit to the reduction that can be achieved due to the yield strength of the material (i.e. the inherent strength when the strain-rate approaches zero).
4. Comparing the stick model and the slip models with the same heat generation, if the slip coefficient in slip model is very low, there will be some discrepancies of the temperature distribution near the tool. This is because the heat generation was applied at the tool surface in the slip model rather than volumetrically for the stick model.
5. When applying the slip models to the 7449-T7 Flexi-stir welds, it was only possible to generate a model for the 8 mm/s travel speed. The comparison between the slip and stick models indicated that slip model generates less strain-rate but larger deformation region.

References

1. H. Valberg and T. Malvik: 'Experimental investigation of the material flow inside the bearing channel in aluminium extrusion', *International Journal of Materials and Product Technology*, 1994, 9, 428-463.

2. T. H. North, G. J. Bendzsak, C. B. Smith and G. H. Luan: 'Numerical modeling and validation during friction stir welding of aluminum alloys', *7th Internat.Symp.*, 2001, 621-632.

3. F. Palm, V. Erofeev, E. Karpuchin and O. Zaitzev: Proc. 4th International Symposium on Friction Stir Welding Park City, Park City, Utah, USA.

4. P. Vilaça, L. Quintino and J. F. Dos Santos: 'ISTIR - Analytical thermal model for friction stir welding', *J. Mater. Process. Technol.*, 2005, 169, 452-465.

5. P. A. Colegrove and H. R. Shercliff: 'Two-dimensional CFD [computational fluid dynamics] modelling of flow round profiled FSW [friction stir welding] tooling', *Science and Technology of Welding and Joining*, 2004, 9, 483-492.

6. H. Schmidt, J. Hattel and J. Wert: 'An analytical model for the heat generation in friction stir welding', *Modelling and Simulation in Materials Science and Engineering*, 2004, 12, 143-157.

7. H. Schmidt and J. Hattel: 'A local model for the thermomechanical conditions in friction stir welding', *Modelling and Simulation in Materials Science and Engineering*, 2005, 13, 77-93.

8. C. Hamilton, S. Dymek and A. Sommers: 'A thermal model of friction stir welding in aluminum alloys', *International Journal of Machine Tools and Manufacture*, 2008, 48, 1120-1130.

9. R. Nandan, G. G. Roy, T. J. Lienert and T. Debroy: 'Three-dimensional heat and material flow during friction stir welding of mild steel', *Acta Materialia*, 2007, 55, 883-895.

10. B. C. Liechty and B. W. Webb: 'Modeling the frictional boundary condition in friction stir welding', *International Journal of Machine Tools and Manufacture,* 2008, .

11. J. P. Holman: 'Heat Transfer', 6th edition, New York, McGraw-Hill Book Co, 1986.

12. P. A. Colegrove and H. R. Shercliff: 'CFD modelling of friction stir welding of thick plate 7449 aluminium alloy', *Science and Technology of Welding and Joining,* 2006, 11, 429-441.

13. A. Askari, S. Silling, B. London and M. Mahoney: Proc. Friction Stir Welding and Processing, 43-54.

14. H. Schmidt and J. Hattel: Proc. Friction Stir Welding and Processing III - Proceedings of a Symposium sponsored by the Shaping and Forming Committee of (MPMD) of the Minerals, Metals and Materials Society, TMS, 225-232.

15. A. Moal and E. Massoni: 'Finite element simulation of the inertia welding of two similar parts', *Engineering Computations,* 1995, 12, 497-512.

16. H. Zhang, Z. Zhang, J. Bie, L. Zhou and J. Chen: 'Effect of viscosity on material behavior in friction stir welding process', *Transactions of Nonferrous Metals Society of China (English Edition),* 2006, 16, 1045-1052.

17. Z. Zhang and J. T. Chen: 'The simulation of material behaviors in friction stir welding process by using rate-dependent constitutive model', *Journal of Materials Science,* 2008, 43, 222-232.

18. J. -. Ponthot: 'An extension of the radial return algorithm to account for rate-dependent effects in factional contact and visco-plasticity', *J. Mater. Process. Technol.,* 1998, 80-81, 628-634.

19. C. M. Sellars and W. J. M. Tegart: 'Hot workability', *Int. Met. Rev.,* 1972, 17, 1-24.

20. P. A. Colegrove, H. R. Shercliff and R. Zettler: 'Model for predicting heat generation and temperature in friction stir welding from the material properties', *Science and Technology of Welding and Joining,* 2007, 12, 284-297.

21. T. Sheppard and A. Jackson: 'Constitutive equations for use in prediction of flow stress during extrusion of aluminium alloys', *Materials Science and Technology*, 1997, 13, 203-209.

22. J. N. DuPont and A. R. Marder: 'Thermal efficiency of arc welding processes', *Weld J (Miami Fla)*, 1995, 74, 406-s.

23. U. U. Ofem, P. A. Colegrove, A. Addison and M. J. Russell: 'Energy and force analysis of linear friction welds in medium carbon steel', *Science and Technology of Welding and Joining*, 2010, 15, 479-485.

CHAPTER 6

Conclusions and Further Work

6.1 Conclusions

This work demonstrates how to use the experimental methodology, numerical modelling and ANN techniques, to reach a better understanding of some uncertain points in the FSW process, i.e. the material constitutive behaviour under extreme conditions, the thermal boundary conditions and the slip conditions at tool surfaces.

The Gleeble experiments were conducted to investigate the material constitutive behaviour under high strain-rates and near solidus temperatures. From the experimental data, a new set of Zener-Holloman constants was found for 6082-T6, and a modified equation was determined for 7449-T7. The main finding was that no rapid softening regime was observed for either material at temperatures approaching the solidus. However, there was a slight reduction in the 7449-T7 flow stress curves, which could be the result of complete dissolution of precipitates. The derived flow curves were compared with ones from the literature and the mismatch was concluded due to the different experimental conditions. The noise and its reasons in the Gleeble results was also studied. It was related to the process temperature and strain-rate, as they increased the level noise would increase. The strain-rate had a greater effect on the noise than the temperature.

A number of new model types were developed and the results demonstrated that it is possible to find the accurate power and thermal boundary conditions by combining a FE thermal model and an ANN model. Within the study, the selection of the training data range is found to be critical for successful application of the ANN models. The technique was applied to thermal models with several different types of boundary conditions, such as the constant convective, constant contact gap conductance and temperature dependent types. However due to the different level of complexity in each FE models, the necessary requirements of the inputs for ANN models varied. For simpler conditions, such as the model with a single contact gap conductance, a 4 input

method is enough to train the ANN model. Meanwhile more training data was required for the temperature dependent contact gap conductance model, where the 9 input method was used. The prediction quality was also influenced by the increasing complexity, and could to be improved by implementing a second stage ANN which involved adding more training data around the region of interest. In terms of the ANN structure, different topologies were compared, and it was found that the MLP topology worked well for the single contact gap conductance model and the GFF topology for the double and temperature dependent contact gap conductance models. In all cases, the LM BP was required because of the plateau effects that occur with extreme boundary condition coefficients.

The hybrid modelling technique was applied to a FSW process model, to investigate the contact shoulder radius ratio (CSRR which directly affected the power), and the thermal boundary conditions at the interface between the workpiece and backing bar. During the study, the hybrid model was able to predict both the CSRR and the temperature dependent thermal boundary condition. The calculated CSRR and thermal boundary condition was validated against a group of experimental results, and a close match was obtained, with the GFF ANN topology, and 4 input method based on integrated temperature vs. time and the cooling slope. The dynamic coupling between the CSRR and the thermal boundary condition made it difficult to analyse either independently, i.e. a high CSRR could lead to a high heat loss to the backing bar. A universal set of CSRR and boundary conditions values was found by averaging the individual results for each travel speed. By applying the averaged result for each model to the different travel speeds, a close match was found for some speeds and a poorer match was found for others. There was a correlation between the prediction quality and the plunge depths of the FSW tool into the material.

In the final chapter, the contact condition at the interface between the tool and the workpiece was studied. The stick and slip conditions were compared for two types of aluminium alloys. The study showed that for both materials, applying the slip boundary condition can reduce the strain-rate dramatically, and applying the slip boundary condition would reduce the heat generation. Between the stick model and the slip model

with the same heat generation, some discrepancies of the temperature distribution near the tool could be observed because the heat generation occurs at the shoulder with the slip model and volumetrically with the stick model. The slip method was validated with FSW process model with 8 mm/s, and the process was also modelled with stick condition. The comparison between the two conditions indicated that slip model generated less strain-rate but a larger deformation region.

6.2 Further work

Some following future work can be carried out based on the studies described in this thesis, including:

1. Further refinement of slip model so that different conditions are applied for different parts of the tool. The contact condition at the interface between the tool and workpiece is complex, and the application of a uniform slip coefficient is a simplification. Relating some process factors such as local temperature, pressure or stress strain conditions will lead to a better understanding of the FSW process.
2. Do experiments to more accurately predict the stick/slip behaviour at the tool interface. To validate the simulation outcomes, marker experiments can be carried out specifically at the welding direction to observe the macro material flow behaviour.
3. To observe the material flow motion during the welding, stop-action trails are ideal. With a proper cooling treatment, the results can also be used for microstructural evolution study.
4. Application of methodology to other friction based processes. The hybrid modelling method covers the fundamental principles of heat transferring during friction deforming procedure, which indicates it can be applied to other process such as linear friction welding and friction spot welding.
5. The methodology of determining the material constitutive properties can be applied to other alloys, such as magnesium or steel, particularly for high temperature and strain-rate conditions.

APPENDICES

Appendix A1. Experimental data processing

A plot of the experimental temperature is shown in Figure A-1, which shows the heat stage, hold, test and cool down period. There was a very slight temperature increase when the material was deformed. The experimental temperature was kept mostly steady after the heat-up and before the cooling. As mentioned in chapter 2, the deformation velocity was kept constant by the Gleeble machine during the test, which resulted in a non-uniform strain-rate. The strain-rate vs. time is shown in Figure A-2(a), which indicates how the average slope was calculated to determine the strain-rate. The range used to calculate the average strain-rate was specified from 0.02 to 0.5, after the initial acceleration of the machine had occurred. The corresponding stress values (Figure A-2(b)) were calculated from the average stress value between strain of 0.02 and 0.5.

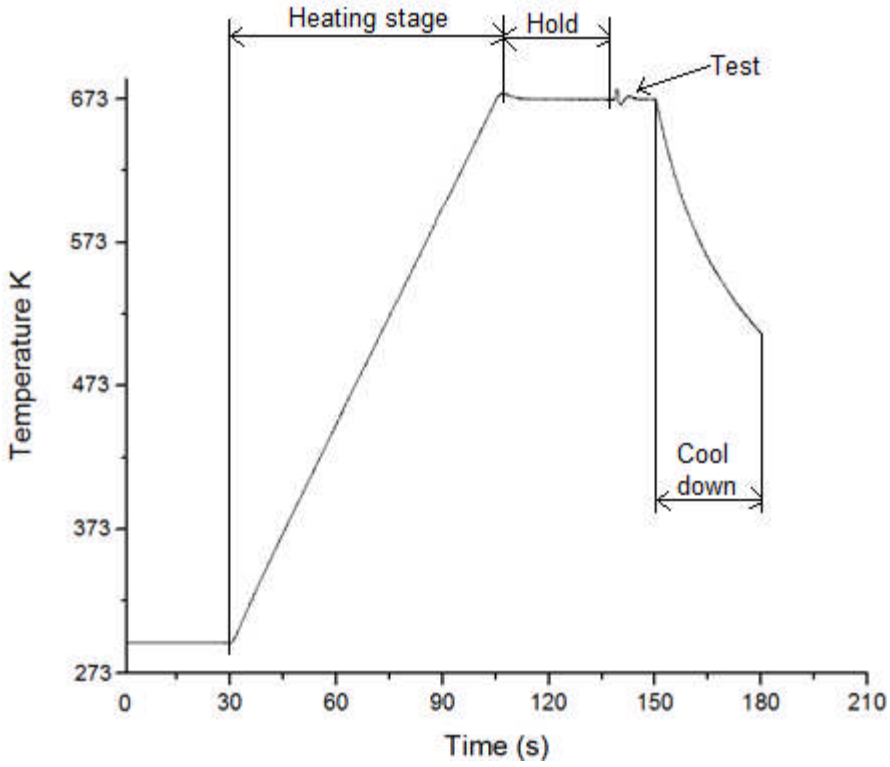

Figure A-1: The experimental temperature reading from Gleeble machine for 6082-T6 deformed with 1 s^{-1} at 672 K

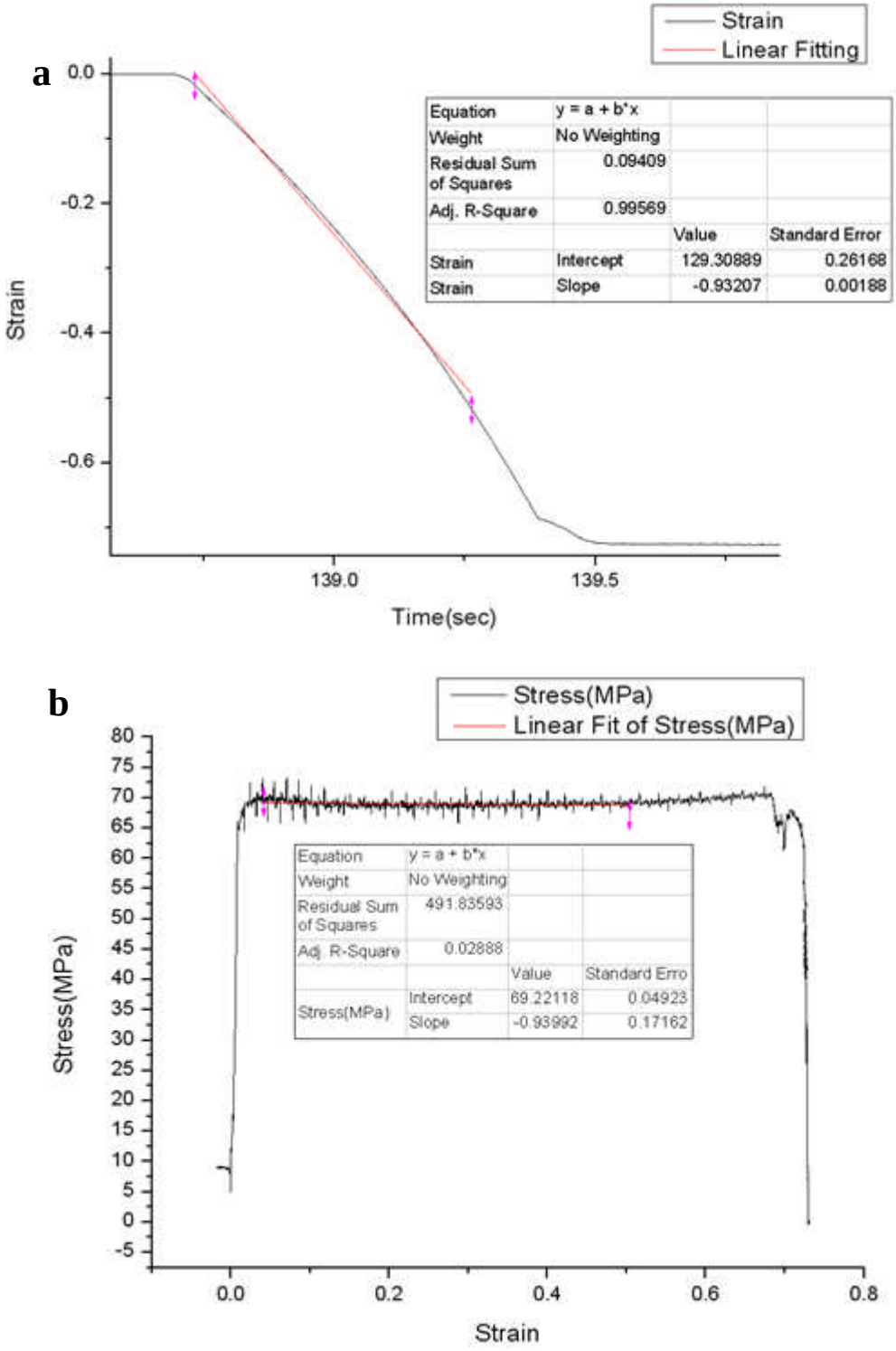

Figure A-2: The experimental (a) strain-rate and (b) stress reading from Gleeble machine for 6082-T6 deformed with 1 s^{-1} at 672 K, and the averaging method is also indicated in the plot. Note for strain-rate plot, only part of the curve is shown for a better observation

Appendix A2. The derivation of Gaussian heat distribution

The Gaussian heat distribution equation was used in chapter 3 of this thesis. The detailed derivation steps of the equation are described as follow. The Gaussian heat distribution is given by:

$$Q_G = C \cdot \exp\left(-\frac{r^2}{R_{heating}^2}\right) \quad \text{Eq. A-1}$$

where the Q_G is the Gaussian heat flux, C is the distribution factor needed to be derived, $R_{heating}$ is the distribution radius of the heat, which is 1/3 of the total radius R, and r is distance of a random point to the centre of the heat source given by:

$$r = \sqrt{x^2 + y^2} \quad \text{Eq. A-2}$$

Since it is know that the distribution radius is 1/3 of the total radius R, the integral of the heat over the surface is given by:

$$Q = \int_0^{\frac{R_{heating}}{3}} C \cdot \exp\left(-\frac{r^2}{R_{heating}^2}\right) 2\pi R \, dR \quad \text{Eq. A-3}$$

The distribution factor C is given by:

$$C = \frac{Q}{\left(1 - \exp\left(-\frac{1}{9}\right)\right)\pi R_{heating}^2} \cdot \exp\left(-\frac{r^2}{R_{heating}^2}\right) \quad \text{Eq. A-4}$$

By merging Eq. A-4 into Eq. A-1, the Gaussian heat distribution equation is found, which is given by:

$$Q_G = Q \cdot \frac{\exp\left(-\frac{r^2}{R_{heating}^2}\right)}{\left(1 - \exp\left(-\frac{1}{9}\right)\right)\pi R_{heating}^2} \quad \text{Eq. A-5}$$

Appendix B1. Single heat transfer coefficient model

B1.1 Numerical model description

The first application uses a simplified thermal model. The ANN technique is applied to models that use a convective heat transfer coefficient, which could be used to represent the heat flows during arc or laser welding (in conduction mode). A FE thermal model is built with COMSOL multiphysics[1], to study whether the ANN technique is capable of predicting a single constant heat transfer coefficient with a Gaussian power input. The geometry for the model is shown in Figure A-3. The model is steady state and is symmetric along the welding axis. The FE model is 700 mm in length, 200 mm in width and 3.2 mm in depth. The half-circle area where the heat flux is applied has a radius of 15 mm. The equation of the Gaussian distributed heat flux is given by

$$Q_G = Q \cdot \frac{\exp\left(\frac{-\left(x^2+y^2\right)}{R_{heating}{}^2}\right)}{\left(1-\exp\left(-\frac{1}{9}\right)\right)\cdot\pi\cdot R_{heating}{}^2} \qquad \text{Eq. A-6}$$

where Q_G is the Gaussian heat flux (W/m^2) distribution, Q is the power input, x and y are the coordinate geometry, and $R_{heating}$ describes the distribution of the heat which is set to a constant value of 5 mm, i.e. the model is not used to predict the distribution of heat. The welding speed is 400 mm/min and is fixed. The thermal properties of the materials used for the models in this report are given in Table A-1.

Item	Material	Thermal Conductivity (W/(m^{2}K))	Specific Heat (kJ/kgK)	Density (kg/m^3)
Workpiece	Aluminium alloy 2024	121[2]	0.875[3]	2780[2]

Table A-1: Material properties used in FE model

The convective heat loss coefficient from the top surface has a fixed value[4] of 10 W/(m^{2}K). The heat loss from the bottom surface is represented by a convective heat transfer coefficient, and is the subject of this investigation.

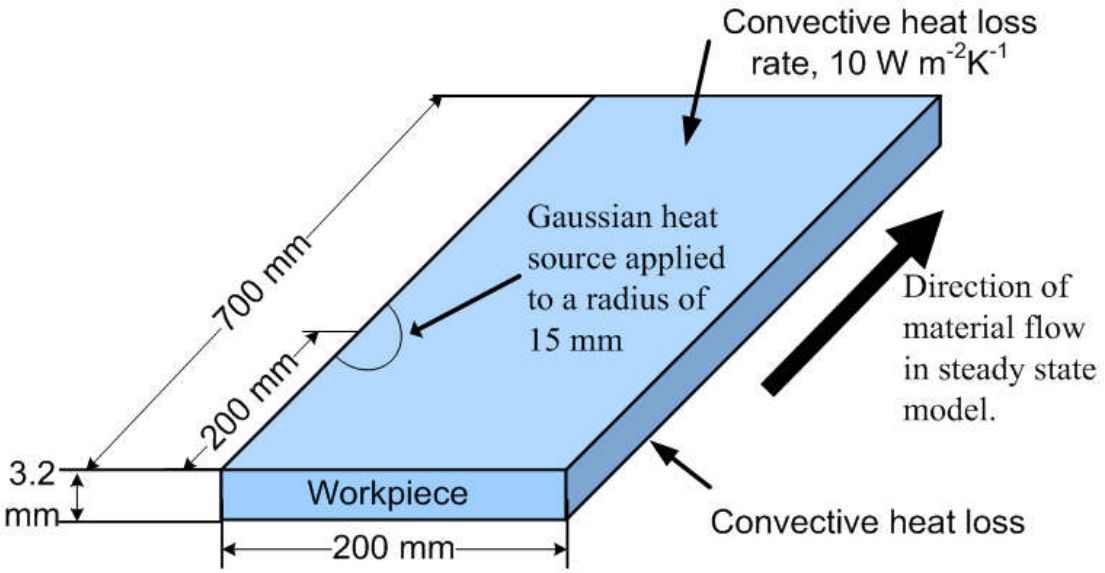

Figure A-3: Simple geometry and boundary settings in first study

B1.2 ANN methodology

The training data used four power input values (Q) and three convective heat transfer coefficients (h) forming twelve combinations. For each combination three thermal profiles are obtained at distances of 10, 15 and 20mm from the heat source. These twelve combinations are shown in Table A-2. The power input and convective heat transfer coefficients used for testing are shown in Table A-3.

Q (W)	h (W/(m^{2}K))
1902	500
3803	400
8557	1000
19016	

Table A-2: Data used for training the single heat transfer coefficient model

Combinations for testing	
Q (W)	h (W/(m^{2}K))
5705	200
14262	700
5705	700
14262	200

Table A-3: Data used for testing the single heat transfer coefficient model

The thermal profile abstracting methods used for the 3 thermal profiles (at 10, 15 and 20 mm) are described in section 2. The 9 input thermal abstracting method is used in this study. The ANN model is applied with MLP topology under LM gradient descent method, and the transfer function is Sigmoid. Three hidden layers are included with a structure of 6-4-3.

B1.3 Results and discussion

Table A-4 shows the desired heat transfer coefficients and powers as well as the predicted values for the single heat transfer coefficient model. Although there are some discrepancies, the prediction is close to the desired values, which indicates the ANN technique is capable of predicting the desired output.

Desired Q (W)	Desired h ($W/(m^2K)$)	Predicted Q (W)	Predicted h ($W/(m^2K)$)	MRE
5705	200	5390	236	11.8%
14262	700	16224	793	13.6%
5705	700	5295	797	10.5%
14262	200	16171	203	7.66%
			Average	10.9%

Table A-4: Results for single heat transfer coefficient with MLP topology under LM learning rule

A visual validation was also applied. The predicted power input and heat transfer coefficient was applied to the FE model, and the new thermal curves are compared with original curves. The predicted values with the lowest average error are shown in Figure A-4(a), and the worst are shown in Figure A-4(b). The comparison indicates that although the average errors are reasonably small, there is a reasonable large discrepancy in the prediction of the thermal profiles.

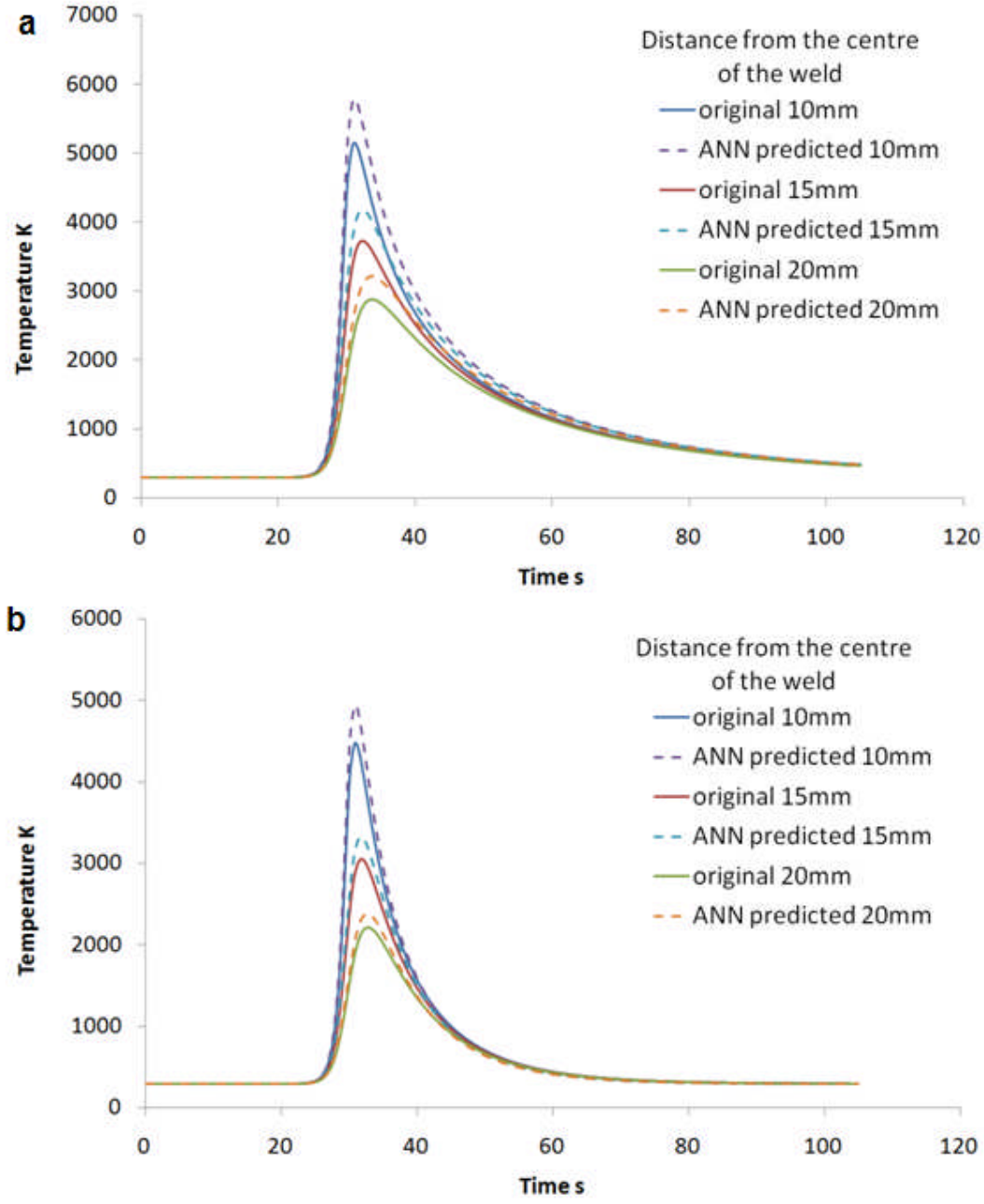

Figure A-4: Comparison between the original thermal profiles and the curves from the ANN predicted values for test conditions of (a) Q= 14262 W, and h = 200 W/(m^2K); and (b) Q= 5705 W, and k = 700 W/(m^2K). The results are from the 9 input method model with MLP topology and LM BP method applied to the single heat transfer coefficient model.

Appendix B2. Double heat transfer coefficient model

B2.1 Numerical model description

In this stage, a more complex problem is represented by the ANN model. As shown in Figure A-5, the bottom surface is separated into two areas with different heat transfer coefficients: the yellow area is defined as the welded area which has a higher heat transfer coefficient (h_c1), and a white area which has a lower value (h_c2). Separating the heat transfer coefficients in this way is similar to the separation of contact conductance by Colegrove et al.[5]. The other settings are the same as the previous model.

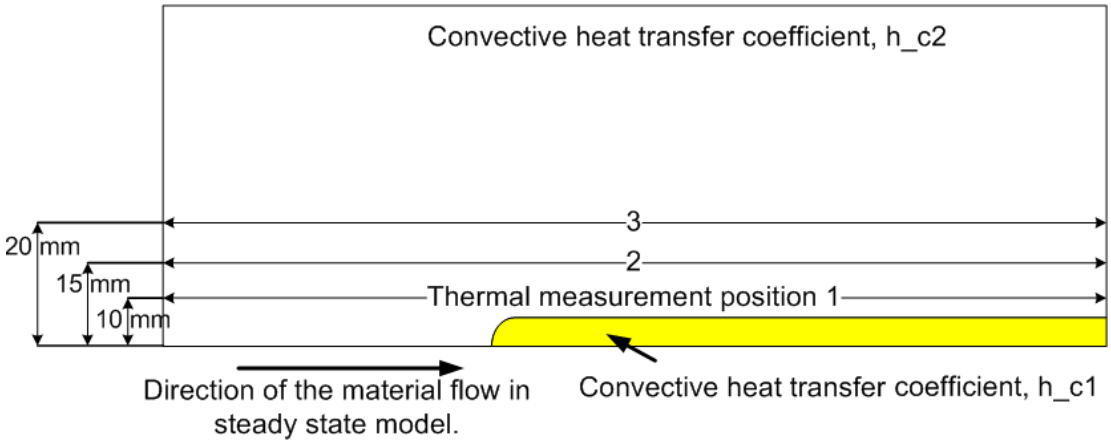

Figure A-5: Regions where the two convective heat transfer coefficients are applied

B2.2 Training thermal data

Three power input values, four values of h_c1 and four values of h_c2 formed forty-eight training combinations. Three thermal profiles were obtained for each training combination at distances of 10, 15 and 20 mm from the heat source. The heat transfer coefficients and power inputs used for training are shown in Table A-5. The combinations used for testing are shown in Table A-6.

Q (W)	h_c1 (W/(m^{2}K))	h_c2 (W/(m^{2}K))
4754	50	0.5
9508	100	5
14262	1000	50
	10000	100

Table A-5: Data used for training the double heat transfer coefficient model

Combinations for testing		
Q (W)	h_c1 (W/(m^{2}K))	h_c2 (W/(m^{2}K))
11410	500	50
13311	5000	10
7606	1500	75
5705	8000	1

Table A-6: Data used for testing the double heat transfer coefficient model

B2.3 ANN models applied

At the same time, the influence of different ANN models with different topologies and gradient descent methods are also studied. The different ANN models applied to the problem are summarized in Table A-7.

	Abstracting methods		
ANN types	9 input	6 input	Five point temperatures
MLP, momentum	n/a	n/a	ANN5
MLP, LM	ANN1	n/a	n/a
Feedforward, LM	ANN2	n/a	n/a
MFF, LM	ANN3	ANN4	n/a

Table A-7: ANN models and abstracting methods applied to the double heat transfer coefficient model

B2.4 Results

The results from the 9 input method with the MLP topology and LM gradient descent method are shown Table A-7. The ANN model takes a long time to solve and fails to predict the heat transfer coefficients accurately, particularly h_c2.

Desired Values			Predicted Values			MRE
Q (W)	h_c1(W/(m^{2}K))	h_c2 (W/(m^{2}K))	Q (W)	h_c1 (W/(m^{2}K))	h_c2 (W/(m^{2}K))	
11410	500	50	12139	257	105	82.9%
13311	5000	10	14774	9982	-5.02	130.5%
7606	1500	75	5305	1264	105	43.3%
5705	8000	1	14398	10005	-5.02	389%
					Average	161%

Table A-8: Results from ANN1 (9 input method and MLP under LM rule)

To determine whether this is a poor result was a consequence of the ANN structure, the neural network model topology is modified into a GFF network. The results are shown in Table A-9, which indicates that there is an improvement in the prediction of h_c1, however some of the results are still poor, especially the one for the last training value.

Desired Values			Predicted Values			MRE
Q (W)	h_c1 (W/(m^{2}K))	h_c2 (W/(m^{2}K))	Q (W)	h_c1 (W/(m^{2}K))	h_c2 (W/(m^{2}K))	
11410	500	50	11722	-36	20.4	84.7%
13311	5000	10	14031	7400	25.6	105%
7606	1500	75	7915	1358	104	26.0%
5705	8000	1	4924	9500	102	5090%
					Average	1326.38%

Table A-9: Results from ANN2 (9 input method and GFF under LM rule)

The ANN topology was then changed to a MFF networks, and the hidden layer is reduced to 5-5-5 to have a tolerable training speed. The results (Table A-10) give a similarly poor prediction.

Desired Values			Predicted Values			MRE
Q (W)	h_c1 (W/(m^{2}K))	h_c2 (W/(m^{2}K)	Q (W)	h_c1 (W/(m^{2}K))	h_c2 (W/(m^{2}K)	
11410	500	50	12334	608	28.6	36.3%
13311	5000	10	14628	9214	101	505.2%
7606	1500	75	7359	2645	97.2	54.6%
5705	8000	1	5211	9947	88.5	4390%
					Average	1247%

Table A-10: Results from ANN3 (9 input method and MFF under LM rule)

After discussing the influences of neural network structure, this stage will explore results from different methods of abstracting the thermal curves. To discover whether the neural network model is over-trained (using more than the required input data will confuse the neural network), the cooling slope is omitted. The inputs are peak temperature and integral of temperature against time. The results in Table A-11 show that the prediction performance is no better or worse than the previous one. This method was not investigated further.

Desired Values			Predicted Values			MRE
Q (W)	h_c1 (W/(m^{2}K))	h_c2 (W/(m^{2}K))	Q (W)	h_c1 (W/(m^{2}K))	h_c2 (W/(m^{2}K))	
11410	500	50	5286	9590	105	991 %
13311	5000	10	4228	10545	4.97	114 %
7606	1500	75	4756	-502	104	104 %
5705	8000	1	14742	-502	-5.03	433 %
					Average	411 %

Table A-11: Results from ANN4 (6 input method and MLP under LM rule)

Finally the five point temperature method was implemented with the MLP and the momentum decent method. Three hidden layers are included with a structure of 300-200-100 (more neurons to make the networks complex enough). The results in Table A-12 show that this method is able to provide better predictions of the heat transfer coefficients than the power input. The clustering of the input values around the end of the thermal profile enable the heat transfer coefficients to be predicted. The five point temperature method is not applied with the MFF topology because of the large amount of training data and extremely long training time (more than 200 hours).

Desired Values			Predicted Values			MRE
Q (W)	h_c1 (W/(m^{2}K))	h_c2 (W/(m^{2}K))	Q (W)	h_c1 (W/(m^{2}K))	h_c2 (W/(m^{2}K))	
11410	500	50	6744	2208	12.5	229%
13311	5000	10	12224	2091	25	108 %
7606	1500	75	12432	1913	22.6	80.5%
5705	8000	1	11144	2065	33.5	1707.5%
					Average	531%

Table A-12: Results from ANN5 (4 input method and MLP under momentum rule)

Among the low quality predictions, one of the closer matching results (first group from ANN3) were applied into the FE model for validation, and the curves are shown in Figure A-6. Although there is a discrepancy with the temperature, the cooling slopes matches well.

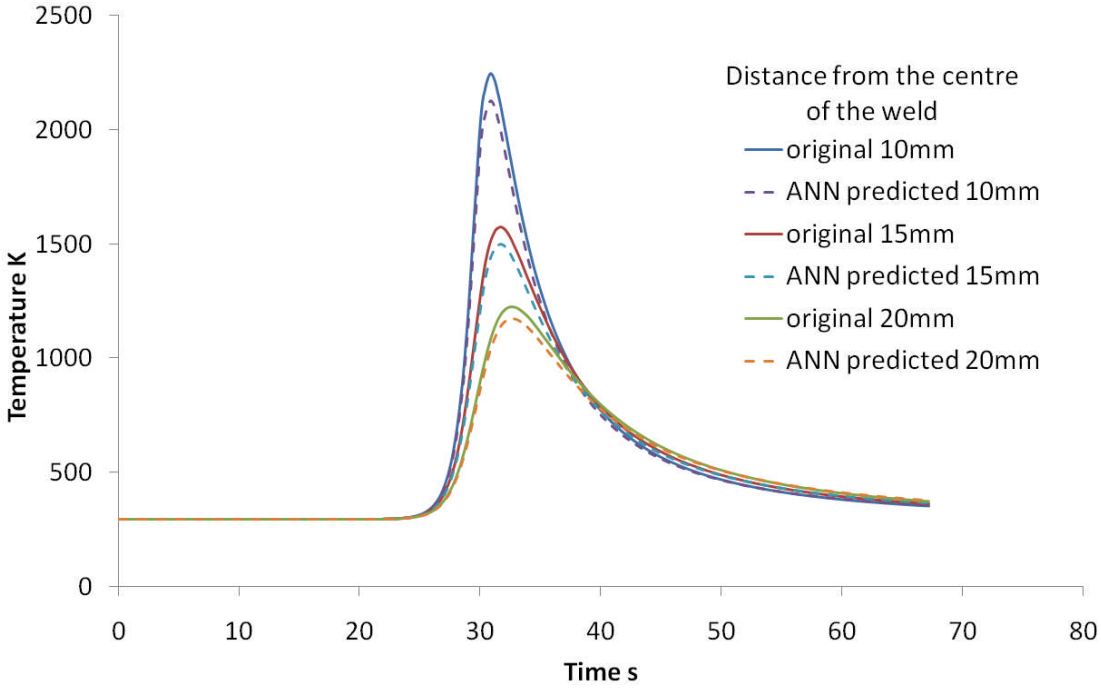

Figure A-6: Comparison between the original thermal profiles and the curves from the ANN predicted values for test conditions of (a) Q= 11410 W, h_c1 = 500 W/(m^{2}K)and h_c2 = 50 W/(m^{2}K). The result is from the 9 input method model with MFF topology and LM BP method applied to the double heat transfer coefficients model.

B2.5 Discussion

To conclude, the ANN method is able to represent a single heat transfer coefficient reasonably well, with typical errors of 10% in the prediction of the power and heat transfer coefficients. Predicting the boundary condition where two heat transfer coefficients are used has proven more difficult. Table A-13 summarises the models attempted and the quality of the predictions.

	Abstracting methods		
ANN types	9 input	6 input	Five point temperatures
MLP, momentum	n/a	n/a	partially predictable
MLP, LM	unable to predict	n/a	n/a
Feedforward, LM	unable to predict	n/a	n/a
MFF, LM	partially predictable	unable to predict	n/a

Table A-13: Summarized prediction results

The '9 input with overall cooling slope' with MFF topology and the LM decent method, and 'point temperatures' with MLP topology under momentum decent method are able to give the best predictions. The first method gave the best overall prediction while the second gave a better prediction of the heat transfer coefficients. It is clear however, that neither provides a particularly good prediction for the double heat transfer coefficient model, and the reason is further investigated.

B2.6 Investigation into the poor prediction performance of the double heat transfer coefficient model

The study of the double constant heat transfer coefficient model was not successful. After some detailed analysis, the reason for the failure was found to be the selection of the training data range for the heat transfer coefficients. In particular, it was too wide to represent the sample space. As shown in Table A-5, the training data chosen for the heat transfer coefficients are very scattered, particularly for h_c1 from 1000 to 10000. The other problem is that h_c1 values are much larger than h_c2, which results in an insensitivity of the ANN model to changes in the value of h_c2.

The effect of these parameters can be seen in some of the training data, which is shown in Table A-14. This shows the effect of changing the value of h_c2, while the input power and h_c1 are kept constant of 1000 W and 10000W/(m^2K) respectively. In the data sample for the failed heat transfer coefficients study, changing h_c2 had very little effect on the peak temperature, integral of temperature and cooling slope. The training data used in Table A-5 appears to confuse the ANN model, since it learns from understanding the variation in the data. In this case, the failure of heat transfer

coefficients study is due to the training data range selection, which is able to be fixed by applying a more restricted training data range.

Training data sample for heat transfer coefficients study (failure)					
Training output data			Training input data		
Q (W)	h_c1 (W/(m^{2}K))	h_c2 (W/(m^{2}K))	Peak temperature	Integral of Temperature	Cooling Slope
1000	10000	0.5	766.33	33717	-99.1
1000	10000	5	766.18	33710	-99.1
1000	10000	50	764.71	33647	-99.2
1000	10000	100	763.11	33587	-99.3

Table A-14: Table illustrating the effect of changing the value of h_c2 when the value of h_c1 is maximised

To demonstrate this, a less scattered training data range was selected for the heat transfer coefficient study. The training data set is shown in Table A-15, where forty-eight combinations were generated for training.

Q	h_c1 (W/(m^{2}K))	h_c2 (W/(m^{2}K))
5705	500	10
9508	800	100
13311	1000	300
	2000	500

Table A-15: Data used for training the neural network

An ANN model is developed with MFF topology (three hidden layers: 5-5-5) with LM learning rule for 1000 iterations (32 minutes). The results are shown in Table A-16, and demonstrate a considerable improvement in prediction quality.

Desired Values			Predicted Values			MRE
Q (W)	h_c1 (W/(m^{2}K))	h_c2 (W/(m^{2}K))	Q (W)	h_c1 (W/(m^{2}K))	h_c2 (W/(m^{2}K))	
7131	750	200	6329	754	209	8.21%
8557	1500	400	7876	1623	313	18.9%
11410	1800	50	12376	1927	40.5	17.3%
12360	600	150	12974	624	152.7	5.4%
					Average	12.4%

Table A-16: Updated results from9 input with MFF topology under LM rule

In summary, this preliminary study suggests the ANN technique can predict the thermal model power input and thermal boundary conditions, however careful selection of the training data set is essential.

Appendix C1. Detailed results from the application of the ANN technique to a single contact gap conductance model

The applied ANN models are shown in Table A-17, and have different thermal abstracting methods, gradient descent method and topologies.

New	Abstracting methods				
ANN topologies	Five point temperatures	9 input	6 input	4 input	2 input
MLP, momentum	n/a	ANN3	ANN7	ANN11	ANN15
MLP, LM	ANN1	ANN4	ANN8	ANN12	ANN16
MFF, LM	ANN2	ANN5	ANN9	ANN13	ANN17
GFF, LM	n/a	ANN6	ANN10	ANN14	ANN18

Table A-17: ANN topologies and thermal curve abstracting methods applied in the study, note the trails are sequenced

The results of this study are categorized according to the different thermal curve abstracting methods.

C1.1 The five point temperatures method

With this abstracting method, the ANN topology was modified and the MLP topology (three hidden layers: 6-4-3) with LM method was used and iterated for 1000 times. This method took approximately 31 minutes.

Desired Q (W)	Desired k (W/(m^{2}K))	Predicted Q (W)	Predicted k (W/(m^{2}K))	MRE
7131	2500	14011	4927	96.8%
9508	6000	14058	7878	39.6%
4754	1500	13910	884	116 %
12361	4000	14121	7875	55.6%
			Average	77.2%

Table A-18: Results from ANN1 (4 input method with MLP under LM rule)

The results in Table A-18 indicate that the selected training data is not able to predict the desired values accurately, providing further evidence that this was not an effective abstracting method.

A complex ANN model with MFF topology (three hidden layer: 5-5-5) with LM method was applied for 1000 iterations, which took nearly 150 minutes. The results are shown in Table A-19, and percentage errors indicate that this abstracting method was not able to predict the power and gap conductance as effectively as the previous abstracting method.

Desired Q (W)	Desired k (W/(m^{2}K))	Predicted Q (W)	Predicted k (W/(m^{2}K))	MRE
7131	2500	13390	7457	143 %
9508	6000	13593	7888	37.2%
4754	1500	13058	6924	268 %
12361	4000	13760	7888	54.3%
			Average	125%

Table A-19: Results from ANN2 (4 input method with MFF under LM rule)

C1.2 The 9 input method

This group of results are approached using nine inputs with overall cooling slope abstracting method. A simpler topology is established, MLP with momentum method (three hidden layers: 6-4-3), and the results are shown in Table A-20 which show large discrepancies.

Desired Q (W)	Desired k (W/(m^{2}K))	Predicted Q (W)	Predicted k (W/(m^{2}K))	MRE
7131	2500	7393	3394	19.7%
9508	6000	8003	3282	30.6%
4754	1500	5520	3755	83.2%
12361	4000	11604	2597	20.6%
			Average	38.6%

Table A-20: Results from ANN3 (9 input method with MLP under momentum rule)

To achieve a better prediction, the ANN model is modified into MLP topology with LM method (three hidden layers: 6-4-3), and iterated for 1000 times, which took approximately 4 minutes, the results are shown in Table A-21, which is an obvious improvement over the previous one.

Desired Q (W)	Desired k (W/(m^{2}K))	Predicted Q (W)	Predicted k (W/(m^{2}K))	MRE
7131	2500	7263	2535	1.64%
9508	6000	9333	5948	1.34%
4754	1500	4587	1470	2.74%
12361	4000	12577	3957	1.40%
			Average	1.78%

Table A-21: Results from ANN4 (9 input method with MLP under LM rule)

To observe whether more complex topology aims for better prediction, model is altered into a MFF topology with LM method (three hidden layers: 5-5-5) for 1000 iterations, and GFF with LM method (three hidden layers: 6-4-3). Results of MFF model are shown in Table A-22, which show another small overall improvement, but results of GFF model in Table A-23 showed that the GFF topology is not capable to predict as well as MFF.

Desired Q (W)	Desired k (W/(m^{2}K))	Predicted Q (W)	Predicted k (W/(m^{2}K))	MRE
7131	2500	7159	2543	1.07%
9508	6000	9516	6091	0.80%
4754	1500	4684	1484	1.26%
12361	4000	12528	4069	1.54%
			Average	1.17%

Table A-22: Results from ANN5 (9 input method with MFF under LM rule)

Desired Q (W)	Desired k (W/(m^{2}K))	Predicted Q (W)	Predicted k (W/(m^{2}K))	MRE
7131	2500	7313	2673	4.74%
9508	6000	9388	6315	3.26%
4754	1500	4576	1422	4.44%
12361	4000	12544	3706	4.42%
			Average	4.21%

Table A-23: Results from ANN6 (9 input method with GFF under LM rule)

All the results except MLP with momentum gradient method indicate that the ANN model is capable of predicting desired values with this thermal curve abstracting method.

C1.3 The 6 input method

The previous results led to a question, whether the cooling slope is necessary as an input component. To test this, the cooling slope is omitted from the input components, with the only inputs being the peak temperature and integral of temperature against time.

The first ANN model applied on 6 input method is MLP with momentum method (three hidden layers: 6-4-3), and the results are shown in Table A-24, which show that this ANN model is not capable to generate accurate predictions.

Desired Q (W)	Desired k (W/(m^{2}K))	Predicted Q (W)	Predicted k (W/(m^{2}K))	MRE
7131	2500	6837	3556	23.2%
9508	6000	7322	3466	32.6%
4754	1500	5794	3735	85.5%
12361	4000	11031	2736	21.2%
			Average	40.6%

Table A-24: Results from ANN7 (6 input method with MLP under momentum rule)

Similar to previous one, the second topology applied is the MLP topology with LM method (three hidden layers: 6-4-3). A group of much improved overall results were obtained, as shown in Table A-25.

Desired Q (W)	Desired k (W/(m^{2}K))	Predicted Q (W)	Predicted k (W/(m^{2}K))	MRE
7131	2500	7226	2504	0.75%
9508	6000	9434	5959	0.73%
4754	1500	4608	1491	1.81%
12361	4000	12498	4030	0.94%
			Average	1.06%

Table A-25: Results from ANN8 (6 input method with MLP under LM rule)

More complex topologies the MFF topology (three hidden layers: 5-5-5) under LM method, and the GFF with LM method (three hidden layers: 6-4-3). The results are shown in Table A-26 and Table A-27 respectively. Both the model can give accurate predictions very close to one from ANN8.

Desired Q (W)	Desired k (W/(m^{2}K))	Predicted Q (W)	Predicted k (W/(m^{2}K))	MRE
7131	2500	7258	2523	1.38%
9508	6000	9413	6016	0.63%
4754	1500	4578	1472	2.75%
12361	4000	12560	3993	0.90%
			Average	1.41%

Table A-26: Results from ANN9 (6 input method with MFF under LM rule)

Desired Q (W)	Desired k (W/(m^{2}K))	Predicted Q (W)	Predicted k (W/(m^{2}K))	MRE
7131	2500	7324	2493	1.48%
9508	6000	9332	5946	1.37%
4754	1500	4529	1503	2.49%
12361	4000	12609	4006	1.09%
			Average	1.61%

Table A-27: Results from ANN10 (6 input method with GFF under LM rule)

The results in this section show that the ANN can give a close prediction of the desired values without the cooling slopes as one input component.

C1.4 The 4 input method

Similarly to 6 input method, four topologies were applied to 4 input methods:

1. ANN11: MLP with momentum method
2. ANN12: MLP with LM method
3. ANN13: MFF with LM method
4. ANN14: GFF with LM method

The results of the models are shown in Table A-28, Table A-29, Table A-30 and Table A-31 respectively. The ANN12 (MLP with LM method) gives the best prediction

quality, while the one that used the momentum gradient descent method ANN11 failed to provide an accurate prediction of the input parameters.

Desired Q (W)	Desired k (W/(m^{2}K))	Predicted Q (W)	Predicted k (W/(m^{2}K))	MRE
7131	2500	6786	3665	25.7%
9508	6000	6978	3607	33.2%
4754	1500	5847	3966	93.7%
12361	4000	10752	2554	24.6%
			Average	44.3%

Table A-28: Results from ANN11 (4 input method with MLP under momentum)

Desired Q (W)	Desired k (W/(m^{2}K))	Predicted Q (W)	Predicted k (W/(m^{2}K))	MRE
7131	2500	7203	2500	0.52%
9508	6000	9429	6061	0.93%
4754	1500	4636	1492	1.50%
12361	4000	12504	4020	0.84%
			Average	0.95%

Table A-29: Results from ANN12 (4 input method with MLP under LM rule)

Desired Q (W)	Desired k (W/(m^{2}K))	Predicted Q (W)	Predicted k (W/(m^{2}K))	MRE
7131	2500	7258	2503	0.96%
9508	6000	9382	6009	0.74%
4754	1500	4591	1491	2.00%
12361	4000	12563	4015	1.02%
			Average	1.18%

Table A-30: Results from ANN13 (4 input method with MFF under LM rule)

Desired Q (W)	Desired k (W/(m^{2}K))	Predicted Q (W)	Predicted k (W/(m^{2}K))	MRE
7131	2500	7264	2508	1.11%
9508	6000	9360	6006	0.83%
4754	1500	4573	1483	2.45%
12361	4000	12557	4016	1.01%
			Average	1.35%

Table A-31: Results from ANN14 (4 input method with GFF under LM rule)

C1.5 The 2 input method

It is worth testing the 2 input method, since it inputs less information into the ANN model. Four topologies were applied to 2 input methods:

1. ANN11: MLP with momentum method
2. ANN12: MLP with LM method
3. ANN13: MFF with LM method
4. ANN14: GFF with LM method

The results of the models are shown in Table A-28, Table A-29, Table A-30 and Table A-31 respectively. The results show that 2 input method gives poor predictions due to the little information inputted into the ANN models.

Desired Q (W)	Desired k (W/(m^{2}K))	Predicted Q (W)	Predicted k (W/(m^{2}K))	MRE
7131	2500	6445	3551	25.8%
9508	6000	6957	3465	34.5%
4754	1500	5713	3669	82.4%
12361	4000	11374	2713	20.1%
			Average	40.7%

Table A-32: Results from ANN15 (2 input method with MLP under momentum)

Desired Q (W)	Desired k (W/(m^{2}K))	Predicted Q (W)	Predicted k (W/(m^{2}K))	MRE
7131	2500	7447	2599	4.21%
9508	6000	7265	1117	52.5%
4754	1500	5944	2025	30.0%
12361	4000	13503	4927	16.2%
			Average	25.7%

Table A-33: Results from ANN16 (2 input method with MLP under LM rule)

Desired Q (W)	Desired k (W/(m^{2}K))	Predicted Q (W)	Predicted k (W/(m^{2}K))	MRE
7131	2500	6778	1796	16.5%
9508	6000	5452	946	63.4%
4754	1500	6085	4294	107%
12361	4000	13832	5932	30.1%
			Average	54.3%

Table A-34: Results from ANN17 (2 input method with MFF under LM rule)

Desired Q (W)	Desired k (W/(m^{2}K))	Predicted Q (W)	Predicted k (W/(m^{2}K))	MRE
7131	2500	11205	937	59.8%
9508	6000	6261	976	58.9%
4754	1500	3790	5357	138%
12361	4000	13641	5356	22.1%
			Average	69.9%

Table A-35: Results from ANN18 (2 input method with GFF under LM rule)

Appendix C2. Detailed results from the application of the ANN technique to a double contact gap conductance model

As described previously, the 4 input abstracting method was the best one for representing a single contact gap conductance model. Therefore, when representing the double contact gap conductance model, the 4 input is applied with the 9 input method as shown in Table A-36 below. In addition, only the LM gradient descent method was used as this proved the most successful in the previous section.

ANN types	Abstracting methods	
	4 input	9 input
MFF, LM	ANN1	ANN3
GFF, LM	ANN2	ANN4

Table A-36: ANN topologies used in the study

C2.1 The 4 input method

The ANN model with MFF topology (three hidden layers: 5-5-5) with LM method applied for 1000 iterations, which took approximately 17 minutes. The results are shown in Table A-37.

Desired Values			Predicted Values			MRE
Q (W)	k_c1 (W/(m^{2}K))	k_c2 (W/(m^{2}K))	Q (W)	k_c1 (W/(m^{2}K))	k_c2 (W/(m^{2}K))	
7606	3000	400	6890	3101	426	9.77%
11410	1000	200	12262	818	164	21.7%
13311	7000	50	13914	7644	44	12.6%
7131	2500	250	6457	2475	246	5.85%
					Average	12.5%

Table A-37: Results from ANN1 (4 input method with MFF under LM rule)

The results are not as precise as those obtained for the single gap conductance model. The ANN topology is altered into a GFF topology (three hidden layers: 9-6-6) with LM method and trained for 1000 iterations, which took 50 minutes.

Desired Values			Predicted Values			MRE
Q (W)	k_c1 (W/(m^{2}K))	k_c2 (W/(m^{2}K))	Q (W)	k_c1 (W/(m^{2}K))	k_c2 (W/(m^{2}K))	
7606	3000	400	6922	3020	426	8.20%
11410	1000	200	12382	944	164	15.9%
13311	7000	50	13910	7293	44.3	10.0%
7131	2500	250	6474	2525	246	5.74%
					Average	9.97%

Table A-38: Results from ANN2 (4 input method with GFF under LM rule)

As shown in Table A-38, the results are slightly improved with this topology.

C2.2 The 9 input method

The nine inputs method is applied to compare with four inputs method. The ANN model is with MFF topology (three hidden layers: 5-5-5) with LM method and applied for 1000 iterations, which took 25 minutes. The results are shown in Table A-39.

Desired Values			Predicted Values			MRE
Q (W)	k_c1 (W/(m^{2}K))	k_c2 (W/(m^{2}K))	Q (W)	k_c1 (W/(m^{2}K))	k_c2 (W/(m^{2}K))	
7606	3000	400	6882	2904	317	16.6%
11410	1000	200	12404	1100	115	30.5%
13311	7000	50	13922	7390	42.1	13.0%
7131	2500	250	6436	2474	272	9.86%
					Average	17.5%

Table A-39: Results from ANN3 (9 input method with MFF under LM rule)

The results are even worse compared to those from the four inputs method. The ANN model is tested with GFF topology (three hidden layers: 9-6-6) with LM method for 1000 iterations, which took almost 725 minutes.

Desired Values			Predicted Values			MRE
Q (W)	k_c1 (W/(m^{2}K))	k_c2 (W/(m^{2}K))	Q (W)	k_c1 (W/(m^{2}K))	k_c2 (W/(m^{2}K))	
7606	3000	400	6980	3059	453	11.7%
11410	1000	200	12422	964	188	9.09%
13311	7000	50	14091	7876	43.1	16.1%
7131	2500	250	6527	2495	274	9.14%
					Average	11.5%

Table A-40: Results from ANN4 (9 input method with GFF under LM rule)

The results (Table A-40) are closer to the previous ones, but the error is larger than the 4 input method and it took longer to solve.

Appendix C3. Detailed results from the application of the ANN technique to a temperature dependent contact gap conductance model

The applied ANN models are shown in Table A-41, varying by the thermal abstracting methods, and ANN topologies.

ANN types	Abstracting methods		
	4 input	9 input	6 input
MFF (5-5-5), LM	ANN1	ANN5	ANN9
MFF (9-6-6), LM	ANN2	ANN6	ANN10
GFF, LM	ANN3	ANN7	ANN11
MLP, LM	ANN4	ANN8	ANN12

Table A-41: ANN topologies and thermal curve abstracting methods applied in the study

C3.1 The 4 input method

The ANN model with MFF topology (three hidden layers: 5-5-5) with LM method and iterated for 1000 times took 16 minutes to solve. The results in Table A-42 show a reasonably large discrepancy.

Desired Values			Predicted Values			MRE
Q (W)	a (W/(m^{2}K))	b (K^{-1})	Q (W)	a (W/(m^{2}K))	b (K^{-1})	
2377	12.86	1.40E-02	2162	8.78	1.54E-02	17.0%
2852	21.44	1.10E-02	2470	35.5	1.13E-02	27.1%
4754	30.02	8.00E-03	5108.	30.6	8.16E-03	3.73%
5229	23.59	6.00E-03	5453	26.8	5.50E-03	8.71%
					Average	14.2%

Table A-42: Results from ANN1 (4 input method with MFF under LM rule, hidden layer 5-5-5)

To reduce the discrepancy, the neurons in the hidden layer were increased to 9-6-6 for testing. The results are shown in Table A-43 which shows no improvements, although it took longer to train.

Desired Values			Predicted Values			MRE
Q (W)	a (W/(m^{2}K))	b (K^{-1})	Q (W)	a (W/(m^{2}K))	b (K^{-1})	
2377	12.86	1.40E-02	2169	1.74	1.45E-02	18.1%
2852	21.44	1.10E-02	2437	8.07	1.18E-02	27.9%
4754	30.02	8.00E-03	5121	7.66	8.43E-03	7.52%
5229	23.59	6.00E-03	5465	5.53	5.70E-03	3.37%
					Average	14.2%

Table A-43: Results from ANN2 (4 input method with MFF under LM rule, hidden layer 9-6-6)

As a more rapid working method, MLP topology (three hidden layers: 9-6-3) with LM method is also applied for 1000 iterations, which took 4 minutes. The results as shown in Table A-44 are similar.

Desired Values			Predicted Values			MRE
Q (W)	a (W/(m^{2}K))	b (K^{-1})	Q (W)	a (W/(m^{2}K))	b (K^{-1})	
2377	12.86	1.40E-02	1905	12.8	1.42E-02	7.23%
2852	21.44	1.10E-02	1925	23.3	1.05E-02	15.2%
4754	30.02	8.00E-03	5702	25.5	9.94E-03	19.7%
5229	23.59	6.00E-03	5596	26.8	5.01E-03	12.3%
					Average	13.6%

Table A-44: Results from ANN3 (4 input method with MLP under LM rule)

Further tried ANN model is with GFF topology (three hidden layers: 9-6-6) with LM method for 1000 iterations and took 26 minutes. The results shown in Table A-45 are again poor.

Desired Values			Predicted Values			MRE
Q (W)	a (W/(m^{2}K))	b (K^{-1})	Q (W)	a (W/(m^{2}K))	b (K^{-1})	
2377	12.86	1.40E-02	2086	9.38	1.46E-02	14.6%
2852	21.44	1.10E-02	2339	13.5	1.09E-02	18.6%
4754	30.02	8.00E-03	5242	34.6	1.12E-02	21.8%
5229	23.59	6.00E-03	5407	16.3	6.04E-03	11.6%
					Average	16.7%

Table A-45: Results from ANN4 (4 input method with GFF under LM rule)

The results from MFF topology under LM method are better although they are still not considered to be a good prediction. It is therefore worth investigating different abstracting methods for this complex problem.

C3.2 The 9 input method

The first ANN model with this abstracting method is a MFF topology (three hidden layers: 5-5-5) with LM learning method for 1000 iterations, which took 30 minutes. The results are shown in Table A-46, which show that this method is able to predict the results better for some conditions. Although the overall prediction is better than the previous models, it is worth checking whether increasing the neurons in the hidden layers into 9-6-6 improves the prediction quality. The result is shown in Table A-47, the overall quality is slightly worse.

Desired Values			Predicted Values			MRE
Q (W)	a (W/(m^{2}K))	b (K^{-1})	Q (W)	a (W/(m^{2}K))	b (K^{-1})	
2377	12.86	1.40E-02	2214	7.91	1.51E-02	17.7%
2852	21.44	1.10E-02	2548	21.7	1.16E-02	5.58%
4754	30.02	8.00E-03	5040	30.2	7.81E-03	2.97%
5229	23.59	6.00E-03	5476	21.5	5.69E-03	6.22%
					Average	8.11%

Table A-46: Results from ANN5 (9 input method with MFF under LM rule, hidden layer 5-5-5)

Desired Values			Predicted Values			MRE
Q (W)	a (W/(m^{2}K))	b (K^{-1})	Q (W)	a (W/(m^{2}K))	b (K^{-1})	
2377	12.86	1.40E-02	1995	2.08	1.46E-02	17.1%
2852	21.44	1.10E-02	2276	6.89	9.81E-03	22.9%
4754	30.02	8.00E-03	5163	8.27	8.75E-03	12.0%
5229	23.59	6.00E-03	5541	5.63	5.53E-03	5.37%
					Average	14.4%

Table A-47: Results from ANN6 (9 input method with MFF under LM rule, 9-6-6)

Applying MLP (three hidden layers: 9-6-3) with LM for 1000 iterations (7 minutes) resulted in a poorer prediction, as shown in Table A-48.

Desired Values			Predicted Values			MRE
Q (W)	a (W/(m^{2}K))	b (K^{-1})	Q (W)	a (W/(m^{2}K))	b (K^{-1})	
2377	12.86	1.40E-02	1925	34.8	1.14E-02	69.5%
2852	21.44	1.10E-02	1921	7.46	1.49E-02	44.4%
4754	30.02	8.00E-03	5570	35.7	5.73E-03	21.5%
5229	23.59	6.00E-03	5642	35.7	5.07E-03	25.0%
					Average	40.1%

Table A-48: Results from ANN7 (9 input method with MLP under LM rule)

Finally altering the ANN model into GFF topology (three hidden layers: 9-6-6) with LM method for 1000 iterations (42 minutes) resulted in the best prediction of the desired values, as shown in Table A-49.

Desired Values			Predicted Values			MRE
Q (W)	a (W/(m^{2}K))	b (K^{-1})	Q (W)	a (W/(m^{2}K))	b (K^{-1})	
2377	12.86	1.40E-02	2110	10.1	1.45E-02	12.3%
2852	21.44	1.10E-02	2517	19.9	1.12E-02	7.00%
4754	30.02	8.00E-03	5094	35.7	8.01E-03	8.75%
5229	23.59	6.00E-03	5364	23.7	5.75E-03	2.39%
					Average	7.62%

Table A-49: Results from ANN8 (9 input method with GFF under LM rule)

C3.3 The 6 input method

To investigate whether using cooling slope is necessary in this case, six input method is applied for different ANN models. The first model is applied with MFF topology (three hidden layers: 5-5-5) under LM method for 1000 iterations, which took 23 minutes. The results are shown in Table A-50, which does not predict the desired values accurately. The ANN model is modified into 9-6-6 for testing, and the results are given in Table A-51, which are much better than the previous prediction.

Desired Values			Predicted Values			MRE
Q (W)	a (W/(m^{2}K))	b (K^{-1})	Q (W)	a (W/(m^{2}K))	b (K^{-1})	
2377	12.86	1.40E-02	1957	14.33	1.23E-02	13.65%
2852	21.44	1.10E-02	2149	32.70	6.60E-03	39.03%
4754	30.02	8.00E-03	5071	31.45	8.09E-03	4.18%
5229	23.59	6.00E-03	5255	31.90	5.19E-03	16.42%
					Average	18.32%

Table A-50: Results from ANN9 (6 input method with MFF under LM rule, hidden layer 5-5-5)

Desired Values			Predicted Values			MRE
Q (W)	a (W/(m^{2}K))	b (K^{-1})	Q (W)	a (W/(m^{2}K))	b (K^{-1})	
2377	12.86	1.40E-02	2057	1.80	1.52E-02	20.7%
2852	21.44	1.10E-02	2284	4.15	1.24E-02	16.6%
4754	30.02	8.00E-03	5127	7.53	7.07E-03	9.02%
5229	23.59	6.00E-03	5479	5.32	5.55E-03	5.19%
					Average	12.9%

Table A-51: Results from ANN10 (6 input method with MFF under LM rule, hidden layer 9-6-6)

The usage of MLP topology (three hidden layers: 9-6-3) with LM method for 1000 iterations (4 minutes) resulted in a worse prediction quality (Table A-52), but this method needs much less time for training:

Desired Values			Predicted Values			MRE
Q (W)	a (W/(m^{2}K))	b (K^{-1})	Q (W)	a (W/(m^{2}K))	b (K^{-1})	
2377	12.86	1.40E-02	1943	15.7	1.51E-02	16.0%
2852	21.44	1.10E-02	1990	35.6	8.65E-03	39.2%
4754	30.02	8.00E-03	5582	8.61	7.75E-03	30.6%
5229	23.59	6.00E-03	5654	7.16	5.30E-03	29.8%
					Average	28.9%

Table A-52: Results from ANN11 (6 input method with MLP under LM rule)

Alerting the ANN model into GFF topology (three hidden layers: 9-6-6) under LM method for 1000 iterations (41 minutes) is able to improve the prediction to an acceptable level, as shown in Table A-53.

Desired Values			Predicted Values			MRE
Q (W)	a (W/(m^{2}K))	b (K^{-1})	Q (W)	a (W/(m^{2}K))	b (K^{-1})	
2377	12.86	1.40E-02	2105	9.69	1.39E-02	12.3%
2852	21.44	1.10E-02	2470	13.7	1.03E-02	18.6%
4754	30.02	8.00E-03	5133	34.1	7.90E-03	7.63%
5229	23.59	6.00E-03	5343	23.3	5.33E-03	4.83%
					Average	10.9%

Table A-53: Results from ANN12 (6 input method with GFF under LM rule)

Appendix D

The numerical results of the applied model types are given in the Table A-54 and Table A-55, including the model conditions, heat generation results and deformation region areas.

Rotation speed: 400 RPM						
Model type	CSRR	Slip coefficient	Viscous heat (W)	Friction heat (W)	Total heat (W)	Area (m^2)
1	100%		1816.4		1816.4	1.23E-04
2	100%		1816.5		1816.5	1.23E-04
3	100%	0.999	1814.5	1.83	1816.3	1.23E-04
4	68.4%		999.0		999.0	3.73E-05
5	68.4%		999.1		999.1	3.75E-05
6	68.4%	0.999	998.0	1.03	999.0	3.75E-05
Rotation speed: 600 RPM						
Model type	CSRR	Slip coefficient	Viscous heat (W)	Friction heat (W)	Total heat (W)	Area (m^2)
1	100%		2145.2		2145.2	1.40E-04
2	100%		2086.4		2086.4	1.33E-04
3	100%	0.64	1331.6	755.78	2087.4	1.29E-04
4	68.4%		1227.4		1227.4	4.21E-05
5	68.4%		1227.3		1227.3	4.23E-05
6	68.4%	0.99	1214.1	12.49	1226.6	4.22E-05
Rotation speed: 800 RPM						
Model type	CSRR	Slip coefficient	Viscous heat (W)	Friction heat (W)	Total heat (W)	Area (m^2)
1	100%		2395.8		2395.8	1.51E-04
2	100%		2114.2		2114.2	1.01E-04
3	100%	0.125	237.3	1877.23	2114.6	9.41E-05
4	68.4%		1404.0		1404.0	4.76E-05
5	68.4%		1403.9		1403.9	4.78E-05
6	68.4%	0.99	1388.8	14.21	1403.0	4.76E-05
Rotation speed: 1200 RPM						
Model type	CSRR	Slip coefficient	Viscous heat (W)	Friction heat (W)	Total heat (W)	Area (m^2)
1	100%		2786.1		2786.1	1.65E-04
2	100%		2134.4		2134.4	2.38E-05
3	100%	No model was possible.				
4	68.4%		1672.9		1672.9	5.65E-05
5	68.4%		1621.6		1621.6	5.33E-05
6	68.4%	0.62	999.8	621.35	1621.2	5.02E-05

Table A-54: The results of applying the different model types on 6082-T6, including the heat generation, deformed region areas and corresponding boundary condition values, categorized by different rotation speeds

Rotation speed: 400 RPM						
Model type	CSRR	Slip coefficient	Viscous heat (W)	Friction heat (W)	Total heat (W)	Area (m^2)
1	100%		2139.3		2139.3	1.46E-04
2	100%		1716.0		1716.0	4.10E-05
3	100%	0.105	47.5	1668.9	1716.4	8.51E-05
4	68.4%		1207.9		1207.9	4.76E-05
5	68.4%		1206.6		1206.6	4.80E-05
6	68.4%	0.99	1194.4	12.4	1206.8	4.79E-05
7	100%	0.999				1.23E-04
8	68.4%	0.999				3.75E-05
Rotation speed: 600 RPM						
Model type	CSRR	Slip coefficient	Viscous heat (W)	Friction heat (W)	Total heat (W)	Area (m^2)
1	100%		2492.7		2492.7	1.57E-04
2	100%		1714.9		1714.9	2.35E-05
3	100%	No model was possible.				
4	68.4%		1481.1		1481.1	5.57E-05
5	68.4%		1304.6		1304.6	3.79E-05
6	68.4%	0.255	290.3	1015.2	1305.5	4.44E-05
7	100%	0.64				1.29E-04
8	68.4%	0.99				4.22E-05
Rotation speed: 800 RPM						
Model type	CSRR	Slip coefficient	Viscous heat (W)	Friction heat (W)	Total heat (W)	Area (m^2)
1	100%		2783.7		2783.7	1.63E-04
2	100%		1717.0		1717.0	2.19E-05
3	100%	No model was possible.				
4	68.4%		1661.1		1661.1	5.90E-05
5	68.4%		1295.7		1295.7	3.12E-05
6	68.4%	0.096	23.0	1272.6	1295.6	5.07E-05
7	100%	0.125				9.41E-05
8	68.4%	0.99				4.76E-05
Rotation speed: 1200 RPM						
Model type	CSRR	Slip coefficient	Viscous heat (W)	Friction heat (W)	Total heat (W)	Area (m^2)
1	100%		3269.1		3269.1	1.73E-04
2	100%		1726.0		1726.0	1.88E-05
3	100%	No model was possible.				
4	68.4%		1951.2		1951.2	6.53E-05
5	68.4%		1292.7		1292.7	2.64E-05
6	68.4%	No model was possible.				
7	n/a	No model was possible.				
8	68.4%	0.62				5.02E-05

Table A-55: The results of applying difference model types on 7449-T7, including the heat generations, deformed region areas and corresponding boundary condition values, categorized by different rotation speeds

References

1. COMSOL: "Heat Transfer Module User's Guide", in *COMSOL Multiphysics*, COMSOL AB. 2005.

2. Y. S. Touloukian: 'Thermal Conductivity: Non Metallic Solids', 1970, New York, Plenum.

3. Y. S. Touloukian: 'Specific Heat: Non Metallic Solids', 1970, New York, Plenum.

4. Y. J. Chao and X. Qi: 'Thermal and thermo-mechanical modeling of friction stir welding of aluminum alloy 6061-T6', *Journal of Materials Processing and Manufacturing Science*, 1998, 7, 215-233.

5. P. A. Colegrove, H. R. Shercliff and R. Zettler: 'Model for predicting heat generation and temperature in friction stir welding from the material properties', *Science and Technology of Welding and Joining*, 2007, 12, 284-297.